

<https://doi.org/10.15388/vu.thesis.508>
<https://orcid.org/0000-0002-4725-6498>

VILNIUS UNIVERSITY
CENTRE OF PHYSICAL SCIENCES AND TECHNOLOGY

Rasa Karalkevičienė

Development of New Methods for the Synthesis of Bulk and Coatings of Calcium Hydroxyapatite

DOCTORAL DISSERTATION

Natural Sciences,
Chemistry N 003

VILNIUS 2023

This dissertation was written between 2019 and 2023 at Vilnius University

Academic Supervisor:

Prof. Habil. Dr. Aivaras Kareiva (Vilnius University, Natural Sciences, Chemistry – N 003).

Academic Consultant:

Prof. Dr. Aleksej Žarkov (Vilnius University, Natural Sciences, Chemistry – N 003).

This doctoral dissertation will be defended in a public meeting of the Dissertation Defence Panel:

Chairman – Assoc. Prof. Dr. Tatjana Kochanė (Vilnius University, Natural Sciences, Chemistry – N 003).

Members:

Prof. Dr. Jurgis Barkauskas (Vilnius University, Natural Sciences, Chemistry – N 003).

Assoc. Prof. Dr. Eglė Fataraitė-Urbonienė (Kaunas University of Technology, Technological Sciences, Materials Engineering – T 008).

Prof. Dr. Giovanni Calogero Li Destri Nicosia (University of Catania, Department of CHEMICAL SCIENCES, PHYSICAL CHEMISTRY (CHIM/02).

Assoc. Prof. Dr. Evaldas Naujalis (Centre for Physical Sciences and Technology, Natural Sciences, Chemistry – N 003).

The dissertation shall be defended at a public meeting of the Dissertation Defence Panel at 16 p.m. on 29 September 2023 in Inorganic Chemistry auditorium 141 of the Institute of Chemistry, Faculty of Chemistry and Geoscience, Vilnius University. Address: Naugarduko street 24, LT-03225 Vilnius, Lithuania. Tel.: +370 5 2193108. Fax: +370 5 2330987.

The text of this dissertation can be accessed at the **Vilnius University and Center for Physical Sciences and Technology libraries**, as well as on the website of Vilnius University: www.vu.lt/lt/naujienos/ivykiu-kalendarius

<https://doi.org/10.15388/vu.thesis.508>

<https://orcid.org/0000-0002-4725-6498>

VILNIAUS UNIVERSITETAS
FIZINIŲ IR TECHNOLOGIJOS MOKSLŲ CENTRAS

Rasa Karalkevičienė

Naujų kalcio hidroksiapatito miltelių ir dangų sintezės metodų vystymas

DAKTARO DISERTACIJA

Gamtos mokslai,
Chemija N 003

VILNIUS 2023

Disertacija rengta 2019–2023 metais studijuojant doktorantūroje Vilniaus universiteto Chemijos ir geomokslų fakulteto Chemijos institute.

Mokslinis vadovas:

prof. habil. dr. Aivaras Kareiva (Vilniaus universitetas, gamtos mokslai, chemija – N 003).

Mokslinis konsultantas:

prof. dr. Aleksej Žarkov (Vilniaus universitetas, gamtos mokslai, chemija – N 003).

Gynimo taryba:

Pirmininkė – **doc. dr. Tatjana Kochanė** (Vilniaus universitetas, gamtos mokslai, chemija – N 003).

Nariai:

prof. dr. Jurgis Barkauskas (Vilniaus universitetas, gamtos mokslai, chemija – N 003);

doc. dr. Eglė Fataraitė-Urbonienė (Kauno technologijos universitetas, technologijos mokslai, medžiagų inžinerija – T 008);

prof. dr. Giovanni Calogero Li Destri Nicosia (Katelijos universitetas, Chemijos mokslų katedra, Fizikinė chemija (CHIM/02)).

doc. dr. Evaldas Naujalis (Fizinių ir technologijos mokslų centras, gamtos mokslai, chemija – N 003).

Disertacija ginama viešame Gynimo tarybos posėdyje 2023 m. rugsėjo mėn. 29 d. 16 val. Vilniaus universiteto Chemijos ir geomokslų fakulteto Chemijos instituto Neorganinės chemijos auditorijoje.

Adresas: Naugarduko g. 24, LT-03225 Vilnius, Lietuva. Tel.: 2193108. Faksas: 2330987.

Disertaciją galima peržiūrėti Vilniaus universiteto, Fizinių ir technologijos mokslų centro bibliotekose ir VU interneto svetainėje adresu: <https://www.vu.lt/naujienos/ivykiu-kalendorius>

CONTENTS

| | |
|--|----|
| LIST OF ABBREVIATIONS..... | 7 |
| INTRODUCTION..... | 8 |
| 1. LITERATURE OVERVIEW..... | 12 |
| 1.1 Basic aspects of human bone | 12 |
| 1.2 Synthetic calcium hydroxyapatite ($\text{Ca}_{10}(\text{PO}_4)_6(\text{OH})_2$)..... | 14 |
| 1.3 Synthesis methods..... | 17 |
| 1.3.1 Bulk | 17 |
| 1.3.2 Coatings..... | 18 |
| 1.4 Applications | 23 |
| 2. EXPERIMENTAL | 24 |
| 2.1 Materials..... | 24 |
| 2.2 Synthesis of $\text{Ca}_{10}(\text{PO}_4)_6(\text{OH})_2$ coatings..... | 24 |
| 2.3 Synthesis of $\text{Ca}_{10}(\text{PO}_4)_6(\text{OH})_2$ powders..... | 26 |
| 2.4 Characterization techniques | 28 |
| 3. RESULTS AND DISCUSSION | 30 |
| 3.1 Development of low-temperature method for the formation of bioceramic nano-calcium hydroxyapatite coatings using sol-gel and dissolution-precipitation processing..... | 30 |
| 3.1.1 Formation of $\text{Ca}_{10}(\text{PO}_4)_6(\text{OH})_2$ coatings on silicon substrate.. | 30 |
| 3.1.2 Formation of $\text{Ca}_{10}(\text{PO}_4)_6(\text{OH})_2$ coatings on titanium substrate | 35 |
| 3.1.3 Electrochemical characterization..... | 40 |
| 3.2 Solvothermal synthesis of calcium-deficient hydroxyapatite via hydrolysis of α -tricalcium phosphate | 43 |
| 3.2.1 Investigation of influence of organic solvent on the formation of CHAp | 44 |
| 3.2.2 Investigation of influence of different organic additives on the formation of CHAp..... | 55 |
| CONCLUSIONS | 66 |
| LIST OF PUBLICATIONS AND CONFERENCES PARTICIPATION ... | 68 |

| | |
|------------------------------|-----|
| ACKNOWLEDGEMENTS | 70 |
| REFERENCES | 72 |
| SUMMARY IN LITHUANIAN | 83 |
| CURRICULUM VITAE | 107 |
| COPIES OF PUBLICATIONS | 109 |

LIST OF ABBREVIATIONS

| | |
|--------------------|---|
| ALD | Atomic layer deposition |
| Asp | DL-Aspartic acid |
| BET | Brunauer-Emmett-Teller |
| BJH | Barrett-Joyner-Halenda |
| CaCO ₃ | Calcium carbonate |
| CaHPO ₄ | Calcium hydrogen phosphate |
| CDHA | Calcium-deficient hydroxyapatite |
| CHAp | Calcium hydroxyapatite |
| ClAp | Chlorapatite |
| CP | Calcium phosphate |
| CVD | Chemical vapour deposition |
| DDDA | Dodecanedioic acid |
| DSC | Differential scanning calorimetry |
| DTA | Differential thermal analysis |
| DTG | Derivative thermogravimetry |
| FAP | Fluorapatite |
| FT-IR | Fourier-transform infrared spectroscopy |
| IR | Infrared spectroscopy |
| PVA | Poly(vinyl alcohol) |
| SEM | Scanning electron microscopy |
| Sa | Suberic acid |
| Si | Silicium (substrate) |
| SLS | Sodium lauryl sulfate |
| α -TCP | α -Tricalcium phosphate |
| Ti | Titanium (substrate) |
| TEM | Transmission electron microscopy |
| TG | Thermogravimetry |
| XRD | X-ray diffraction |

INTRODUCTION

Calcium hydroxyapatite (CHAp, $\text{Ca}_{10}(\text{PO}_4)_6(\text{OH})_2$) is the main inorganic part of bone tissue being involved in bone growth and characterized by excellent biocompatibility. Synthetic CHAp shows strong osteopermeable properties making it a particularly attractive material for biomedical applications [1]. A high surface area, reactivity and biomimetic morphology make nano-CHAp more favourable in applications such as orthopaedic implant coatings or bone substitute fillers [2]. CHAp presents in the human body both inside bone and teeth. The architecture of the bone comprises of type-I collagen as an organic component and the CHAp as an inorganic component (Fig. 1). These two components form a composite structure at the nanoscale, in which nano-CHAp is interspersed in the collagen network. In the bone, the CHAp particles present in the shape of spherical particles, plates, needles or other, are about 40 to 60 nm long, 20 nm wide, and 1.5 to 5 nm thick [3, 4].

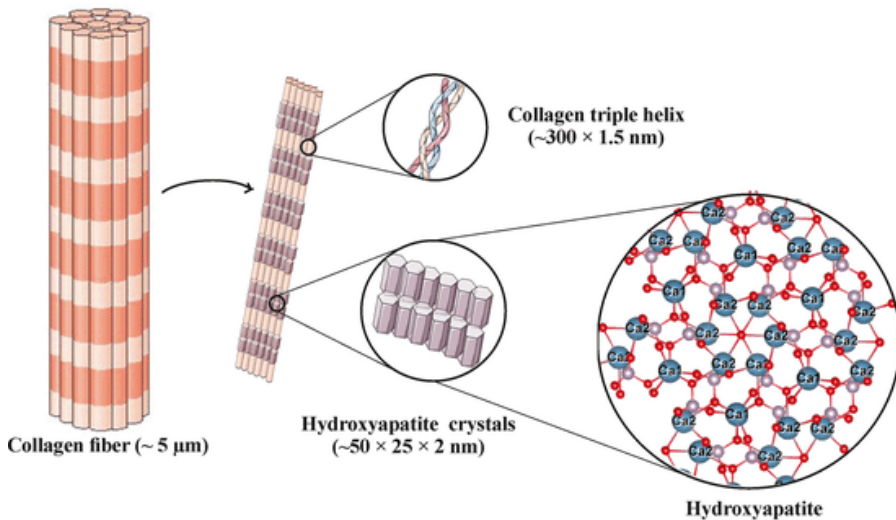


Fig. 1. The hierarchical structure of collagen and hydroxyapatite as main constituents of natural bone tissue [5].

The arrangement of different CHAp crystalline sizes and shapes provides support for this tissue's structural stability, hardness and function [6, 7]. CHAp application in orthopedics can vary from bone defects repair and bone augmentation to coatings for human body metallic implants. The CHAp-based implants can provide an interlocked porous structure [8-10]. This structure can act as the extracellular matrix, promoting the natural process of

cellular development and tissue regeneration [10, 11]. Furthermore, CHAp can enhance the osseointegration process by promoting rigid anchorage between the implant and the surrounding tissue without the growth of fibrous tissue. The successful osseointegration retains the bone anchorage for a long period, hence completely restoring functional ability [12, 13].

To build more effective CHAp bulk and coatings with increased biocompatibility still is a challenge and hot area of scientific investigations. Therefore, the synthesis processes and chemistry have to be thoroughly investigated. The use of artificial calcium phosphate (CP) biomaterials has been gaining therapeutic scope in diverse clinical applications. However, an equally attractive field of application involving CHAp is its use in various sensors [14–17]. Using the aqueous sol-gel method, CHAp coatings can be synthesized on various substrates (e.g., titanium, quartz, silicon) by controlling the temperature, pH and concentration of starting materials [18]. In order to produce a coating that is more resistant to physiological conditions, various new methods are being sought for the modern synthesis of CHAp layers that replicate bone tissue. Recently, it was demonstrated that silicon-containing CHAp provide enhanced bioactivity and antibacterial properties over pure CHAp [19]. Besides, silicon could improve osteoblastic response on calcium phosphate bioceramics, probably, since it presents in trace concentrations in natural bone. Sol-gel method for the synthesis of CHAp, however, is considered a high-temperature approach, requiring elevated temperatures to obtain the CHAp crystalline phase. However, high temperatures do not support the formation of nanocrystalline materials [20]. The CHAp coatings obtained at 1000 °C could be inhomogeneous, for example, consisting of two distinct regions: one with small grains, approximately 200 nm in size, and one with larger grains, approximately 800 nm in diameter [21]. Additionally, the formation of the TiO₂ phase at high temperatures reduces adhesion of CHAp films on Ti substrates [22].

Calcium-deficient hydroxyapatite (CDHA, Ca_{10-x}(HPO₄)_x(PO₄)_{6-x}(OH)_{2-x}) is CHAp with a Ca/P ratio from 1.50–1.67 [23]. Previous studies have reported a larger specific surface area and superior incorporating efficacy of CDHA when compared to other CaPs [18, 24]. The chemical composition of CHAp can be modified from the stoichiometric form to the Ca-deficient form by selecting an appropriate Ca/P molar ratio [22]. Solubility, specific surface area, surface wettability, and hence the adsorption characteristics of CHAp depend greatly on their morphology and crystallinity [25, 26]. The crystal structure of CHAp is notable due to the fact, that it has two types of crystal planes, namely, a-face and c-face. The a-face is positively charged due to calcium ions, while the c-face is negatively charged due to oxygen atoms

belonging to phosphate ions [27]. Anisotropic growth of CHAp crystals in one or another crystallographic direction is an important factor from the point of view of specific interaction of oriented crystals with other substances, which may lead to enhanced performance and specific application of this material. For example, the adsorption of proteins on CHAp crystals depends on their morphology, different types of proteins, such as basic and acidic proteins, adsorb selectively on the crystal planes of CHAp [28, 29]. Thus, tuning the morphology of CHAp crystals may lead to enhanced biological properties as well. In this light, the controllable synthesis of plate-like or rod-like crystals with different aspect ratio and surface charge is an important task.

The aim of this dissertation was the development of new methods for the synthesis of bulk and coatings of calcium hydroxyapatite with controlled morphological features. For this reason, the tasks to achieve the main goal were formulated as follows:

1. Development of a low-temperature synthetic approach for the fabrication of calcium hydroxyapatite coatings on a silicon substrate.
2. Development of a low-temperature synthetic approach for the fabrication of calcium hydroxyapatite coatings on a titanium substrate.
3. Investigation of the effects of various organic solvents and solvothermal synthesis conditions on the formation of calcium hydroxyapatite via hydrolysis of α -tricalcium phosphate.
4. Investigation the effects of different organic additives on the formation of calcium hydroxyapatite via hydrolysis of α -tricalcium phosphate.

Novelty and originality of the work

In this study, for the first time the calcium hydroxyapatite thin films were fabricated at a sufficiently low temperature applying environmentally friendly sol-gel using the spin-coating technique and dissolution-precipitation synthesis methods on Si substrate. This low-temperature synthetic approach was also developed for the fabrication of calcium hydroxyapatite coatings on Ti substrate. In the present PhD thesis, the effects of various organic solvents and solvothermal conditions on the formation of calcium hydroxyapatite via hydrolysis of α -tricalcium phosphate were investigated. Moreover, the effects of sodium lauryl sulphate and various amino acids (DL-aspartic acid, dodecanedioic acid, suberic acid) on the formation and morphological properties of calcium hydroxyapatite have been also estimated.

Defensive statements

1. The CHAp coatings on Si substrate could be easily synthesized by environmentally friendly sol-gel and dissolution-precipitation synthesis methods. The coatings were obtained for the first time using the spin-coating technique.
2. The CHAp coatings could be synthesized by the same sol-gel and dissolution-precipitation synthesis methods on Ti substrate as well. Almost single phase CHAp could be obtained with negligible amount of side phases.
3. Methyl alcohol and ethylene glycol have a stronger inhibitory effect on α -TCP hydrolysis than ethyl alcohol, isopropyl alcohol and butyl alcohol. The morphology of the obtained CDHA samples could be changed from plate-shaped to rod-shaped. The ethylene glycol had the highest impact on the sample morphology.
4. The nature and the concentration of organic additives influence the phase purity and morphology of the final CDHA specimens. Higher concentrations of sodium lauryl sulphate and dodecanedioic acid induce the formation of impurities, while aspartic and suberic acid do not affect the phase purity. The morphology of the samples could be changed from plate-shaped to rod-shaped.

1. LITERATURE OVERVIEW

1.1 Basic aspects of human bone

Humans are born with 270 bones, but this number drops to 206 as an adults. The tubular bone is made up of the periosteum, bone tissue and bone marrow. In the bone tissue, its elastic framework is formed by proteins, mainly collagen type I and minerals, which fill the cavities in the bone. Bone tissue also contains bone cells: osteocytes, osteoclasts and osteoblasts, and bone tissue itself has three main functions [30, 31]:

1. Mechanical – supports and protects vital organs and the nervous system. Bones allow the transfer of force from one part of the body to another. Mechanical stiffness and low elasticity reduce tension in the bone tissue, while the flexibility of the bone helps to absorb shock and reduce the risk of fractures.
2. Metabolic – bone tissue is a dynamic tissue, constantly regenerating itself under mechanical stresses. This tissue has accumulated stores of calcium ions. Bone is therefore involved in the homeostasis of mineral ions in the body.
3. Haematopoiesis – the bone marrow in the bone tissue is responsible for the production of all three types of blood cells.

Bone is a natural composite material consisting of about 45-60 % minerals, 20-30 % matrix and 10-20 % water. When the water fraction is included in the organic phase, the composition of bone can be illustrated as follows in Figure 2 [32].

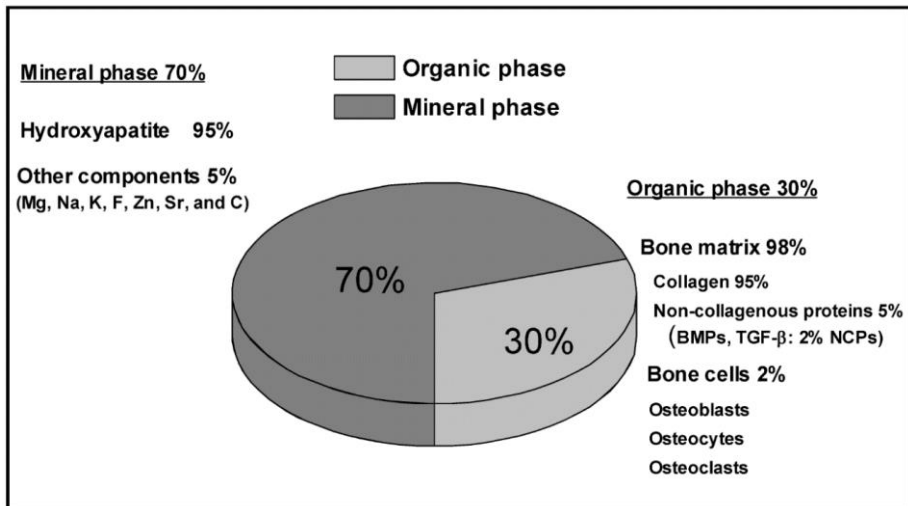


Fig. 2. Chemical composition of bone tissue.

The inorganic part of the bone tissue consists of abundant calcium and phosphorus, which form hydroxyapatite (CHAp, $\text{Ca}_{10}(\text{PO}_4)_6(\text{OH})_2$) crystals. The latter are found close to collagen fibres. Small amounts of calcium phosphate, magnesium, sodium, potassium and small amounts of other elements (copper, manganese, zinc, etc.) are also present, as well as mineralised inorganic phases, such as chlorapatite (ClAp), fluorapatite (FAP), sodium and magnesium-bearing apatites. The inorganic phase allows the bone to have high stiffness and mechanical strength.

The organic phase consists mainly of type I collagen (about 90 %), whose fibres regulate the formation and spatial orientation of CHAp crystals, and small amounts of type III and IV collagen, which regulate the diameter of collagen fibrils. The remaining 10 % are proteins such as glycoproteins, proteoglycans, osteopontin, osteocalcin and others [33, 34].

The structure and composition of bone determine its mechanical properties. The mechanical behaviour of the whole bone is not discrete, but rather continuous, varying according to local composition and geometry. In general, whole bone is more resistant to compressive forces than to tensile forces, and the volumetric mechanical properties of bone at the macroscopic level are highly dependent on geometry [35]. Both of these generalisations are consistent with what might be expected when thinking about bone functionality. It is advantageous for bone to be more resistant to compression due to the presence of such forces during weight bearing and the mechanism of compression injuries. Bone, like other biological materials, has so-called hierarchical structure, consisting of different levels (Figure 3) depending on the scale [36].

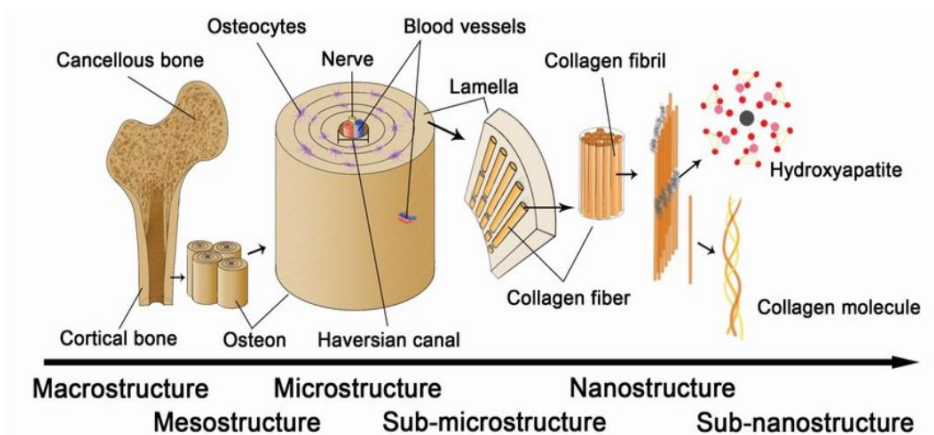


Fig. 3. The hierarchical structure of bone.

Calcium hydroxyapatite is one of the substances found in bone tissue that is involved in bone growth and has excellent biocompatibility. CHAp crystals oriented along the collagen fibres contribute to the strength of the bone itself (Figure 1). Synthetic calcium hydroxyapatite has many advantages as a biomaterial. CHAp, as an inorganic biomaterial, has strong osteoconductive properties, making it a particularly attractive material in the biomedical field [37]. Calcium hydroxyapatite has a Ca:P ratio of 1.67 (5:3), but the Ca:P ratio in bone tissue actually ranges from 1.37 to 1.87, indicating that other additional ions such as strontium, zinc, and carbonate may be present in the bone mineral.

1.2 Synthetic calcium hydroxyapatite ($\text{Ca}_{10}(\text{PO}_4)_6(\text{OH})_2$)

Synthetic CHAp is partially resorbed in body fluids and the resorption itself depends on the crystallinity of the material. When CHAp was immersed in an equilibrium salt solution, which mimics the human body fluid medium, a significant loss of OH^- groups and a decrease of amorphous Ca-P material in the coating was observed [38]. Studies have shown that bone tissue growth is faster when the coating contains a higher amount of amorphous phase due to faster initial dissolution [39]. The crystal structure of hydroxyapatite crystals is shown in Figure 4 [40].

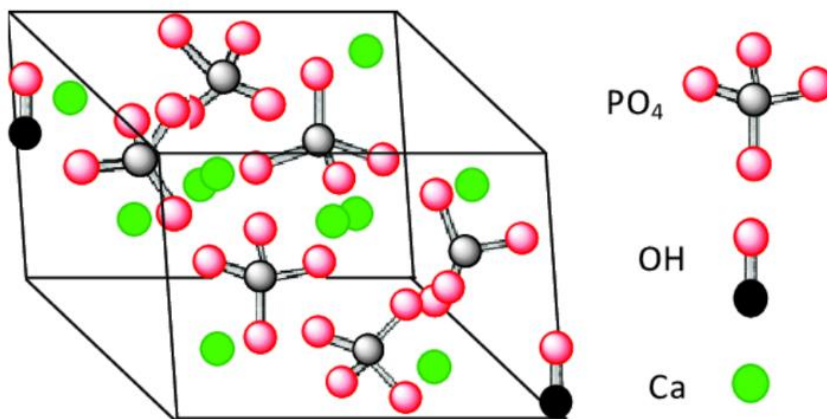


Fig. 4. The structure of hydroxyapatite crystals [40].

CHAp is a brittle material and not fully suitable for use as an artificial substitute for hard tissue, so it is often combined with other materials (e.g. collagen, strontium, or titanium) that improve bioimplant properties such as

flexibility and hardness. Calcium hydroxyapatite can be obtained in several ways – naturally and chemically. In the first way, it can be extracted from mammalian bones or coral. Most natural calcium phosphates can be found as small polycrystalline structures. It is worth noting that large crystals are quite rare [41]. Compared to synthetic calcium hydroxyapatite, natural CHAp is non-stoichiometric because it contains trace elements such as Na^+ , Zn^{2+} , Mg^{2+} , K^+ , Si^{2+} , Ba^{2+} , F^- and CO_3^{2-} [42, 43]. As mentioned above, CHAp can also be produced synthetically. Although many methods have been developed for the synthesis of CHAp, such as sol-gel, electrochemical, chemical precipitation, etc., the preparation of calcium hydroxyapatite with specific properties remains challenging, as the synthesis of CHAp can lead to the formation of toxic intermediates [44]. Therefore, the development of new methods for CHAp synthesis are still very desired.

Recent studies have shown that calcium hydroxyapatite can also exist in a monoclinic form. This form is the most thermodynamically stable at room temperature and the main difference between the monoclinic and hexagonal forms is the orientation of the OH^- groups (Figure 5). In the hexagonal form of CHAp, the two adjacent hydroxyl groups are oriented in opposite directions, whereas in the monoclinic form, all the OH^- groups are oriented in the same direction in the same column, with the opposite direction between the columns [45]. Although the structural differences between monoclinic and hexagonal CHAp are small, they are sufficient to strongly influence some of the physicochemical properties of CHAp. As monoclinic CHAp is structurally more stoichiometric than hexagonal CHAp, it is expected that this will lead to quite different solubility and diffusion kinetics. Therefore, knowledge of the origin and synthesis of the monoclinic CHAp phase is crucial to understand the mechanisms of calcium hydroxyapatite formation and its promising applications in bone remodelling and enhancement [46].

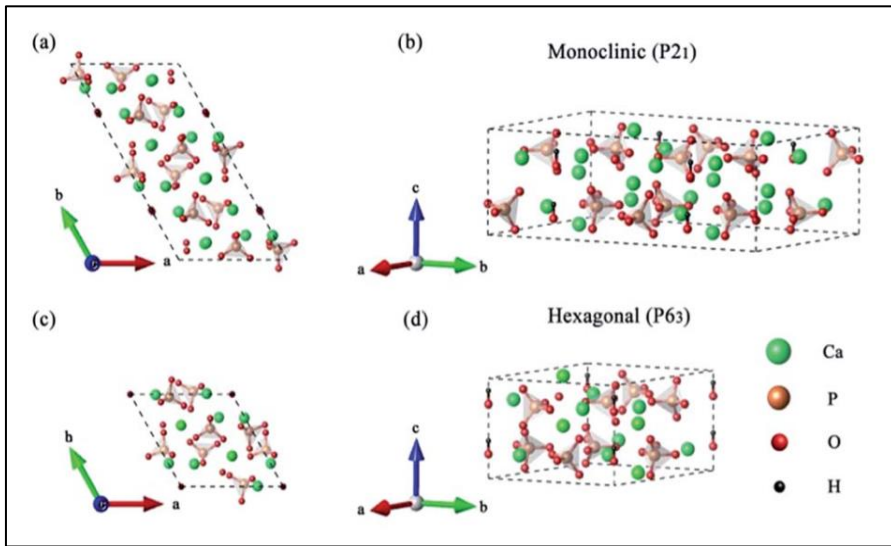
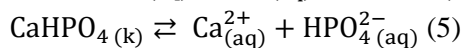
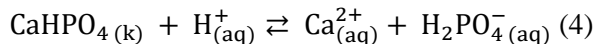
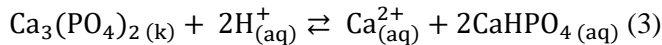
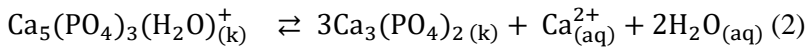
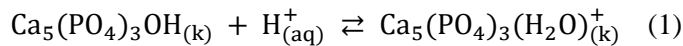


Fig. 5. Crystal structures of the low-temperature monoclinic $P2_1$ phase (a) and (b), and the high-temperature hexagonal $P6_3$ phase (c) and (d) hydroxyapatite $\text{Ca}_{10}(\text{PO}_4)_6(\text{OH})_2$ [47].

Calcium hydroxyapatite is an important inorganic component of human and other vertebrate bones and teeth. Due to its biocompatibility with living tissues, CHAp, together with other materials such as various biosticks, carbon nanostructures, etc., is known as bioceramics. These bioceramics are resistant to microbial attack and pH changes [48]. In order to characterise the interaction between CHAp-based bioceramics and bone tissue, a model has been proposed (Figure 6) [48]. This model proposes series of initial steps (1-3) that take place before the equilibrium between the hydroxyapatite and the biological fluids occurs. The implantation of hydroxyapatite into the body initially leads to the dissolution of the material, as shown in reactions 1-5:



After some time, an equilibrium is established between the modified hydroxyapatite surface and the biological fluids and calcium hydrogen

phosphate (CaHPO_4) is formed on the surface. The implant is then integrated into the tissue, e.g. by protein adsorption and cell adhesion. The more detailed mechanism consists of the 8 steps shown in Figure 6:

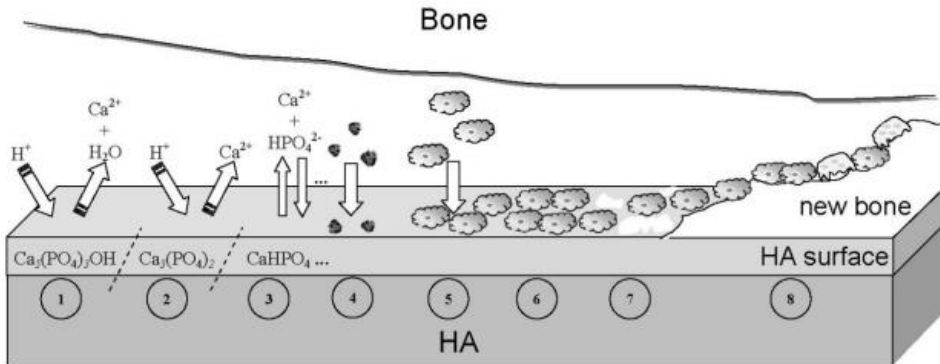


Fig. 6. Diagram of the phenomena occurring on the surface of the HA post-implantation: (1) start of the implantation procedure, when HA dissolution occurs solubilisation of the HA surface begins; (2) continuation of solubilisation of the HA surface; (3) the equilibrium between saline solutions and the modified HA surface (Changes in the composition of the HA surface do not imply the onset of a new phase the formation of a new phase on the surface of DCPA or DCPD); (4) adsorption of proteins and/or other bio-organic substances compounds; (5) cell adhesion; (6) cell proliferation; (7) initiation of new bone formation; and (8) formation of new bone [49].

1.3 Synthesis methods

1.3.1 Bulk

Synthetic CHAp can be obtained in a variety of ways including the simple, fast and cost-efficient solid-state reaction [50], sol-gel method, techniques based on ammonium hydrogen phosphate as a phosphorus precursor and calcium acetate monohydrate as a calcium ion source [51], as well as wet precipitation [26], hydrothermal [23] and solvothermal syntheses [18] and others. Another group of synthetic approaches employed for the synthesis of CHAp considers the phase conversion from other less stable CPs. For instance, calcium-deficient hydroxyapatite CDHA can be obtained through the transformation from alpha-tricalcium phosphate ($\text{Ca}_3(\text{PO}_4)_2$), α -

TCP) or amorphous CP in aqueous medium [24]. Synthetic pathways employing high-temperature treatment usually result in the formation of large agglomerated particles. Crystallographically oriented products are usually obtained by low-temperature chemical methods.

Functional groups of organic substances, such as carboxyl or amino, can specifically interact with the planes of CHAp particles during the crystal growth process and affect particle growth in one or another direction. Different additives were previously employed in order to investigate their effect on the crystal growth, morphology and properties of CHAp. For instance, Suchanek et al. [22] successfully synthesized CHAp nanofibers in the presence of monoethanolamine under hydrothermal conditions. The role of sebacic acid on the formation of CHAp was investigated in [1]. Jiang et al. [52] showed that poly(acrylic acid) depending on its concentration can promote or inhibit CHAp crystallization. Moreover, the composition of mixed aqueous-organic reaction medium also has an effect on the crystallization and morphology of CHAp [53].

1.3.2 Coatings

Plasma spraying method requires that the metal surface of the implant be rough, as this will result in better adhesion to the sprayed CHAp. To form CHAp or other coatings, the powder is injected into the plasma stream where it acquires a velocity of 50 to 600 m/s and impacts with high force on the substrate, adhering to it to form the desired coating. Although this method is known as one of the main coating technologies, the properties of the resulting coatings depend on the design of the plasmotron, the power of the plasmotron, the location of the injection of the powder, the type of gas used to form the plasma, and the temperature of the substrate [54, 55].

CHAp coatings can be deposited using atomic layer deposition (ALD) technology. This process involves chemisorption, i.e. the molecules of the precursor react with the surface to be coated until there are no active sites on the surface. The ALD method is one of the best in the field of thin-film forming, as it allows the production of very thin layers with precise thickness and extremely smooth and homogeneous layers. One of the advantages of this method is that it uses lower temperatures than classical CVD (chemical vapour deposition) processes, which allows the use of more reactive materials and different substrates.

The deposition process involves the reaction of two substances (Figure 7). First, reagent A is sprayed into the cell until it is fully adsorbed and the reaction proceeds no further. This is followed by the second step, purification.

In this step, the unreacted precursor and reaction by-products are removed. Reagent B is then sprayed until the surface becomes saturated and the cleaning procedure is repeated. The number of cycles in the tests is determined by the thickness of the coating to be obtained [56].

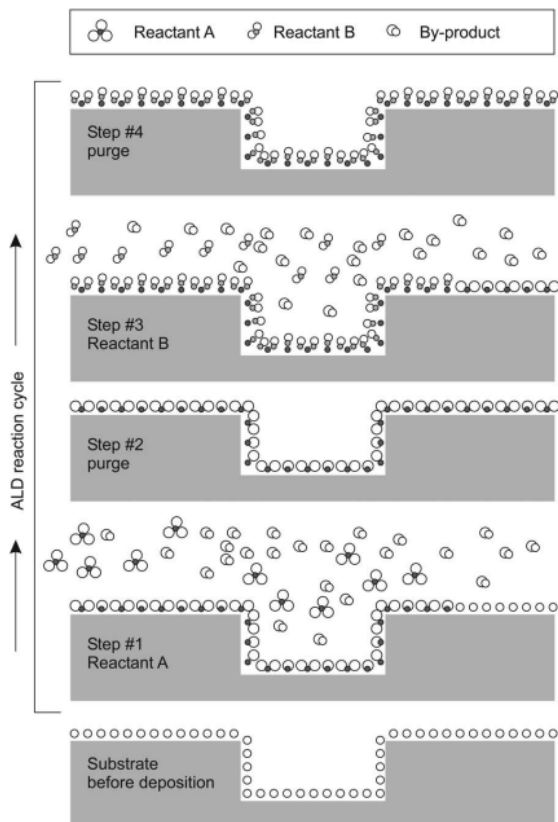


Fig. 7. Schematic illustration of one ALD reaction cycle.

Calcium hydroxyapatite coatings can be deposited by magnetron sputtering. This is a versatile technique where thin, nanostructured layers of materials are deposited from a gas phase (plasma). Due to the quality of the coatings produced, this method has become one of the main technologies for the formation of thin films under vacuum. The magnetic field causes the electrons to be concentrated at the surface of the target by the Lorentz force. Increasing the sputtering yield and the growth rate of the coating can be achieved by increasing the number of inert gas ions in the electric field. In recent years, this preparation method of coatings has been particularly popular, for example, CHAp coatings on polytetrafluoroethylene (PTFE) have

been simulated using this method [57]. Depending on the type of energy source used, magnetron sputtering can be divided into two types: (1) direct current magnetron sputtering (DC) and (2) radio frequency sputtering (RF). DC magnetron sputtering is relatively cheaper compared to RF, but only electrically conductive targets such as metals or doped semiconductors are used (Figure 8) [58].

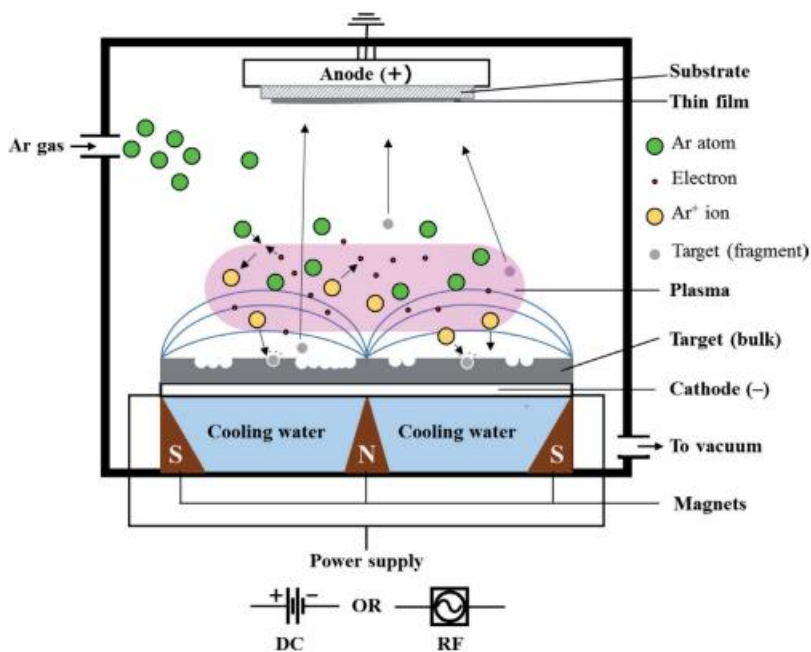


Fig. 8. Schematic representation of a magnetron sputtering equipment and deposition process.

Electrochemical deposition of CHAp coatings is an increasingly popular method of forming coatings by electrolysis from an electrolyte of appropriate composition. The method does not require expensive apparatus and the thickness and structure of the deposited coatings can be controlled by selecting the appropriate potential, current density, electrolyte composition and pH [59]. However, the method has a disadvantage for the coatings, such as poor adhesion to the surface. In addition, metallic implants with poor adhesion of the coating can easily form small debris, which leads to implant rejection in the body [59].

The sol-gel method is a convenient and increasingly popular synthesis method that can form thin coatings (Figure 9). The advantages of this method are: low temperature, low-cost synthesis equipment, easy control of the

process, and technological simplicity. The parameters of the coating to be formed are controlled by varying the sol-gel concentration, the technical parameters of the equipment and the heating temperature. The synthesis of sol-gels consists of several steps. First, the sol (colloidal solution) is heated until a two-phase gel system is achieved. Once the gel consistency is reached, surface coating is possible.

The aqueous sol-gel method can be used to synthesise calcium hydroxyapatite on a variety of substrates (e.g. titanium, quartz, silicon) by controlling the temperature, pH and concentration. The calcium hydroxyapatite obtained by this synthesis method can be alloyed with various metals or alloys of metals quite easily, thus modifying the properties of the compound obtained.

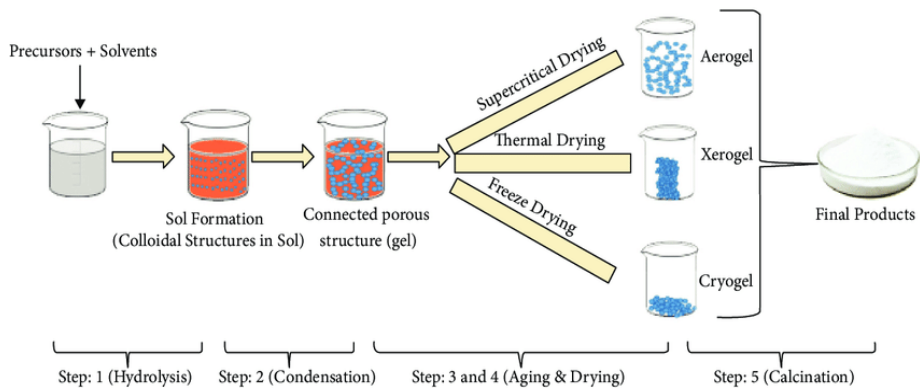


Fig. 9. Schematic of different stages of sol-gel process [60].

Spin coating is used to obtain thin ($<1 \mu\text{m}$) and uniform coatings on flat surfaces (Figure 10).

The coating fluid is dripped into the centre of the target (substrate) and the substrate starts to spin. The dropped solution is distributed on the surface of the substrate by centrifugal force and gravity. The thickness of the coating formed depends on the viscosity of the solution dropped, the evaporation rate of the solution and the rotational speed. Generally, at higher rotational speeds, thinner coatings are formed. One of the disadvantages of the spin coating method in industrial applications is the loss of material, as the excess droplet solution is dispersed off-target by the centrifugal force of rotation [61].

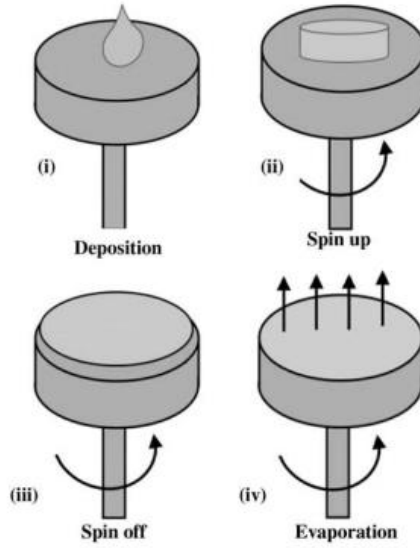


Fig. 10. Stages of spin coating on substrate [61].

Dip coating is the deposition of a liquid film by controlling the rate and time of dipping and lifting of the substrate (Figure 11). The substrate is first dipped and soaked in the solution, followed by the formation of a thin film on the substrate as the solvents evaporate. This method is convenient for coating irregularly shaped substrates and is popular in industry and laboratories because of its low cost and simple processing steps. The required coating properties can be obtained by controlling the soaking time and the extraction rate, but the coating obtained by the dipping method may be uneven due to the non-uniformity of the substrate [62].

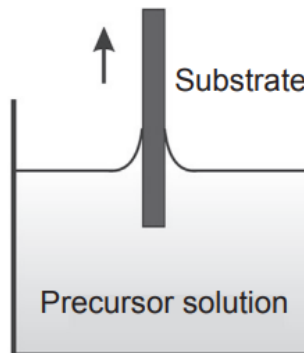


Fig. 11. Schematic diagram of dip coating [62].

1.4 Applications

Synthetic calcium hydroxyapatite is used in dentistry and orthopaedics because CHAp is part of the chemical composition of tooth enamel and bone. CHAp coatings on implants increase the biocompatibility of implants. Calcium hydroxyapatite nanoparticles are also used to mineralise tooth enamel. The mineralisation of tooth enamel reduces tooth sensitivity and tooth damage caused by various acids and helps to remove the calcium fluorapatite that forms. Calcium hydroxyapatite is used in dentistry as a filler for damaged teeth into which the tooth has grown [63–66].

Another application is the removal of fluoride from water. Calcium fluorapatite is thermodynamically more stable than hydroxyapatite. However, this method of fluorine removal requires the addition of calcium ions [67] as washing calcium hydroxyapatite with water dissolves some of the mineral in the water and introduces phosphates into the water, which would make the water unsuitable for human drinking. Recently, a new process has been presented that produces water with a higher calcium content and the removal of fluoride.

In archaeology, the results of the analysis of calcium hydroxyapatite in archaeological finds are important. As trace elements accumulate in bones and mineral fractions, their concentrations can tell us a great deal about animal diets (whether marine or terrestrial), migrations and even a great deal about prehistoric climates [68]. We can also learn about migration routes and geographical origins [69]. Oxygen in fossilised calcium hydroxyapatite can provide information about past climates [70]. Calcium hydroxyapatite is also used in the delivery of a variety of drugs and drug preparation due to its stability. Porous block calcium hydroxyapatite is used in the delivery of antibiotics and anticancer drugs and CHAp nanoparticles are even used in gene therapy [71, 72].

To summarise the information in this chapter, calcium hydroxyapatite and its different structures have the potential to expand medical capabilities, archaeological knowledge and improve the quality of life. Finding a cheap, efficient and reliable way of obtaining calcium hydroxyapatite could expand the possibilities and the wider applicability of the areas discussed.

2. EXPERIMENTAL

2.1 Materials

Disodium hydrogen phosphate (Na_2HPO_4 , pure p. a., Chempur), calcium acetate monohydrate ($\text{Ca}(\text{CH}_3\text{COO})_2 \cdot \text{H}_2\text{O}$, 99.9 %, Fluka), calcium nitrate tetrahydrate ($\text{Ca}(\text{NO}_3)_2 \cdot 4\text{H}_2\text{O}$, 99 %, Fluka), citric acid monohydrate ($\text{C}_6\text{H}_8\text{O}_7 \cdot \text{H}_2\text{O}$, 99.9 %, Fluka), 1,2-ethanediol ($\text{C}_2\text{H}_6\text{O}_2$, 99 %, Alfa Aesar), acetyl acetone ($\text{C}_5\text{H}_8\text{O}_2$, 99.9 %, Merck), 2-propanol ($\text{C}_3\text{H}_8\text{O}$, 99 %, Alfa Aesar), polyvinyl alcohol (PVA7200) ($[-\text{CH}_2\text{CHOH}-]_n$, 99.5 % Aldrich), sulphuric acid (H_2SO_4), hydrogen peroxide (H_2O_2), were used for the synthesis of calcium hydroxyapatite. Calcium nitrate tetrahydrate ($\text{Ca}(\text{NO}_3)_2 \cdot 4\text{H}_2\text{O}$, 99 %, Roth, Karlsruhe, Germany), diammonium hydrogen phosphate ($(\text{NH}_4)_2\text{HPO}_4$, 98 %, Roth, Karlsruhe, Germany), ammonium hydroxide (NH_4OH , 25 %, Roth, Karlsruhe, Germany) were used for the synthesis of the α -TCP. The obtained TCP was further used as a precursor for the synthesis of CHAp *via* a hydrolysis reaction under hydrothermal conditions with ethylene glycol (EG, >99 %, Roth), methyl alcohol (MeOH, >99.9 %, Roth), ethyl alcohol (EtOH, >96 %, Roth), isopropyl alcohol (PrOH, >99.5 %, Roth), butyl alcohol (BuOH, >99.5 %, Roth), sodium lauryl sulfate (SLS, $\text{NaC}_{12}\text{H}_{25}\text{SO}_4$, ≥ 99.0 %, Roth, Karlsruhe, Germany), dodecanedioic acid (DDDA, $\text{C}_{12}\text{H}_{22}\text{O}_4$, 99 %, Sigma Aldrich, Germany), DL-aspartic acid (Asp, $\text{C}_4\text{H}_7\text{NO}_4$, 99 %, Sigma Aldrich, Germany) and suberic acid (Sa, $\text{C}_8\text{H}_{14}\text{O}_4$, 99 %, Sigma Aldrich, Germany).

2.2 Synthesis of $\text{Ca}_{10}(\text{PO}_4)_6(\text{OH})_2$ coatings

Firstly, calcium carbonate (CaCO_3) layers on silicon and titanium substrates were fabricated by sol-gel method. In the sol-gel process 20 ml of $\text{C}_3\text{H}_8\text{O}$ were mixed with 1.8 ml of $\text{C}_5\text{H}_8\text{O}_2$ with stirring at room temperature. An appropriate amount (1.0920 g) of $\text{Ca}(\text{NO}_3)_2 \cdot 4\text{H}_2\text{O}$ was added to the solution and stirred for 1 h until the material dissolved [73]. The solution used for coating was mixed with the PVA solution (0.5 g of PVA dissolved in 49.5 ml of distilled water with stirring at 90 °C for 1 h) in a ratio of 5:3. The silicon substrate was repeatedly coated with 10, 20 and 30 layers of solution by spin-coating method using two different spinning procedures (A) and (B) (Table 1) and on a titanium substrate using a single spin-coating procedure (A). After evaporation of solvent the substrates were dried in an oven for 10 min at 200 °C and heated at 600 °C for 5 h with a heating rate of 5 °C/min. Calcium

hydroxyapatite coatings were synthesized by low-temperature dissolution-precipitation method. Silicon substrates coated with partially amorphous and/or crystalline CaCO₃ were soaked in disodium phosphate solution (1 mol/l) for 28 days in a thermostat at 80 °C.

Table 1. Parameters of two different spinning procedures (A) and (B).

| Parameter | Spinning procedure (A), sec | Spinning procedure (B), sec |
|------------------|--|--|
| RPM1 | 1000 | 500 |
| RAMP1 | 1 | 2 |
| TIME1 | 1 | 5 |
| RPM2 | 3000 | 1000 |
| RAMP2 | 2 | 2 |
| TIME2 | 1 | 5 |
| RPM3 | 3000 | 1500 |
| RAMP3 | 1 | 2 |
| TIME3 | 30 | 90 |
| RAMP4 | 10 | 10 |

Before the coating the silicon and titanium substrates were prepared by different cleaning techniques. Silicon substrates (10x10 mm squares) were washed with Piranha solution (3 parts of concentrated sulfuric acid and 1 part of 30 % hydrogen peroxide solution) and distilled water. The titanium substrates (Alfa Aesar 1 mm thick titanium alloy sheet, 15 mm diameter, 0.5 mm thick discs and 10x10 mm squares) were successively mechanically polished with 600, 800 and 1200 grit sandpaper, and wet polished with an ethanol-based oil (Struers, DP-Lubricant Brown). The polished substrates were immersed in a 5M NaOH solution and left at 60 °C for 24 h. The substrates were rinsed with distilled water and dried at room temperature before the coating procedure.

The spin-coating method was applied by dripping a prepared sol-gel solution onto the prepared substrates. Two procedures for the spin coating method were used, as shown in Table 1. The main difference between the two methods is spin rate. After each spin-coating procedure, the samples were heated in an oven at 200 °C for 10 min. The low-temperature heated substrates were then heated for 5 h at 600 °C with a temperature rise of 5 °C/min. The spin-coating and heating procedures were repeated 10, 20 and 30 times.

2.3 Synthesis of $\text{Ca}_{10}(\text{PO}_4)_6(\text{OH})_2$ powders

For the synthesis of α -TCP an appropriate amount (3.42 g) of $\text{Ca}(\text{NO}_3)_2 \cdot 4\text{H}_2\text{O}$ was dissolved in 20 ml of deionized water. 1.27 g of $(\text{NH}_4)_2\text{HPO}_4$ were dissolved in 15 ml of deionized water in a separate beaker. After dissolution, concentrated ammonium hydroxide was added to the latter solution until pH of the solution reached 10. After stirring for 1 min, an aqueous solution of $\text{Ca}(\text{NO}_3)_2 \cdot 4\text{H}_2\text{O}$ was added rapidly. A white precipitate formed which was stirred for 10 minutes at 400 rpm. The obtained precipitate was subsequently vacuum filtered and washed with an appropriate volume of deionized water and PrOH [74]. The synthesis product was dried overnight in an oven at 50 °C. The dried powders were ground in agate mortar and annealed in a furnace at 700 °C for 5 h at a heating rate of 5 °C/min.

Solvothermal reactions were performed with different proportions of water and organic reagent. The water to alcohol v/v ratios of 0:100, 20:80, 40:60, 60:40, and 80:20 were applied. For the synthesis, 0.3 g of α -TCP powder was placed into a 90 ml polytetrafluoroethylene-lined stainless-steel pressure vessels and diluted with 20 ml of water-organic solvent mixture. Solvothermal treatment was performed under 120 °C for 3 h and at 200 °C for 5 h. Finally, the resulting powders were filtered, washed with EtOH, and dried at 50 °C overnight. The sample notations and treatment conditions are given in Table 2.

Table 2. Solvothermal treatment conditions for the alcohol-based synthesis.

| Notation | Solvothermal conditions | Organic solvent applied |
|-----------------|--------------------------------|--------------------------------|
| 120-W-EG | 120 °C, 3 h | ethylene glycol |
| 120-W-MeOH | 120 °C, 3 h | methyl alcohol |
| 120-W-EtOH | 120 °C, 3 h | ethyl alcohol |
| 120-W-PrOH | 120 °C, 3 h | isopropyl alcohol |
| 120-W-BuOH | 120 °C, 3 h | butyl alcohol |
| 200-W-EG | 200 °C, 5 h | ethylene glycol |
| 200-W-MeOH | 200 °C, 5 h | methyl alcohol |
| 200-W-EtOH | 200 °C, 5 h | ethyl alcohol |
| 200-W-PrOH | 200 °C, 5 h | isopropyl alcohol |
| 200-W-BuOH | 200 °C, 5 h | butyl alcohol |

The solvothermal synthesis reactions were performed also in the presence of different concentrations of sodium lauryl sulfate (SLS) and amino

acids: dodecanedioic acid, DL-aspartic acid and suberic acid. In a typical procedure, 0.3 g of α -TCP powder and appropriate amount of SLS or amino acids were placed into a 90 mL polytetrafluoroethylene-lined stainless-steel pressure vessels, diluted with 20 mL of water and treated at 200 °C for 5 h. Solvothermal reactions were performed in the presence of different concentrations of DL-aspartic acid and suberic acid in water and ethylene glycol (W:EG) mixture (v/v ratio of 40:60). The synthetic procedure was analogical to that previous. After the hydrothermal treatment the resulting powders were filtered, washed with ethyl alcohol, and dried at 50 °C overnight. The sample notations and concentrations of additives in the reaction solution are given in Table 3.

Table 3. Solvothermal treatment conditions for the SLS and organic acids-based synthesis.

| Notation | Organic additive | Concentration of additive | Water to ethylene glycol ratio (v/v) |
|-----------------|-------------------------|----------------------------------|---|
| SLS:005 | Sodium lauryl sulfate | 0.005 mol/L | 100:0 |
| SLS:025 | Sodium lauryl sulfate | 0.025 mol/L | 100:0 |
| SLS:05 | Sodium lauryl sulfate | 0.05 mol/L | 100:0 |
| SLS:075 | Sodium lauryl sulfate | 0.075 mol/L | 100:0 |
| SLS:1 | Sodium lauryl sulfate | 0.1 mol/L | 100:0 |
| DDDA:005 | Dodecanedioic acid | 0.005 mol/L | 100:0 |
| DDDA:025 | Dodecanedioic acid | 0.025 mol/L | 100:0 |
| DDDA:05 | Dodecanedioic acid | 0.05 mol/L | 100:0 |
| DDDA:075 | Dodecanedioic acid | 0.075 mol/L | 100:0 |
| DDDA:1 | Dodecanedioic acid | 0.1 mol/L | 100:0 |
| Asp:005 | DL-Aspartic acid | 0.005 mol/L | 100:0 |
| Asp:025 | DL-Aspartic acid | 0.025 mol/L | 100:0 |
| Asp:05 | DL-Aspartic acid | 0.05 mol/L | 100:0 |
| Asp:075 | DL-Aspartic acid | 0.075 mol/L | 100:0 |
| Asp:1 | DL-Aspartic acid | 0.1 mol/L | 100:0 |
| Sa:005 | Suberic acid | 0.005 mol/L | 100:0 |
| Sa:025 | Suberic acid | 0.025 mol/L | 100:0 |
| Sa:05 | Suberic acid | 0.05 mol/L | 100:0 |
| Sa:075 | Suberic acid | 0.075 mol/L | 100:0 |
| Sa:1 | Suberic acid | 0.1 mol/L | 100:0 |
| Asp:005:EG | DL-Aspartic acid | 0.005 mol/L | 40:60 |
| Asp:025:EG | DL-Aspartic acid | 0.025 mol/L | 40:60 |

| Notation | Organic additive | Concentration of additive | Water to ethylene glycol ratio (v/v) |
|-----------------|-------------------------|----------------------------------|---|
| Asp:05:EG | DL-Aspartic acid | 0.05 mol/L | 40:60 |
| Asp:075:EG | DL-Aspartic acid | 0.075 mol/L | 40:60 |
| Asp:1:EG | DL-Aspartic acid | 0.1 mol/L | 40:60 |
| Sa:005:EG | Suberic acid | 0.005 mol/L | 40:60 |
| Sa:025:EG | Suberic acid | 0.025 mol/L | 40:60 |
| Sa:05:EG | Suberic acid | 0.05 mol/L | 40:60 |
| Sa:075:EG | Suberic acid | 0.075 mol/L | 40:60 |
| Sa:1:EG | Suberic acid | 0.1 mol/L | 40:60 |

2.4 Characterization techniques

Raman spectroscopy studies were performed using a scanning near-field spectroscopy system with a Raman spectroscopy attachment (Alpha300R, WiTec). In addition, an Axiomcam 208 COLOR microscope was used to study the morphology of the samples. Images were captured using a high resolution digital camera.

Images of the surface morphology of coatings on titanium substrates obtained with the Contour GT-K 3D optical profilometer (Bruker). This system operates in non-contact mode using white light and phase shift interferometry. The 3D profilometer produces an electrical topographic image of the surface. The scanned area of the samples was 0,25 mm².

Powder X-ray diffraction data were collected on a Rigaku miniFlex II (Rigaku, The Woodlands, TX, USA) or SmartLab (Rigaku) diffractometers operating in Bragg-Brentano ($\theta/2\theta$) geometry, using Ni-filtered Cu $K\alpha$ radiation. The data were collected within a 2θ angle range from 10 to 60° at a step width of 0.01° and speed of 5°/min.

Infrared (FT-IR) spectra were recorded in the range of 4000–400 cm⁻¹ employing Bruker ALPHA ATR spectrometer (Bruker, Billerica, Ma, USA).

In order to study the morphology of the samples, a field-emission scanning electron microscopes (FE-SEM) Hitachi SU-70 and Hitachi SU-3500 (FE-SEM, Hitachi, Tokyo, Japan) were used.

Electrochemical measurements were carried out using a Solartron 1280C electrochemical measurement system (Ametek, Inc.) and a three-electrode cell. The auxiliary electrode was a ~4 cm² platinum plate. A standard electrode of Ag/AgCl in saturated KCl solution was used as a reference electrode and a titanium substrate as a working electrode. The working

electrode was mounted in a special cell window in such a way that only one side of the electrode was in contact with the solution and tightened through a silicone gasket. Contact with the coating was achieved via a Pt wire which was pressed against the electrode surface. The electrochemical cell was filled with a Hanks' balanced salt solution (Sigma-Aldrich), the composition of which is given in Table 4, and the measurements started after 10-15 s.

Table 4. Composition of Hanks' solution.

| Component | Concentration, g/L |
|--------------------------------------|--------------------|
| CaCl ₂ ·2H ₂ O | 0.18 |
| MgSO ₄ | 0.09 |
| KCl | 0.40 |
| KH ₂ PO ₄ | 0.06 |
| NaHCO ₃ | 0.35 |
| NaCl | 8.00 |
| Na ₂ HPO ₄ | 0.05 |
| D-glucose | 1.00 |
| Phenol red Na | 0.01 |

The following measurements were carried out to determine the corrosion parameters of the coatings under test: 1. Open circuit potential (E_{ocp}) measurements in Hanks' solution; and 2. Potentiodynamic voltammetric measurements: the potential emission rate of the working electrode was $1 \text{ mV}\cdot\text{s}^{-1}$ and the range of the potential emission was from -200 to 500 mV with respect to E_{ocp} .

Textural properties of the prepared samples were estimated from N₂ adsorption/desorption isotherms at -196 °C using a Micromeritics TriStar 3020 analyser. Before the measurements, all the samples were outgassed in the N₂ atmosphere at 100 °C. The total surface area (S_{BET}) was estimated using the Brunauer–Emmet–Teller (BET) equation, while Barrett-Joyner-Halenda (BJH) equation was used to calculate pore size distribution of the samples [75].

3. RESULTS AND DISCUSSION

3.1 Development of low-temperature method for the formation of bioceramic nano-calcium hydroxyapatite coatings using sol-gel and dissolution-precipitation processing

The main purpose of this part of doctoral dissertation was the development of new fabrication methodological approach (sol-gel and dissolution-precipitation) for the preparation of calcium hydroxyapatite coatings on two different substrates.

3.1.1 Formation of $\text{Ca}_{10}(\text{PO}_4)_6(\text{OH})_2$ coatings on silicon substrate

Firstly, for the development of a low-temperature synthetic approach for the fabrication of calcium hydroxyapatite coatings the silicon substrate was selected as model case. Moreover, it was demonstrated previously, that in order to produce a coating that is more resistant to physiological conditions, various new modern synthesis of CHAp layers that replicate bone tissue are developed. Interestingly, the Si could be used for the formation of interfacial layer on the metal alloys to increase the adhesion strength of biomaterials substantially. For the synthesis of CaCO_3 layer, the silicon substrates were repeatedly coated with 10, 20 and 30 layers of Ca-O sol-gel solution. However, the XRD patterns of the samples obtained after 10 coatings procedures did not contain any reflections attributable to crystalline CaCO_3 phase. Fig. 12 represents the XRD patterns of CaCO_3 thin films obtained after 20 coatings using slightly different spin-coating procedures.

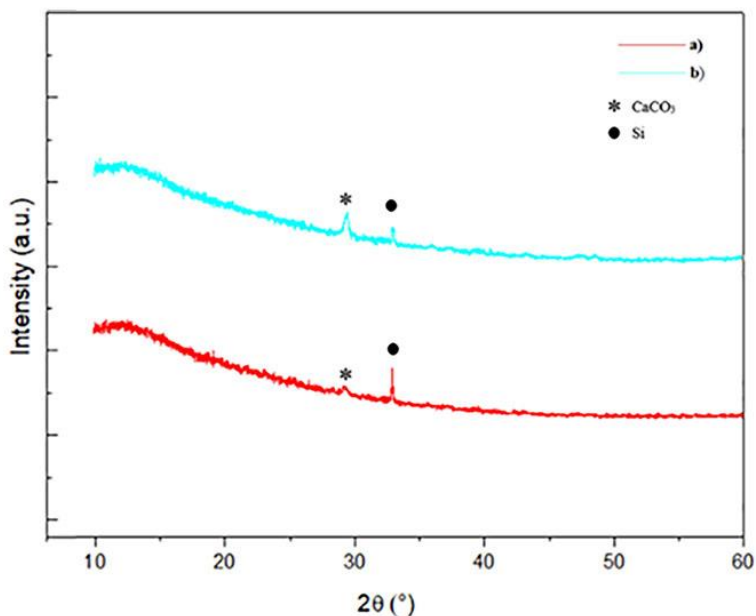


Fig. 12. XRD patterns of the sol-gel derived CaCO_3 samples on Si substrate obtained after 20 coatings and annealed at $600\text{ }^\circ\text{C}$ for 5 h after each spinning procedure, using different (A) and (B) spin-coating techniques.

As seen from Fig. 12, the peaks attributable to the CaCO_3 ($2\theta \approx 29.5$; PDF [96-210-0190]) could be determined in the XRD patterns confirming the formation of crystalline calcium carbonate. The XRD patterns of CaCO_3 layers fabricated after 30 spin-coating procedures were almost identical to ones presented in Fig. 12.

The SEM micrographs of the surfaces of obtained CaCO_3 samples showed the formation partially even surface with clearly pronounced formation of individual crystallites. Interestingly, the quality of sol-gel coated thin films of the CaCO_3 was not influenced by used spin-coating technique. The Raman spectra of synthesized CaCO_3 coatings contained characteristic CaCO_3 peaks located at 153, 281, 617, 668, 709, 1084 cm^{-1} [76, 77]. It is interesting to note, that the positions of Raman bands determined in the Raman spectra of synthesized CaCO_3 according to [76] could be attributed to the partially amorphous calcium carbonate phase.

Calcium hydroxyapatite coatings were synthesized by low-temperature dissolution-precipitation method. Silicon substrates coated with partially amorphous and/or crystalline CaCO_3 were soaked in disodium hydrogen

phosphate Na_2HPO_4 solution for 28 days at 80 °C. Fig. 13 presents XRD patterns of CHAp coatings on Si substrate.

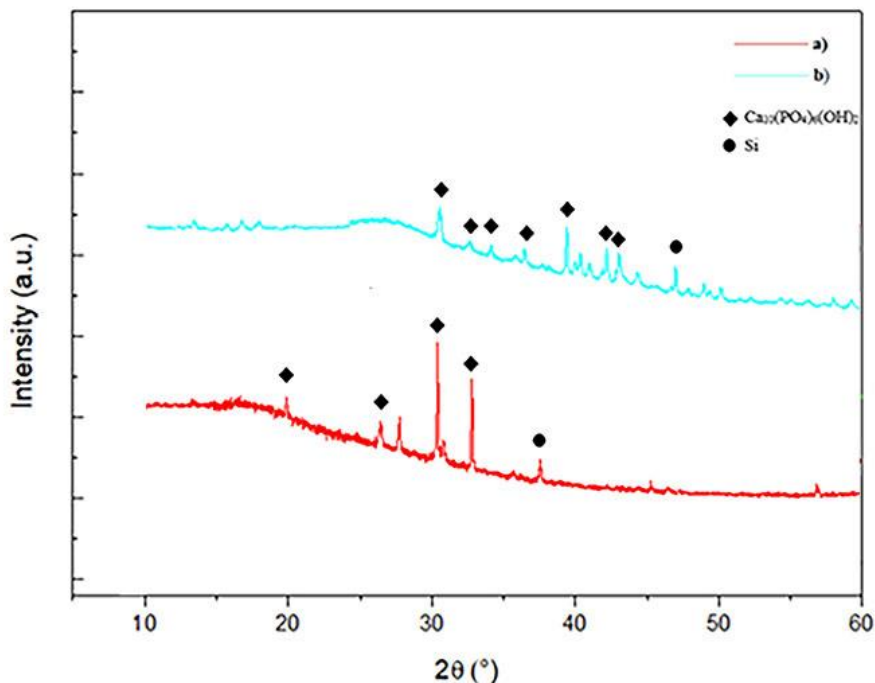


Fig. 13. XRD patterns of calcium hydroxyapatite thin films fabricated by sol-gel and dissolution-precipitation method using different spin-coating techniques: a) - (A) and b) - (B).

The XRD analysis results show the negligible influence of parameters of spinning on the crystallization of calcium hydroxyapatite on Si substrate. The characteristic CHAp reflections could be easily distinguished (PDF [74-0566]). Thus, the XRD analysis data proved that calcium hydroxyapatite could be easily obtained at 80 °C from the Ca-O sol-gel precursor solution on Si substrate using a spin-coating technique and following dissolution-precipitation approach.

Thickness of CHAp coatings was measured using SEM analysis of cross-sections of the films, and was found to be approximately 900-945 nm. Fig. 14 shows Raman spectra in wavenumber region from 100 to 1250 cm^{-1} of CHAp sample containing 30 layers of CaCO_3 on Si substrate.

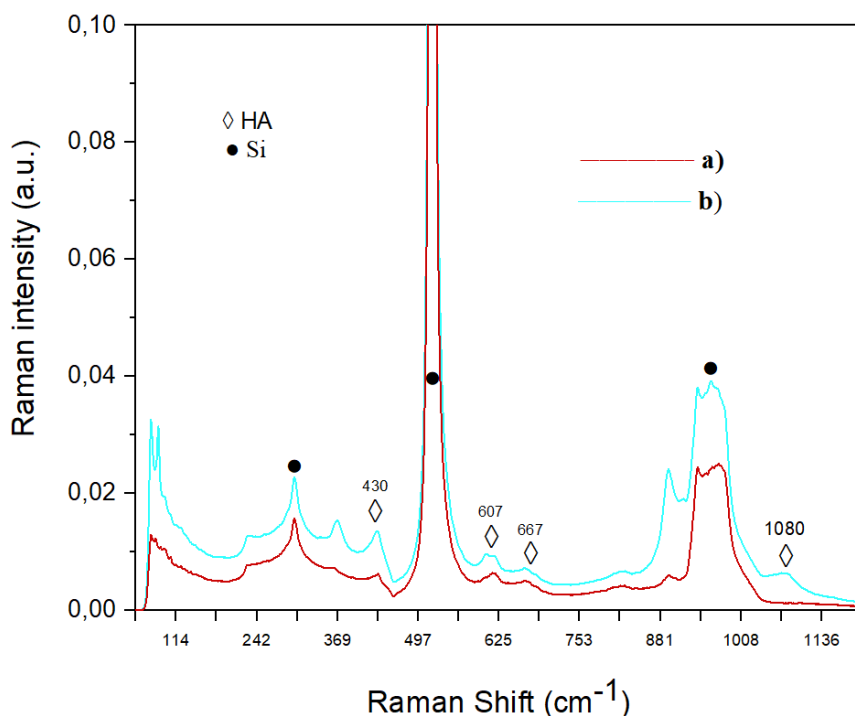


Fig. 14. Raman spectra of CHAp synthesized by sol-gel and dissolution-precipitation method using different spin-coating techniques: a) - (A) and b) - (B).

The broad bands with sharp peaks near 300, 500 and 950 cm^{-1} belongs to overtone spectrum of Si substrate. However, the intense bands corresponding to the symmetric stretching vibration of phosphate groups in $\text{Ca}_{10}(\text{PO}_4)_6(\text{OH})_2$ are also seen [78, 79]. The Raman spectroscopy results are in a good agreement with XRD analysis data. Using Raman optical microscopy system, the representative optical images are presented in Fig. 15. Taken images demonstrate the formation of individual crystallites in the film matrix. By pointing the laser at the formed individual crystallites, CHAp signals have been observed. Defects commonly present in 2D materials, such as cracks, vacancies and crystal boundaries [80, 81] were not detected in the CHAp samples synthesized by low-temperature sol-gel and dissolution-precipitation method.

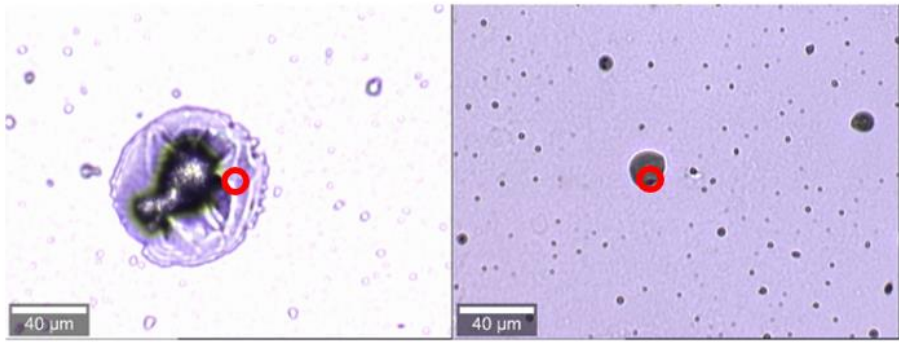
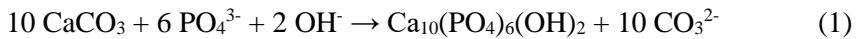


Fig. 15. Images of CHAp thin films obtained by Raman optical microscopy system. Red circles marks the location of focused laser beam for measuring Raman spectra.

In conclusion, the final formation of CHAp on the surface of Si could be expressed by following equation [82–84]:



The possible mechanism of formation of calcium hydroxyapatite by suggested low-temperature sol-gel and dissolution-precipitation method is presented in Fig. 16.

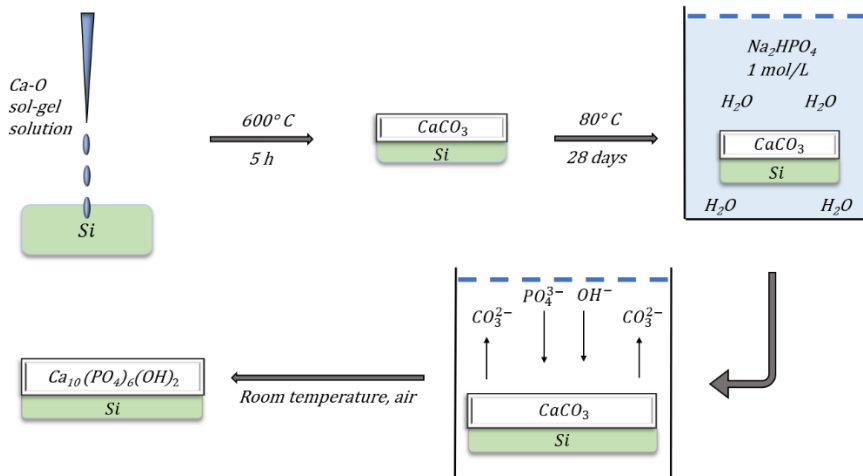


Fig. 16. The possible mechanism of formation of calcium hydroxyapatite by suggested low-temperature sol-gel and dissolution-precipitation method on Si substrate.

3.1.2 Formation of $\text{Ca}_{10}(\text{PO}_4)_6(\text{OH})_2$ coatings on titanium substrate

In this part of PhD thesis a low-temperature synthetic approach for the fabrication of calcium hydroxyapatite coatings on a titanium substrate was developed.

The phase composition of the obtained calcium carbonate coatings on the titanium substrate was determined by X-ray diffraction analysis (Fig. 17).

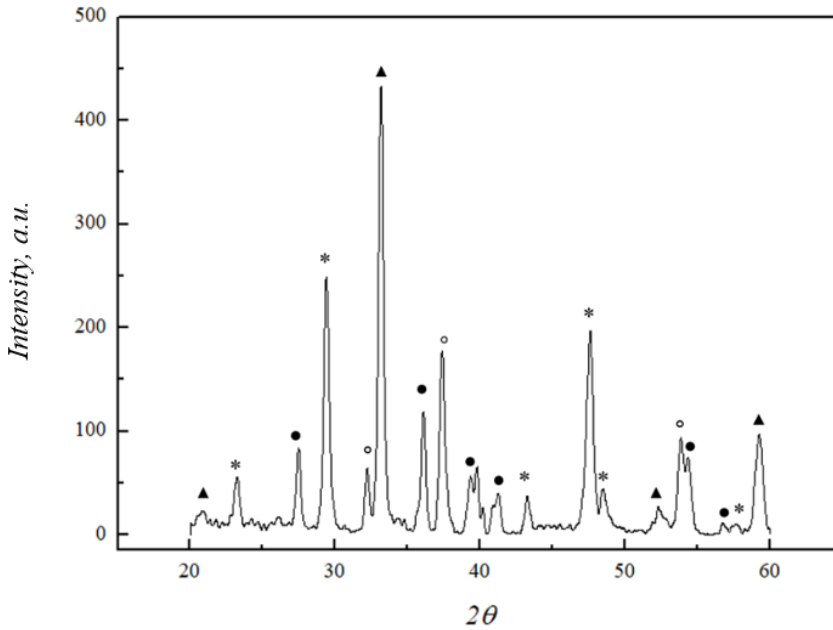


Fig. 17. The XRD patterns of CaCO_3 coatings obtained by spin coating on a Ti substrate after 20 of spin-coating and thermal treatment procedures. Diffraction peaks: *- CaCO_3 (ICDD 01-086-2339), ▲- CaTiO_3 (ICDD 03-065-3287), ○- CaO (ICDD 01-082-1691), ●- TiO_2 (ICDD 01-083-2241).

According to the obtained results, the formation of CaCO_3 after 20 coating procedures was evidently observed. Additionally, the XRD patterns contained intense diffraction peaks corresponding to TiO_2 (rutile) CaO and CaTiO_3 crystalline phases. Fig. 18 shows the XRD patterns of the resulting CaCO_3 coating on the titanium substrate after 28 days of immersion in Na_2HPO_4 solution and the Ti substrate was annealed at 600 °C. It can be seen that the CHAp coating was successfully formed. The diffraction peaks characteristic of the crystalline CHAp phase were observed [19, 85]. Additionally, the peaks attributed to secondary phases such as Na_2HPO_4 (from immersion solution), Ti (substrate) and TiO_2 were also detected. It could be

concluded that CHAp formed, but it did not prevent the formation of TiO_2 . On the other hand, the characteristic peaks of CaTiO_3 are not visible, which may have been due to the fact that the CaTiO_3 layer was coated with CHAp. One of the key advantages of the sol-gel technique is its capacity to produce homogeneous materials [86]. It is evident from the XRD results that the combined sol-gel and dissolution-precipitation reactions method also produces homogeneous CHAp coatings.

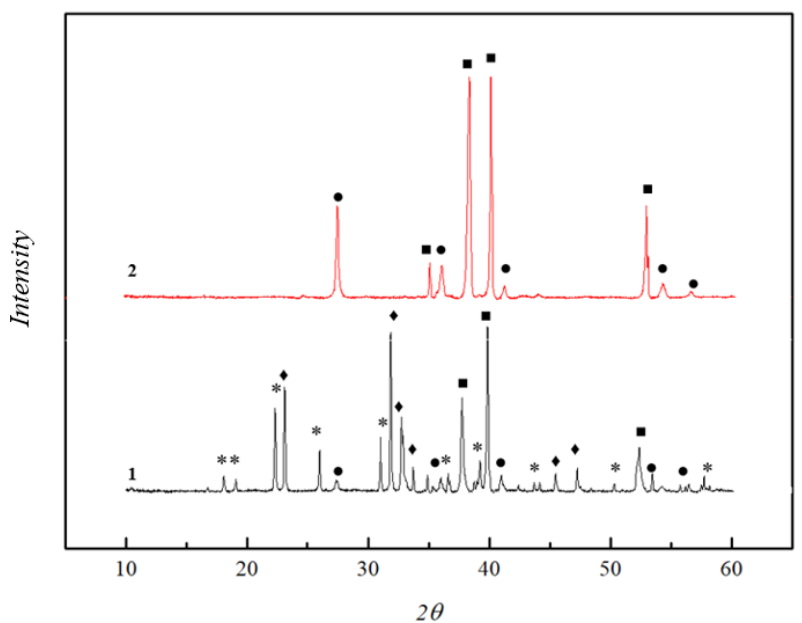


Fig. 18. XRD patterns of CHAp coating obtained after immersion of CaCO_3 coating for 28 days in Na_2HPO_4 solution (1) and Ti substrate annealed at 600 °C (2). Diffraction reflections are marked: \blacklozenge -CHAp (ICDD 00-054-0022), $*$ - Na_2HPO_4 (ICDD 01-076-2287), \blacksquare -Ti (ICDD 01-089-5009), \bullet - TiO_2 (ICDD 01-076-0318).

Raman spectra of the sol-gel-derived CaCO_3 coating and CHAp coating obtained following the dissolution-precipitation reaction are shown in Fig. 19. A high background is visible in the Raman spectrum of the CaCO_3 coating; however, the observed peak at 1084 cm^{-1} corresponds to the symmetric stretching of calcium carbonate [87]. In the Raman spectrum of the CHAp coating, the peaks of phosphate group vibrations at 400 , 574 , 590 , 950 and 1085 cm^{-1} are seen. The peak at about 280 cm^{-1} is attributed to the Ca-PO_4 lattice. All this confirms that the CHAp coating was formed by the dissolution-

precipitation process. The most intense peak observed, at 690 cm^{-1} , is ascribed to the Ti substrate. In addition, the peaks at 159, 220 and 485 could be attributed to the TiO_2 phase [88]. The obtained results of Raman spectroscopy correlate well with the results of X-ray diffraction analysis. The absorption bands observed in the FTIR spectra of synthesized coatings at 1411 cm^{-1} and 879 cm^{-1} in the spectrum of the CaCO_3 coating can be assigned to the stretch vibrations of the carbonate ion [89, 90]. The intense absorption band detected at $\sim 590\text{ cm}^{-1}$ is attributed to the vibration of Ti-O in titania.

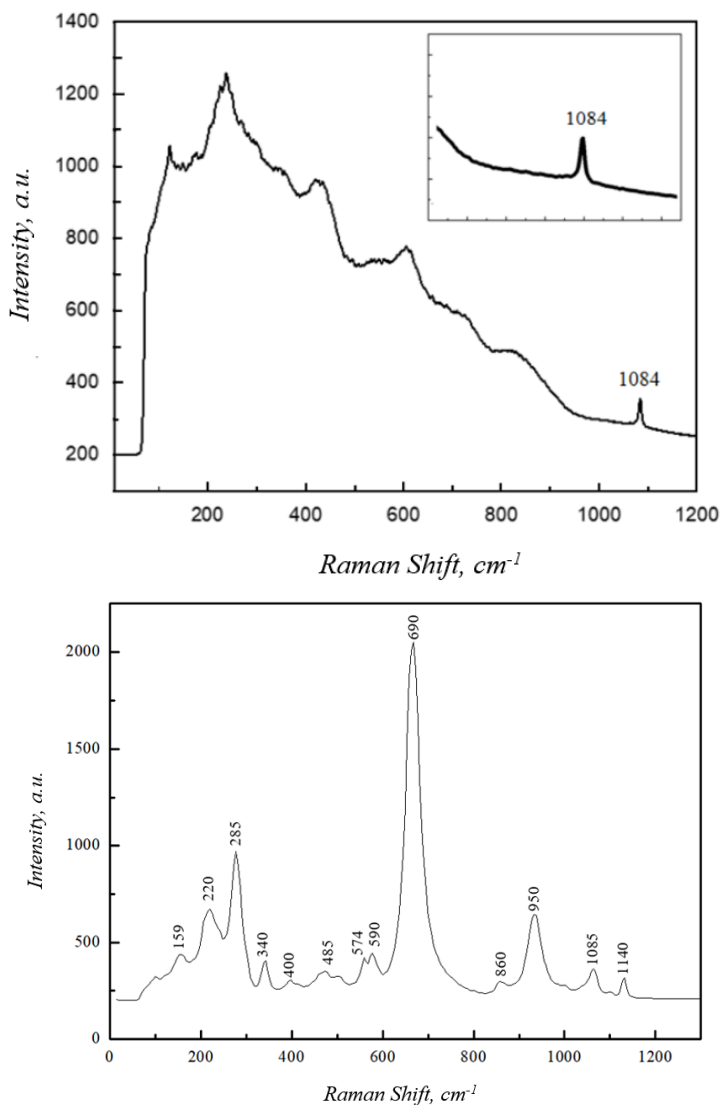


Fig. 19. Raman spectra of CaCO_3 (top) and CHAP (bottom) coatings.

The results deduced from the FTIR spectrum of the formed CHAP coating are in good agreement with the results of XRD and Raman spectroscopy, confirming the formation of intermediate (CaCO_3) and end products ($\text{Ca}_{10}(\text{PO}_4)_6(\text{OH})_2$). According to the origin of observed absorption bands, the formation of carbonated hydroxyapatite ($\text{Ca}_{10-x}(\text{PO}_4)_6-x(\text{CO}_3)_x(\text{OH})_{2-x-2y}(\text{CO}_3)_y$) occurred during the dissolution-precipitation reaction [90, 91].

The SEM micrographs of the formed CaCO_3 after spin-coating and thermal treatment procedures confirmed that the Ti substrate was uniformly covered. SEM micrographs of CHAP coatings after immersion of the CaCO_3 coating in Na_2HPO_4 solution are presented in Fig. 20.

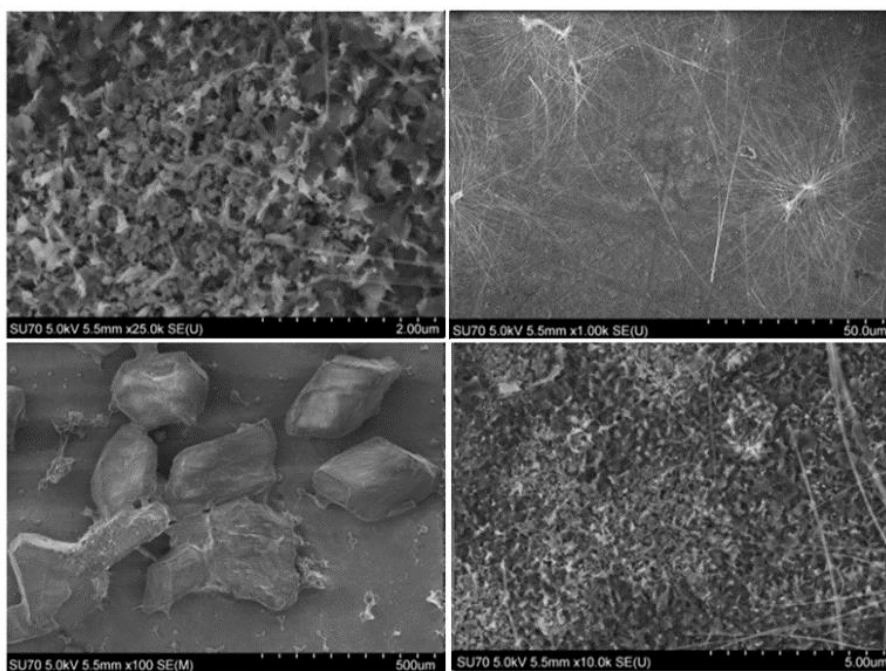


Fig. 20. SEM micrographs of CHAP coating obtained at different magnifications.

It can be seen from the SEM micrographs obtained at lower magnification that dendritic clusters of CHAP and Na_2HPO_4 crystallites formed on the titanium surface. The surface of CHAP is rough and porous [92]. However, at higher magnification, the formation of homogeneously distributed plate-like crystals and spherical particles is seen. After annealing the obtained CHAP coating at 900°C , the morphology of the crystals changed

dramatically, with the formation of rods of 1–2 μm in length and 100–150 nm in width (see Fig. 21). This is in good agreement with literature data [19, 93].

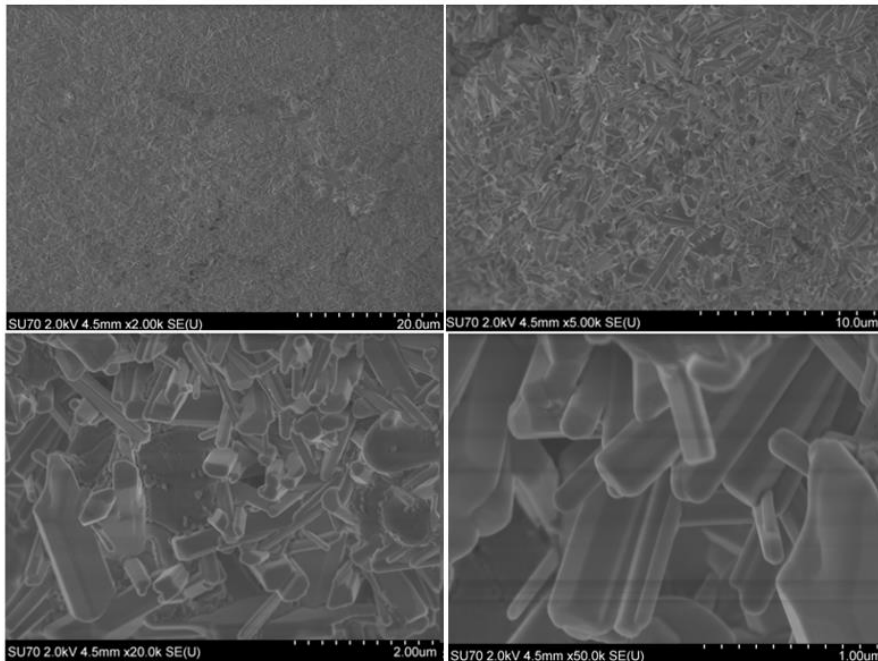


Fig. 21. SEM micrographs of CHAp coating obtained after annealing at 900 $^{\circ}\text{C}$.

The surface morphology of CHAp films was also studied with an optical 3D profilometer (see Fig. 22). The results presented in Fig. 22 show that the formed CHAp coatings were not evenly distributed on the Ti substrate. Moreover, the surface roughness observed for CHAp coatings was higher than that seen for the CaCO_3 coating. These results partially correlate with morphological features determined by SEM analysis. The surface roughness and average coating height were observed to increase slightly after annealing at 900 $^{\circ}\text{C}$. The maximum roughness (7905 nm) and average height (10,296 nm) were determined for these coatings.

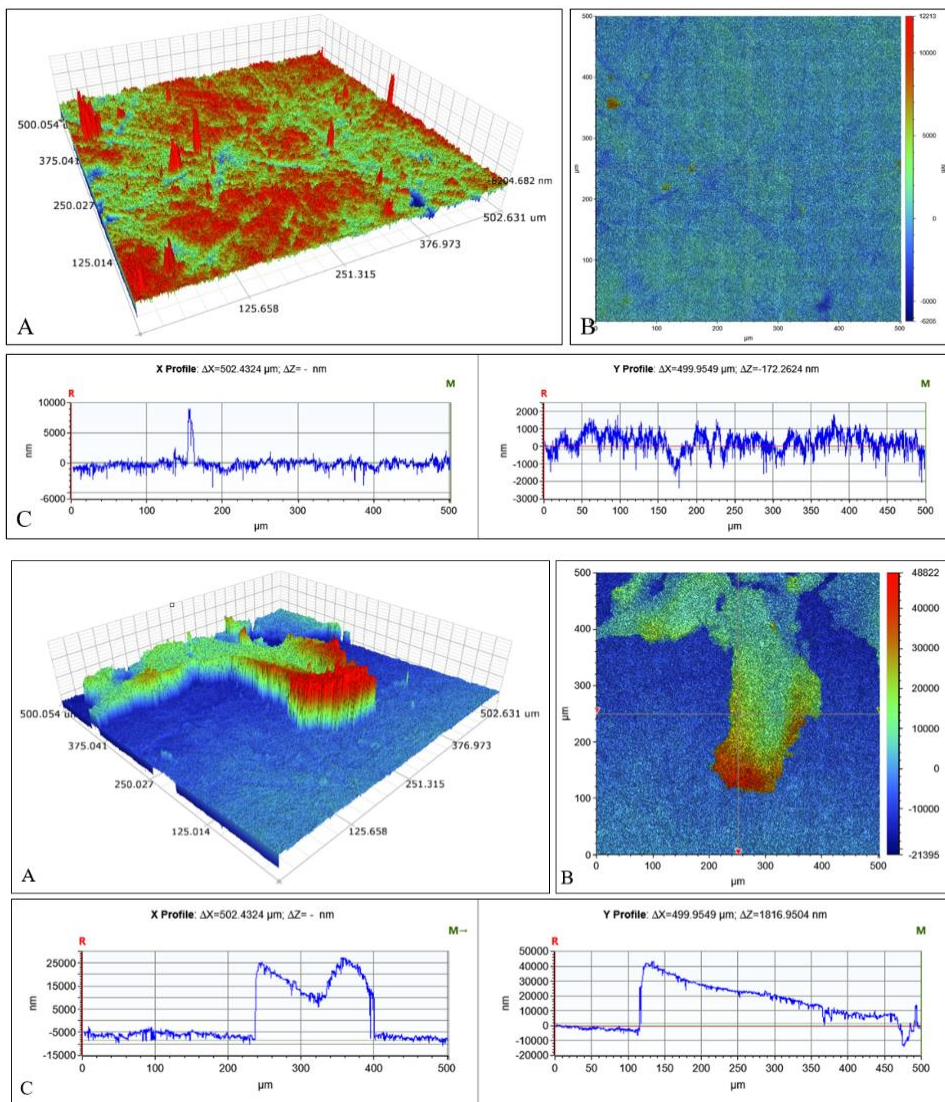


Fig. 22. The results of optical 3D profilometry for the as-prepared CHAp coating (top) and that annealed at 900 °C (bottom): optical 3D (A) and 2D contour (B) images and roughness (C) profiles.

3.1.3 Electrochemical characterization

In order to study the corrosion behaviour of fabricated coatings, first of all, the time dependences of the open-circuit potentials (E_{ocp}) of the samples were measured in Hanks' balanced salt solution (Fig. 23).

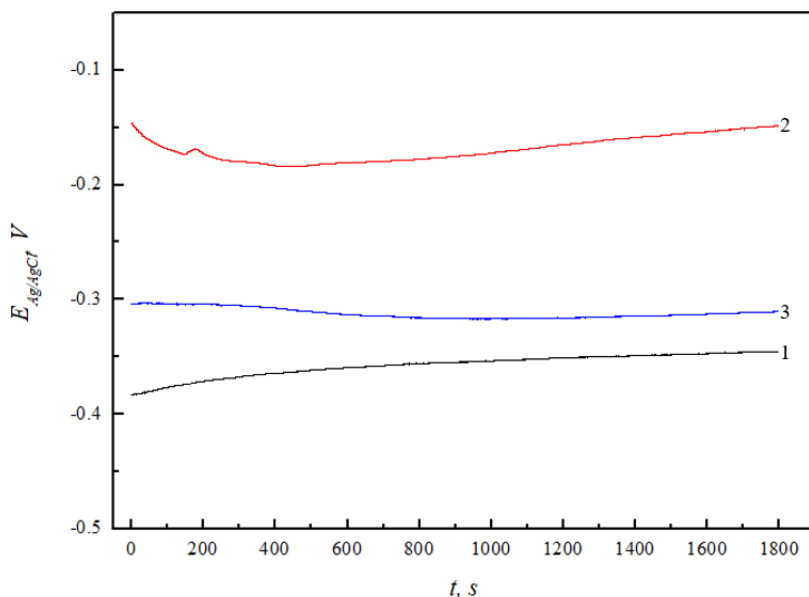


Fig. 23. Exposure time dependences of the E_{ocp} potential of titanium/CHAp films in Hanks' solution: 1-annealed Ti substrate, 2-CHAp coating, 3-CHAp coating after annealing at 900 °C.

The open-circuit potential is a parameter that describes the relative corrosion stability of the sample in the solution. The stability of E_{ocp} shows that all the processes that determine its value are in a stationary state. The rates of spontaneous reactions have stabilized and the investigated electrode surface is stable. If E_{ocp} shifts to more positive values, it indicates a decrease in the corrosivity of the electrode, i.e., blocking of the surface by a passive layer. If E_{ocp} shifts to more negative potentials, it indicates that the investigated system is in the corrosion zone. As can be seen from Fig. 23, the E_{ocp} value of the CHAp coating initially decreased to ~ -0.18 V, indicating that the corrosion activity increased, which is related to the formation of a protective layer of the formed CHAp coating. The E_{ocp} of the working electrode began to shift to more positive values after 7 min. and reached a quasi-stationary value. In this case, a new passivation layer was formed on the surface of the tested electrode. The E_{ocp} of the annealed CHAp coating did not change much with increasing exposure time. It was observed that this coating reached a quasi-stationary value after ~ 6 min., and the passivation layer was formed quite quickly, which indicates the formation of stable coating. The E_{ocp} of the Ti substrate started to become positive in the initial stage of immersion, and the time-invariant value of the E_{ocp} settled after ~ 11 min. The difference in E_{ocp} values between the tested samples was negligible, indicating that the surface properties of

formed CHAp coatings were similar. The influence of the formed CHAp coating on the corrosion rate of the titanium in Hanks' balanced salt solution was evaluated using the Tafel dependences of the electrodes. The Tafel polarization curves were recorded when the E_{ocp} of the electrodes reached quasi-stationary values (Fig. 24).

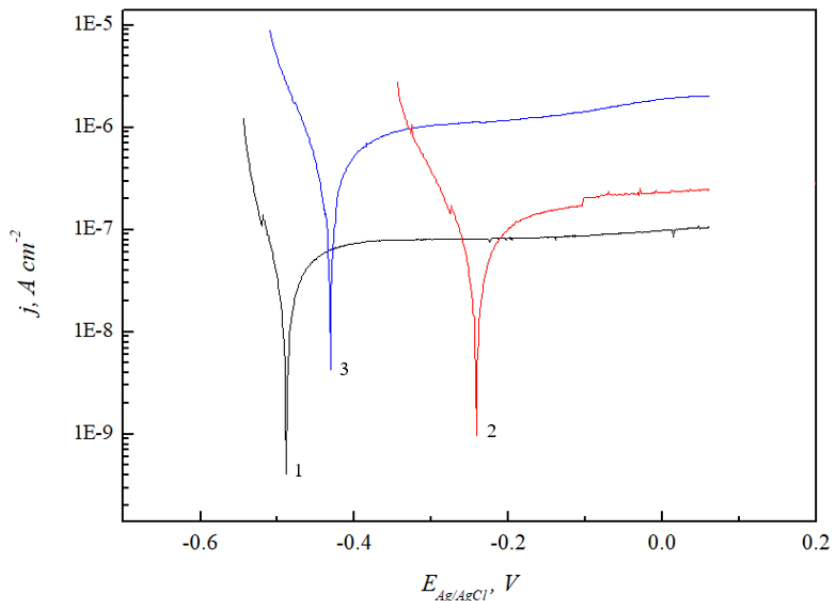


Fig. 24. Tafel dependencies: 1-heated Ti substrate, 2-CHAp coating, 3-CHAp coating after annealing at 900 °C.

The corrosion rates (j_{corr}) were determined by extrapolation from linear ranges of cathodic and anodic Tafel dependencies. The determined corrosion rates are presented in Table 5.

Table 5. Corrosion parameters of the investigated coatings.

| Sample | b_c , V | b_a , V | J_{corr} , $A \cdot cm^{-2}$ |
|---------------------------------|-----------|-----------|--------------------------------|
| Ti substrate | 0.0209 | 0.0163 | 2.27×10^{-8} |
| CHAp coating | 0.0302 | 0.0154 | 3.34×10^{-8} |
| CHAp coating annealed at 900 °C | 0.0420 | 0.0106 | 1.82×10^{-7} |

The polarization curves of the CHAp coating shifted towards more positive values, indicating a less active corrosion process. Table 5 also presents the tendencies of the cathodic (b_c) and anodic (b_a) Tafel dependencies

of the tested samples. It can be seen that the CHAp coating was characterized by higher bc values than the uncoated Ti substrate. The anodic tendency of the Tafel dependence of the obtained coatings decreased compared to that of the titanium substrate. The largest positive boost was determined for the as-prepared CHAp coating. Interestingly, the E_{ocp} of the post-annealed CHAp coating was lower. This may have been influenced by the porosity of the coating, which did not prevent the Hanks' balanced salt solution from contacting the metal and causing corrosion. Evidently, these newly fabricated porous and sufficiently rough CHAp films can be successfully used not only as biomimetic nanotherapeutic coatings but also as electrochemical sensors [94], thermoluminescent sensors [95], or pH-sensitive fluorescent protein sensors [96]. The CHAp could be easily doped with lanthanide ions [97]. These nanostructures could be applied for the development of novel pH-responsive systems, which can determine the acidity of biofilms fluorometrically [98]. Finally, it is well known that pH is a critical indicator of bone physiological function and disease status. The suggested CHAp coatings fabricated at low temperatures could be applied for the development of non-invasive and real-time sensing of bone pH in vivo [99]. Therefore, the application of our CHAp system as a bone pH sensor currently is under investigation.

In conclusion, it was found that a CHAp coatings were formed on the silicon and titanium substrates using a novel low-temperature synthesis method. SEM and 3D optical microscopy showed that the CHAp coatings formed were non-uniform, porous, coarse crystalline and with large variations in height. It was observed, that more uniform coatings of calcium hydroxyapatite were obtained on Ti substrate. The corrosion behaviour of the formed CHAp coatings on the titanium substrate was also evaluated by electrochemical methods.

3.2 Solvothermal synthesis of calcium-deficient hydroxyapatite via hydrolysis of α -tricalcium phosphate

The effects of various organic solvents (solvent nature and fraction in the solution) and solvothermal conditions on the formation of calcium-deficient hydroxyapatite (CDHA) via hydrolysis of α -tricalcium phosphate (α -TCP) were investigated in this part of PhD thesis. The effects of sodium lauryl sulfate and various amino acids (DL-aspartic acid, dodecanedioic acid, suberic acid) on the formation of calcium-deficient hydroxyapatite *via* hydrolysis of α -tricalcium phosphate (α -TCP) were investigated as well. Moreover, a combined effect of these additives and ethylene glycol as a synthesis medium

was also estimated. The hydrolysis reaction was performed in solutions containing different concentrations of additives in aqueous and mixed aqueous-organic media under solvothermal conditions.

3.2.1 Investigation of influence of organic solvent on the formation of CHAp

Some properties and characteristics of the α -TCP precursor used in further investigations are presented in Fig. 25.

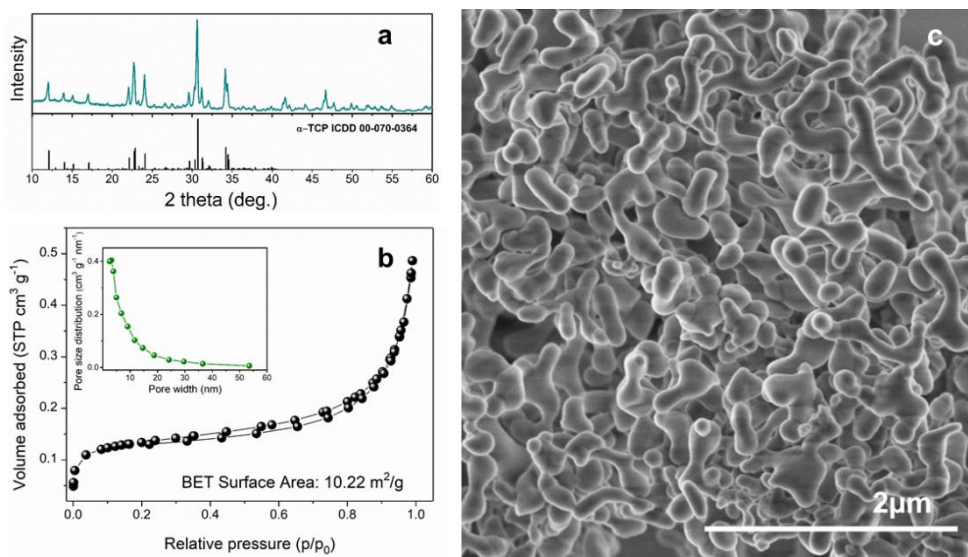


Fig. 25. Characteristics of the obtained α -TCP precursor: XRD pattern (a), Nitrogen adsorption-desorption isotherms and the corresponding BJH pore size distribution (b), and SEM image (c).

As it could be seen from the XRD diffraction pattern (Fig. 25 (a)), all the diffraction peaks match very well the standard XRD data of monoclinic $\text{Ca}_3(\text{PO}_4)_2$ (ICDD #00-070-0364). The sample exhibited type IV isotherms and displayed H3 hysteresis loop (Fig. 25 (b)). Based on the pore size distribution results, illustrated in the inset image of Fig. 25 (b), the sample was mainly characterized by the pores smaller than 10 nm, albeit larger pores up to 55 nm were also present. BET surface area (S_{BET}) of the precursor was 10.22 $\text{m}^2 \text{g}^{-1}$. The starting powders consisted of the agglomerates of nanodimensional elongated particles of irregular shape (Fig. 25 (c)).

Under the reaction with water, α -TCP hydrolyzes and converts to CDHA as described by the following equation [16]:



The phase crystallinity and purity of synthesized CDHA powders were investigated by XRD analysis, which revealed some differences among the obtained products. The samples treated with organic solvent only (0:100) showed no evidence of CDHA formation: due to the absence of water, no hydrolysis reaction occurred, and the phase of such samples remained α -TCP (ICDD 00-070-0364).

In the case of EtOH, PrOH, and BuOH, introduction of even small fraction (20:80) of water resulted in the formation of single-phased CDHA (ICDD 00-76-0694), while an increasing water content provided the same results. This was observed under various solvothermal conditions applied. Under harsher solvothermal conditions (200 °C for 5 h), formation of monetite was observed in the presence of EtOH, PrOH, and BuOH. This was especially notable in the case of BuOH. For comparison between the solvents, XRD patterns of the samples prepared under different solvothermal conditions using W:O ratio of 40:60 are given in Fig. 26 as representative.

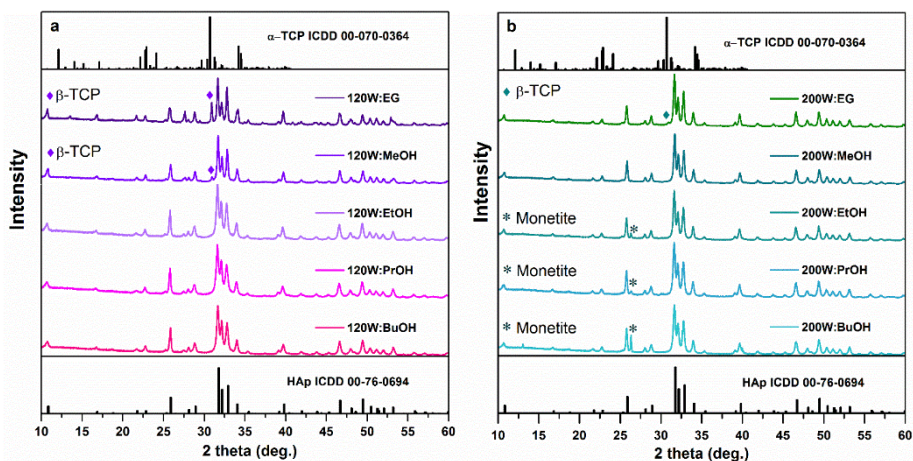


Fig. 26. XRD patterns of the samples prepared using water to organic solvent ratio of 40:60 after solvothermal treatment at 120 °C for 3 h (a) and at 200 °C for 5 h (b).

In contrast, MeOH and EG had a stronger inhibitory effect on α -TCP hydrolysis. These effects were especially notable for EG under the milder solvothermal conditions. Fig. 27 shows powder XRD patterns of the samples

prepared under different solvothermal treatment (120 °C for 3 h and 200 °C for 5 h) using varying water to MeOH and water to EG ratios. After treatment at 120 °C for 3 h, the sample with water to EG ratio of 20:80 remained a single phase α -TCP (ICDD 00-070-0364, Fig. 27 (b)). Increasing water content induced formation of CDHA, but a strong peak attributed to β -tricalcium phosphate (β -TCP, ICDD 00-070-2065) was visible in the sample 120-W-EG-40:60, while only a trace of β -TCP could be observed in the XRD pattern of 120-W-EG-60:40 (Fig. 27 (b)). MeOH has also inhibited formation of CDHA, albeit to a lesser extent. The sample 120-W-MeOH-20:80 contained large fractions of CDHA, β -TCP and α -TCP, traces of β -TCP were detected in the sample 120-W-MeOH-40:60, while the samples with a larger amount of water consisted of single-phase CDHA (Fig. 27 (a)).

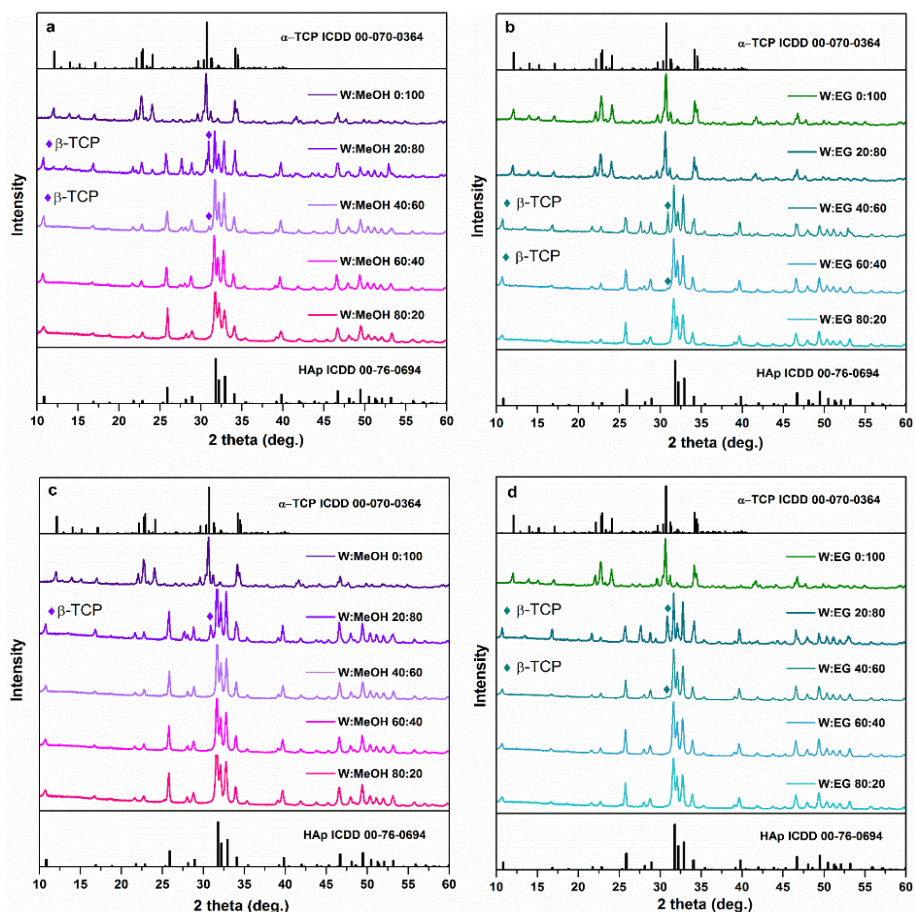


Fig. 27. XRD patterns of the samples prepared using different water to MeOH (a, c) and water to EG (b, d) ratios under different solvothermal conditions: 120 °C for 3 h (a, b) and 200 °C for 5 h (c, d).

Increased temperature and prolonged time of the solvothermal synthesis caused a shift in the inhibitory effect: single-phase CDHA was observed for the sample 200-W-EG-60:40, only a trace of β -TCP was detected in the XRD pattern of 200-W-EG-40:60, whereas formation of CDHA was also obvious in 200-W-EG-20:80, even though a significant fraction of β -TCP was still present in the latter sample (Fig. 27 (d)). Higher temperature and longer reaction time have also resulted in the decreased β -TCP fraction in the sample 200-W-MeOH-20:80 (Fig. 27 (c)).

FTIR spectra of the products prepared by the solvothermal treatment are presented in Fig. 28.

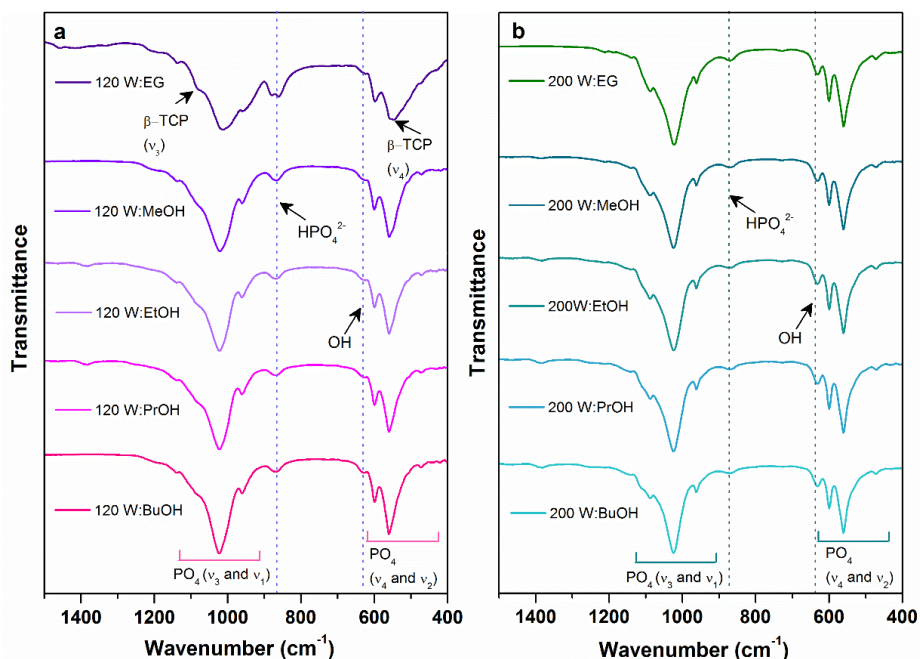


Fig. 28. FTIR spectra of the samples prepared using water to organic solvent ratio of 40:60 after solvothermal treatment at 120 °C for 3 h (a) and at 200 °C for 5 h (b).

The FTIR range of 1500–400 cm^{-1} was chosen as representative since the main bands attributed to HAp and TCP polymorphs could be observed in this region, and the differences between the samples were hardly distinguishable in the full range spectra. Stretching modes of hydroxyl group usually observed at 3572 cm^{-1} was hardly visible in our case, and its intensity was similar in all the samples [51]. Several absorption bands at around 1095–960 and 636–550 cm^{-1} were observed in all the samples. The bands centred at 561–556 and 603–599 cm^{-1} are assigned to ν_4 O-P-O bending mode of CDHA

[100]. Bands centred at 1020–1017 and 1090–1084 cm^{-1} correspond to ν_3 asymmetric P-O stretching vibrations, the peak centred at 961–960 cm^{-1} corresponds to symmetric P-O stretching vibrations (ν_1) of CDHA [100]. The peak centred at 633–625 cm^{-1} corresponds to the bending vibrational mode of hydroxyl (-OH) group [18, 100]. An absorption band centered at 871–868 cm^{-1} is assigned to P-O(H) stretching mode of the HPO_4^{2-} group, which is present in the structure of calcium-deficient CDHA [24]. The aforementioned bands were visible in the FTIR spectra of all the samples. Additional bands attributed to β -TCP phase were only visible in the FTIR spectra of the samples prepared using larger fractions of EG (120-W-EG-20:80; 120-W-EG-40:60; 200-W-EG-20:80). As it could be seen from Fig. 28 (a), bands at 544 and 1083 cm^{-1} of the sample 120-W-EG-40:60 could be attributed to β -TCP phase (ν_4 and ν_3 , respectively) [101]. Such results are in agreement with XRD data.

Morphology of the obtained samples varied from plate-shaped to rod-shaped. Samples fabricated without organic solvents consisted of plate-shaped crystals arranged into flower-like structures. In this study, only slight effects on morphology were observed due to the introduction of EtOH, PrOH and BuOH. Under the milder solvothermal conditions (120 °C for 3 h), large proportion of EtOH and PrOH (120-W-EtOH-20:80; 120-W-PrOH-20:80) caused formation of large plates with no prominent self-assembly (Figs. 29–31).

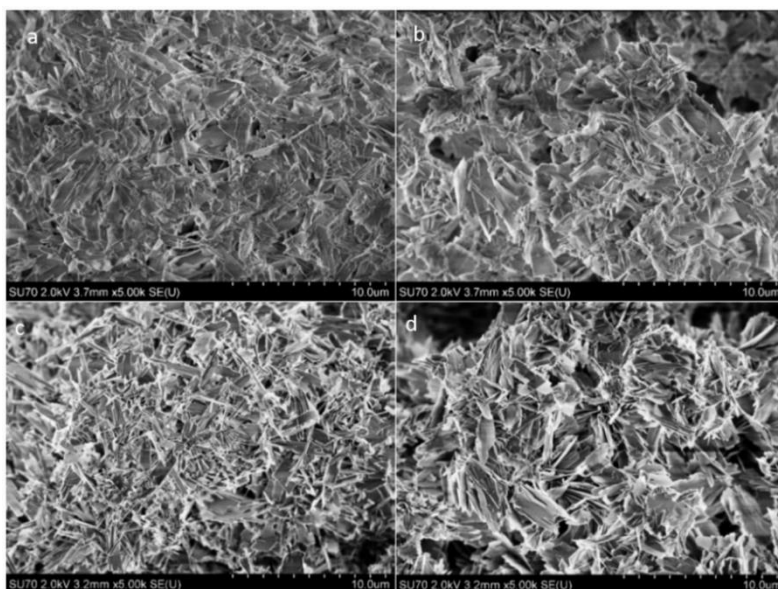


Fig. 29. SEM images of the samples after solvothermal treatment with W-EtOH: a) 120-W-EtOH-80:20; b) 120-W-EtOH-60:40; c) 200-W-EtOH-80:20; d) 200-W-EtOH-60:40.

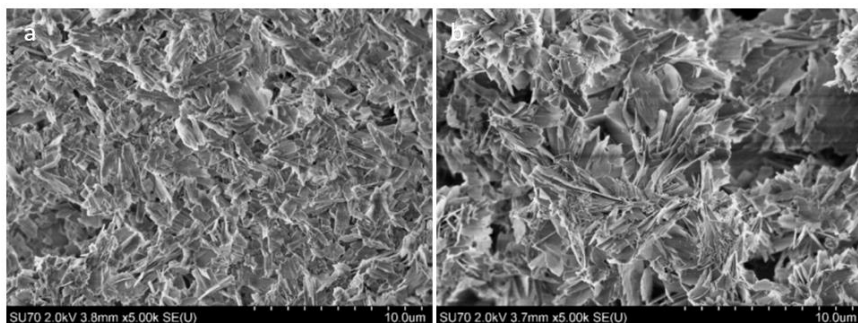


Fig. 30. SEM images of the samples after solvothermal treatment with W-PrOH: a) 120-W-PrOH-80:20; b) 120-W-PrOH-60:40.

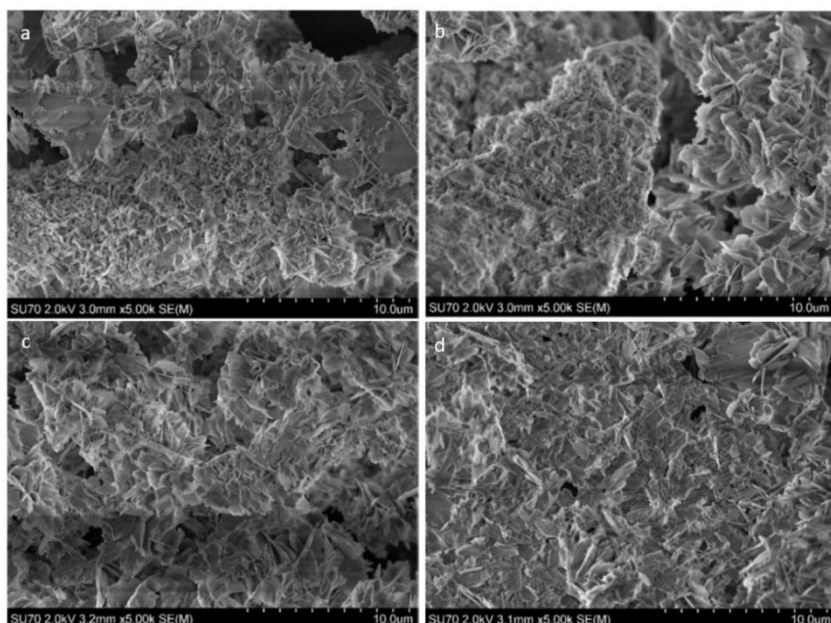


Fig. 31. SEM images of the samples after solvothermal treatment with W-BuOH: a) 120-W-BuOH-80:20; b) 120-W-BuOH-60:40; c) 200-W-BuOH-80:20; d) 200-W-BuOH-60:40.

With an increasing proportion of water (W:O 40:60; 60:40; and 80:20), formation of narrower plates and some rods was observed, moreover, the crystals were arranged in the flower-like structures. When the reaction time and temperature were increased, higher proportions of EtOH, PrOH and BuOH resulted in the formation of rods. Moreover, more rods have formed at the same W:O ratios under harsher conditions. However, plate-like crystals were still prevailing in all of the samples. SEM images of the samples prepared under different solvothermal conditions using W:O ratio of 40:60 are presented in Fig. 32.

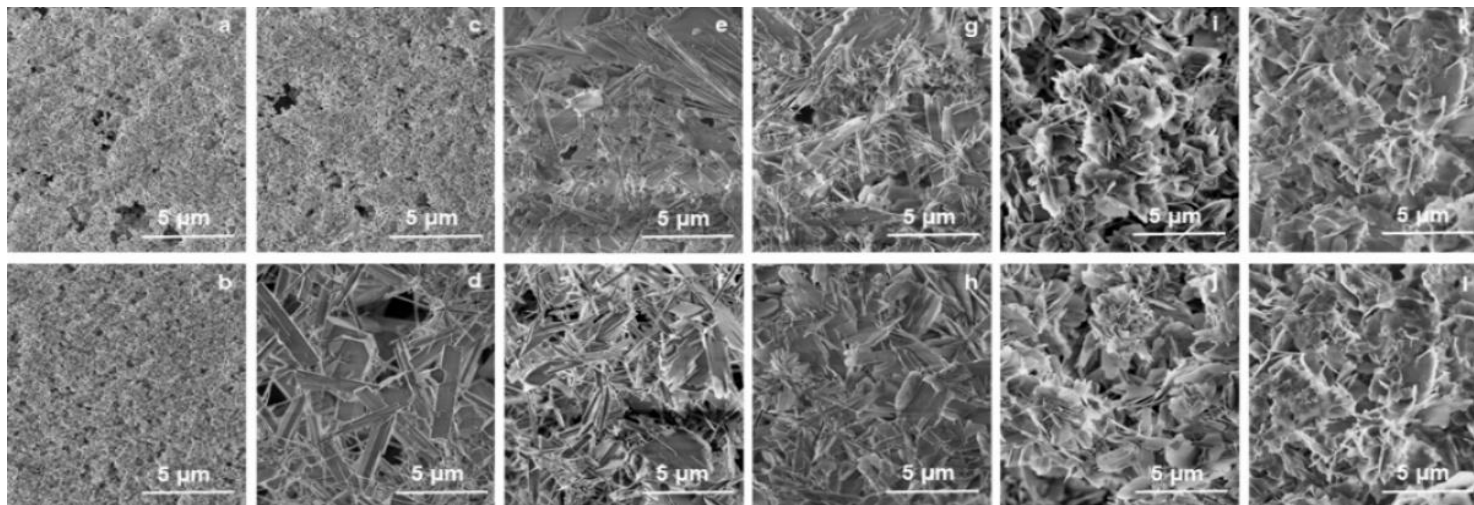


Fig. 32. SEM images of the samples after solvothermal treatment with W:O ratio 40:60: (a) 120-W-EG-40:60; (b) 200-W-EG-40:60; (c) 120-W-MeOH-40:60; (d) 200-W-MeOH-40:60; (e) 120-W-EtOH-40:60; (f) 200-W-EtOH-40:60; (g) 120-W-PrOH-40:60; (h) 200-W-PrOH-40:60; (i) 120-W-BuOH-40:60; (j) 200-W-BuOH-40:60.

The use of MeOH and BuOH had a more prominent effect on the sample morphology. In this case, the samples were also dominated by plate-like crystals, but a trend of long and narrow plates formation was observed. Moreover, more rods were present in the MeOH and BuOH treated samples if compared to the samples prepared in W:EtOH and W:PrOH solutions.

From all the solvents analysed, EG had the highest impact on the sample morphology. Under the milder solvothermal conditions (120 °C for 3 h), formation of CHAp was completely suspended in the sample 120-W-EG-20:80 (Fig. 33 (c)).

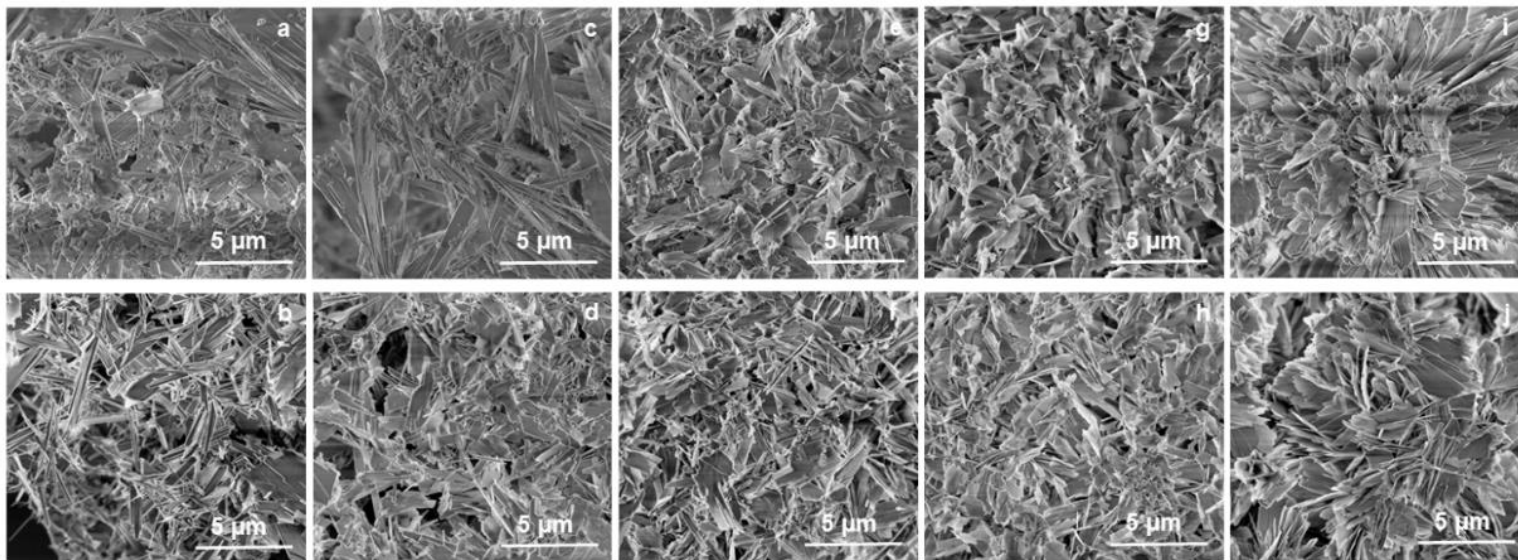


Fig. 33. SEM images of the samples prepared with different ratios of water and ethylene glycol: (a) 120-W-EG-0:100; (b) 200-W-EG-0:100; (c) 120-W-EG-20:80; (d) 200-W-EG-20:80; (e) 120-W-EG-40:60; (f) 200-W-EG-40:60; (g) 120-W-EG-60:40; (h) 200-W-EG-60:40; (i) 120-W-EG-80:20; (j) 200-W-EG-80:20; (k) 120-W-EG-100:0; (l) 200-W-EG-100:0.

Sample 120-W-EG-40:60 consisted of large plates, some rods, and some particles of different shape which could probably be attributed to β -TCP phase. Sample 120-W-EG-60:40 was characterised by a large amount of rods in addition to the plates. In contrast, no rods were observed in a sample prepared with a minimal amount of EG (120-W-EG-80:20). Prolonged reaction time and increased temperature resulted in a rod-dominated morphology of the CDHA samples. The sample 200-W-EG-20:80 was characterised by larger and smaller rods, as well as some minor particles of different shape which should be attributed to β -TCP phase. Slightly lower proportion of EG (samples 200-W-EG-40:60 and 200-W-EG-60:40) resulted in formation of both plate-shaped and a large amount of rod-shaped crystals. No rods were observed in a sample prepared with a minimal amount of EG (200-W-EG-80:20).

It is assumed that the solvothermally assisted formation of rod-like crystals comprises two main stages: nucleation step (reaction of ions) when small crystalline nuclei are formed in a supersaturated matrix, and a growth step during which nuclei grow into their final shape and size [102]. In our case, the changes in crystal morphology might be related to the decreased supply of water when more organic solvent is introduced to the system. This would limit the hydrolysis reaction of α -TCP [18]. Previous studies stated that the increasing amount of alcohol in the aqueous reaction solution reduces solubility of α -TCP and hence limits the supply of Ca^{2+} and PO_4^{3-} ions [18, 103, 104]. Such an effect is related to the changes in dielectric constant ($\epsilon_r(\omega)$) of the solution: with a decreasing dielectric constant of the solvent, solubility decreases due to the decreased solvation energy [105, 106]. Dielectric constant of pure water is 78.5 at 25 °C, whereas dielectric constants of alcohols are significantly lower. Dielectric constants at 25 °C of the organic solvents used in this study are as follows: $\epsilon_r(\omega)_{\text{EG}} = 38.5$; $\epsilon_r(\omega)_{\text{MeOH}} = 32.70$; $\epsilon_r(\omega)_{\text{EtOH}} = 24.3$; $\epsilon_r(\omega)_{\text{PrOH}} = 19.92$; $\epsilon_r(\omega)_{\text{BuOH}} = 17.5$ [106]. Variations in $\epsilon_r(\omega)$ of water- organic solvent mixtures depend on the composition of the solution, but in general, $\epsilon_r(\omega)$ values decrease with the increasing fraction of organic solvent [107]. Solvents with different physicochemical properties influence solubility, crystal nucleation and growth rate which in turn has an effect on the crystallinity and morphology of the final products [106]. When the hydrolysis reaction is not suspended and the solution is supersaturated with Ca^{2+} and PO_4^{3-} ions, nucleation is dominating over the crystal growth and smaller crystals are formed. When on the contrary, the supply of Ca^{2+} and PO_4^{3-} ions is limited, fewer nuclei form and larger crystals tend to grow [102, 106]. Other properties of different solvents might have also affected the processes of α -TCP hydrolysis and HAp crystallisation. For instance, EG present in the

reaction mixture would significantly change the viscosity of the suspension [108, 109]. Subsequently, ion mobility and diffusion rate would be reduced, which would in turn inhibit the hydrolysis reaction and retard the nucleation process [109]. Viscosity of the reaction media decreases with the increasing temperature, and thus the inhibitory effects of EG on are less significant when the solvothermal synthesis is performed at higher temperature (Fig. 27 (b, d)).

It is worth to note that the results obtained in this study differ from those reported by Goto et al. [18] who managed to prepare needle-like CDHA crystals arranged into flower-like structures by using water-ethyl alcohol solutions. We assume such discrepancies could originate due to the different starting materials used and slightly different solvothermal conditions applied: Goto et al. applied commercial α -TCP (Taihei Chemical Industrial Co., Ltd., Osaka, Japan) synthesized at high temperature and consisting of large particles, while in our study we used low-temperature synthesized metastable α -TCP.

Fig. 34 shows the nitrogen adsorption-desorption isotherms and the corresponding BJH pore size distribution for CDHA particles. According to the new classification by the IUPAC, all the samples exhibited type IV isotherms and displayed H3 hysteresis loops.

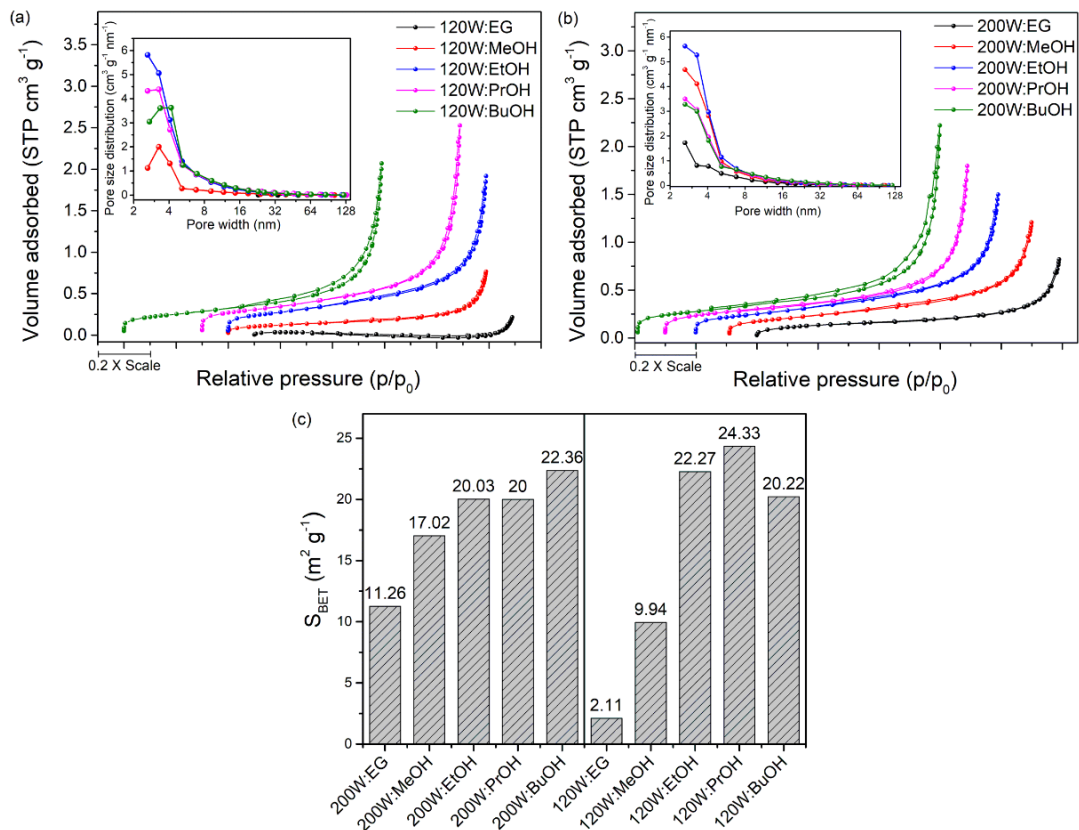


Fig. 34. Nitrogen adsorption-desorption isotherms and the corresponding BJH pore size distribution for the samples after solvothermal treatment with W:O ratio of 40:60: (a) 120 °C; (b) 200 °C; and (c) BET surface area for the samples after solvothermal treatment with W:O ratio of 40:60 at 120 °C and 200 °C.

This type of isotherms indicates the existence of mesopores in the structure of all the samples. The hysteresis loop type H3 is associated with the existence of aggregated plate-like particles [110]. Such results are in agreement with SEM data. Based on the pore size distribution results illustrated in the inset image of Fig. 34 (a, b), there were no significant differences between the samples. All the samples were characterised by a wide pore size distribution. Multi-scale pores ranged from 2.6 to 128 nm, suggesting that both mesopores and macropores were present in the CDHA structure. All the samples except those prepared with EG contained both mesopores of smaller sizes (from 2.6 nm up to 9.0 nm), and small number of larger mesopores (from 9.0 nm up to 128 nm). On the contrary, in the sample 120-W-EG-40:60 mainly mesopores of larger width (from 23.0 nm up to 50.2 nm) were found. We assume the pores of smaller sizes presented in the structure of this sample were probably partially blocked by the viscous ethylene glycol. As it can be seen from Fig. 34 (c), the mesoporous 120-W-PrOH-40:60 had the highest BET surface area (S_{BET}) of $24.3 \text{ m}^2\text{g}^{-1}$. Extremely low surface area was observed for the samples prepared using EG: S_{BET} of $2.1 \text{ m}^2\text{g}^{-1}$ and $11.3 \text{ m}^2\text{g}^{-1}$ were obtained for the samples 120-W-EG-40:60 and 200-W-EG-40:60, respectively. One reasonable explanation for this decrease is that residues of EG may have increased blockage of the nitrogen gas penetration. Also, this decrease of S_{BET} could be the result of the structural changes occurring during the synthesis of CDHA. The remaining samples were characterised by similar S_{BET} values ranging from 9.9 to $22.4 \text{ m}^2\text{g}^{-1}$.

3.2.2 Investigation of influence of different organic additives on the formation of CHAp

The characteristics of CDHA sample prepared in aqueous solution under hydrothermal conditions without any additives are given in Fig. 35.

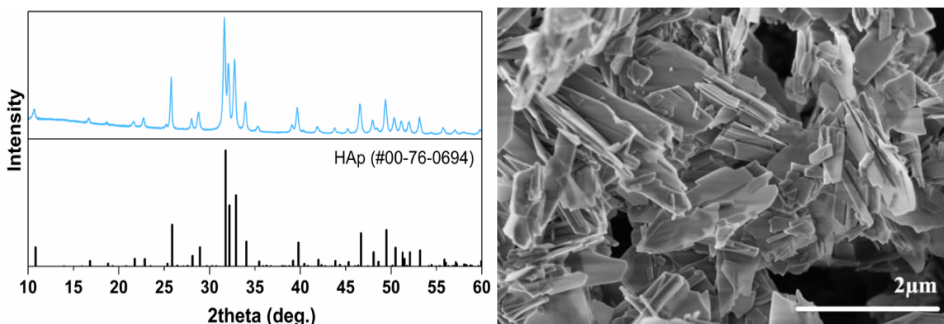


Fig. 35. XRD patterns (left) and SEM image (right) of HAp synthesized from α -TCP without additives. Vertical lines represent the standard XRD pattern of HAp.

As seen from the XRD pattern, under selected synthesis conditions α -TCP was fully converted to CDHA, all diffraction peaks matched the standard XRD data of $\text{Ca}_{10}(\text{PO}_4)_6(\text{OH})_2$ (ICDD #00-76-0694). There were no peaks associated with starting material. SEM image revealed that the morphology of the sample was dominated by plate-like particles of micrometric dimensions.

Different results were observed when varying concentrations of SLS and amino acids were applied as additives. The XRD patterns of the final products are given in Fig. 36. The lowest concentration of SLS (0.005 mol/L) did not affect the formation of CDHA in terms of phase purity, however increasing SLS amount in the reaction solution resulted in the formation of neighboring phase.

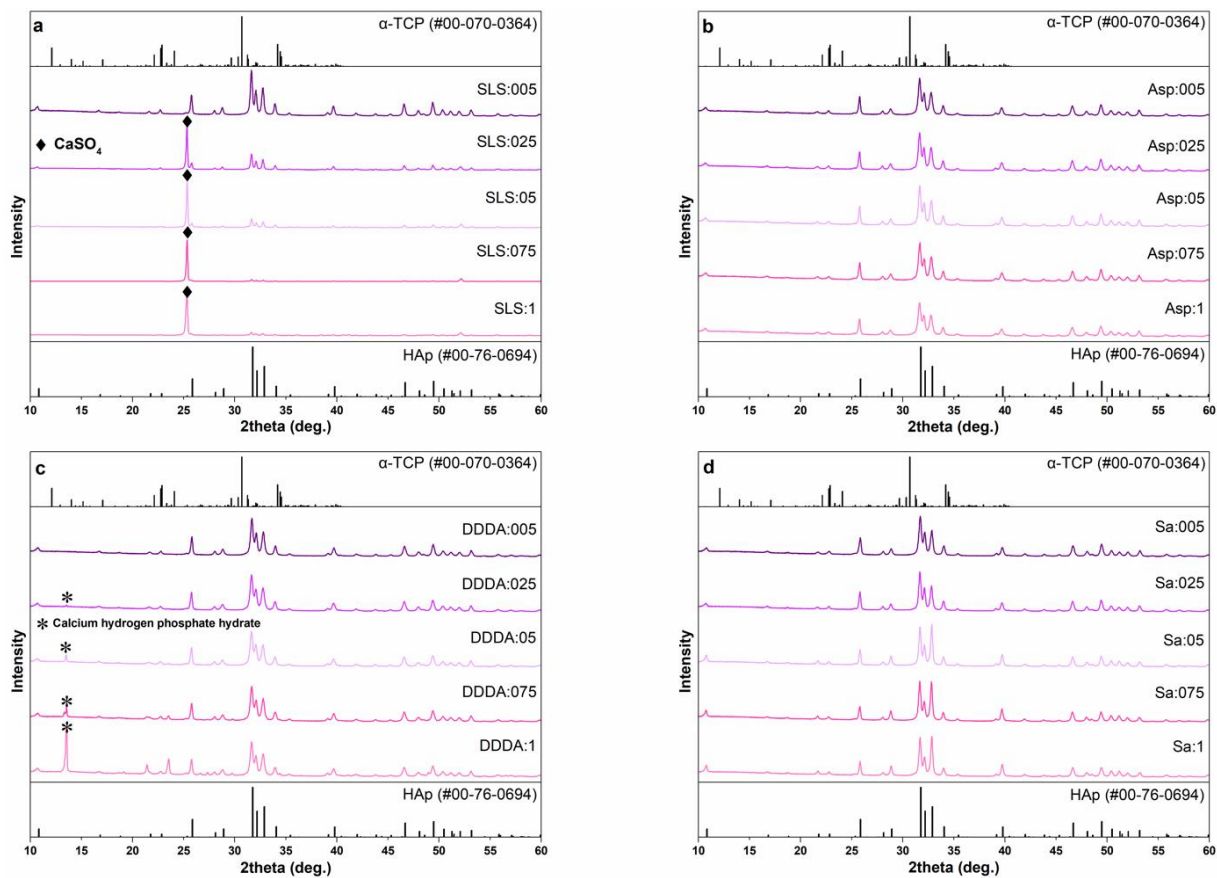


Fig. 36. XRD patterns of the samples prepared using various concentrations of SLS (a), DL-aspartic acid (b), dodecanedioic acid (c) and suberic acid (d) after a hydrothermal treatment at 200 °C for 5 h.

In addition to the typical CDHA diffraction pattern, a sharp peak at ca. 25.4° could be seen, the intensity of this peak gradually increased with an increase of SLS concentration. This peak was attributed to calcium sulfate (CaSO_4 , ICDD #00-072-0503). The observed results suggest that under selected synthesis conditions the released Ca^{2+} ions were more easily precipitated by SO_4^{2-} counterions rather than phosphate species. Similar trend was observed for DDDA: the lowest concentration of DDDA (0.005 mol/L) did not affect the formation of CDHA, but higher DDDA content resulted in the formation of secondary crystal phase. The diffraction peak centered at ca. 13.6° emerged in the XRD pattern of the sample prepared using 0.025 mol/L DDDA. The intensity of this peak increased significantly with an increase of DDDA concentration. This peak corresponded to calcium hydrogen phosphate hydrate ($\text{CaH}_3\text{O}_5\text{P}$, ICDD #00-046-0494). Hydrothermal reactions in the presence of DL-aspartic and suberic acids resulted in the formation of single-phase CDHA regardless of the concentration of additives. No formation of impurities or traces of TCP were observed in these cases. It should be noted, that in the case of suberic acid the intensity of 3 major peaks varied depending on the concentration of additive, which could suggest the change in powders morphology. To summarize, 2 of 4 selected additives led to the formation of secondary phases, while 2 others did not affect the phase purity.

In this study, we also aimed to check the combined effect of amino acids and organic solvents on the phase purity and morphology of the sample. Since single-phase CDHA was obtained using DL-aspartic and suberic acids, these two additives were used for further experiments. Previous studies revealed that among various organic solvents, ethylene glycol had the greatest influence on the sample morphology [53]. The highest effect on morphology was observed with water to ethylene glycol ratio of 40:60. Hence, solvothermal synthesis with DL-aspartic and suberic acids was performed with this mixture. The XRD patterns of the reaction products are demonstrated in Fig. 37.

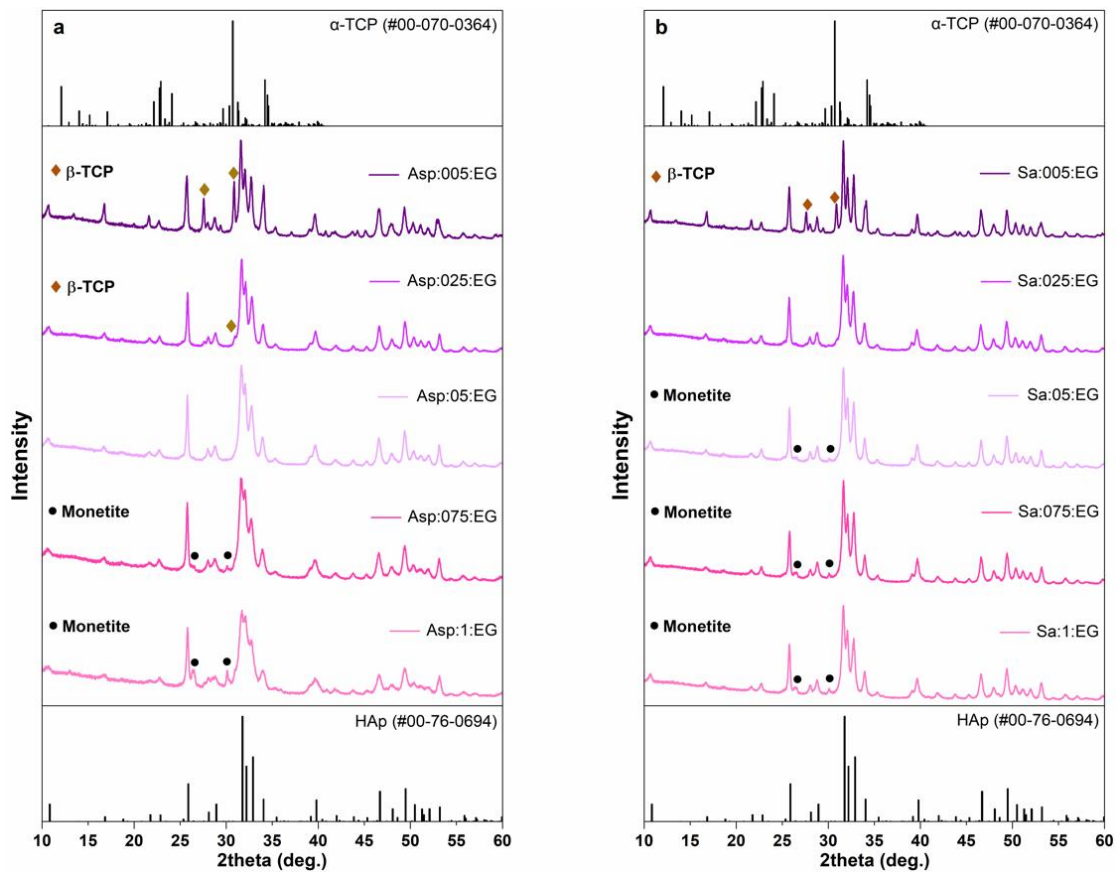


Fig. 37. XRD patterns of the samples prepared using various concentrations of DL-aspartic (a) and suberic (b) acids in water-ethylene glycol mixture (40:60, v/v) after a solvothermal treatment at 200 °C for 5 h.

It is seen that phase composition strongly depends on the concentration of additive. With the lowest concentration of DL-aspartic acid (0.005 mol/L), a significant amount of neighboring β -TCP phase was obtained along with a major CDHA phase, however, the amount of β -TCP was reduced with an increase of the concentration of additive. The XRD pattern of the sample synthesized with 0.05 mol/L of aspartic acid did not reveal the presence of any secondary crystal phase. At the same time, the diffraction peaks attributed to monetite (CaHPO_4) emerged in the XRD patterns with the highest concentrations of acid (0.075 and 0.1 mol/L). The presence of suberic acid demonstrated a very similar effect with a minor difference in phase composition. In this case a negligible amount of monetite was detected already in the sample with the concentration of acid of 0.05 mol/L. In our previous study, the formation of monetite in the presence of organic solvents was also observed at higher temperatures (200 °C) of the solvothermal treatment. However, in this case increasing concentrations of amino acids promoted the formation of monetite revealing complex nature of phase transitions in CPs.

FTIR spectra of the samples prepared by hydrothermal and solvothermal treatment were also recorded. The spectral ranges of 1500–400 cm^{-1} of FTIR spectra for the representative samples are displayed in Fig. 38.

As was expected, all the spectra exhibited the absorption bands characteristic of CDHA [74]. The absorption bands of phosphate group in CDHA structure were observed at ca. 560 and 603 cm^{-1} (ν_4), 1020 and 1090 cm^{-1} (ν_3), 960 cm^{-1} (ν_1) which were assigned to O-P-O bending, asymmetric P-O stretching and symmetric P-O stretching vibrations, respectively. The O-P-O bending vibration mode (ν_2) was observed at 470 cm^{-1} and the band at ca. 630 cm^{-1} was assigned to the hydroxyl group [74]. The absorption band centered at around 870 cm^{-1} was ascribed to the P-O(H) stretching mode of the HPO_4^{2-} group, which confirms the formation of CDHA, since this group is absent in stoichiometric non-deficient HAp [24].

The morphology of the samples was found to be dependent both on the nature and concentration of organic additive (Fig. 39).

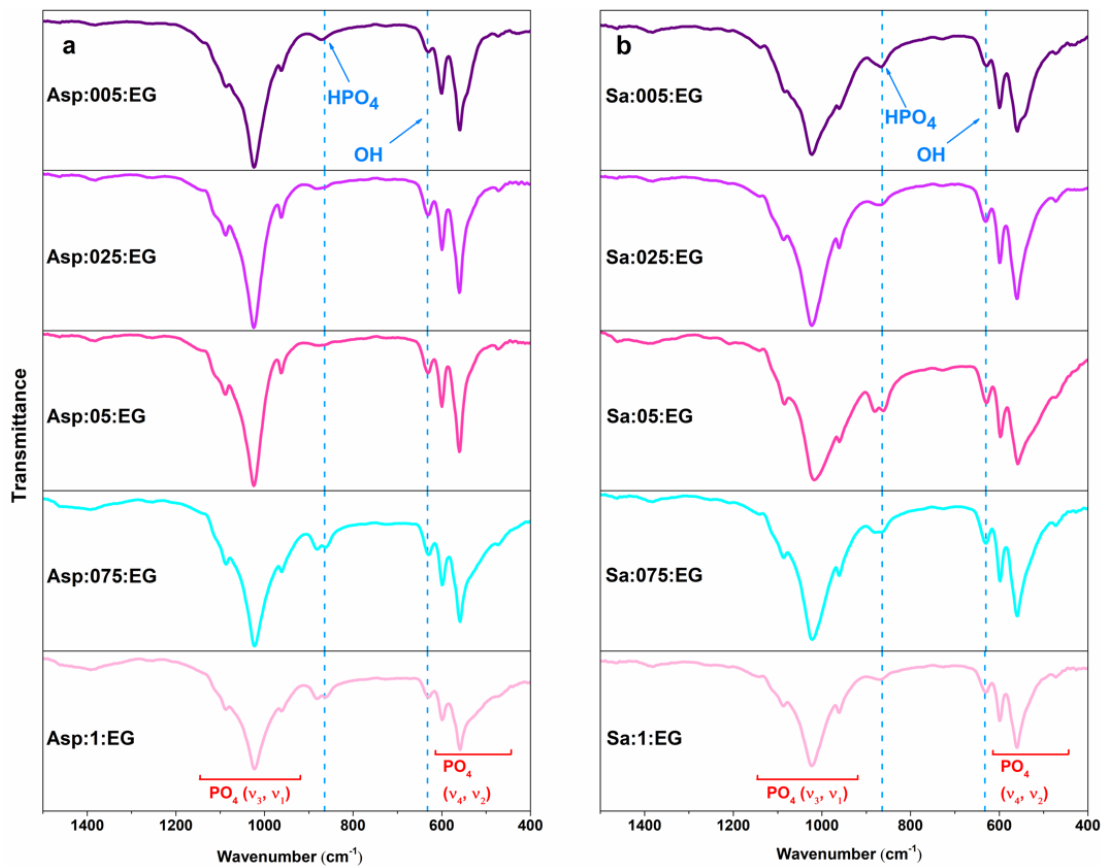


Fig. 38. FTIR spectra of the samples prepared using various concentrations of DL-aspartic (a) and suberic (b) acids in water-ethylene glycol mixture (40:60, v/v) after a solvothermal treatment at 200 °C for 5 h.

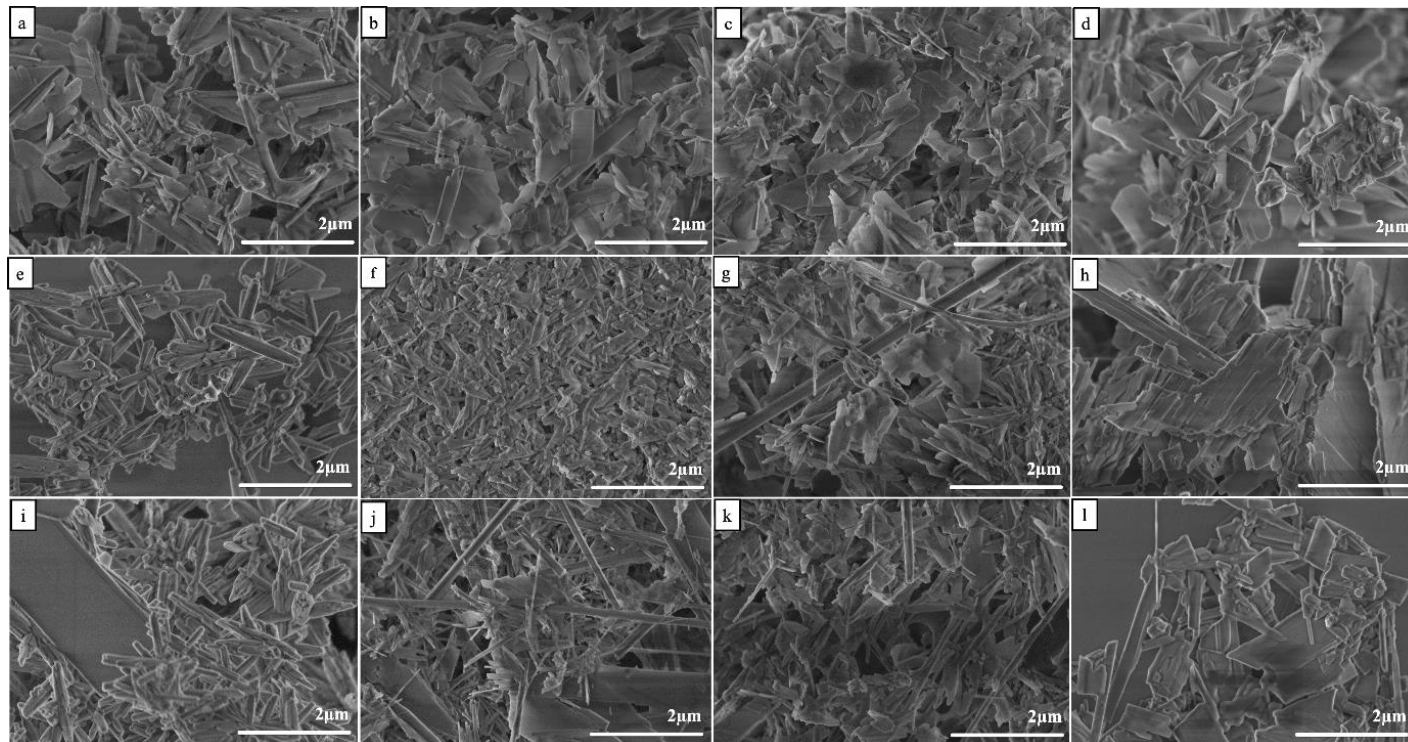


Fig. 39. SEM micrographs of the samples after hydrothermal treatment SLS:005 (a), SLS:05 (e), SLS:1 (i); Asp:005 (b), Asp:05 (f), Asp:1 (j); DDDA:005 (c), DDDA:05 (g), DDDA:1 (k); Sa:005 (d), Sa:05 (h), Sa:1 (l).

When a small amount of SLS (0.005 mol/L) was used in the hydrothermal reaction, the plate-like crystals dominated in the sample, however a small amount of rods was also seen. After increasing the amount of organic compound (0.05-0.1 mol/L), the morphology of CDHA powders changed considerably and rod-shaped assemblies started to form. The use of low concentration of DL-aspartic acid resulted in the formation of micrometric plate-like particles while increasing the amount of acid first led to the reduction of particle size and further formation of some rods. The effect of DDDA was similar to that of aspartic acid and the morphology evolution from plate-like particles to the mixture of plates and rods was observed with an increase of additive concentration. The influence of suberic acid on the morphology of CDHA samples was found to be minor, plate like particles were obtained regardless of the concentration of acid.

The SEM images of the samples synthesized in a mixture of water and ethylene glycol in the presence of DL-aspartic and suberic acids are given in Fig. 40.

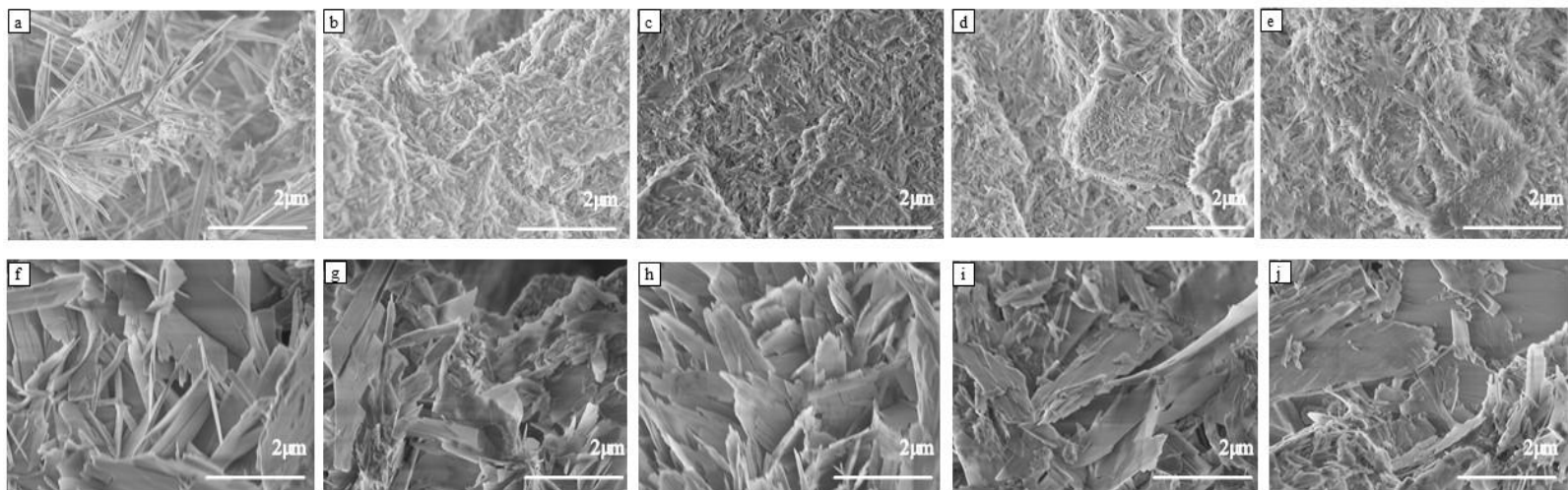


Fig. 40. SEM micrographs of the samples after solvothermal treatment under ratio 40:60 of water to ethylene glycol Asp:005:EG (a), Asp:025:EG (b), Asp:05:EG (c), Asp:075:EG (d), Asp:1:EG (e); Sa:005:EG (f), Sa:025:EG (g), Sa:05:EG (h), Sa:075:EG (i), Sa:1:EG (j).

In the case of aspartic acid, the presence the lowest concentration of additive resulted in the formation of a mixture of relatively long rods and short rods. Using a higher concentration of aspartic acid the obtained powders consisted of micrometric agglomerates, which in they turn were composed of smaller plate- and rod-like particles. The size of the particles was significantly smaller compared to those of synthesized in aqueous medium. In the case of suberic acid, relatively large plate-like particles were obtained regardless of the concentration of additive. The morphology was comparable with that of powders obtained by the hydrothermal synthesis with no additives. To summarize, different impact of additives on the morphology of HAp is probably related to different structures and chemical compositions of organic additives, which leads to a different interaction with HAp particles during the nucleation and crystal growth process.

CONCLUSIONS

1. The wet chemistry route has been developed to prepare calcium hydroxyapatite ($\text{Ca}_{10}(\text{PO}_4)_6(\text{OH})_2$, HA) thin films on silicon substrate using for the first time low-temperature sol-gel and dissolution-precipitation approach. The calcium carbonate thin films on silicon substrate were obtained by spin-coating technique when substrates were repeatedly coated with 10, 20 and 30 layers of sol-gel solution. The composites formed of crystalline and amorphous CaCO_3 were obtained by calcination the coatings for different time at 600°C .
2. These CaCO_3 coatings were used for the fabrication of calcium hydroxyapatite thin films on silicon substrate using a dissolution-precipitation procedure. The silicon substrates coated with partially amorphous and/or crystalline CaCO_3 were soaked in disodium phosphate Na_2HPO_4 solution for 28 days at 80°C . The XRD analysis and Raman spectroscopy data proved that calcium hydroxyapatite could be easily obtained by the developed synthesis method.
3. The possible mechanism of formation of calcium hydroxyapatite using low-temperature sol-gel and dissolution-precipitation method was suggested. The elaborated low-temperature synthesis method for HAp coatings allow much more efficiently to control the surface morphology of the end product.
4. The same low-temperature synthetic approach including the sol-gel and dissolution-precipitation procedures was developed for the fabrication of calcium hydroxyapatite coatings on titanium substrate. It was determined that HAp with small amount of side phases have formed on the Ti substrate. In the Raman and FTIR spectra the characteristic HAp absorption bands were observed. The HAp surface formed on the Ti substrate was rough and porous with homogenously distributed plate-like crystals and spherical particles on the surface.
5. The corrosion behaviour of HAp coatings in Hanks' solution was also evaluated. The HAp coating increased the corrosion resistance of the titanium substrate. Also, the analysis of the corrosion behaviour and parameters of the electrochemical tests showed that the protective capacity of HAp coatings obtained by the sol-gel and dissolution-precipitation methods is sufficiently high and could be increased after forming a HAp coating of uniform thickness. These CHAp thin films obtained by suggested synthesis method may be potential candidates in the development of bone implants and different sensors for various analytes.

6. The effects of different organic solvents on the hydrolysis of α -TCP and its conversion to CDHA under different solvothermal conditions have been investigated. Methyl alcohol and ethylene glycol had a stronger inhibitory effect on α -TCP hydrolysis than ethyl, isopropyl and butyl alcohols.
7. The morphology of the obtained samples varied from plate-shaped to rod-shaped. Samples containing some rods were obtained by applying certain ethyl alcohol and isopropyl alcohol proportions, albeit plate-like structures were still prevailing. The use of water-methyl alcohol and water-butyl alcohol mixtures leads to the formation of more rods in addition to the long and narrow plates. From all the solvents analysed, ethylene glycol had the highest impact on the sample morphology.
8. The effects of sodium lauryl sulfate and various amino acids (DL-aspartic acid, dodecanedioic acid, suberic acid) on the formation of calcium-deficient hydroxyapatite *via* a hydrolysis of α -tricalcium phosphate have been investigated. It was demonstrated that the nature and the concentration of organic additives influence the phase purity and morphology of the final product.
9. The higher concentrations of sodium lauryl sulfate and dodecanedioic acid induced the formation of impurities in addition to hydroxyapatite, while aspartic and suberic acid did not affect the phase purity. The morphology of the samples prepared in aqueous medium varied from plate- to rod-like depending on the concentrations of specific organic additive. The use of a mixture of water and ethylene glycol led to the formation of significantly smaller particles having a shape of rods and narrow plates.

LIST OF PUBLICATIONS AND CONFERENCES PARTICIPATION

Articles in Journals

1. R. Karalkeviciene, G. Briedyte, T. Murauskas, M. Norkus, A. Zarkov, J.-C. Yang, A. Kareiva. A novel method for the formation of bioceramic nano-calcium hydroxyapatite coatings using sol-gel and dissolution-precipitation processing. *Chemija*, **33** (2022) 27-34. (DOI: <https://doi.org/10.6001/chemija.v33i2.4705>).
2. R. Karalkeviciene, E. Raudonyte-Svirbutaviciene, J. Gaidukevic, A. Zarkov, A. Kareiva, Solvothermal synthesis of calcium-deficient hydroxyapatite via hydrolysis of α -tricalcium phosphate in different aqueous-organic media. *Crystals*, **12** (2022) 253. (<https://doi.org/10.3390/cryst12020253>).
3. R. Karalkeviciene, G. Briedyte, A. Popov, S. Tutliene, A. Zarkov, A. Kareiva. Low-Temperature Synthesis Approach for Calcium Hydroxyapatite Coatings on Titanium Substrate. *Inorganics*, **11** (2023) 33. (<https://doi.org/10.3390/inorganics11010033>).
4. R. Karalkeviciene, E. Raudonyte-Svirbutaviciene, A. Zarkov, J.-C. Yang, A. I. Popov, A. Kareiva. Solvothermal synthesis of calcium hydroxyapatite via hydrolysis of α -tricalcium phosphate in the presence of different organic additives. *Crystals*, **13** (2023) 265. (<https://doi.org/10.3390/cryst13020265>).

Attended Conferences

1. R. Karalkeviciene, A. Zarkov, G. Briedyte, T. Murauskas, M. Norkus, A. Kareiva. A new method for the formation of bioceramic nano-calcium hydroxyapatite coatings. International Conference-School “Advanced Materials and Technologies 2021”. Palanga, Lithuania, August 23-27, (2021) 153.
2. R. Karalkeviciene, A. Zarkov, G. Briedyte, T. Murauskas, M. Norkus, A. Kareiva. Bioceramic nano-calcium hydroxyapatite coatings on silicon substrates. 16th International Scientific Conference of Lithuanian Chemists “Chemistry & Chemical Technology 2021“. Vilnius, Lithuania, September 24, (2021) 87.
3. R. Karalkeviciene, E. Raudonyte-Svirbutaviciene, A. Zarkov, A. Kareiva. Hydroxyapatite formation by solvothermal treatment of alpha-

tricalcium phosphate with water-alcohol solution. 65th International conference for students and natural science “Open Readings“, Vilnius, Lithuania, March 15-18 (2022) 215.

4. R. Karalkeviciene, E. Raudonyte-Svirbutaviciene, A. Zarkov, A. Kareiva. Solvothermal synthesis of calcium hydroxyapatite in water-organic solvent media. 1st International Conference on Advanced Materials for Bio-Related Applications “AMBRA 2022“, Wrocław, Poland, May 16–19, (2022) P-15.
5. R. Karalkeviciene, E. Raudonyte-Svirbutaviciene, J. Gaidukevic, A. Zarkov, and A. Kareiva. Solvothermal Synthesis of Calcium Hydroxyapatite via Hydrolysis of α -Tricalcium Phosphate in Different Aqueous-Organic Media. International conference “Functional Inorganic Materials“, Vilnius, Lithuania, October 6-8, (2022) 46 (oral report).

ACKNOWLEDGEMENTS

I would like to thank:

Prof. Habil. Dr. Aivaras Kareiva, who was my academic supervisor during my PhD studies.

To my academic advisor Prof. Dr. Aleksej Žarkov, thank you for taking the time to explain, offer suggestion, and comment.

Dr. Eva Raudonytė-Svirbutavičienė. Eva, it was a pleasure to work in a team with you, to take decisions and to keep the lab clean and tidy. You know what I mean.

Special gratitude for the opportunity to experience the welcoming and professional atmosphere of the Department of Inorganic Chemistry.

Greta Briedytė, a wonderful Master's student, who was very interesting to interact with, to work with, to solve chemical problems, to come to conclusions and to have a laugh.

PhD student Mantas Norkus, thank you so much for your help in answering any questions, for explaining how the Rigaku miniFlex II works, for taking the time to teach me how to prepare the samples for measurement, patiently explaining how Origin programme works and for your friendliness.

Dr. Tomas Murauskas for patiently explaining how the Raman spectroscope works and for helping with measurements.

Dr. Jolanta Raudonienė, who has always been there to help with any questions. Thank you for saving me many hours with your help.

Dr. Aleksandra Prichodko, for professional administration team support.

PhD student Andrius Pakalniškis and Dr. Andrius Laurikėnas, for the SEM micrographs of the surfaces.

PhD student Greta Inkrataitė, for explaining how to submit an article to the journal.

Assoc. prof. dr. Justina Gaidukevič and Assoc. prof. dr. Živilė Stankevičiūtė thank You for cooperation.

Special thanks to my lovely husband for patience and overall support.

Special thanks to my lovely daughter Viktorija Karalkevičiūtė, for helping me find my way in the world of references, for helping me weigh up the compounds for the synthesis of sol-gel synthesis (which, by the way, was a great success), and for all my help in scientific matters.

Special thanks to my lovely daughter Margarita Karalkevičiūtė, for motivation and support.

Special thanks to my lovely mother prof. dr. Jūratė Senvaitienė for correcting spelling and style errors.

I would like to express my gratitude to all of those who enabled me to develop and produce my PhD research work.

This work has received funding from the European Social Fund (project No 09.3.3-LMT-K-712-23-0070) under grant agreement with the Research Council of Lithuania (LMTLT).

MY SINCERE THANKS TO EVERYONE!

REFERENCES

- [1] Y. In, U. Amornkitbamrung, M.-H. Hong, and H. Shin, "On the Crystallization of Hydroxyapatite under Hydrothermal Conditions: Role of Sebacic Acid as an Additive," *ACS Omega*, vol. 5, no. 42, pp. 27204–27210, Oct. 2020, doi: 10.1021/acsomega.0c03297.
- [2] A. C. Tas, "Synthesis of biomimetic Ca-hydroxyapatite powders at 37 degrees C in synthetic body fluids," *Biomaterials*, vol. 21, no. 14, pp. 1429–1438, Jul. 2000, doi: 10.1016/s0142-9612(00)00019-3.
- [3] A. K. Teotia *et al.*, "Nano-Hydroxyapatite Bone Substitute Functionalized with Bone Active Molecules for Enhanced Cranial Bone Regeneration," *ACS Appl. Mater. Interfaces*, vol. 9, no. 8, pp. 6816–6828, Mar. 2017, doi: 10.1021/acsomega.6b14782.
- [4] A. Szewczyk, A. Skwira, M. Ginter, D. Tajer, and M. Prokopowicz, "Microwave-Assisted Fabrication of Mesoporous Silica-Calcium Phosphate Composites for Dental Application," *Polymers*, vol. 13, no. 1, p. 53, Dec. 2020, doi: 10.3390/polym13010053.
- [5] A. Ressler, A. Žužić, I. Ivanišević, N. Kamboj, and H. Ivankovic, "Ionic substituted hydroxyapatite for bone regeneration applications: A Review," *Open Ceram.*, vol. 6, p. 100122, May 2021, doi: 10.1016/j.oceram.2021.100122.
- [6] S. M. Zakaria, S. H. Sharif Zein, M. R. Othman, F. Yang, and J. A. Jansen, "Nanophase hydroxyapatite as a biomaterial in advanced hard tissue engineering: a review," *Tissue Eng. Part B Rev.*, vol. 19, no. 5, pp. 431–441, Oct. 2013, doi: 10.1089/ten.TEB.2012.0624.
- [7] T. Debnath, A. Chakraborty, and T. K. Pal, "A clinical study on the efficacy of hydroxyapatite - Bioactive glass composite granules in the management of periodontal bony defects," *J. Indian Soc. Periodontol.*, vol. 18, no. 5, pp. 593–600, Sep. 2014, doi: 10.4103/0972-124X.142451.
- [8] A. Rogina, M. Antunović, and D. Milovac, "Biomimetic design of bone substitutes based on cuttlefish bone-derived hydroxyapatite and biodegradable polymers," *J. Biomed. Mater. Res. B Appl. Biomater.*, vol. 107, no. 1, pp. 197–204, Jan. 2019, doi: 10.1002/jbm.b.34111.
- [9] A. Lode, A. Bernhardt, K. Kroonen, M. Springer, A. Briest, and M. Gelinsky, "Development of a mechanically stable support for the osteoinductive biomaterial COLLOSS[®] E," *J. Tissue Eng. Regen. Med.*, vol. 3, no. 2, pp. 149–152, Feb. 2009, doi: 10.1002/term.138.
- [10] M. Kumar, R. Kumar, and S. Kumar, "Coatings on orthopedic implants to overcome present problems and challenges: A focused review," *Mater.*

- Today Proc.*, vol. 45, pp. 5269–5276, 2021, doi: 10.1016/j.matpr.2021.01.831.
- [11] Y. Cheng, G. Zhao, and H. Liu, “[Histological evaluation of collagen-hydroxyapatite composite as osseous implants in the repair of mandibular defect],” *Zhongguo Xiu Fu Chong Jian Wai Ke Za Zhi Zhongguo Xiufu Chongjian Waike Zazhi Chin. J. Reparative Reconstr. Surg.*, vol. 12, no. 2, pp. 74–76, Mar. 1998.
- [12] J. Park *et al.*, “In-Vitro Mechanical Performance Study of Biodegradable Polylactic Acid/Hydroxyapatite Nanocomposites for Fixation Medical Devices,” *J. Nanosci. Nanotechnol.*, vol. 18, no. 2, pp. 837–841, Feb. 2018, doi: 10.1166/jnn.2018.14884.
- [13] P. Shi, M. Liu, F. Fan, C. Yu, W. Lu, and M. Du, “Characterization of natural hydroxyapatite originated from fish bone and its biocompatibility with osteoblasts,” *Mater. Sci. Eng. C Mater. Biol. Appl.*, vol. 90, pp. 706–712, Sep. 2018, doi: 10.1016/j.msec.2018.04.026.
- [14] Z. Zhuang, T. J. Fujimi, M. Nakamura, T. Konishi, H. Yoshimura, and M. Aizawa, “Development of a,b-plane-oriented hydroxyapatite ceramics as models for living bones and their cell adhesion behavior,” *Acta Biomater.*, vol. 9, no. 5, pp. 6732–6740, May 2013, doi: 10.1016/j.actbio.2013.02.001.
- [15] B. J. Melde and A. Stein, “Periodic Macroporous Hydroxyapatite-Containing Calcium Phosphates,” *Chem. Mater.*, vol. 14, no. 8, pp. 3326–3331, Aug. 2002, doi: 10.1021/cm020259b.
- [16] G. Bernardi, “Chromatography of Nucleic Acids on Hydroxyapatite,” *Nature*, vol. 206, no. 4986, pp. 779–783, May 1965, doi: 10.1038/206779a0.
- [17] J. Zhao *et al.*, “Facile synthesis of ultralong hydroxyapatite nanowires using wormlike micelles as soft templates,” *CrystEngComm*, vol. 23, no. 32, pp. 5498–5503, 2021, doi: 10.1039/D1CE00488C.
- [18] T. Goto, I. Y. Kim, K. Kikuta, and C. Ohtsuki, “Hydroxyapatite formation by solvothermal treatment of α -tricalcium phosphate with water–ethanol solution,” *Ceram. Int.*, vol. 38, no. 2, pp. 1003–1010, Mar. 2012, doi: 10.1016/j.ceramint.2011.08.023.
- [19] K. Ishikawa, A. Kareiva, “Sol-gel synthesis of calcium phosphate-based coatings - A review,” pp. 25–41, 2020.
- [20] K. Kaviyarasu *et al.*, “Photocatalytic performance and antimicrobial activities of HAp-TiO₂ nanocomposite thin films by sol-gel method,” *Surf. Interfaces*, vol. 6, pp. 247–255, Mar. 2017, doi: 10.1016/j.surfin.2016.10.002.

- [21] K. Teshima *et al.*, “Well-Formed One-Dimensional Hydroxyapatite Crystals Grown by an Environmentally Friendly Flux Method,” *Cryst. Growth Des.*, vol. 9, no. 6, pp. 2937–2940, Jun. 2009, doi: 10.1021/cg900159j.
- [22] K. Suchanek, A. Bartkowiak, M. Perzanowski, and M. Marszałek, “From monetite plate to hydroxyapatite nanofibers by monoethanolamine assisted hydrothermal approach,” *Sci. Rep.*, vol. 8, no. 1, p. 15408, Oct. 2018, doi: 10.1038/s41598-018-33936-4.
- [24] L. Sinusaite, A. Popov, E. Raudonyte-Svirbutaviciene, J.-C. Yang, A. Kareiva, and A. Zarkov, “Effect of Mn doping on hydrolysis of low-temperature synthesized metastable alpha-tricalcium phosphate,” *Ceram. Int.*, vol. 47, no. 9, pp. 12078–12083, May 2021, doi: 10.1016/j.ceramint.2021.01.052.
- [25] L. Sinusaite *et al.*, “Synthesis and luminescent properties of Mn-doped alpha-tricalcium phosphate,” *Ceram. Int.*, vol. 47, no. 4, pp. 5335–5340, Feb. 2021, doi: 10.1016/j.ceramint.2020.10.114.
- [26] S. Ferraris *et al.*, “Bioactive materials: In vitro investigation of different mechanisms of hydroxyapatite precipitation,” *Acta Biomater.*, vol. 102, pp. 468–480, Jan. 2020, doi: 10.1016/j.actbio.2019.11.024.
- [27] A. Monkawa *et al.*, “Fabrication of hydroxyapatite ultra-thin layer on gold surface and its application for quartz crystal microbalance technique,” *Biomaterials*, vol. 27, no. 33, pp. 5748–5754, Nov. 2006, doi: 10.1016/j.biomaterials.2006.07.029.
- [28] G. C. Petrucelli, E. Y. Kawachi, L. T. Kubota, and C. A. Bertran, “Hydroxyapatite-based electrode: a new sensor for phosphate,” *Anal. Commun.*, vol. 33, no. 7, p. 227, 1996, doi: 10.1039/ac9963300227.
- [29] C. S. Park *et al.*, “Fast and sensitive near-infrared fluorescent probes for ALP detection and 3d printed calcium phosphate scaffold imaging in vivo,” *Biosens. Bioelectron.*, vol. 105, pp. 151–158, May 2018, doi: 10.1016/j.bios.2018.01.018.
- [30] S. Standring, N. Ananad, H. Gray, and H. Gray, Eds., *Gray’s anatomy: the anatomical basis of clinical practice ; [get full access and more at ExpertConsult.com]*, 41. ed. Philadelphia, Pa.: Elsevier, 2016.
- [31] R. Florencio-Silva, G. R. da S. Sasso, E. Sasso-Cerri, M. J. Simões, and P. S. Cerri, “Biology of Bone Tissue: Structure, Function, and Factors That Influence Bone Cells,” *BioMed Res. Int.*, vol. 2015, pp. 1–17, 2015, doi: 10.1155/2015/421746.
- [32] K. Alvarez and H. Nakajima, “Metallic Scaffolds for Bone Regeneration,” *Materials*, vol. 2, no. 3, pp. 790–832, Jul. 2009, doi: 10.3390/ma2030790.

- [33] X. Liu, H. Wu, M. Byrne, S. Krane, and R. Jaenisch, "Type III collagen is crucial for collagen I fibrillogenesis and for normal cardiovascular development," *Proc. Natl. Acad. Sci.*, vol. 94, no. 5, pp. 1852–1856, Mar. 1997, doi: 10.1073/pnas.94.5.1852.
- [34] J.-Y. Rho, L. Kuhn-Spearing, and P. Zioupos, "Mechanical properties and the hierarchical structure of bone," *Med. Eng. Phys.*, vol. 20, no. 2, pp. 92–102, Mar. 1998, doi: 10.1016/S1350-4533(98)00007-1.
- [35] "Biomechanics and bone (& II) : Trials in different hierarchical levels of bone and alternative tools for the determination of bone strength," 2013. Accessed: Feb. 18, 2023. [Online]. Available: [https://www.semanticscholar.org/paper/Biomechanics-and-bone-\(-%26-II\)-%3A-Trials-in-levels/03d16090f39020c188608df817b1179c3b418801](https://www.semanticscholar.org/paper/Biomechanics-and-bone-(-%26-II)-%3A-Trials-in-levels/03d16090f39020c188608df817b1179c3b418801)
- [36] J. Fan *et al.*, "A Review of Recent Advances in Natural Polymer-Based Scaffolds for Musculoskeletal Tissue Engineering," *Polymers*, vol. 14, no. 10, p. 2097, May 2022, doi: 10.3390/polym14102097.
- [37] K. Fox, P. A. Tran, and N. Tran, "Recent Advances in Research Applications of Nanophase Hydroxyapatite," *ChemPhysChem*, vol. 13, no. 10, pp. 2495–2506, Jul. 2012, doi: 10.1002/cphc.201200080.
- [38] R. Y. Whitehead, L. C. Lucas, and W. R. Lacefield, "The effect of dissolution on plasma sprayed hydroxylapatite coatings on titanium," *Clin. Mater.*, vol. 12, no. 1, pp. 31–39, Jan. 1993, doi: 10.1016/0267-6605(93)90025-3.
- [39] L. Sun, C. C. Berndt, K. A. Gross, and A. Kucuk, "Material fundamentals and clinical performance of plasma-sprayed hydroxyapatite coatings: A review," *J. Biomed. Mater. Res.*, vol. 58, no. 5, pp. 570–592, 2001, doi: 10.1002/jbm.1056.
- [40] S. Rujitanapanich, P. Kumpapan, and P. Wanjanoi, "Synthesis of Hydroxyapatite from Oyster Shell via Precipitation," *Energy Procedia*, vol. 56, pp. 112–117, 2014, doi: 10.1016/j.egypro.2014.07.138.
- [41] S. V. Dorozhkin, "Calcium orthophosphates: Occurrence, properties, biomineralization, pathological calcification and biomimetic applications," *Biomatter*, vol. 1, no. 2, pp. 121–164, Oct. 2011, doi: 10.4161/biom.18790.
- [42] M. Akram, R. Ahmed, I. Shakir, W. A. W. Ibrahim, and R. Hussain, "Extracting hydroxyapatite and its precursors from natural resources," *J. Mater. Sci.*, vol. 49, no. 4, pp. 1461–1475, Feb. 2014, doi: 10.1007/s10853-013-7864-x.
- [43] D. Milovac, T. C. Gamboa-Martínez, M. Ivankovic, G. Gallego Ferrer, and H. Ivankovic, "PCL-coated hydroxyapatite scaffold derived from

- cuttlefish bone: In vitro cell culture studies,” *Mater. Sci. Eng. C*, vol. 42, pp. 264–272, Sep. 2014, doi: 10.1016/j.msec.2014.05.034.
- [44] N. A. S. Mohd Pu’ad, P. Koshy, H. Z. Abdullah, M. I. Idris, and T. C. Lee, “Syntheses of hydroxyapatite from natural sources,” *Heliyon*, vol. 5, no. 5, p. e01588, May 2019, doi: 10.1016/j.heliyon.2019.e01588.
- [45] N. Eliaz and N. Metoki, “Calcium Phosphate Bioceramics: A Review of Their History, Structure, Properties, Coating Technologies and Biomedical Applications,” *Materials*, vol. 10, no. 4, p. 334, Mar. 2017, doi: 10.3390/ma10040334.
- [46] G. Ma and X. Y. Liu, “Hydroxyapatite: Hexagonal or Monoclinic?,” *Cryst. Growth Des.*, vol. 9, no. 7, pp. 2991–2994, Jul. 2009, doi: 10.1021/cg900156w.
- [47] S. Hu *et al.*, “Ferroelectric polarization of hydroxyapatite from density functional theory,” *RSC Adv.*, vol. 7, no. 35, pp. 21375–21379, 2017, doi: 10.1039/C7RA01900A.
- [48] S. J. Kalita, A. Bhardwaj, and H. A. Bhatt, “Nanocrystalline calcium phosphate ceramics in biomedical engineering,” *Mater. Sci. Eng. C*, vol. 27, no. 3, pp. 441–449, Apr. 2007, doi: 10.1016/j.msec.2006.05.018.
- [49] S. Dorozhkin, “Calcium Orthophosphate-Based Bioceramics,” *Materials*, vol. 6, no. 9, pp. 3840–3942, Sep. 2013, doi: 10.3390/ma6093840.
- [50] A. Ezerskyte-Miseviciene and A. Kareiva, “Everything old is new again: a reinspection of solid-state method for the fabrication of high quality calcium hydroxyapatite bioceramics,” *Mendeleev Commun.*, vol. 29, no. 3, pp. 273–275, May 2019, doi: 10.1016/j.mencom.2019.05.010.
- [51] I. Bogdanoviciene, A. Beganskiene, K. Tõnsuaadu, J. Glaser, H.-J. Meyer, and A. Kareiva, “Calcium hydroxyapatite, $\text{Ca}_{10}(\text{PO}_4)_6(\text{OH})_2$ ceramics prepared by aqueous sol–gel processing,” *Mater. Res. Bull.*, vol. 41, no. 9, pp. 1754–1762, Sep. 2006, doi: 10.1016/j.materresbull.2006.02.016.
- [52] S. Jiang, Y. Cao, S. Li, Y. Pang, and Z. Sun, “Dual function of poly(acrylic acid) on controlling amorphous mediated hydroxyapatite crystallization,” *J. Cryst. Growth*, vol. 557, p. 125991, Mar. 2021, doi: 10.1016/j.jcrysgro.2020.125991.
- [53] Ellen Marie Flaten, Marion Seiersten, Jens-Petter Andreassen, Polymorphism and morphology of calcium carbonate precipitated in mixed solvents of ethylene glycol and water, *Journal of Crystal Growth*, Volume 311, Issue 13, 2009, Pages 3533–3538, ISSN 0022-0248, <https://doi.org/10.1016/j.jcrysgro.2009.04.014>.

- [54] “Plazminis purškimas ir jo taikymas,” *Matematikos ir gamtos mokslų fakultetas*. <https://mgmf.ktu.edu/news/plazminis-purskimas-ir-jo-taikymas/> (accessed Mar. 04, 2023).
- [55] P. Robotti and G. Zappini, “Thermal Plasma Spray Deposition of Titanium and Hydroxyapatite on PEEK Implants,” in *PEEK Biomaterials Handbook*, Elsevier, 2019, pp. 147–177. doi: 10.1016/B978-0-12-812524-3.00010-7.
- [56] R. L. Puurunen, “Surface chemistry of atomic layer deposition: A case study for the trimethylaluminum/water process,” *J. Appl. Phys.*, vol. 97, no. 12, p. 121301, Jun. 2005, doi: 10.1063/1.1940727.
- [57] R. A. Surmenev *et al.*, “RF magnetron sputtering of a hydroxyapatite target: A comparison study on polytetrafluorethylene and titanium substrates,” *Appl. Surf. Sci.*, vol. 414, pp. 335–344, Aug. 2017, doi: 10.1016/j.apsusc.2017.04.090.
- [58] P. N. Hishimone, H. Nagai, and M. Sato, “Methods of Fabricating Thin Films for Energy Materials and Devices,” in *Lithium-ion Batteries - Thin Film for Energy Materials and Devices*, M. Sato, L. Lu, and H. Nagai, Eds., IntechOpen, 2020. doi: 10.5772/intechopen.85912.
- [59] N. Y. Mostafa and M. M. Kamel, “Enhancement of adhesion bonding between titanium metal and electrodeposited calcium phosphate,” *Surf. Eng. Appl. Electrochem.*, vol. 52, no. 6, pp. 520–523, Nov. 2016, doi: 10.3103/S1068375516060119.
- [60] D. Bokov *et al.*, “Nanomaterial by Sol-Gel Method: Synthesis and Application,” *Adv. Mater. Sci. Eng.*, vol. 2021, pp. 1–21, Dec. 2021, doi: 10.1155/2021/5102014.
- [61] B. S. Yilbas, *Self-cleaning of surfaces and water droplet mobility*. Amsterdam, Netherlands; Cambridge, MA, United States: Elsevier, 2019.
- [62] J. E. ten Elshof, “Chemical solution deposition techniques for epitaxial growth of complex oxides,” in *Epitaxial Growth of Complex Metal Oxides*, Elsevier, 2015, pp. 69–93. doi: 10.1016/B978-1-78242-245-7.00004-X.
- [63] C. de Melo Alencar, B. L. F. de Paula, M. I. Guanipa Ortiz, M. Baraúna Magno, C. Martins Silva, and L. Cople Maia, “Clinical efficacy of nano-hydroxyapatite in dentin hypersensitivity: A systematic review and meta-analysis,” *J. Dent.*, vol. 82, pp. 11–21, Mar. 2019, doi: 10.1016/j.jdent.2018.12.014.
- [64] I. R. Bordea *et al.*, “Nano-hydroxyapatite use in dentistry: a systematic review,” *Drug Metab. Rev.*, vol. 52, no. 2, pp. 319–332, Apr. 2020, doi: 10.1080/03602532.2020.1758713.

- [65] E. Pepla, L. K. Besharat, G. Palaia, G. Tenore, and G. Migliau, “Nano-hydroxyapatite and its applications in preventive, restorative and regenerative dentistry: a review of literature,” *Ann. Stomatol. (Roma)*, vol. 5, no. 3, pp. 108–114, Jul. 2014.
- [66] C. M. Marto *et al.*, “Evaluation of the efficacy of dentin hypersensitivity treatments—A systematic review and follow-up analysis,” *J. Oral Rehabil.*, vol. 46, no. 10, pp. 952–990, Oct. 2019, doi: 10.1111/joor.12842.
- [67] R. Sankannavar and S. Chaudhari, “An imperative approach for fluorosis mitigation: Amending aqueous calcium to suppress hydroxyapatite dissolution in defluoridation,” *J. Environ. Manage.*, vol. 245, pp. 230–237, Sep. 2019, doi: 10.1016/j.jenvman.2019.05.088.
- [68] M. P. Richards, R. J. Schulting, and R. E. M. Hedges, “Sharp shift in diet at onset of Neolithic,” *Nature*, vol. 425, no. 6956, pp. 366–366, Sep. 2003, doi: 10.1038/425366a.
- [69] K. Britton, V. Grimes, J. Dau, and M. P. Richards, “Reconstructing faunal migrations using intra-tooth sampling and strontium and oxygen isotope analyses: a case study of modern caribou (*Rangifer tarandus granti*),” *J. Archaeol. Sci.*, vol. 36, no. 5, pp. 1163–1172, May 2009, doi: 10.1016/j.jas.2009.01.003.
- [70] J. Daniel Bryant, B. Luz, and P. N. Froelich, “Oxygen isotopic composition of fossil horse tooth phosphate as a record of continental paleoclimate,” *Palaeogeogr. Palaeoclimatol. Palaeoecol.*, vol. 107, no. 3–4, pp. 303–316, Feb. 1994, doi: 10.1016/0031-0182(94)90102-3.
- [71] S. Lara-Ochoa, W. Ortega-Lara, and C. E. Guerrero-Beltrán, “Hydroxyapatite Nanoparticles in Drug Delivery: Physicochemistry and Applications,” *Pharmaceutics*, vol. 13, no. 10, p. 1642, Oct. 2021, doi: 10.3390/pharmaceutics13101642.
- [72] “A review of drug delivery systems based on hydroxyapatite.” <https://www.icbcongress.com/2018/en/prp.php?o=1201&st=A-review-of-drug-delivery-systems-based-on-hydroxyapatite> (accessed Mar. 04, 2023).
- [73] A. Zarkov *et al.*, “On the synthesis of yttria-stabilized zirconia: a comparative study,” *J. Sol-Gel Sci. Technol.*, vol. 76, no. 2, pp. 309–319, Nov. 2015, doi: 10.1007/s10971-015-3778-1.
- [74] L. Sinusaite, I. Grigoraviciute-Puroniene, A. Popov, K. Ishikawa, A. Kareiva, and A. Zarkov, “Controllable synthesis of tricalcium phosphate (TCP) polymorphs by wet precipitation: Effect of washing procedure,” *Ceram. Int.*, vol. 45, no. 9, pp. 12423–12428, Jun. 2019, doi: 10.1016/j.ceramint.2019.03.174.

- [75] S. Brunauer, P. H. Emmett, and E. Teller, "Adsorption of Gases in Multimolecular Layers," *J. Am. Chem. Soc.*, vol. 60, no. 2, pp. 309–319, Feb. 1938, doi: 10.1021/ja01269a023.
- [76] M. M. Tlili, M. B. Amor, C. Gabrielli, S. Joiret, G. Maurin, and P. Rousseau, "Characterization of CaCO₃ hydrates by micro-Raman spectroscopy," *J. Raman Spectrosc.*, vol. 33, no. 1, pp. 10–16, Jan. 2002, doi: 10.1002/jrs.806.
- [77] A. Yashina, F. Meldrum, and A. deMello, "Calcium carbonate polymorph control using droplet-based microfluidics," *Biomicrofluidics*, vol. 6, no. 2, p. 022001, Jun. 2012, doi: 10.1063/1.3683162.
- [78] G. B. Ramírez-Rodríguez, J. M. Delgado-López, and J. Gómez-Morales, "Evolution of calcium phosphate precipitation in hanging drop vapor diffusion by in situ Raman microspectroscopy," *CrystEngComm*, vol. 15, no. 12, p. 2206, 2013, doi: 10.1039/c2ce26556g.
- [79] S. Koutsopoulos, "Synthesis and characterization of hydroxyapatite crystals: A review study on the analytical methods," *J. Biomed. Mater. Res.*, vol. 62, no. 4, pp. 600–612, Dec. 2002, doi: 10.1002/jbm.10280.
- [80] F. Zhong *et al.*, "Recent progress and challenges on two-dimensional material photodetectors from the perspective of advanced characterization technologies," *Nano Res.*, vol. 14, no. 6, pp. 1840–1862, Jun. 2021, doi: 10.1007/s12274-020-3247-1.
- [81] J. F. Schultz, S. Li, S. Jiang, and N. Jiang, "Optical scanning tunneling microscopy based chemical imaging and spectroscopy," *J. Phys. Condens. Matter*, vol. 32, no. 46, p. 463001, Nov. 2020, doi: 10.1088/1361-648X/aba8c7.
- [82] K. Ishikawa, "Bone Substitute Fabrication Based on Dissolution-Precipitation Reactions," *Materials*, vol. 3, no. 2, pp. 1138–1155, Feb. 2010, doi: 10.3390/ma3021138.
- [83] I. Grigoravičiute-Puroniene, Y. Tanaka, V. Vegelyte, Y. Nishimoto, K. Ishikawa, and A. Kareiva, "A novel synthetic approach to low-crystallinity calcium deficient hydroxyapatite," *Ceram. Int.*, vol. 45, no. 12, pp. 15620–15623, Aug. 2019, doi: 10.1016/j.ceramint.2019.05.072.
- [84] R. Kishida, M. Elsheikh, K. Hayashi, A. Tsuchiya, and K. Ishikawa, "Fabrication of highly interconnected porous carbonate apatite blocks based on the setting reaction of calcium sulfate hemihydrate granules," *Ceram. Int.*, vol. 47, no. 14, pp. 19856–19863, Jul. 2021, doi: 10.1016/j.ceramint.2021.03.324.
- [85] P. Usinskas, Z. Stankeviciute, A. Beganskiene, and A. Kareiva, "Sol-gel derived porous and hydrophilic calcium hydroxyapatite coating on

- modified titanium substrate,” *Surf. Coat. Technol.*, vol. 307, pp. 935–940, Dec. 2016, doi: 10.1016/j.surfcoat.2016.10.032.
- [86] G. Choi, A. H. Choi, L. A. Evans, S. Akyol, and B. Ben-Nissan, “A review: Recent advances in sol-gel-derived hydroxyapatite nanocoatings for clinical applications,” *J. Am. Ceram. Soc.*, vol. 103, no. 10, pp. 5442–5453, Sep. 2020, doi: 10.1111/jace.17118.
- [87] Mi, T., Li, Y., Liu, W. *et al.* Quantitative evaluation of cement paste carbonation using Raman spectroscopy. *npj Mater Degrad* **5**, 35 (2021). <https://doi.org/10.1038/s41529-021-00181-6>.
- [88] W. T. Pawlewicz, G. J. Exarhos, and W. E. Conaway, “Structural characterization of TiO₂ optical coatings by Raman spectroscopy,” *Appl. Opt.*, vol. 22, no. 12, p. 1837, Jun. 1983, doi: 10.1364/AO.22.001837.
- [89] M. A. Legodi, D. de Waal, J. H. Potgieter, and S. S. Potgieter, “Rapid determination of CaCO₃ in mixtures utilising FT—IR spectroscopy,” *Miner. Eng.*, vol. 14, no. 9, pp. 1107–1111, Sep. 2001, doi: 10.1016/S0892-6875(01)00116-9.
- [90] I. Grigoraviciute-Puroniene, Z. Stankeviciute, K. Ishikawa, and A. Kareiva, “Formation of calcium hydroxyapatite with high concentration of homogeneously distributed silver,” *Microporous Mesoporous Mater.*, vol. 293, p. 109806, Feb. 2020, doi: 10.1016/j.micromeso.2019.109806.
- [91] E. Garskaite, K.-A. Gross, S.-W. Yang, T. C.-K. Yang, J.-C. Yang, and A. Kareiva, “Effect of processing conditions on the crystallinity and structure of carbonated calcium hydroxyapatite (CHAp),” *CrystEngComm*, vol. 16, no. 19, p. 3950, 2014, doi: 10.1039/c4ce00119b.
- [92] T.-L. Nguyen, C.-C. Tseng, T.-C. Cheng, V.-T. Nguyen, and Y.-H. Chang, “Formation and characterization of calcium phosphate ceramic coatings on Ti-6Al-4V alloy,” *Mater. Today Commun.*, vol. 31, p. 103686, Jun. 2022, doi: 10.1016/j.mtcomm.2022.103686.
- [93] K. Ishikawa and A. Kareiva, “Sol–gel synthesis of calcium phosphate-based coatings – A review,” *Chemija*, vol. 31, no. 1, Feb. 2020, doi: 10.6001/chemija.v31i1.4169.
- [94] F. Gao, X. Chen, H. Tanaka, A. Nishitani, and Q. Wang, “Alkaline phosphatase mediated synthesis of carbon nanotube–hydroxyapatite nanocomposite and its application for electrochemical determination of luteolin,” *Adv. Powder Technol.*, vol. 27, no. 3, pp. 921–928, May 2016, doi: 10.1016/j.appt.2016.02.016.
- [95] S. L. Ortiz *et al.*, “Dy₂O₃-unpurified hydroxyapatite: a promising thermoluminescent sensor and biomimetic nanotherapeutic,” *Appl. Phys.*

- A, vol. 127, no. 12, p. 893, Dec. 2021, doi: 10.1007/s00339-021-05010-w.
- [96] S. Kollenda *et al.*, “A pH-sensitive fluorescent protein sensor to follow the pathway of calcium phosphate nanoparticles into cells,” *Acta Biomater.*, vol. 111, pp. 406–417, Jul. 2020, doi: 10.1016/j.actbio.2020.05.014.
- [97] A. Prichodko, F. Enrichi, Z. Stankeviciute, A. Benedetti, I. Grigoraviciute-Puroniene, and A. Kareiva, “Study of Eu³⁺ and Tm³⁺ substitution effects in sol–gel fabricated calcium hydroxyapatite,” *J. Sol-Gel Sci. Technol.*, vol. 81, no. 1, pp. 261–267, Jan. 2017, doi: 10.1007/s10971-016-4194-x.
- [98] P. Merkl, M.-S. Aschtgen, B. Henriques-Normark, and G. A. Sotiriou, “Biofilm interfacial acidity evaluation by pH-Responsive luminescent nanoparticle films,” *Biosens. Bioelectron.*, vol. 171, p. 112732, Jan. 2021, doi: 10.1016/j.bios.2020.112732.
- [99] Y. Li, Y. Fu, H. Zhang, J. Song, and S. Yang, “FITC-Labeled Alendronate as an In Vivo Bone pH Sensor,” *BioMed Res. Int.*, vol. 2020, pp. 1–9, May 2020, doi: 10.1155/2020/4012194.
- [100] D. Gopi *et al.*, “Single walled carbon nanotubes reinforced mineralized hydroxyapatite composite coatings on titanium for improved biocompatible implant applications,” *RSC Adv.*, vol. 5, no. 46, pp. 36766–36778, 2015, doi: 10.1039/C5RA04382D.
- [101] R. G. Carrodegua and S. De Aza, “ α -Tricalcium phosphate: Synthesis, properties and biomedical applications,” *Acta Biomater.*, vol. 7, no. 10, pp. 3536–3546, Oct. 2011, doi: 10.1016/j.actbio.2011.06.019.
- [102] M. Sadat-Shojai, M.-T. Khorasani, E. Dinpanah-Khoshdargi, and A. Jamshidi, “Synthesis methods for nanosized hydroxyapatite with diverse structures,” *Acta Biomater.*, vol. 9, no. 8, pp. 7591–7621, Aug. 2013, doi: 10.1016/j.actbio.2013.04.012.
- [103] M. J. Larsen, A. Thorsen, and S. J. Jensen, “Ethanol-induced formation of solid calcium phosphates,” *Calcif. Tissue Int.*, vol. 37, no. 2, pp. 189–193, Mar. 1985, doi: 10.1007/BF02554840.
- [104] E. Lerner, R. Azoury, and S. Sarig, “Rapid precipitation of apatite from ethanol-water solution,” *J. Cryst. Growth*, vol. 97, no. 3–4, pp. 725–730, Oct. 1989, doi: 10.1016/0022-0248(89)90576-9.
- [105] J. D. Termine, R. A. Peckauskas, and A. S. Posner, “Calcium phosphate formation in vitro,” *Arch. Biochem. Biophys.*, vol. 140, no. 2, pp. 318–325, Oct. 1970, doi: 10.1016/0003-9861(70)90072-X.
- [106] J. Wu, X. Lü, L. Zhang, F. Huang, and F. Xu, “Dielectric Constant Controlled Solvothermal Synthesis of a TiO₂ Photocatalyst with Tunable

- Crystallinity: A Strategy for Solvent Selection,” *Eur. J. Inorg. Chem.*, vol. 2009, no. 19, pp. 2789–2795, Jul. 2009, doi: 10.1002/ejic.200900199.
- [107] Jeffries. Wyman, “THE DIELECTRIC CONSTANT OF MIXTURES OF ETHYL ALCOHOL AND WATER FROM -5 TO 40°,” *J. Am. Chem. Soc.*, vol. 53, no. 9, pp. 3292–3301, Sep. 1931, doi: 10.1021/ja01360a012.
- [108] D. Bohne, S. Fischer, and E. Obermeier, “Thermal, Conductivity, Density, Viscosity, and Prandtl-Numbers of Ethylene Glycol-Water Mixtures,” *Berichte Bunsenges. Für Phys. Chem.*, vol. 88, no. 8, pp. 739–742, Aug. 1984, doi: 10.1002/bbpc.19840880813.
- [109] M.-G. Ma, Y.-J. Zhu, and J. Chang, “Monetite Formed in Mixed Solvents of Water and Ethylene Glycol and Its Transformation to Hydroxyapatite,” *J. Phys. Chem. B*, vol. 110, no. 29, pp. 14226–14230, Jul. 2006, doi: 10.1021/jp061738r.
- [110] M. Thommes *et al.*, “Physisorption of gases, with special reference to the evaluation of surface area and pore size distribution (IUPAC Technical Report),” *Pure Appl. Chem.*, vol. 87, no. 9–10, pp. 1051–1069, Oct. 2015, doi: 10.1515/pac-2014-1117.

SUMMARY IN LITHUANIAN

ĮVADAS

Kalcio hidroksiapatitas (CHAp, $\text{Ca}_{10}(\text{PO}_4)_6(\text{OH})_2$) yra pagrindinė neorganinė kaulinio audinio dalis, dalyvaujanti augant kaulams ir pasižyminti puikiu biologiniu suderinamumu. Sintetinis kalcio hidroksiapatitas pasižymi stipriu biologiniu aktyvumu, todėl tai ypač patraukli medžiaga biomedicininėms reikmėms. Dėl didelio paviršiaus ploto, reaktyvumo ir biomimetinės metodikos nanokalcio hidroksiapatitas yra patogus naudoti tokiose srityse kaip ortopedinių implantų dangos ar kaulų pakaitalų užpildai. Kalcio hidroksiapatitas yra kauluose, dantyse. Kaulo struktūrą sudaro I tipo kolagenas, kaip organinis komponentas, ir CHAp, kaip neorganinis komponentas. Šie du komponentai sudaro kompozitinę nanoskalinę struktūrą, kurioje nanokalcio hidroksiapatitas įsiterpia į kolageno tinklą. Kauluose esančios CHAp dalelės yra sferos formos, plokštelių, adatėlių ar kitokio pavidalo, maždaug 40–60 nm ilgio, 20 nm pločio ir 1,5–5 nm storio. Skirtingi CHAp kristalų dydžiai ir formos užtikrina šio audinio struktūrinį stabilumą, kietumą ir funkciją. CHAp taikymas ortopedijoje gali būti įvairus, pavyzdžiui, kaulams priauginti, kaulų defektams šalinti, žmogaus kūno metaliniams implantams padengti ir kt. Iš CHAp pagaminti implantai gali užtikrinti tvarią akytą struktūrą. Be to, CHAp gali paspartinti osteointegracijos procesą, skatindamas standų implanto ir aplinkinių audinių suaugimą, nevesėjant skaiduliniam audiniui. Sėkminga osteointegracija ilgam išlaiko kaulinį įtvirtinimą ir visiškai atkuria funkcinį gebėjimą.

Sukurti efektyvesnes CHAp dangas, pasižyminčias didesniu biologiniu suderinamumu, vis dar yra iššūkis ir aktuali mokslinių tyrimų sritis. Todėl reikia nuodugniai ištirti sintezės procesus. Dirbtinio kalcio fosfato (CP) biomedžiagos vis plačiau naudojamos įvairiose klinikinėse srityse, tačiau ne mažiau patraukli CHAp taikymo sritis, yra jo naudojimas įvairiuose jutikliuose. Naudojant vandeninį zolių-gelių metodą, CHAp dangas galima sintetinti ant įvairių padėklų (pvz., titano, kvarco, silicio), kontroliuojant pradinių medžiagų temperatūrą, pH ir koncentraciją. Siekiant pagaminti fiziologinėms sąlygoms atsparesnę dangą, ieškoma įvairių naujų metodų šiuolaikinei CHAp sluoksnių, atkartojančių kaulinį audinį, sintezei. Neseniai buvo įrodyta, kad silicio turintys CHAp pasižymi didesniu biologiniu aktyvumu ir antibakterinėmis savybėmis nei gryni kalcio hidroksiapatitai. Be to, silicis gali pagerinti osteoblastinę reakciją į kalcio fosfato biokeramiką, nes natūraliame kaule jo koncentracija yra labai maža. CHAp sintezei naudojamas

zolių-gelių metodas laikomas aukštos temperatūros metodu, nes CHAp kristalinei fazei gauti reikia aukštesnės temperatūros. Tačiau aukšta temperatūra nepadeda susidaryti nanokristalinėms medžiagoms. CHAp dangos, gautos 1000 °C temperatūroje, gali būti nehomogeniškos, pavyzdžiui, sudarytos iš dviejų skirtingų sričių: vienos su mažais, maždaug 200 nm dydžio grūdėliais, ir kitos su didesniais, maždaug 800 nm skersmens, grūdėliais. Be to, aukštoje temperatūroje susidaro TiO₂ fazė, sumažinanti CHAp dangų adheziją ant Ti padėklų.

Kalcio stokojantis hidroksiapatitas (CDHA, Ca_{10-x}(HPO₄)_x(PO₄)_{6-x}(OH)_{2-x}) yra CHAp, kurio Ca/P santykis yra 1,50–1,67. Ankstesnių tyrimų duomenimis, CDHA, palyginti su kitais CP, pasižymi didesniu specifiniu paviršiumi ir geresniu bendru efektyvumu. CHAp cheminę sudėtį galima keisti iš stochiometrinės formos į Ca neturinčią formą parenkant tinkamą Ca/P molinį santykį. CHAp tirpumas, savitasis paviršiaus plotas, paviršiaus drėgnumas, taigi ir adsorbcijos savybės labai priklauso nuo jų morfologijos ir kristališkumo. CHAp kristalinė struktūra charakteringa tuo, kad turi dviejų tipų, a ir c, kristalines plokštumas. A-plokštuma yra teigiamai įkrauta dėl kalcio jonų, o c-plokštuma yra neigiamai įkrauta dėl fosfato jonams priklausančių deguonies atomų. Anizotropinis CHAp kristalų augimas viena ar kita kristalografine kryptimi yra svarbus specifinės orientuotų kristalų sąveikos su kitomis medžiagomis veiksnys, o tai gali lemti geresnes šios medžiagos eksploatacines savybes ir specifinį taikymą. Pavyzdžiui, baltymų adsorbcija ant CHAp kristalų priklauso nuo jų morfologijos: skirtingų rūšių baltymai, pavyzdžiui, baziniai ir rūgštiniai, selektyviai adsorbuojasi ant CHAp kristalų plokštumų. Taigi CHAp kristalų morfologijos derinimas gali pagerinti ir biologines savybes. Todėl kontroliuojama plokštelių ar lazdelių pavidalo kristalų sintezė yra svarbus uždavinys.

Šios disertacijos tikslas – sukurti naujus kalcio hidroksiapatito miltelių ir dangų su kontroliuojamomis morfologinėmis savybėmis sintezės metodus. Šiam tikslui pasiekti suformuluoti tokie uždaviniai:

1. Sukurti žematemperatūrį kalcio hidroksiapatito sintezės metodą dangoms ant silicio padėklo gauti.
2. Sukurti žematemperatūrį kalcio hidroksiapatito sintezės metodą dangoms ant titano padėklo gauti.
3. Ištirti įvairių organinių tirpiklių ir solvoterminės sintezės sąlygų poveikį kalcio hidroksiapatito susidarymui hidrolizuojant α -trikalcio fosfatą.
4. Ištirti įvairių organinių priedų poveikį kalcio hidroksiapatito susidarymui hidrolizuojant α -trikalcio fosfatą.

Darbo naujumas ir originalumas

Pirmą kartą kalcio hidroksiapatito plonasluoksnės dangos buvo pagamintos pakankamai žemoje temperatūroje, taikant aplinkai nekenksmingą zolių-gelių metodą, naudojant sukimo dengimo metodą ir tirpinimo-nusodinimo sintezės metodą ant silicio dangų. Toks žemoje temperatūroje išbandytas sintezės būdas buvo pritaikytas ir kalcio hidroksiapatito dangoms ant titano padėklų gauti. Ištirtas įvairių organinių tirpiklių ir solvoterminių sąlygų poveikis kalcio hidroksiapatito susidarymui hidrolizuojant α -trikalčio fosfatą. Įvertintas natrio laurilsulfato ir organinių rūgščių (DL-asparto aminorūgšties, dodekano dikarboksirūgšties, oktano dikarboksirūgšties) poveikis kalcio hidroksiapatito susidarymui ir jo morfologinėms savybėms.

Ginamieji teiginiai

1. Kalcio hidroksiapatito plonasluoksnės dangas ant silicio padėklo galima susintetinti aplinkai nekenksmingais paprastais zolių-gelių ir tirpinimo-nusodinimo sintezės metodais pirmą kartą naudojant sukimo dengimo metodą.
2. Taikant tuos pačius zolių-gelių ir tirpinimo-nusodinimo sintezės metodus galima gauti beveik vienfazes kalcio hidroksiapatito plonasluoksnės dangas ant titano padėklo.
3. Metilo alkoholis ir etilenglikolis turi stipresnį slopinamąjį poveikį α -TCP hidrolizei nei etilo, izopropilo ir butilo alkoholiai. Gautų kalcio stokojančių hidroksiapatito mėginių morfologiją galima pakeisti iš plokštuminės formos į adatėlių pavidalą. Didžiausią poveikį mėginių morfologijai turi etilenglikolis.
4. Organinių priedų prigimtis turi įtakos kalcio stokojančių hidroksiapatito mėginių fazės grynumui ir morfologijai. Didesnės natrio laurilsulfato ir dodekano dikarboksirūgšties koncentracijos skatina priemaišų susidarymą. DL-asparto rūgštis ir oktano dikarboksirūgštis neturi įtakos fazės grynumui. Mėginių morfologiją galima keisti nuo plokštelių formos iki strypelių pavidalo.

EKSPERIMENTINĖ DALIS

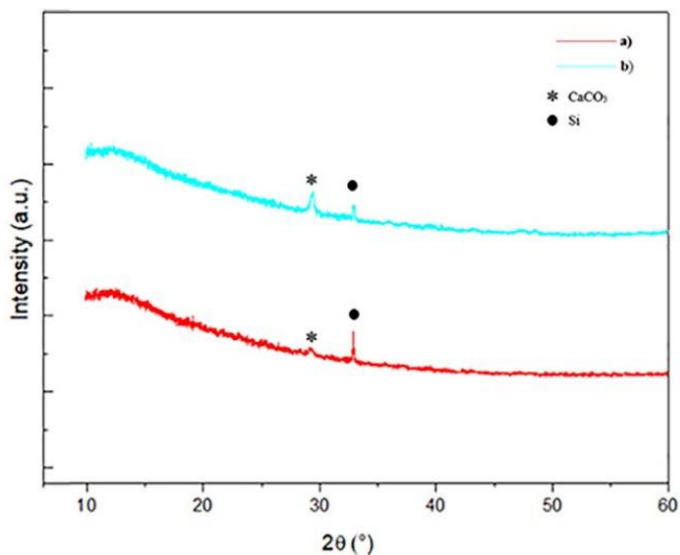
Eksperimento metodikos skyrius sudarytas iš keturių poskyrių. Pirmajame poskyryje yra išvardintos pradinių junginių, zolių-gelių, hidroterminei ir solvoterminei sintezėms naudotos medžiagos, nurodant jų grynumą bei gamintoją. Kalcio hidroksiapatito plonasluoksninių dangų ant

silicio ir titano padėklų sintezė zolių-gelių ir tirpinimo-nusodinimo metodais – antrajame poskyryje; įvairių organinių tirpiklių ir solvoterminės sintezės sąlygų poveikis kalcio hidroksiapatito susidarymui vykstant α -trikalčio fosfato hidrolizei bei įvairių organinių priedų poveikis kalcio hidroksiapatito susidarymui vykstant α -trikalčio fosfato hidrolizei – trečiajame poskyryje; ketvirtajame poskyryje išsamiai aprašytos susintetintų junginių fazinio grynumo, struktūros, morfologijos ir elektrocheminių savybių tyrimams naudotos priemonės, programinė įranga bei aparatūra.

REZULTATAI IR JŲ APTARIMAS

1. Biokeraminių nanokalčio hidroksiapatito dangų formavimo žemoje temperatūroje metodo sukūrimas naudojant zolių-gelių ir tirpinimo-nusodinimo metodus

Šiame skyriuje pateiktas sukurtas naujas zolių-gelių ir tirpinimo-nusodinimo metodas, kalcio hidroksiapatito dangoms ant dviejų skirtingų padėklų (silicio ir titano) paruošti.

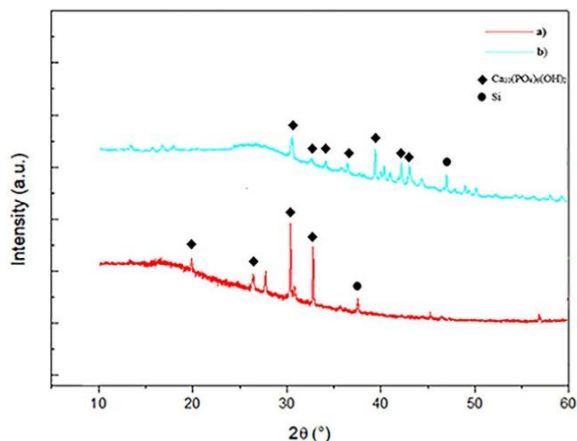


1 pav. CaCO₃ dangų ant Si padėklo, gautų zolių-gelių metodu dengiant 20 kartų ir po kiekvieno dengimo atkaitinant 5 val. 600 °C temperatūroje bei naudojant skirtingus (a) ir (b) sukimo dengimo metodus, Rentgeno spindulių difraktogramos.

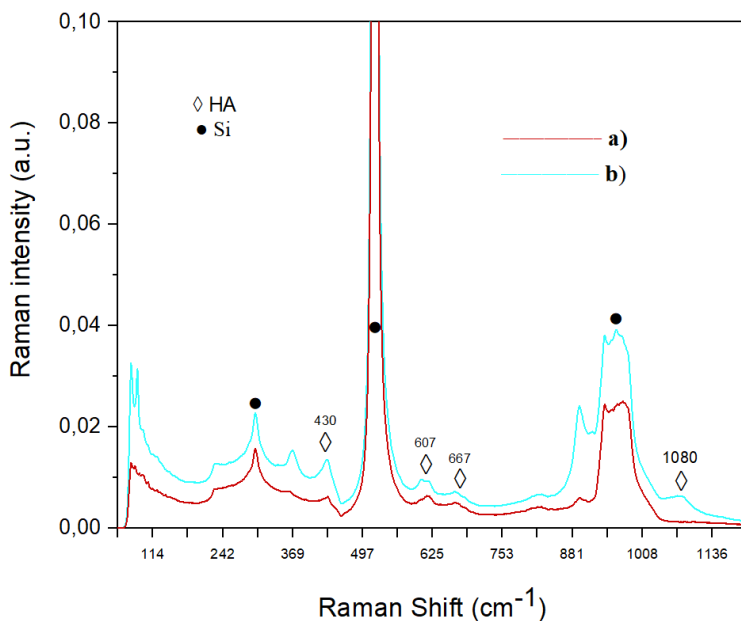
Rentgeno spindulių difraktogramose (1 pav.) matyti smailės, kurios priskiriamos CaCO_3 ($2\theta \approx 29,5$; PDF [96-210-0190]) ir patvirtinančios, kad susidarė kristalinis kalcio karbonatas.

Gautų CaCO_3 dangų paviršių morfologija tirta skenuojamąja elektronine mikroskopija (SEM). Tyrimai parodė, kad dangų paviršius iš dalies lygus ir matyti susiformavę atskiri kristalai. Pastebėta, jog pritaikius skirtingus padėklų sukimo dengimo metodus, jie neturėjo įtakos zolių-gelių būdu padengtų CaCO_3 dangų kokybei. Susintetintų CaCO_3 dangų Ramano spektruose aptinkamos CaCO_3 būdingos smailės, esančios ties 153, 281, 617, 617, 668, 709, 1084 cm^{-1} . Įdomu pažymėti, kad pagal nustatytas Ramano juostų padėtis, susintetintą CaCO_3 galima priskirti iš dalies amorfinei fazei.

Silicio padėklai, padengti iš dalies amorfiniu ir (arba) kristaliniu CaCO_3 , buvo mirkomi dinatrio vandenilio fosfato Na_2HPO_4 tirpale 28 dienas 80 °C temperatūroje. Rentgeno spindulių difrakcinės analizės rezultatai (2 pav.) rodo, kad kalcio hidroksiapatitą galima paprastai susintetinti 80 °C temperatūroje iš Ca-O zolių-gelių pirmtako tirpalo ant Si padėklų, naudojant sukimo dengimo metodą ir taikant tirpinimo-nusodinimo metodą. CHAp dangų storis buvo išmatuotas naudojant SEM analizę, atlikus dangų skerspjūvių analizę; nustatyta, kad dangų storis yra apie 900–945 nm. 3 pav. pavaizduotas CHAp mėginio Ramano spektras, registruotas 100–1250 cm^{-1} srityje. Si padėklai dengti 30 sluoksnių CaCO_3 . Plačios juostos su aštriomis viršūnėmis ties 300, 500 ir 950 cm^{-1} priskiriamos Si padėklo spektrui. Matomos intensyvios juostos, atitinkančios $\text{Ca}_{10}(\text{PO}_4)_6(\text{OH})_2$ fosfatinių grupių simetrinius valentinius virpesius. Ramano sklaidos spektroskopijos rezultatai gerai sutampa su XRD analizės duomenimis.

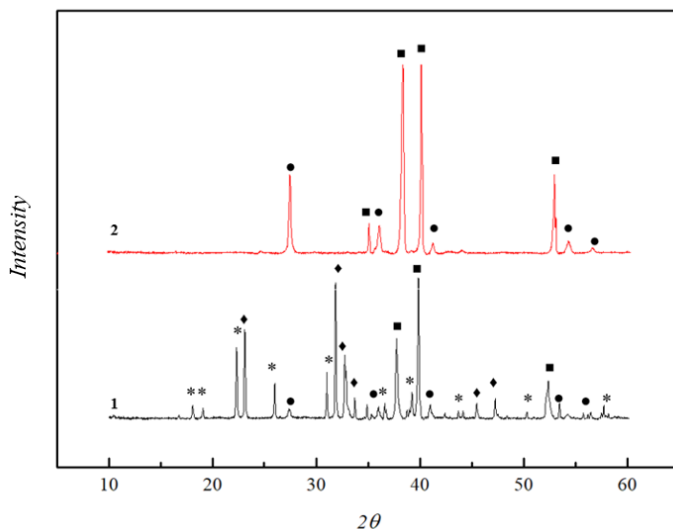


2 pav. Kalcio hidroksiapatito dangų, pagamintų zolių-gelių ir tirpinimo-nusodinimo metodais, naudojant skirtingus sukimo dengimo metodus, Rentgeno spindulių difraktogramos: a) - (A) ir b) - (B).



3 pav. CHAp, susintetinto zolių-gelių ir tirpinimo-nusodinimo metodais, naudojant skirtingus sukimo dengimo metodus, Ramano spektrai: a) - (A) ir b) - (B).

Gautų kalcio karbonato dangų ant titano padėklų fazinė sudėtis buvo nustatyta Rentgeno spindulių difrakcinės analizės metodu. Remiantis gautais rezultatais, po 20 dengimo procedūrų akivaizdžiai matomas susidaręs CaCO_3 . Rentgeno spindulių difraktogramose matyti TiO_2 (rutilo) CaO ir CaTiO_3 kristalinės fazės. 4 paveiksle pateiktos gautų CaCO_3 dangų ant titano padėklo po 28 dienų panardinimo į Na_2HPO_4 tirpalą ir Ti pagrindo, atkaitinto esant 600°C temperatūrai, Rentgeno spindulių difraktogramos.

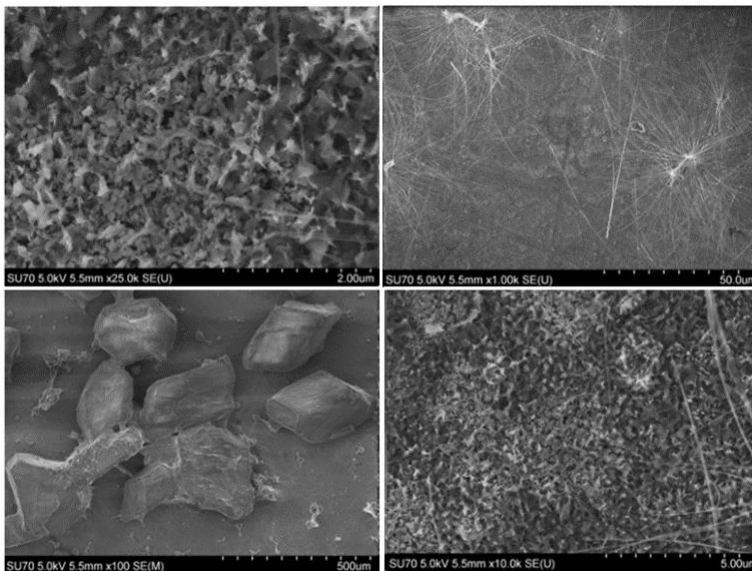


4 pav. CHAp dangos, gautos 28 dienas panardinus CaCO_3 dangą į Na_2HPO_4 tirpalą (1), ir $600\text{ }^\circ\text{C}$ temperatūroje atkaitinto Ti padėklo Rentgeno spindulių difraktogramos (2). Difrakciniai atspindžiai: ◆-CHAp (ICDD 00-054-0022), *- Na_2HPO_4 (ICDD 01-076-2287), ■-Ti (ICDD 01-089-5009), ●- TiO_2 (ICDD 01-076-0318).

Pastebėtos kristalinei CHAp fazei būdingos difrakcijos smailės. Aptiktos smailės, priskiriamos antrinėms fazėms, tokioms kaip Na_2HPO_4 (iš panardinimo tirpalo), Ti (padėklas) ir TiO_2 . Galima daryti išvadą, kad susiformavo CHAp, tačiau jis nesutrukdė susidaryti TiO_2 . CaTiO_3 būdingų smailių nematyti, o tai galėjo būti susiję su tuo, kad CaTiO_3 sluoksnis galėjo būti padengtas CHAp. Gautų CaCO_3 ir CHAp dangų Ramano spektre pastebėta smailė ties 1084 cm^{-1} atitinka karbonato simetrinius valentinius virpesius. CHAp dangų Ramano spektre matomos fosfato grupės virpesių smailės ties $400, 574, 590, 950$ ir 1085 cm^{-1} . Smailė ties maždaug 280 cm^{-1} priskiriama Ca-PO_4 gardelėms. Intensyviausia smailė ties 690 cm^{-1} priskiriama Ti padėklui. Smailės, esančios ties $159, 220$ ir 485 cm^{-1} , gali būti priskirtos TiO_2 fazei. Gauti Ramano sklaidos spektroskopijos rezultatai gerai koreliuoja su Rentgeno spindulių difrakcinės analizės rezultatais. Susintetintų dangų Furjė transformacinės infraraudonųjų spindulių spektroskopijos (FT-IR) spektruose pastebėtos absorbcijos juostos ties 1411 cm^{-1} ir 879 cm^{-1} CaCO_3 dangos spektre gali būti priskirtos karbonato simetriniams valentiniams virpesiams. Intensyvi absorbcijos juosta, aptikta ties $\sim 590\text{ cm}^{-1}$, priskiriama titano Ti-O virpesiams. Rezultatai, gauti iš susidariusios CHAp dangos FT-IR spektro, puikiai sutampa su Rentgeno spindulių difrakcijos ir

Ramano sklaidos spektroskopijos rezultatais, patvirtinančiais tarpinių (CaCO_3) ir galutinių produktų ($\text{Ca}_{10}(\text{PO}_4)_6(\text{OH})_2$) susidarymą. Pagal stebėtų absorbcijos juostų kilmę galima teigti, kad tirpinimo-nusodinimo proceso metu susidarė karbonizuotas hidroksiapatitas ($\text{Ca}_{10-x}(\text{PO}_4)_{6-x}(\text{CO}_3)_x(\text{OH})_{2-x-2y}(\text{CO}_3)_y$).

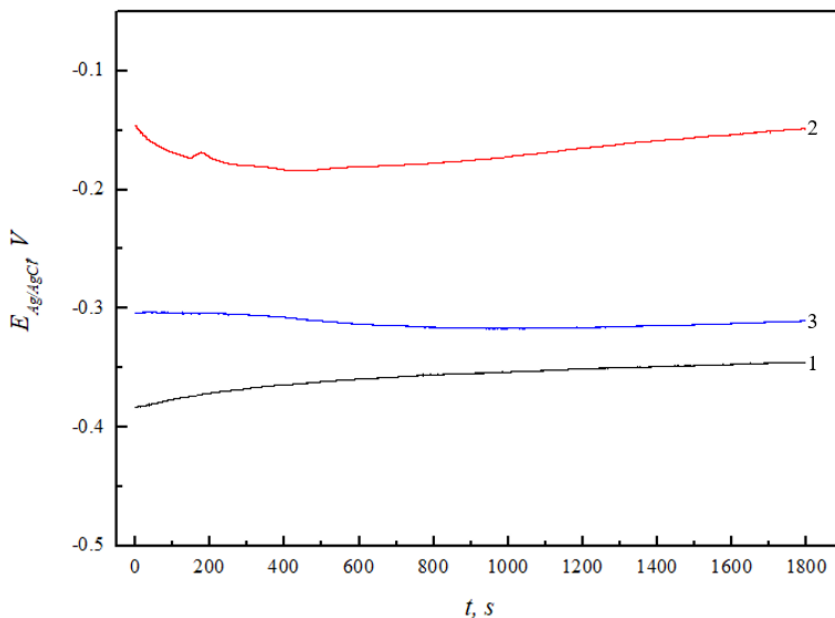
Po sukimo dengimo ir terminio apdorojimo procedūrų susidariusio CaCO_3 SEM paviršiaus morfologijos nuotraukos patvirtino, kad Ti padėklas buvo padengtas tolygiai. CHAp dangų SEM nuotraukos po CaCO_3 dangos panardinimo į Na_2HPO_4 tirpalą pateiktos 5 pav.



5 pav. CHAp dangų paviršių morfologija tirta skenuojamąja elektrone mikroskopija.

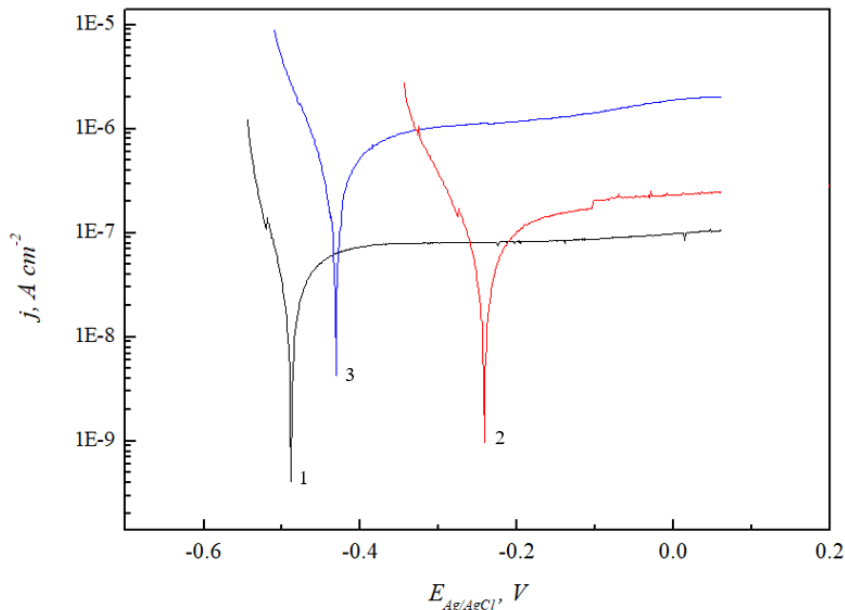
Iš gautų SEM nuotraukų matyti, kad titano paviršiuje susiformavo dendritinės struktūros CHAp ir Na_2HPO_4 kristalų klasteriai. CHAp paviršius yra šiurkštus ir porėtas, susidaro homogeniškai pasiskirstę plokštelių pavidalo kristalai ir sferinės dalelės. Atkaitinus gautą CHAp dangą $900\text{ }^\circ\text{C}$ temperatūroje, kristalų morfologija smarkiai pasikeičia: susidaro $1\text{--}2\text{ }\mu\text{m}$ ilgio ir $100\text{--}150\text{ nm}$ pločio strypeliai. Ant Ti nusodintų CHAp dangų paviršiaus morfologija buvo tirta ir optiniu 3D profilometru. Pastebėta, kad paviršiaus šiurkštumas ir vidutinis dangos aukštis po atkaitinimo $900\text{ }^\circ\text{C}$ temperatūroje šiek tiek padidėjo. Šioms dangoms nustatytas didžiausias šiurkštumas (7905 nm) ir vidutinis aukštis ($10,296\text{ nm}$).

Siekiant ištirti pagamintų dangų atsparumą korozijai, Hankso balansiniame druskų tirpale buvo išmatuotos mėginių atviros grandinės potencialų (E_{ocp}) priklausomybės nuo laiko. CHAp dangų po 28 dienų mirkymo Na_2HPO_4 tirpale, pradiniam panardinimo etape elektrodo E_{ocp} vertės sumažėja iki ~ -0.18 V (6 pav.). Toks atviros grandinės potencialo mažėjimas rodo, jog korozinis aktyvumas didėja. Po 7 min. darbinio elektrodo E_{ocp} pradeda dreifuoti teigiamesnių verčių zonos link ir pasiekia kvazistacionarią būseną. Tiriamo elektrodo paviršiuje formuojasi naujas apsauginis pasyvacinis sluoksnis. Pakaitinus titano dangą iki 900 °C temperatūros, atviros grandinės potencialas E_{ocp} nedaug pakinta didėjant ekspozicijos laikui. Pastebima, jog kvazistacionarią būseną ši danga pasiekė po ~ 6 min., pasyvacinis sluoksnis susiformavo gana greitai, o tai rodo suformuotos dangos stabilumą. Nepadengto titano padėklo E_{ocp} potencialas pradiniam panardinimo etape pradeda didėti ir po ~ 11 min. nusistovi tiriamo elektrodo laike nekintanti atviros grandinės potencialo E_{ocp} vertė. E_{ocp} verčių skirtumas tarp tiriamų mėginių yra nedidelis, o tai rodo, kad suformuotos kalcio hidroksiapatito dangos yra porėtos.



6 pav. Titano/CHAp dangų E_{ocp} potencialo priklausomybė nuo ekspozicijos laiko Hankso balansiniame druskų tirpale: 1 - atkaitintas Ti padėklas, 2 - CHAp danga, 3 - CHAp danga po atkaitinimo 900 °C temperatūroje.

Kalcio hidroksiapatito dangų įtaka titano padėklų korozijos greičiui Hankso balansiniame druskų tirpale buvo įvertinta pagal elektrodų Tafelio priklausomybes (7 pav.).



7 pav. Tafelio priklausomybės. 1 – kaitintas titano padėklas, 2 – po 28 d. panardinimo Na_2HPO_4 tirpale, 3 – po 28 d. panardinimo Na_2HPO_4 tirpale ir papildomai pakaitinus $900\text{ }^\circ\text{C}$ temperatūroje.

Padengtų CHAp dangomis elektrodų koroziniai potencialai pasislinko teigiamesnių verčių link lyginant su nepadengtu titano padėklu (1 kreivė). Didžiausias teigiamas postūmis nustatytas CHAp dangai po 28 d. panardinimo Na_2HPO_4 tirpale. Dangos, kuri buvo papildomai pakaitinta $900\text{ }^\circ\text{C}$ temperatūroje, elektrodo E_{ocp} buvo mažesnis. Įtakos tam galėjo turėti dangų porėtumas, kuris netrukdo Hankso balansiniam druskų tirpalui kontaktuoti su metalu ir vykti korozijai.

CHAp plonasluoksnės dangos gali būti sėkmingai naudojamos ne tik kaip biomimetinės nanoterapinės dangos, bet ir kaip elektrocheminiai jutikliai, termoluminescenciniai jutikliai ar pH jautrūs fluorescencinių baltymų jutikliai. CHAp galima lengvai legiruoti lantanidų jonais. Šios nanostruktūros galėtų būti pritaikytos kuriant naujas į pH reaguojančias sistemas, kurios gali fluorometriškai nustatyti biodangos rūgštingumą. Galiausiai gerai žinoma, kad pH yra labai svarbus kaulų fiziologinės funkcijos ir ligos būklės rodiklis. Siūlomos CHAp dangos, pagamintos žemoje

temperatūroje, galėtų būti taikomos kuriant neinvazinį realaus laiko kaulų pH jutiklį *in vivo*.

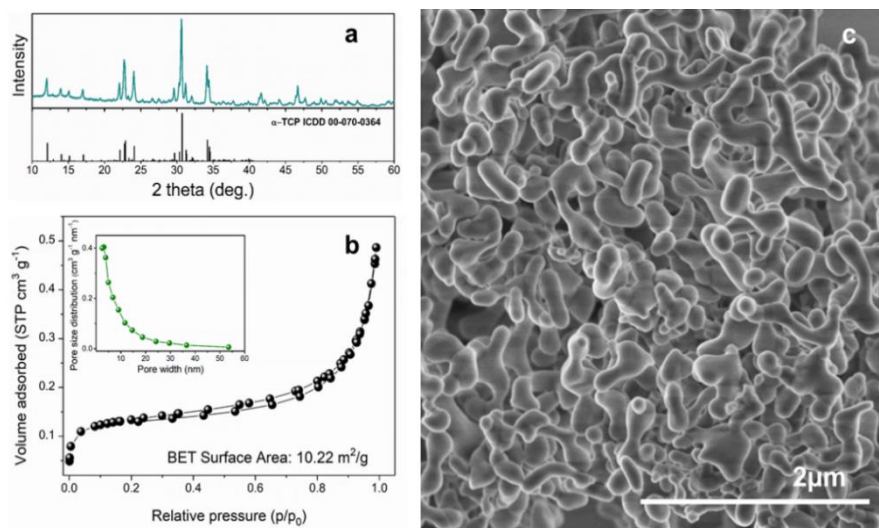
Apibendrinant reikia pažymėti, kad CHAp dangos buvo suformuotos ant silicio ir titano padėklų taikant naują žematemperatūrinę sintezės metodą. SEM ir 3D optinė mikroskopija parodė, kad suformuotos CHAp dangos buvo nevienalytės, porėtos, stambiakristalinės ir su dideliais aukščio svyravimais. Pastebėta, kad vienodesnės kalcio hidroksiapatito dangos gautos ant Ti padėklų. Titano padėklų su ant jų suformuotomis CHAp dangomis korozinis elgesys buvo įvertintas elektrocheminiais metodais.

2. Kalcio stokojančio hidroksiapatito solvoterminė sintezė hidrolizuojant α -trikalčio fosfatą

Šiame skyriuje pateikti duomenys apie tiriamą įvairių organinių tirpiklių, jų prigimties, koncentracijos tirpale ir solvoterminių sąlygų poveikį kalcio stokojančio hidroksiapatito (CDHA) susidarymui hidrolizuojant α -trikalčio fosfatą (α -TCP). Tiriamas natrio laurilsulfato ir įvairių organinių rūgščių (DL-asparto aminorūgšties, dodekano dikarboksirūgšties, oktano dikarboksirūgšties) poveikis kalcio stokojančio hidroksiapatito susidarymui vykstant α -TCP hidrolizei. Įvertintas bendras šių organinių priedų ir etilenglikolio, kaip sintezės terpės, poveikis. Hidrolizės reakcija buvo vykdoma tirpaluose, turinčiuose skirtingas šių organinių priedų koncentracijas vandeninėje ir mišrioje vandeninėje-organinėje terpėje solvoterminėmis sąlygomis.

2.2. Organinio tirpiklio įtaka CHAp susidarymui

Iš Rentgeno spindulių difraktogramos (8 pav., a) matyti, kad visos difrakcijos smailės atitinka monoklininio $\text{Ca}_3(\text{PO}_4)_2$ (ICDD #00-070-0364) standartinės Rentgeno spindulių difraktogramos duomenis. Mėginio izotermas galima priskirti IV tipui, o susiformavusias histerezės kilpas – H3 tipui (8 b pav.). Remiantis porų dydžio pasiskirstymo rezultatais (8 pav. b), mėginyje daugiausia buvo mažesnių nei 10 nm porų, nors buvo ir didesnių porų, iki 55 nm dydžio. Pirmtako BET (Brunauer-Emmett-Teller, paviršiaus ploto nustatymo metodas) paviršiaus plotas (S_{BET}) buvo $10,22 \text{ m}^2\text{g}^{-1}$. Pradinius miltelius sudarė netaisyklingos formos nanovamzdelių ir pailgų dalelių aglomeratai (8 pav. c)).

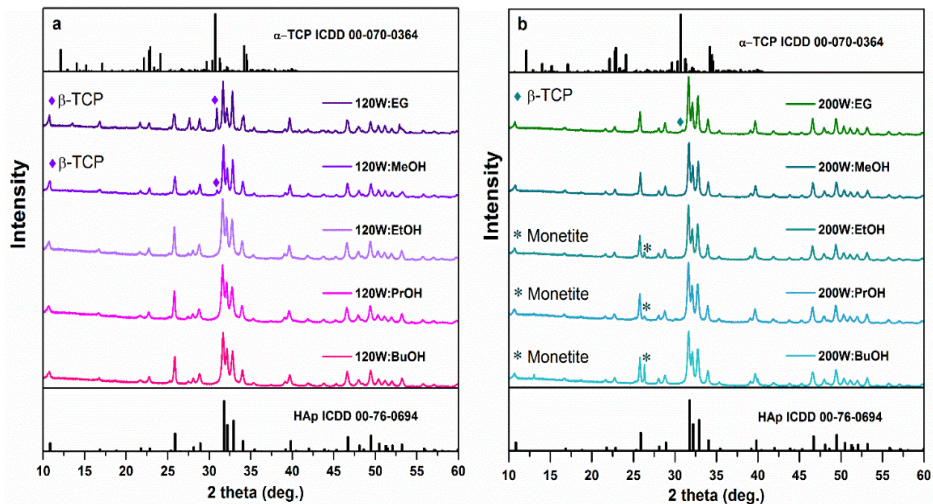


8 pav. α -TCP pirmtako charakteristikos: Rentgeno spindulių difraktograma (a), azoto adsorbcijos-desorbcijos izotermos ir atitinkamas BJH (Barret-Joyner-Halenda (akučių dydžio ir tūrio nustatymo metodas)) porų dydžio pasiskirstymas (b) ir SEM vaizdas (c).

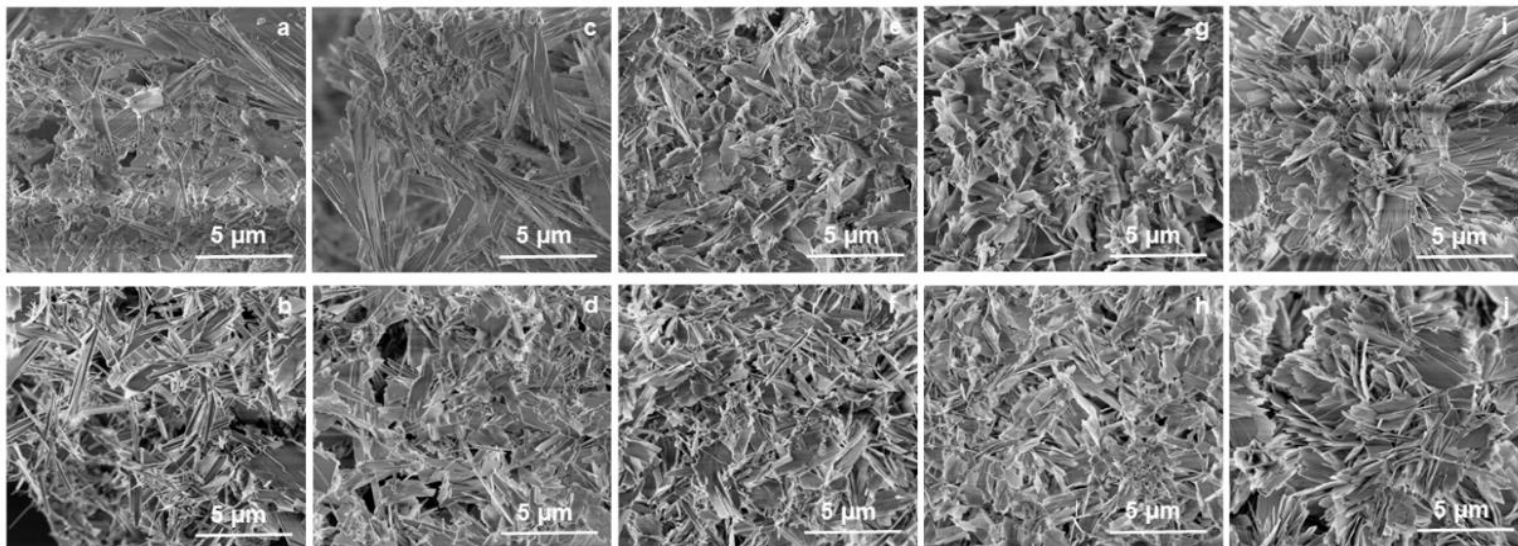
Susintetintų CDHA miltelių fazių kristališkumas ir grynumas buvo ištirtas atliekant Rentgeno spindulių difrakcinę analizę, kuri atskleidė tam tikrus gautų produktų skirtumus. Mėginiuose, apdorotuose tik organiniu tirpikliu (0:100), nesusidarė CDHA, nes nebuvo vandens, t.y. neįvyko hidrolizės reakcija, ir tokių mėginių fazė išliko α -TCP (ICDD 00-070-0364). EtOH, PrOH ir BuOH atveju, įvedus net ir nedidelę dalį, 20 % (20:80), vandens, susidarė vienfazis CDHA (ICDD 00-76-0694), o didėjant vandens kiekiui rezultatai buvo tokie patys. Tai buvo stebima esant įvairioms taikytoms solvoterminėms sąlygoms. Esant griežtesnėms solvoterminėms sąlygoms (200 °C 5 val.), dalyvaujant EtOH, PrOH ir BuOH, buvo stebimas monetito susidarymas. Tai ypač pastebima BuOH atveju. Norint palyginti tirpiklius, 9 pav. kaip pavyzdys, pateikti mėginių, paruoštų skirtingomis solvoterminėmis sąlygomis, naudojant W:O santykį 40:60, Rentgeno spindulių difraktogramos.

IR absorbcinių smailių srityje 1500–400 cm^{-1} pastebėtos pagrindinės juostos, priskiriamos CHAp ir TCP polimorfams. Mėginių morfologija buvo įvairi – nuo plokštelių iki strypelių formos. Mėginius, susintetintus be organinių tirpiklių, sudarė plokštelių formos kristalai, panašūs į „gėlės“ pavidalo struktūras. Tyrime pastebėtas tik nedidelis EtOH, PrOH ir BuOH

poveikis morfologijai. Esant švelnesnėms solvoterminės reakcijos sąlygoms (120 °C 3 val.), didelė EtOH ir PrOH koncentracija (120-W-EtOH-20:80; 120-W-PrOH-20:80) lėmė didelių plokštelių formavimąsi bei matyti išryškėję savitvarčiai sluoksniai (10 pav.).



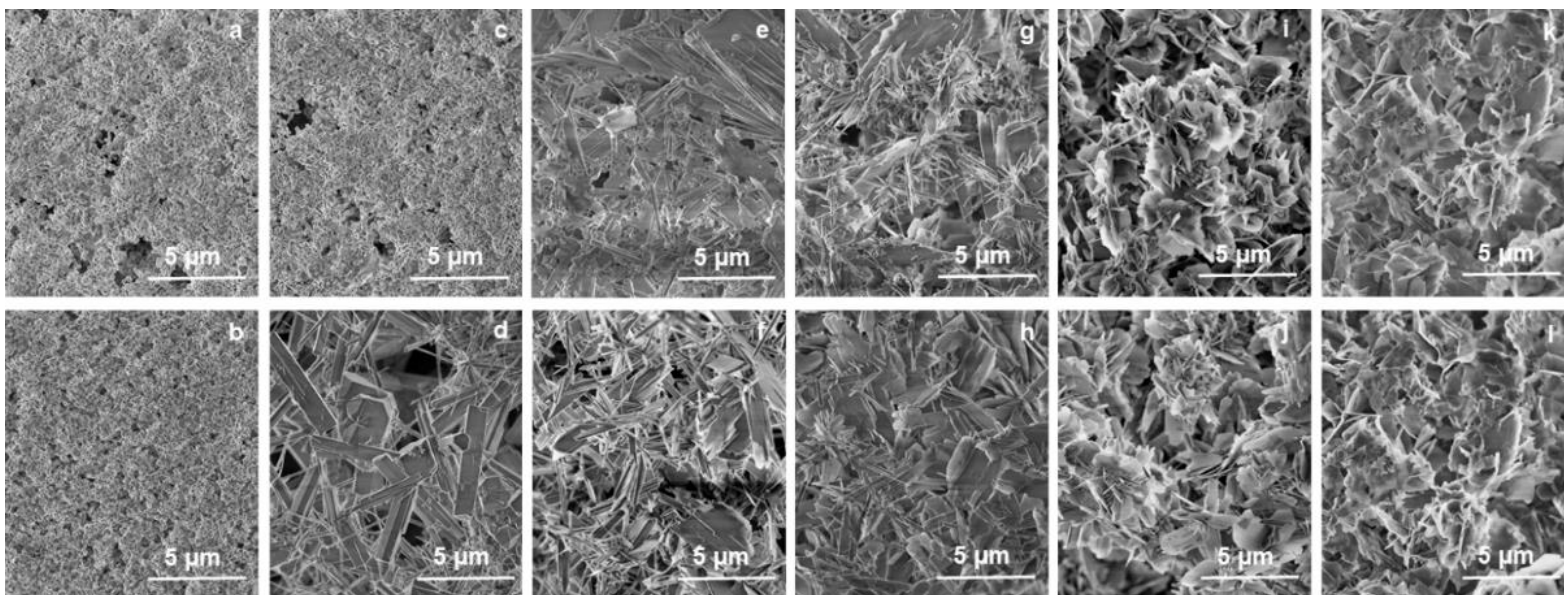
9 pav. Mėginių, paruoštų naudojant vandens ir organinio tirpiklio santykį 40:60 po 3 val. vykstant solvoterminei reakcijai esant 120 °C temperatūrai (a) ir po 5 val. 200 °C temperatūrai (b), Rentgeno spindulių difraktogramos.



10 pav. Mėginių po solvoterminės sintezės reakcijos su W:O santykiu 40:60 SEM nuotraukos: a) 120-W-EG-40:60; b) 200-W-EG-40:60; c) 120-W-MeOH-40:60 d) 200-W-MeOH-40:60; e) 120-W-EtOH-40:60; f) 200-W-EtOH-40:60; g) 120-W-PrOH-40:60; h) 200-W-PrOH-40:60; i) 120-W-BuOH-40:60; j) 200-W-BuOH-40:60.

Didinant vandens kiekį mėginiuose (W:O 40:60; 60:40; ir 80:20), pastebėtas siauresnių plokštelių ir lazdelių susidarymas, be to, kristalai buvo išsidėstę „gėlės“ pavidalo struktūrose. Padidinus reakcijos laiką ir temperatūrą, esant didesnėms EtOH, PrOH ir BuOH koncentracijoms, susidarė strypeliai. MeOH ir BuOH turėjo didesnę įtaką mėginių morfologijai, vyravo plokšteliniai kristalai, pastebėta ilgų ir siaurų plokštelių formavimosi tendencija. Mėginiuose, kurie gauti naudojant grynus MeOH ir BuOH gauta daugiau lazdelių, palyginti su mėginiais, paruoštais W:EtOH ir W:PrOH tirpaluose.

Iš visų tirtų tirpiklių didžiausią poveikį bandinių morfologijai turėjo etilenglikolis (11 pav.).



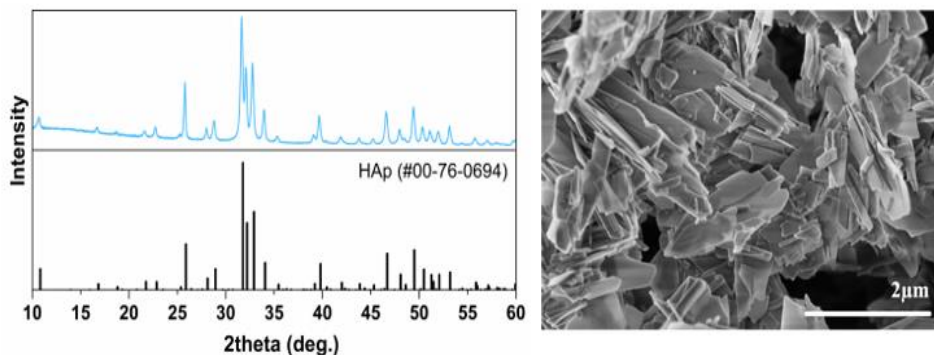
11 pav. Mėginių, paruoštų su skirtingais vandens ir etilenglikolio santykiais, SEM nuotraukos: a) 120-W-EG-0:100; b) 200-W-EG-0:100; c) 120-W-EG-20:80; d) 200-W-EG-20:80 e) 120-W-EG-40:60; f) 200-W-EG-40:60; g) 120-W-EG-60:40; h) 200-W-EG-60:40; i) 120-W-EG-80:20; j) 200-W-EG-80:20; k) 120-W-EG-100:0; j) 200-W-EG-100:0.

Manoma, kad strypelių pavidalo kristalų formavimasis tirpiklių įtakoje susideda iš dviejų pagrindinių etapų: nukleacijos etapo (jonų reakcija), kai persotintoje matricoje susidaro maži kristaliniai branduoliai, ir augimo etapo, kurio metu branduoliai išauga iki galutinės formos ir dydžio. Mūsų atveju kristalų morfologijos pokyčiai gali būti susiję su sumažėjusiu vandens kiekiu, kai į sistemą patenka daugiau organinio tirpiklio. Tai apribotų α -TCP hidrolizės reakciją. Ankstesniuose tyrimuose teigta, kad didėjant alkoholio kiekiui reakcijos vandeniniame tirpale, mažėja α -TCP tirpumas, todėl ribojamas Ca^{2+} ir PO_4^{3-} jonų tiekimas. Toks poveikis susijęs su tirpalo dielektrinės skvarbos ($\epsilon(\omega)$) pokyčiais: mažėjant tirpiklio dielektrinei skvarbai, tirpumas mažėja dėl sumažėjusios tirpinimo energijos. Gryno vandens dielektrinė konstanta 25 °C temperatūroje yra 78,5, o alkoholių dielektrinė konstanta yra gerokai mažesnė. Šiame tyrime naudotų organinių tirpiklių dielektrinės konstantos esant 25 °C temperatūrai yra tokios: $\epsilon(\omega)_{\text{EG}} = 38,5$; $\epsilon(\omega)_{\text{MeOH}} = 32,70$; $\epsilon(\omega)_{\text{EtOH}} = 24,3$; $\epsilon(\omega)_{\text{PrOH}} = 19,92$; $\epsilon(\omega)_{\text{BuOH}} = 17,5$. Vandens ir organinių tirpiklių mišinių $\epsilon(\omega)$ pokyčiai priklauso nuo tirpalo sudėties, tačiau apskritai $\epsilon(\omega)$ reikšmės mažėja didėjant organinio tirpiklio daliai. Skirtingų fizikinių ir cheminių savybių tirpikliai turi įtakos tirpumui, kristalų užuomazgų susidarymui ir augimo greičiui, o tai turi įtakos galutinių produktų kristališkumui ir morfologijai. Kai hidrolizės reakcija nėra sustabdyta ir tirpalas yra persotintas Ca^{2+} ir PO_4^{3-} jonais, nukleacija dominuoja prieš kristalų augimą ir susidaro mažesni kristalai. Ir priešingai, kai Ca^{2+} ir PO_4^{3-} jonų kiekis yra ribotas, formuojasi mažiau branduolių ir linkę augti didesni kristalai. α -TCP hidrolizės ir CHAp kristalizacijos procesams įtakos galėjo turėti ir kitos skirtingų tirpiklių savybės, pavyzdžiui, reakcijos mišinyje esantis etilenglikolis gerokai pakeistų suspensijos klampumą. Vėliau sumažėtų jonų judrumas ir difuzijos greitis, o tai stabdytų hidrolizės reakciją ir sulėtintų nukleacijos procesą. Reakcijos terpės klampumas mažėja didėjant temperatūrai, todėl slopinamasis etilenglikolio poveikis yra mažiau reikšmingas, kai solvoterminė sintezė atliekama aukštesnėje temperatūroje.

Nustatytos sorbcijos-desorbcijos izotermos yra būdingos mezoporinėms struktūroms. Histerezės kilpos H3 tipas siejamas su agreguotų plokštelių pavidalo dalelių egzistavimu. Tokie rezultatai sutampa su SEM analizės duomenimis. Remiantis porų dydžio pasiskirstymo pagal dydį rezultatais, reikšmingų skirtumų tarp mėginių nenustatyta. Visiems mėginiams būdingas platus porų dydžio pasiskirstymas. Itin mažas paviršiaus plotas nustatytas mėginiams, paruoštiems naudojant etilenglikolį.

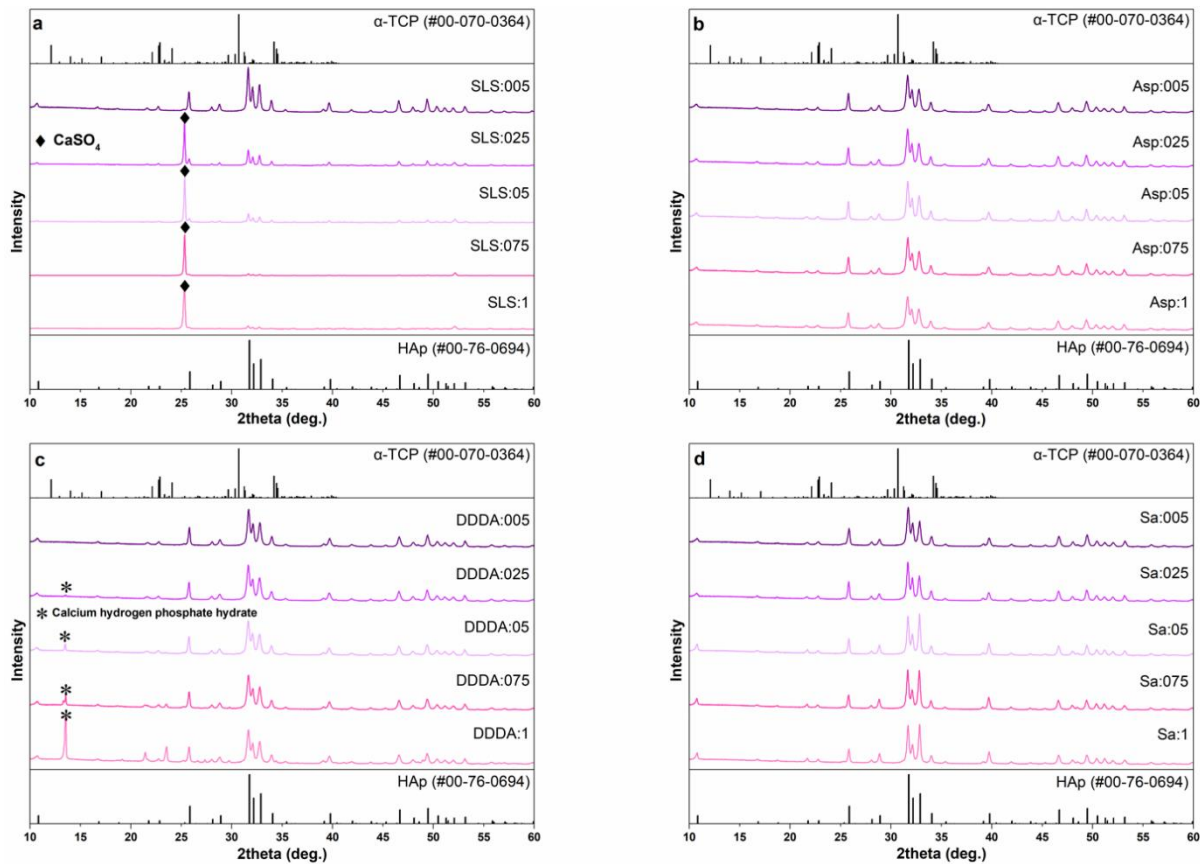
2.3 Skirtingų organinių priedų įtaka CHAp susidarymui.

Kaip matyti iš Rentgeno spindulių difraktogramos (12 pav.), pasirinktomis sintezės sąlygomis α -TCP visiškai virto CDHA, visos difrakcijos smailės atitiko standartinius $\text{Ca}_{10}(\text{PO}_4)_6(\text{OH})_2$ (ICDD #00-76-0694) duomenis. SEM vaizdas atskleidė, kad mėginio morfologijoje vyrauja plokštelės pavidalo mikrometrinių matmenų dalelės.



12 pav. Hidroterminėmis sąlygomis vandeniniame tirpale iš α -TCP be jokių priedų paruošto CDHA mėginio charakteristikos. Rentgeno spindulių difraktograma (kairėje) ir SEM vaizdas (dešinėje). Vertikaliomis linijomis pavaizduota standartinė CHAp Rentgeno spindulių difraktograma.

Mėginių, paruoštų naudojant įvairios koncentracijos natrio laurilsulfatą (a), DL-asparto aminorūgštį (b), dodekano dikarboksirūgštį (c) ir oktano dikarboksirūgštį (d) po hidroterminės reakcijos esant 200 °C temperatūrai po 5 val., Rentgeno spindulių difraktogramos pateiktos 13 pav. Be tipiškos CDHA Rentgeno spindulių difraktogramos, matoma smailė ties 25,4°, kurios intensyvumas palaipsniui didėja, didėjant natrio laurilsulfato koncentracijai. Ši smailė buvo priskirta kalcio sulfatui (CaSO_4 , ICDD #00-072-0503). Panaši tendencija pastebėta ir dodekano dikarboksirūgšties atveju – didesnis jos kiekis lėmė antrinės kristalinės fazės susidarymą. Ši smailė atitiko kalcio vandenilio fosfato hidratą ($\text{CaH}_3\text{O}_5\text{P}$, ICDD #00-046-0494). Nepriklausomai nuo DL-asparto aminorūgšties ir oktano dikarboksirūgšties koncentracijos hidroterminės reakcijos metu susidarė vienfazis CDHA.



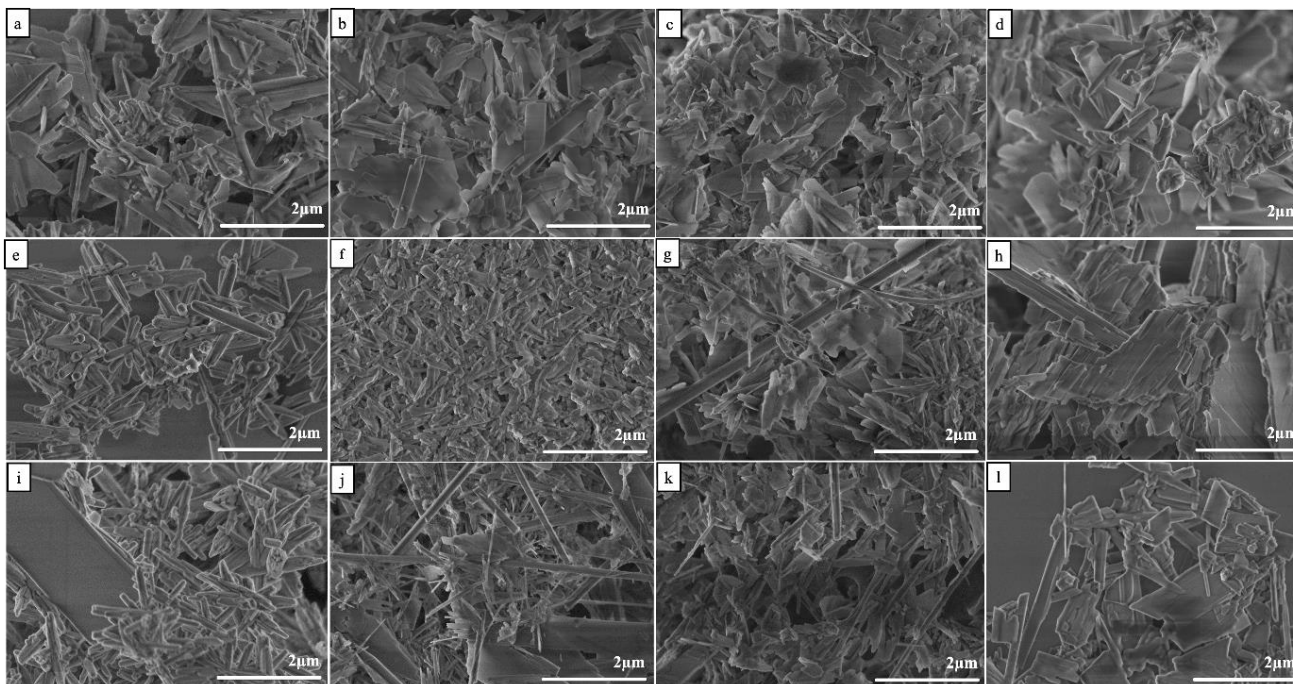
13 pav. Mėginių, paruoštų naudojant įvairios koncentracijos natrio laurilsulfatą (a), DL asparto aminorūgštį (b), dodekano dikarboksirūgštį (c) ir oktano dikarboksirūgštį (d) po hidroterminės reakcijos esant 200 °C temperatūrai po 5 val., Rentgeno spindulių difraktogramos.

Visuose FT-IR spektruose matomos CDHA būdingos absorbcijos juostos. Fosfatinės grupės absorbcijos juostos CDHA struktūroje buvo pastebėtos maždaug ties 560 ir 603 cm^{-1} (ν_4), 1020 ir 1090 cm^{-1} (ν_3), 960 cm^{-1} (ν_1), kurios buvo priskirtos atitinkamai O-P-O lenkimo, asimetrinio P-O tempimo ir simetrinio P-O tempimo virpesiams. O-P-O lenkiamųjų virpesių moda (ν_2) buvo stebima 470 cm^{-1} , o juosta ties 630 cm^{-1} buvo priskirta hidroksilo grupei. Absorbcijos juosta, kurios centras yra apie 870 cm^{-1} , priskirta HPO_4^{2-} grupės P-O(H) tempimo modai, o tai patvirtina CDHA susidarymą.

Nustatyta, kad mėginių morfologija priklauso ir nuo organinio priedo prigimties, ir nuo jo koncentracijos (14 pav.).

Kai hidroterminėje reakcijoje buvo naudojamas nedidelis kiekis natrio laurilsulfato ($0,005\text{ mol/l}$), mėginyje vyravo plokštelių kristalai, tačiau buvo pastebėtas ir nedidelis kiekis lazdelių. Padidinus organinio priedo kiekį ($0,05$ - $0,1\text{ mol/l}$), CDHA miltelių morfologija labai pasikeitė ir ėmė formotis strypelių pavidalo junginiai. Naudojant mažos koncentracijos DL-asparto aminorūgščių susidarė mikrometrinės plokštelių pavidalo dalelės, o didinant aminorūgšties kiekį pirmiausia sumažėjo dalelių dydis ir toliau formavosi strypeliai. Dodekano dikarboksirūgšties (DDDA) poveikis buvo panašus į DL-asparto aminorūgšties poveikį, o didėjant koncentracijai stebėti morfologijos pasikeitimai nuo plokštelių pavidalo dalelių iki plokštelių ir strypelių mišinio. Nustatyta, kad oktano dikarboksirūgšties įtaka CDHA bandinių morfologijai buvo nedidelė, nepriklausomai nuo dikarboksirūgšties koncentracijos gautos į plokšteles panašios dalelės.

Mėginiuose, susintetintuose vandens ir etilenglikolio mišinyje, esant DL-asparto aminorūgšties mažiausiai koncentracijai, susidarė santykinai ilgų ir trumpų lazdelių mišinys. Naudojant didesnę DL-asparto aminorūgšties koncentraciją, gautus miltelius sudarė mikrometriniai aglomeratai, kurie buvo sudaryti iš mažesnių plokštelių ir lazdelių pavidalo dalelių. Dalelių dydis buvo gerokai mažesnis, palyginti su vandeninėje terpėje susintetintomis dalelėmis. Oktano dikarboksirūgšties atveju, nepriklausomai nuo priedo koncentracijos, buvo gautos palyginti didelės plokštelių dalelės. Morfologija buvo panaši į hidroterminės sintezės būdu be organinių priedų gautų miltelių morfologiją.



14 pav. Mėginių po hidroterminės reakcijos SEM vaizdai SLS:005 (a), SLS:05 (e), SLS:1 (i); Asp:005 (b), Asp:05 (f), Asp:1 (j); DDDA:005 (c), DDDA:05 (g), DDDA:1 (k); Sa:005 (d), Sa:05 (h), Sa:1 (l).

IŠVADOS

1. Kalcio hidroksiapatito (CHAp, $\text{Ca}_{10}(\text{PO}_4)_6(\text{OH})_2$) plonasluoksnių dangų ant silicio padėklų sintezei pirmą kartą buvo sukurtas žematemperatūrinis būdas, taikant zolių-gelių ir tirpinimo-nusodinimo metodus. Kalcio karbonato dangos ant silicio padėklų buvo gautos naudojant sukimo dengimo metodą, kai padėklai buvo dengiami 10, 20 ir 30 zolių-gelių tirpalo sluoksnių. CaCO_3 dangos buvo gautos skirtingą laiką dangas kaitinant $600\text{ }^\circ\text{C}$ temperatūroje.
2. Šios CaCO_3 dangos buvo panaudotos kalcio hidroksiapatito plonasluoksnių dangų gamybai ant silicio padėklų, taikant tirpinimo-nusodinimo metodą. Silicio padėklai, padengti iš dalies amorfiniu ir (arba) kristaliniu CaCO_3 , buvo mirkomi dinatrio fosfato Na_2HPO_4 tirpale 28 dienas $80\text{ }^\circ\text{C}$ temperatūroje. Rengeno spindulių difrakcinės analizės ir Ramano sklaidos spektroskopijos duomenys įrodė, kad taikant sukurtą sintezės metodą galima lengvai gauti kalcio hidroksiapatitą.
3. Pasiūlytas galimas kalcio hidroksiapatito susidarymo mechanizmas taikant žematemperatūrį zolių-gelių ir tirpinimo-nusodinimo metodus. Žematemperatūris CHAp dangų sintezės metodas leidžia daug efektyviau kontroliuoti galutinio produkto paviršiaus morfologiją.
4. Tas pats žematemperatūris sintezės metodas, apimantis zolių-gelių ir tirpinimo-nusodinimo metodus, buvo sukurtas kalcio hidroksiapatito dangoms ant titano padėklų sintetinti. Nustatyta, kad ant Ti padėklo susidarė CHAp su nedideliu kiekiu šalutinių produktų. Ramano ir FT-IR spektruose pastebėtos būdingos CHAp absorbcijos juostos. Ant Ti padėklų susidariusios CHAp dangos paviršius buvo šiurkštus ir porėtas, su homogeniškai pasiskirsčiusiais plokštelės pavidalo kristalais ir sferinėmis dalelėmis paviršiuje.
5. Buvo įvertintas CHAp dangų korozinis atsparumas Hankso balansiniame druskų tirpale. CHAp danga padidino titano padėklo atsparumą korozijai. Taip pat korozijos ir elektrocheminių bandymų parametru analizė parodė, kad apsauginių CHAp dangų, gautų zolių-gelių ir tirpinimo-nusodinimo metodais, įtaka yra pakankamai didelė ir gali būti padidinta suformavus vienodo storio CHAp dangą. Šios siūlomu sintezės metodu gautos plonasluoksnės CHAp dangos gali būti potencialūs pretendentai kuriant kaulų implantus ir įvairius jutiklius.
6. Ištirtas skirtingų organinių tirpiklių poveikis α -TCP hidrolizei ir jo virtimui į CDHA skirtingomis solvoterminėmis sąlygomis. Metilo alkoholis ir etilenglikolis turėjo stipresnę slopinamąją poveikį α -TCP hidrolizei nei etilo, izopropilo ir butilo alkoholiai.

7. Gautų mėginių morfologija buvo įvairi – nuo plokštelių pavidalo iki strypelių formos. Naudojant tam tikras etilo alkoholio ir izopropilo alkoholio proporcijas, buvo gautos strypelių formos, tačiau vis dar vyravo plokštelių pavidalo struktūros. Naudojant vandens-metilo alkoholio ir vandens-butilo alkoholio mišinius, be ilgų ir siaurų plokštelių susidarė daugiau strypelių. Iš visų tirtų tirpiklių didžiausią poveikį mėginių morfologijai turėjo etilenglikolis.
8. Ištirtas natrio laurilsulfato ir įvairių organinių rūgščių (DL-asparto aminorūgšties, dodekano dikarboksirūgšties, oktano dikarboksirūgšties) poveikis kalcio stokojančio hidroksiapatito susidarymui per α -trikalčio fosfato hidrolizę. Parodyta, kad organinių priedų prigimtis ir koncentracija turi įtakos galutinio produkto fazės grynumui ir morfologijai.
9. Didesnės natrio laurilsulfato ir dodekano dikarboksirūgšties koncentracijos paskatino ne tik hidroksiapatito, bet ir priemaišų susidarymą, o DL-asparto aminorūgštis ir oktano dikarboksirūgštis neturėjo įtakos fazės grynumui. Vandeninėje terpėje paruoštų bandinių morfologija, priklausomai nuo konkretaus organinio priedo koncentracijos, vyravo nuo plokštelių iki strypelių pavidalo. Naudojant vandens ir etilenglikolio mišinį susidarė gerokai mažesnės dalelės, turinčios strypelių ir siaurų plokštelių formą.

AUTORIAUS PUBLIKUOTŲ DARBŲ SĄRAŠAS

Straipsniai žurnaluose

1. R. Karalkeviciene, G. Briedyte, T. Murauskas, M. Norkus, A. Zarkov, J.-C. Yang, A. Kareiva. A novel method for the formation of bioceramic nano-calcium hydroxyapatite coatings using sol-gel and dissolution-precipitation processing. *Chemija*, **33** (2022) 27-34.
2. R. Karalkeviciene, E. Raudonyte-Svirbutaviciene, J. Gaidukevic, A. Zarkov, A. Kareiva, Solvothermal synthesis of calcium-deficient hydroxyapatite via hydrolysis of α -tricalcium phosphate in different aqueous-organic media. *Crystals*, **12** (2022) 253.
3. R. Karalkeviciene, G. Briedyte, A. Popov, S. Tutliene, A. Zarkov, A. Kareiva. Low-Temperature Synthesis Approach for Calcium Hydroxyapatite Coatings on Titanium Substrate. *Inorganics*, **11** (2023) 33.

4. R. Karalkeviciene, E. Raudonyte-Svirbutaviciene, A. Zarkov, J.-C. Yang, A. I. Popov, A. Kareiva. Solvothermal synthesis of calcium hydroxyapatite via hydrolysis of α -tricalcium phosphate in the presence of different organic additives. *Crystals*, **13** (2023) 265.

Konferencijų tezės

1. R. Karalkeviciene, A. Zarkov, G. Briedyte, T. Murauskas, M. Norkus, A. Kareiva. A new method for the formation of bioceramic nano-calcium hydroxyapatite coatings. International Conference-School “Advanced Materials and Technologies 2021”. Palanga, Lietuva, rugpjūčio 23-27, (2021) 153.
2. R. Karalkeviciene, A. Zarkov, G. Briedyte, T. Murauskas, M. Norkus, A. Kareiva. Bioceramic nano-calcium hydroxyapatite coatings on silicon substrates. 16th International Scientific Conference of Lithuanian Chemists “Chemistry & Chemical Technology 2021“. Vilnius, Lietuva, rugsėjo 24, (2021) 87.
3. R. Karalkeviciene, E. Raudonyte-Svirbutaviciene, A. Zarkov, A. Kareiva. Hydroxyapatite formation by solvothermal treatment of alpha-tricalcium phosphate with water-alcohol solution. 65th International conference for students and natural science “Open Readings“, Vilnius, Lietuva, kovo 15-18 (2022) 215.
4. R. Karalkeviciene, E. Raudonyte-Svirbutaviciene, A. Zarkov, A. Kareiva. Solvothermal synthesis of calcium hydroxyapatite in water-organic solvent media. 1st International Conference on Advanced Materials for Bio-Related Applications “AMBRA 2022“, Wrocław, Poland, gegužės 16–19, (2022) P-15.
5. R. Karalkeviciene, E. Raudonyte-Svirbutaviciene, J. Gaidukevic, A. Zarkov, and A. Kareiva. Solvothermal Synthesis of Calcium Hydroxyapatite via Hydrolysis of α -Tricalcium Phosphate in Different Aqueous-Organic Media. International conference “Functional Inorganic Materials“, Vilnius, Lietuva, spalio 6-8, (2022) 46 (žodinis pranešimas).

CURRICULUM VITAE
Gyvenimo aprašymas

| PERSONAL INFORMATION | |
|------------------------------|---|
| Name, Surname | Rasa Karalkevičienė |
| Date of birth | 02-15-1978 |
| Email address | <u>rasyteka78@gmil.com</u> |
| Telephone number | +370 655 60986 |
| EDUCATION AND QUALIFICATIONS | |
| 2019-09 to present | Doctoral studies. Department of Inorganic Chemistry, Faculty of Chemistry and Geosciences, Institute of Chemistry, Vilnius University. |
| 2014-2016 | Master's degree in Chemistry. Faculty of Chemistry, Vilnius University. |
| 1996-2004 | Bachelor of Chemistry. Faculty of Chemistry, Vilnius University. |
| 1985-1996 | Vilnius 50th Secondary School. |
| WORK EXPERIENCE | |
| April 2019 to present | Member of the Working Council of the National Public Health Laboratory (NPHL) |
| July 2021 to present | National Public Health Laboratory. Quality Management Unit. Acting Head of the Quality Management Unit. |
| August 2020 – July 2021 | National Public Health Laboratory. Customer Service Unit. Acting Head of the Customer Service Unit. National Public Health Laboratory. |
| August 2017 – August 2020 | National Public Health Laboratory Chemical Testing Division. Deputy Head of the Chemical Testing Division. |
| February 2010 – August 2017 | National Public Health Laboratory Instrumental Chemical Testing Subdivision. Chemistry Specialist. |
| 2004-2009 | UAB "GKG-3"; position: laboratory technician, later head of laboratory. |

| | |
|---------------------------|---|
| August 2001 - August 2004 | UAB "GASTA" Laboratory accountant. |
| February 2000 – June 2000 | VU Faculty of Chemistry, Scientific Laboratory of Liquid-Crystalline Materials; position: laboratory assistant. |
| February 1999 – May 1999 | UAB "Geležinis kelias"; position: cashier-saleswoman. |

COPIES OF PUBLICATIONS

A novel method for the formation of bioceramic nano-calcium hydroxyapatite coatings using sol-gel and dissolution-precipitation processing

Rasa Karalkevičienė¹,

Greta Briedytė¹,

Tomas Murauskas¹,

Mantas Norkus¹,

Aleksej Žarkov¹,

Jen-Chang Yang²,

Aivaras Kareiva^{*}

¹ Institute of Chemistry,
Vilnius University,
24 Naugarduko Street,
03225 Vilnius, Lithuania

² Graduate Institute of Nanomedicine and
Medical Engineering,
College of Biomedical Engineering,
Taipei Medical University,
Taipei 11052, Taiwan

The wet chemistry route has been developed to prepare calcium hydroxyapatite ($\text{Ca}_{10}(\text{PO}_4)_6(\text{OH})_2$, (HA)) thin films on a silicon substrate using the novel low-temperature sol-gel and dissolution-precipitation approach. The calcium carbonate thin films on the silicon substrate were obtained by spin-coating technique when substrates were repeatedly coated with 10, 20 and 30 layers of sol-gel solution. The composites formed of crystalline and amorphous CaCO_3 were obtained by calcination of the coatings for different time at 600°C. A dissolution-precipitation procedure was used for the preparation of calcium hydroxyapatite thin films on silicon substrate at 80°C. The obtained synthesis products were characterised by X-ray powder diffraction (XRD) analysis, scanning electron microscopy (SEM) and Raman spectroscopy.

Keywords: calcium hydroxyapatite, thin films, silicon substrate, spin-coating, sol-gel processing

INTRODUCTION

There is a need to reconstruct damaged hard tissue for several reasons that include traumatic or non-traumatic events, congenital abnormalities, or disease. Damaged tissues stemming from these events can become a major issue in orthopedic, dental and maxillofacial surgery. A study on numerous biomaterials revealed that calcium phosphates had been used in hard tissue reconstruction for more than six decades. Calcium hydroxyapatite ($\text{Ca}_{10}(\text{PO}_4)_6(\text{OH})_2$, HA) was the primary material used in orthopedics and dentistry [1, 2].

HA crystals are present in the human body both inside bone and teeth. In terms of the human bone, the HA crystals as a bioactive ceramic cover 65 to 70% by weight of the bone. Furthermore, the architecture of the bone comprises type-I collagen as an organic component and the HA as an inorganic component. These two components form a composite structure at the nanoscale, in which nano-HA is interspersed in the collagen network. This composite forms mineralised collagen and is the precursor of biological mineralised tissue from tendons and skin to hard mineralised tissues such as bone and teeth. Moreover, in the bone, the HA crystals present in the shape of plates or needles are about 40 to 60 nm long, 20 nm wide, and 1.5 to

* Corresponding author. Email: aivaras.kareiva@chf.vu.lt

5 nm thick [3, 4]. The arrangement of different HA crystalline sizes and shapes provides support for this tissue's structural stability, hardness and function [5, 6].

HA application in orthopedics can vary from bone defects repair and bone augmentation to coatings for human body metallic implants. The HA-based implants can provide an interlocked porous structure [7–9]. This structure can act as the extracellular matrix, promoting the natural process of cellular development and tissue regeneration [9, 10]. Furthermore, HA can enhance the osseointegration process by promoting a rigid anchorage between the implant and the surrounding tissue without the growth of fibrous tissue. The successful osseointegration retains the bone anchorage for a long period, hence completely restoring functional ability [11, 12].

HA coatings on different substrates are being widely used in orthopaedics and dentistry [13–19]. Many preparation techniques are used currently in coating of HA onto different substrates [18, 20]. Hydroxyapatite synthesised by different methods has different surface morphology and the products also have different chemical properties [25–29]. In order to produce a coating that is more resistant to physiological conditions, various new methods are being sought for the modern synthesis of HA layers that replicate bone tissue. Si could be used for the formation of an interfacial layer on the metal alloys to increase the adhesion strength of biomaterials substantially [26]. Cha et al. [27] also showed that silicon could be used for improving the biological performance of ZrO₂ substrate. The results revealed that Zr-Si-HA substrates are very promising biomaterials for bone tissue engineering. Interestingly, Hiebl et al. [28] reported that the Si-based substrate is also a promising candidate for the formation of materials which are aimed to be used in cardiovascular tissue engineering approaches. Moreover, silicon substrates modified with graphene oxides could be applied to control living cells on these substrates [29]. These substrates are important for the development of bio-applications, including biosensors and implant biomaterials. Recently, samarium-doped hydroxyapatite (Sm-HA) coatings were fabricated on the Si substrate [30]. This study showed that the Sm-HA samples on the Si substrate are good candidates for the development of new antimicro-

bial agents. A natural rubber-calcium phosphate hybrid for applications as bioactive coatings was also synthesised on the Si substrate [31]. Finally, silicon or silicon-containing composites are very useful substrates for the application for blood-contacting implants, for the patterned cell culture *in vitro* or to improve cell response [32–34].

In this paper, we report the novel low-temperature sol-gel synthetic and dissolution-precipitation approach and the characterisation of HA thin films on a silicon substrate using a spin-coating technique.

EXPERIMENTAL

Firstly, calcium carbonate (CaCO₃) layers on silicon substrates were fabricated by sol-gel synthesis. Silicon substrates were washed with Piranha solution (3 parts of concentrated sulfuric acid and 1 part of 30% hydrogen peroxide solution) and distilled water. In the sol-gel process, 20 ml of 2-propanol (99.0%; Alfa Aesar) were mixed with 1.8 ml of acetylacetone, C₅H₈O₂ (99.9%; Merck) with stirring at room temperature. An appropriate amount (1.0920 g) of calcium nitrate tetrahydrate (Ca(NO₃)₂·4H₂O) (99.0%; Fluka) was added to the solution and stirred for 1 h until the material dissolved [35]. The solution used for coating the silicon substrates was mixed with the polyvinyl alcohol (PVA) (PVA7200, 99.5%; Aldrich) solution in a ratio of 5:3. A polyvinyl alcohol (PVA) solution was obtained by dissolving 0.5 g of polyvinyl alcohol (PVA) in 49.5 ml of distilled water with stirring at 90°C for 1 h. The silicon substrate was repeatedly coated with 10, 20 and 30 layers of solution by the spin-coating method using two different spinning procedures (A) and (B) (Table). After the evaporation of solvent the substrates were dried in an oven for 10 min at 200°C and heated at 600°C for 5 h with a heating rate of 5°C/min. Calcium hydroxyapatite coatings were synthesised by the low-temperature dissolution-precipitation method. Silicon substrates coated with partially amorphous and/or crystalline CaCO₃ were soaked in a disodium phosphate Na₂HPO₄ (pure p.a., Chempur) solution (1 mol/l) for 28 days in a thermostat at 80°C.

For the characterisation of surface properties, the X-ray powder diffraction (XRD) analysis, scanning electron microscopy (SEM) and Raman

Table. Silicon substrate coating techniques

| Parameter | Spinning procedure (A), sec | Spinning procedure (B), sec |
|-----------|-----------------------------|-----------------------------|
| RPM1 | 1000 | 500 |
| RAMP1 | 1 | 2 |
| TIME1 | 1 | 5 |
| RPM2 | 3000 | 1000 |
| RAMP2 | 2 | 2 |
| TIME2 | 1 | 5 |
| RPM3 | 3000 | 1500 |
| RAMP3 | 1 | 2 |
| TIME3 | 30 | 90 |
| RAMP4 | 10 | 10 |

spectroscopy were applied. The XRD studies were performed on a Rigaku miniFlex II diffractometer operating with Cu K α 1 radiation (start angle 10; stop angle 60; sampling W. 0.010; scan speed 5.0; kV 30). In order to study the morphology and microstructure of the samples a scanning electron microscope Hitachi SU-70 was used. The thickness of HA coatings was measured using the SEM analysis of the cross-sections of films. Raman spectroscopy studies were performed using a scanning near-field spectroscopy system with a Raman spectroscopy accessory (Alpha300R, WiTec). Elemental analysis was performed on a Thermo Fischer Scientific Flash 2000 Elemental Analyzer.

RESULTS AND DISCUSSION

As was mentioned, the silicon substrates were repeatedly coated with the 10, 20 and 30 layers of the sol-gel solution. However, the XRD patterns of the samples obtained after 10 coatings procedures did not contain any reflections attributable to a crystalline CaCO₃ phase. Figure 1 represents the XRD patterns of CaCO₃ thin films obtained after 20 coatings using slightly different spin-coating procedures. As seen from Fig. 1, the peaks attributable to CaCO₃ ($2\theta \approx 29.5$; PDF [96-210-0190]) could be determined in the XRD patterns confirming the formation of crystalline calcium carbonate. Additionally, the diffraction peak from the substrate Si ($2\theta \approx 33$; PDF [96-901-1057]) is also seen. It is interesting to note that the XRD patterns of CaCO₃ layers fabricated after 30 spin-coating procedures were almost identical to the ones presented in Fig. 1.

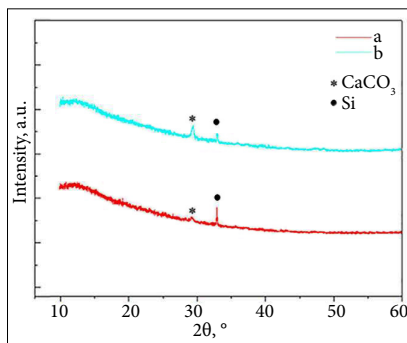


Fig. 1. XRD patterns of the sol-gel derived CaCO₃ samples on the Si substrate obtained after 20 coatings and annealed at 600°C for 5 h after each spinning procedure, using different (A) and (B) spin-coating techniques

The SEM micrographs of the surfaces of obtained CaCO₃ samples are shown in Fig. 2. The surface of the specimen obtained after 30 spinning times is partially even with the clearly pronounced formation of individual crystallites. The quality of the sol-gel coated thin films of CaCO₃ is not influenced by used spin-coating techniques.

The synthesised CaCO₃ coatings were also investigated using Raman spectroscopy. The Raman spectra of the synthesised samples are depicted in Fig. 3. The analysis of Raman spectroscopy results shows the characteristic CaCO₃ peaks located at 153, 281, 617, 668, 709 and 1084 cm⁻¹ formed after 30 coatings using the both spin-coating techniques (A) and (B) [36, 37]. It is interesting to note that the positions of Raman bands determined in the Raman spectra of synthesised CaCO₃ according to [36] could be attributed to the partially amorphous calcium carbonate phase.

Calcium hydroxyapatite coatings were synthesised by a low-temperature dissolution-precipitation method. The silicon substrates coated with partially amorphous and/or crystalline CaCO₃ were soaked in the disodium phosphate Na₂HPO₄ solution for 28 days at 80°C. Figure 4 presents the XRD patterns of the Si substrate coated initially with CaCO₃ following the formation of the calcium phosphate phase. The results of XRD analysis show the negligible influence of the parameters of spinning on the crystallisation of calcium hydroxyapatite on the Si substrate.

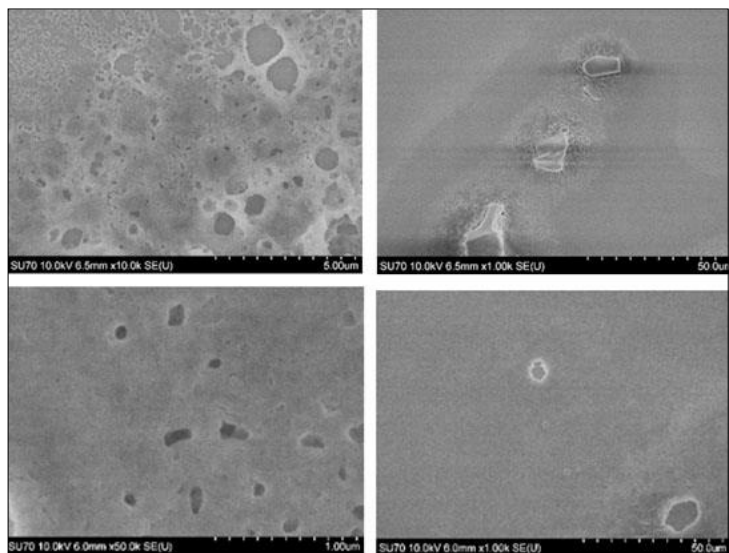


Fig. 2. SEM micrographs of the CaCO₃ thin films on the silicon substrate fabricated after 30 coatings using different (A, top) and (B, bottom) spin-coating techniques and obtained at different magnifications

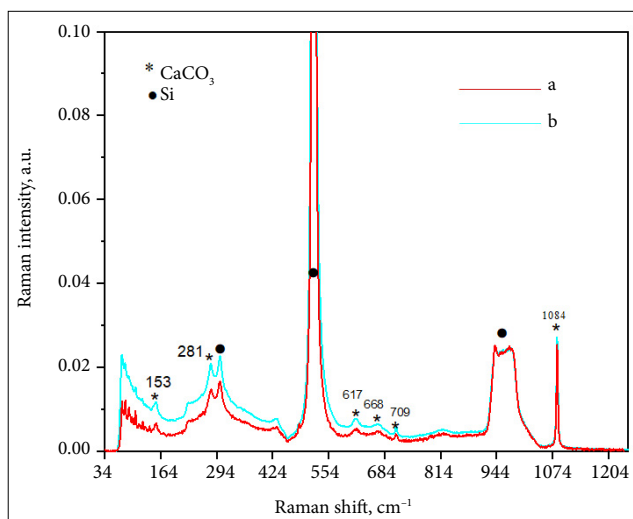


Fig. 3. Raman spectra of the CaCO₃ samples containing 30 layers synthesised using different spin-coating techniques: (a) A and (b) B

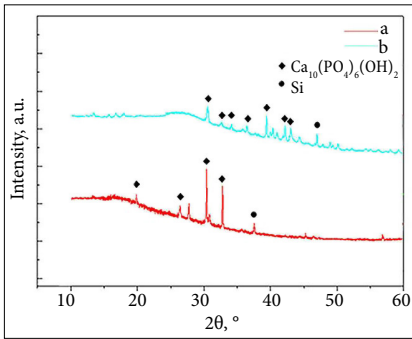


Fig. 4. XRD patterns of the calcium hydroxyapatite thin films fabricated by the sol-gel and dissolution-precipitation method using different spin-coating techniques: (a) A and (b) B

The characteristic HA peaks could be easily distinguished (PDF [74-0566]) despite some reflections originated from the used substrate are also visible. Thus, the data of XRD analysis proved that calcium hydroxyapatite could be easily obtained at 80°C from the Ca-O sol-gel precursor solution on the Si substrate using the spin-coating technique and following dissolution-precipitation approach.

The thickness of HA coatings was measured using the SEM analysis of the cross-sections of films, and was found to be approximately 900–945 nm. The elemental analysis of synthesised products was also performed. No carbon due to a possible formation of carbonate apatite in the synthesis products was detected.

Figure 5 shows the Raman spectra in the wavenumber region from 100 to 1250 cm^{-1} of the CHA sample containing 30 layers of CaCO_3 on the Si substrate. The spectra were recorded at the centre of the specimens. The broad bands with sharp peaks near 300, 500 and 950 cm^{-1} belong to the overtone spectrum of Si substrate. However, the intense bands corresponding to the symmetric stretching vibration of phosphate groups in $\text{Ca}_{10}(\text{PO}_4)_6(\text{OH})_2$ are also seen [38, 39]. The results of Raman spectroscopy are in a good agreement with the XRD analysis data. Using the Raman optical microscopy system in the representative optical images is presented in Fig. 6. The images demonstrate the formation of individual crystallites in the film matrix. By pointing the laser at the formed individual crystallites, HA signals were observed. Defects commonly present in 2D materials, such as cracks, vacancies and crystal boundaries [40, 41], were not detected in the HA

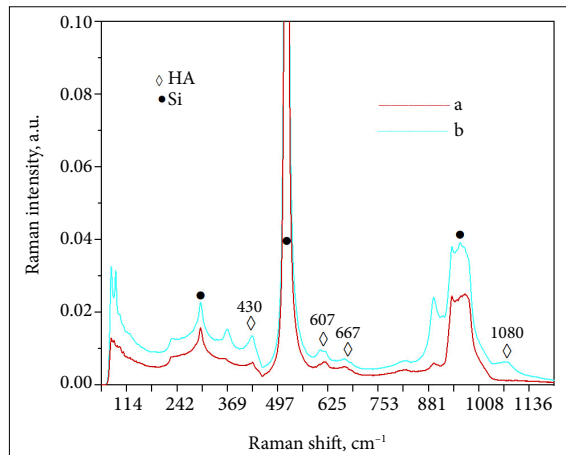


Fig. 5. Raman spectra of the HA synthesised by the sol-gel and dissolution-precipitation method using different spin-coating techniques: (a) A and (b) B

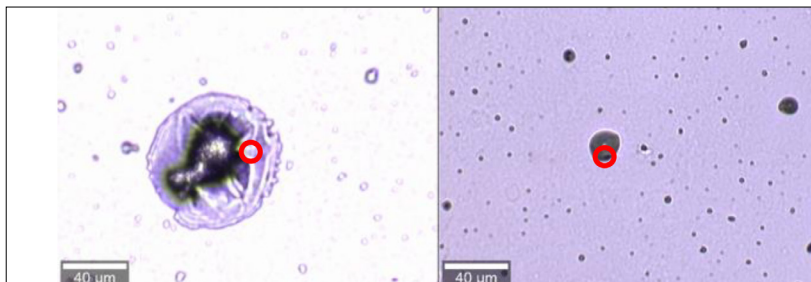
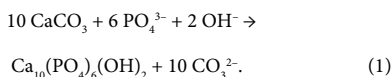


Fig. 6. Images of the HA thin films obtained by Raman optical microscopy system. Red circles mark the location of focused laser beam for measuring Raman spectra

samples synthesised by the low-temperature sol-gel and dissolution-precipitation method.

Thus, the final formation of HA on the surface of Si could be expressed by the following equation [42–44]:



The possible mechanism of the formation of calcium hydroxyapatite by the suggested low-temper-

ature sol-gel and dissolution-precipitation method is presented in Fig. 7.

CONCLUSIONS

The wet chemistry route has been developed to prepare calcium hydroxyapatite ($\text{Ca}_{10}(\text{PO}_4)_6(\text{OH})_2$, HA) thin films on the silicon substrate using for the first time the low-temperature sol-gel and dissolution-precipitation approach. The calcium carbonate thin films on the silicon substrate were obtained by the spin-coating technique when the substrates

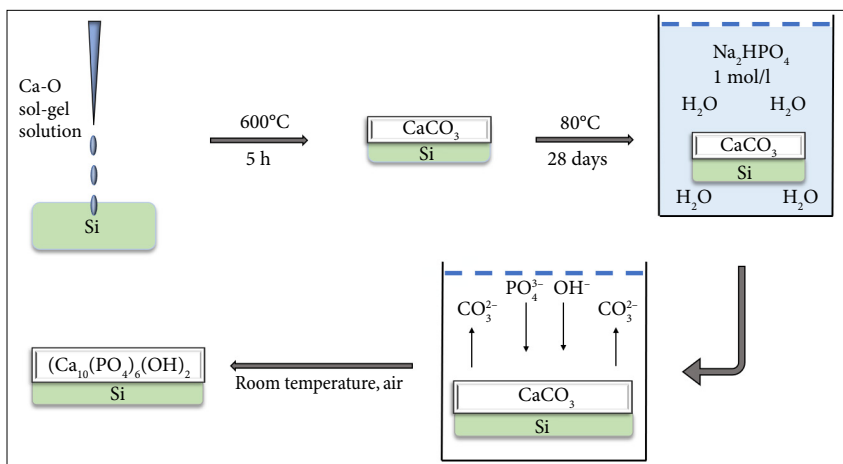


Fig. 7. The possible mechanism of the formation of calcium hydroxyapatite by the suggested low-temperature sol-gel and dissolution-precipitation method on the Si substrate

were repeatedly coated with 10, 20 and 30 layers of the sol-gel solution. It was demonstrated by XRD analysis and Raman spectroscopy that the quality of CaCO₃ coatings was not dependent on the spinning rate. The composites formed of crystalline and amorphous CaCO₃ were obtained by calcination of the coatings for different times at 600°C. These coatings were used for the fabrication of calcium hydroxyapatite thin films on the silicon substrate using the dissolution-precipitation procedure. The silicon substrates coated with partially amorphous and/or crystalline CaCO₃ were soaked in the disodium phosphate Na₂HPO₄ solution for 28 days at 80°C. The data of XRD analysis and Raman spectroscopy again proved that calcium hydroxyapatite could be easily obtained by the developed synthesis method. The possible mechanism of the formation of calcium hydroxyapatite using the low-temperature sol-gel and dissolution-precipitation method was also suggested. It is well known that the main morphological features (particle size, shape and size distribution) of the synthesis products depend very much on the synthesis temperature. The elaborated low-temperature synthesis method for HA coatings would allow a much more efficient control of the surface morphology of the end product.

ACKNOWLEDGEMENTS

This project has received funding from the European Social Fund (Project No. 09.3.3-LMT-K-712-19-0069) under Grant Agreement with the Research Council of Lithuania (LMTLT).

Received 22 February 2022

Accepted 9 March 2022

References

1. T. Habibah, D. Amlani, M. Brizuela, *Hydroxyapatite Dental Material*, StatPearls Publishing, Treasure Island, FL (2018).
2. B. L. Thi, R. Shi, B. D. Long, et al., *Biomed. Mater.*, **15**, 035004 (2020).
3. A. K. Teotia, D. B. Raina, C. Singh, et al., *ACS Appl. Mater. Interf.*, **9**, 6816 (2017).
4. A. Szewczyk, A. Skwira, M. Ginter, D. Tajer, M. Prokopowicz, *Polymers*, **13**, 53 (2021).
5. S. M. Zakaria, S. H. Zein, M. R. Othman, F. Yang, J. A. Jansen, *Tissue Eng. Part B Rev.*, **19**, 431 (2013).
6. T. Debnath, A. Chakraborty, T. K. Pal, *J. Indian Soc. Periodontol.*, **18**, 593 (2014).
7. A. Rogina, M. Antunovic, D. Milovac, *J. Biomed. Mater. Res. B*, **107**, 197 (2019).
8. A. Lode, A. Bernhardt, K. Kroonen, M. Springer, A. Briest, M. Gelinsky, *J. Tissue Eng. Regen. Med.*, **3**, 149 (2009).
9. M. Kumar, R. Kumar, S. Kumar, *Mater. Today Proc.*, **45**, 5269 (2021).
10. Y. Cheng, G. Zhao, H. Liu, *Zhongguo Xiu Fu Chong Jian Wai Ke Za Zhi*, **12**, 74 (1998).
11. J. Park, B. J. Kim, J. Y. Hwang, et al., *J. Nanosci. Nanotechnol.*, **18**, 837 (2018).
12. P. Shi, M. Liu, F. Fan, C. Yu, W. Lu, M. Du, *Mater. Sci. Eng. C*, **90**, 706 (2018).
13. Z. Stankevičiūtė, M. Malakauskaitė, A. Beganskiėnė, A. Kareiva, *Chemija*, **24**, 288 (2013).
14. V. Wagener, A. R. Boccaccini, S. Virtanen, *Appl. Surf. Sci.*, **416**, 454 (2017).
15. Y. Y. Su, K. Z. Li, L. L. Zhang, C. C. Wang, Y. P. Zhang, *Surf. Coat. Technol.*, **352**, 619 (2018).
16. L. F. Sukhodub, L. B. Sukhodub, W. Simka, M. Kumeda, *Mater. Lett.*, **250**, 163 (2019).
17. V. T. Nguyen, T. C. Cheng, T. H. Fang, M. H. Li, *J. Mater. Res. Technol.*, **9**, 4817 (2020).
18. K. Ishikawa, A. Kareiva, *Chemija*, **31**, 25 (2020).
19. S. F. Wen, X. L. Liu, J. H. Ding, et al., *Progr. Nat. Sci.*, **31**, 324 (2021).
20. D. Avnir, T. Coradin, O. Lev, J. Livage, *J. Mater. Chem.*, **16**, 1013 (2006).
21. P. Usinskas, Z. Stankevičiūtė, G. Niaura, J. Ceponkus, A. Kareiva, *Mater. Sci.–Medžiagotyra*, **25**, 365 (2019).
22. V. Jonauske, R. Ramanauskas, R. Platakyte, et al., *Mendeleev Commun.*, **30**, 512 (2020).
23. K. Ishikawa, E. Garskaite, A. Kareiva, *J. Sol-Gel Sci. Technol.*, **94**, 551 (2020).
24. R. Gibson, in: *Biomaterials Science*, 4th edn., An Introduction to Materials in Medicine, 307, Academic Press (2020).
25. F. K. Basak, E. Kayahan, *Ceram. Int.*, **47**, 27880 (2021).
26. A. A. Ahmad, A. M. Alsaad, *Bull. Mater. Sci.*, **30**, 301 (2007).
27. J. Y. Cha, C. H. Kim, Y. J. Kim, *J. Ceram. Soc. Jpn.*, **126**, 940 (2018).
28. B. Hiebl, C. Hopperditzel, H. Huenigen, F. Jung, N. Scharnagl, *Clin. Hemorheol. Microcirc.*, **55**, 491 (2013).
29. J. T. Jeong, M. K. Choi, Y. Sim, et al., *Sci. Rep.*, **6**, 33835 (2016).
30. S. L. Iconaru, A. Groza, S. Gaiaschi, et al., *Coatings*, **10**, 1124 (2020).
31. R. M. do Nascimento, A. J. de Paula, N. C. Oliveira, et al., *Mater. Sci. Eng. C*, **94**, 417 (2019).
32. Z. V. Parlak, S. Wein, R. Zybal, et al., *J. Biomater. Appl.*, **34**, 585 (2019).

33. J. Friguglietti, S. Das, P. Le, et al., *Biomaterials*, **244**, 119927 (2020).
34. S. Petrovic, D. Perusko, A. Mimidis, et al., *Nanomaterials*, **10**, 2531 (2020).
35. A. Zarkov, A. Stanulis, J. Sakaliuniene, et al., *J. Sol-Gel Sci. Technol.*, **76**, 309 (2015).
36. M. M. Tlili, M. Ben Amor, C. Gabrielli, et al., *J. Raman Spectrosc.*, **33**, 10 (2001).
37. A. Dandeu, B. Humbert, C. Carteret, H. Muhr, E. Plasari, J.-M. Bossoutrot, *Chem. Eng. Technol.*, **29**, 221 (2006).
38. G. B. Ramirez-Rodriguez, J. M. Delgado-Lopez, J. Gomez-Morales, *CrystEngComm*, **15**, 2206 (2013).
39. S. Koutsopoulos, *J. Biomed. Mater. Res.*, **62**, 600 (2002).
40. F. Zhong, H. Wang, Z. Wang, et al., *Nano Res.*, **14**, 1840 (2021).
41. J. F. Schultz, S. W. Li, S. Jiang, N. Jiang, *J. Phys. Condens. Matter*, **32**, 463001 (2020).
42. K. Ishikawa, *Materials*, **3**, 1138 (2010).
43. I. Grigoraviciute-Puroniene, Y. Tanaka, V. Vegelyte, Y. Nishimoto, K. Ishikawa, A. Kareiva, *Ceram. Int.*, **45**, 15620 (2019).
44. R. Kishida, M. Elsheikh, K. Hayashi, A. Tsuchiya, K. Ishikawa, *Ceram. Int.*, **47**, 19856 (2021).

**Rasa Karalkevičienė, Greta Briedytė,
Tomas Murauskas, Mantas Norkus, Aleksej Žarkov,
Jen-Chang Yang, Aivaras Kareiva**




**NAUJAS BIOKERAMINIŲ NANOKALCIO
HIDROKSIAPATITO DANGŲ FORMAVIMO
METODAS NAUDOJANT ZOLIŲ-GELIŲ IR
TIRPINIMO-NUSODINIMO PROCESUS**

S a n t r a u k a

Šiame darbe kalcio hidroksiapatito ($\text{Ca}_{10}(\text{PO}_4)_6(\text{OH})_2$, (HA)) plonos plėvelės ant silicio padėklo susintetintos taikant naują žematemperatūrį zolių-gelių ir tirpinimo-nusodinimo metodą. Iš pradžių ant silicio padėklo buvo gautos CaCO_3 dangos kaitinant zolius-gelius skirtingą laiką 600 °C temperatūroje. Kalcio hidroksiapatito plonomis plėvelėmis paruošti ant silicio padėklo 80 °C temperatūroje buvo naudota tirpinimo-nusodinimo procedūra. Gauti sintezės produktai apibūdinti remiantis rentgeno spindulių difrakcijos analize, skenuojančia elektronų mikroskopija ir Ramano spektroskopija. Taip pat buvo pasiūlytas galimos kalcio hidroksiapatito susidarymo mechanizmas.

Article

Low-Temperature Synthesis Approach for Calcium Hydroxyapatite Coatings on Titanium Substrate

Rasa Karalkeviciene¹, Greta Briedyte¹, Anton Popov¹ , Skirmante Tutliene², Aleksej Zarkov¹  and Aivaras Kareiva^{1,*} ¹ Department of Inorganic Chemistry, Vilnius University, Naugarduko 24, LT-03225 Vilnius, Lithuania² Center for Physical Sciences and Technology, Sauletekio 3, LT-10257 Vilnius, Lithuania

* Correspondence: aivaras.kareiva@chgf.vu.lt

Abstract: In this study, a low-temperature synthetic approach was developed for the fabrication of calcium hydroxyapatite (CHAp) coatings on a titanium substrate. The titanium substrates were first coated with CaCO₃ by a spin-coating technique using a sol-gel chemistry approach, and the obtained product was transformed into CHAp during a dissolution-precipitation reaction. The phase purity and structural and morphological features of the obtained CHAp coatings were evaluated by X-ray diffraction (XRD) analysis, FTIR spectroscopy, Raman spectroscopy, scanning electron microscopy (SEM) and using a 3D optical profilometer. It was demonstrated that almost-single-phase CHAp formed on the titanium substrate with a negligible number of side phases, such as Na₂HPO₄ (starting material) and TiO₂. In the Raman spectrum of the CHAp coating, the peaks of phosphate group vibrations were clearly seen. Thus, the obtained results of Raman spectroscopy correlated well with the results of X-ray diffraction analysis. The corrosive behaviour of CHAp coatings on a titanium substrate was also evaluated using electrochemical methods. It was found that the corrosion resistance of titanium coated with CHAp increased significantly. These CHAp thin films may be potential candidates for use in not only in regenerative medicine but also in the development of different sensors.



Citation: Karalkeviciene, R.; Briedyte, G.; Popov, A.; Tutliene, S.; Zarkov, A.; Kareiva, A. Low-Temperature Synthesis Approach for Calcium Hydroxyapatite Coatings on Titanium Substrate. *Inorganics* **2023**, *11*, 33. <https://doi.org/10.3390/inorganics11010033>

Academic Editors: Duncan H. Gregory, Wolfgang Linert, Richard Dronskowski, Vladimir Arion, Claudio Pettinari and Torben R. Jensen

Received: 15 December 2022
Revised: 29 December 2022
Accepted: 3 January 2023
Published: 7 January 2023



Copyright: © 2023 by the authors. Licensee MDPI, Basel, Switzerland. This article is an open access article distributed under the terms and conditions of the Creative Commons Attribution (CC BY) license (<https://creativecommons.org/licenses/by/4.0/>).

Keywords: calcium hydroxyapatite; thin films; titanium substrate; spin coating

1. Introduction

Calcium hydroxyapatite (Ca₁₀(PO₄)₆(OH)₂; CHAp) is one of the substances found in bone tissue, being involved in bone growth and characterized by excellent biocompatibility. CHAp shows strong osteopermeable properties, making it a particularly attractive material for biomedical applications [1]. A high surface area, reactivity and biomimetic morphology make nano-CHAp more favourable in applications such as orthopaedic implant coating or bone substitute filler [2]. Recent efforts have been focused on the possibility of combining nano-CHAp with other drugs and materials for multipurpose applications, such as antimicrobial treatment, osteoporosis treatment, sensing and magnetic manipulation [3]. To build more effective nano-CHAp and composite systems, the synthesis processes, chemistry and toxicity have to be thoroughly investigated. These nanomaterials have a significant role in many biomedical areas, such as sustained drug and gene delivery, bioimaging, magnetic resonance, cell separation and hyperthermia treatment, due to their promising biocompatibility [4].

The use of artificial biomaterials has been gaining therapeutic scope in diverse clinical applications. However, an equally attractive field of application involving CHAp is its use in various sensors. The CO-gas-sensing property of CHAp ceramics with an average crystallite size of 31–54 nm was investigated by Mahabole et al. [5]. It was concluded that CHAp can be used as a CO gas sensor at an optimum temperature near 125 °C. The results presented in the study [6] indicate that the CHAp sensor is applicable for qualitative

and conformational analysis of protein adsorption. CHAp was also used to develop a potentiometric sensor for phosphate ions [7]. Alkaline phosphatase (ALP) is a critical biological marker for osteoblast activity during early osteoblast differentiation. The highly sensitive and rapidly responsive novel near-infrared fluorescent probes for the fluorescent detection of ALP were described [8]. ALP detection *in vivo* was achieved using NIR probe-labelled three-dimensional calcium-deficient hydroxyapatite (CDHA) scaffolds. The results suggest the possibility of early-stage ALP detection during neo-bone formation inside a bone defect, by *in vivo* fluorescent evaluation using 3D CDHA scaffolds. Recent trends in the application of calcium apatite compounds for electrochemical detection of heavy metals or H_2O_2 are shown in the studies [9,10].

Continuous research on CHAp nanomaterials (CHAp-NMs) has explored novel fabrication approaches coupled with functionalization and characterization methods [11,12]. CHAp coatings can be deposited using atomic layer deposition (ALD) technology [13] or magnetron sputtering [14]. Due to the quality of the produced coatings, these methods are the main technologies for the fabrication of thin layers in a vacuum. The electrochemical method of CHAp coating deposition is a popular way of forming coatings by electrolysis from an electrolyte with the appropriate composition. The method does not require the above-mentioned expensive equipment, and the thickness and structure of the deposited coatings can be controlled by varying the appropriate potential, current density, electrolyte composition and pH [15]. Using the aqueous sol–gel method, CHAp can be synthesized on various substrates (e.g., titanium, quartz, silicon) by controlling the temperature, pH and concentration [16]. This method is considered a high-temperature approach, requiring elevated temperatures to obtain the CHAp crystalline phase. However, high temperatures do not support the formation of nanocrystalline materials [17]. The CHAp coatings obtained at 1000 °C could be inhomogeneous, for example, consisting of two distinct regions: one with small grains, approximately 200 nm in size, and one with larger grains, approximately 800 nm in diameter [18]. Additionally, the formation of the TiO_2 phase at high temperatures reduces adhesion of CHAp films on Ti substrates [19].

In this study, we investigated the possibility of fabricating CHAp thin films at a sufficiently low temperature, applying environmentally friendly sol–gel and dissolution–precipitation methods [1,20–22] for the first time using the spin-coating technique. The spin-coating method offers great promise for the fabrication of thin films with desirable properties [23]. The spin-coating technique allows very homogeneous samples composed of nano-scaled particles to be fabricated [16]. This low-temperature synthetic approach was developed for the fabrication of CHAp coatings on Ti substrates; however, it could be easily used for the formation of CHAp nanostructures on different substrates. The results of characterization of the obtained CHAp are presented herein.

2. Results

2.1. X-ray Diffraction Analysis

The phase composition of the obtained calcium carbonate coatings on the titanium substrate was determined by X-ray diffraction analysis (Figure 1).

According to the obtained results, the formation of $CaCO_3$ after 20 coating procedures was evidently observed. Additionally, the XRD patterns contained intense diffraction peaks corresponding to TiO_2 (rutile) CaO and $CaTiO_3$ crystalline phases.

Figure 2 shows the XRD patterns of the resulting $CaCO_3$ coating on the titanium substrate after 28 days of immersion in Na_2HPO_4 solution and the Ti substrate was annealed at 600 °C.

It can be seen that the CHAp coating was successfully formed. The diffraction peaks characteristic of the crystalline CHAp phase were observed [16,19]. Additionally, the peaks attributed to secondary phases such as Na_2HPO_4 (from immersion solution), Ti (substrate) and TiO_2 were also detected. It could be concluded that CHAp formed, but it did not prevent the formation of TiO_2 . On the other hand, the characteristic peaks of $CaTiO_3$ are not visible, which may have been due to the fact that the $CaTiO_3$ layer was

coated with CHAp. The influence of Ti substrate modification on the formation of CHAp coatings was previously deeply investigated [19]. To achieve a better quality of CHAp coatings, Ti substrates were modified by adding a calcium titanate sublayer or additional preheating at 650 °C. One of the key advantages of the sol-gel technique is its capacity to produce homogeneous materials [24]. It is evident from the XRD results that the combined sol-gel and dissolution-precipitation reactions method also produces homogeneous CHAp coatings.

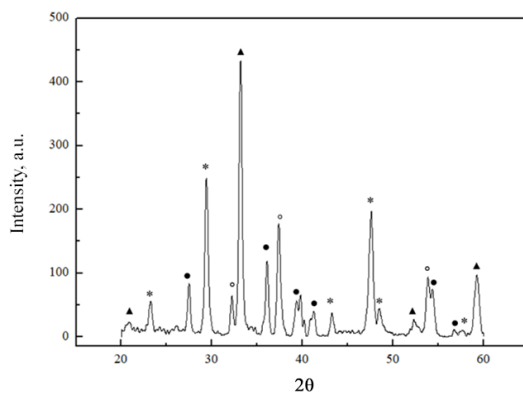


Figure 1. The XRD patterns of CaCO_3 coatings obtained by spin coating on a Ti substrate after 20 of spin-coating and thermal treatment procedures. Diffraction peaks: *— CaCO_3 (ICDD 01-086-2339), ▲— CaTiO_3 (ICDD 03-065-3287), ○— CaO (ICDD 01-082-1691), ●— TiO_2 (ICDD 01-083-2241).

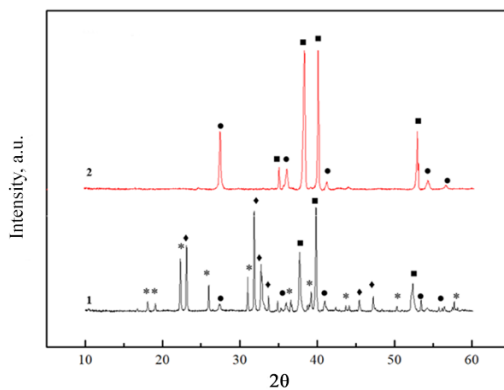


Figure 2. XRD patterns of CHAp coating obtained after immersion of CaCO_3 coating for 28 days in Na_2HPO_4 solution (1) and Ti substrate annealed at 600 °C (2). Diffraction reflections are marked: ◆—CHAp (ICDD 00-054-0022), *— Na_2HPO_4 (ICDD 01-076-2287), ■—Ti (ICDD 01-089-5009), ●— TiO_2 (ICDD 01-076-0318).

2.2. Raman and FTIR Spectroscopy

Raman spectra of the sol-gel-derived CaCO_3 coating and CHAp coating obtained following the dissolution-precipitation reaction are shown in Figure 3.

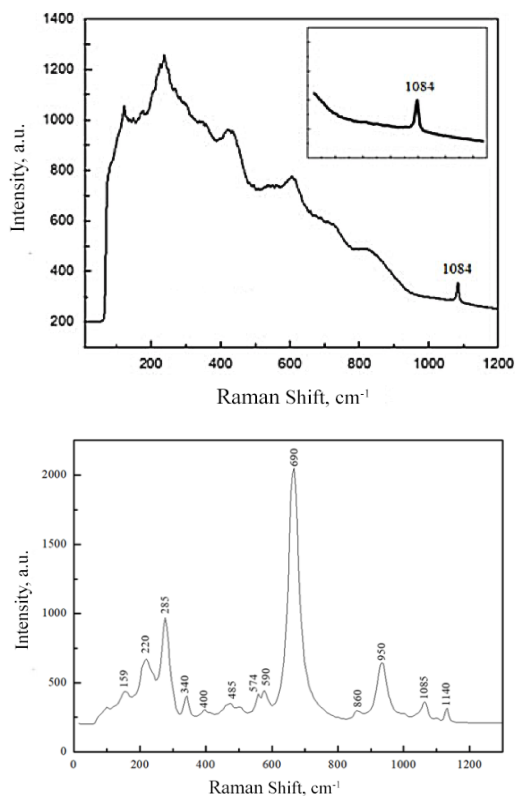


Figure 3. Raman spectra of CaCO_3 (top) and CHAp (bottom) coatings.

A high background is visible in the Raman spectrum of the CaCO_3 coating; however, the observed peak at 1084 cm^{-1} corresponds to the symmetric stretching of calcium carbonate [25]. In the Raman spectrum of the CHAp coating, the peaks of phosphate group vibrations at 400 , 574 , 590 , 950 and 1085 cm^{-1} are seen [25]. The peak at about 280 cm^{-1} is attributed to the Ca-PO_4 lattice. All this confirms that the CHAp coating was formed by the dissolution-precipitation process. The most intense peak observed, at 690 cm^{-1} , is ascribed to the Ti substrate. In addition, the peaks at 159 , 220 and 485 could be attributed to the TiO_2 phase [26]. The obtained results of Raman spectroscopy correlate well with the results of X-ray diffraction analysis.

Figure 4 demonstrates the FTIR spectra of synthesized coatings. The absorption bands observed at 1411 cm^{-1} and 879 cm^{-1} in the spectrum of the CaCO_3 coating can be assigned to the stretch vibrations of the carbonate ion [27,28]. The intense absorption band detected at $\sim 590\text{ cm}^{-1}$ is attributed to the vibration of Ti-O in titania.

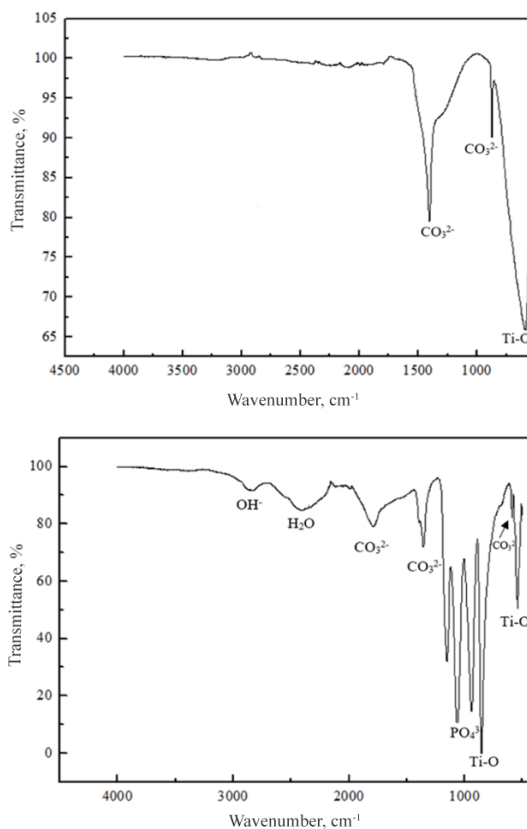
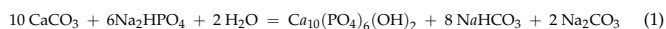


Figure 4. FTIR spectra of CaCO_3 (top) and CHAp (bottom) coatings.

The results deduced from the FTIR spectrum of the formed CHAp coating are in good agreement with the results of XRD and Raman spectroscopy, confirming the formation of intermediate (CaCO_3) and end products ($\text{Ca}_{10}(\text{PO}_4)_6(\text{OH})_2$):



According to the origin of observed absorption bands, the formation of carbonated hydroxyapatite ($\text{Ca}_{10-x}(\text{PO}_4)_{6-x}(\text{CO}_3)_x(\text{OH})_{2-x-2y}(\text{CO}_3)_y$) occurred during the dissolution-precipitation reaction [28,29].

2.3. Microscopical Characterization

Figure 5 shows the SEM micrographs of the formed CaCO_3 after spin-coating and thermal treatment procedures. The resulting porous surface was homogeneous with evenly distributed particles. The obtained SEM images confirm that CaCO_3 layers were formed and the Ti substrate was uniformly covered.

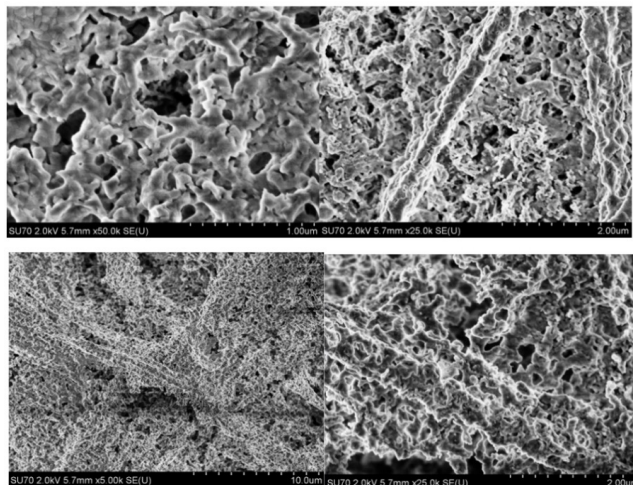


Figure 5. SEM micrographs of CaCO_3 coating obtained at different magnifications.

SEM micrographs of CHAp coatings after immersion of the CaCO_3 coating in Na_2HPO_4 solution are presented in Figure 6. It can be seen from the SEM micrographs obtained at lower magnification that dendritic clusters of CHAp and Na_2HPO_4 crystallites formed on the titanium surface. The surface of CHAp is rough and porous [30]. However, at higher magnification, the formation of homogeneously distributed plate-like crystals and spherical particles is seen. After annealing the obtained CHAp coating at $900\text{ }^\circ\text{C}$, the morphology of the crystals changed dramatically, with the formation of rods of $1\text{--}2\text{ }\mu\text{m}$ in length and $100\text{--}150\text{ nm}$ in width (see Figure 7). This is in good agreement with literature data [1,16].

The surface morphology of CHAp films was also studied with an optical 3D profilometer (see Figures 8 and 9). As seen from Figure 8, the surface roughness of the Ti substrate increased with the formation of the CaCO_3 coating. The results presented in Figure 9 show that the formed CHAp coatings were not evenly distributed on the Ti substrate. Moreover, the surface roughness observed for CHAp coatings was higher than that seen for the CaCO_3 coating. These results partially correlate with morphological features determined by SEM analysis. The surface roughness and average coating height were observed to increase slightly after annealing at $900\text{ }^\circ\text{C}$. The maximum roughness (7905 nm) and average height ($10,296\text{ nm}$) were determined for these coatings.

2.4. Electrochemical Characterization

In order to study the corrosion behaviour of fabricated coatings, first of all, the time dependences of the open-circuit potentials (E_{ocp}) of the samples were measured in Hanks' balanced salt solution (Figure 10).

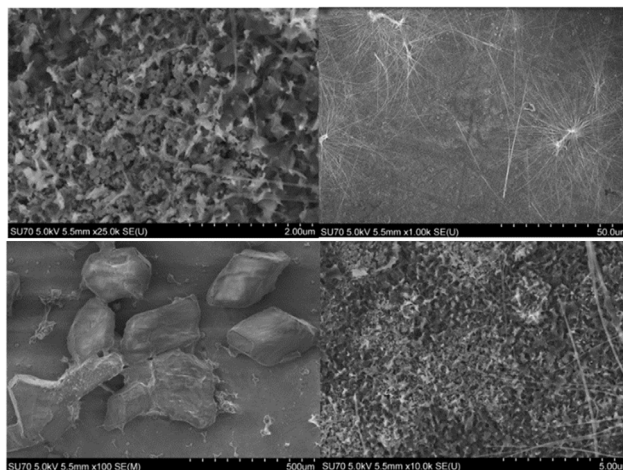


Figure 6. SEM micrographs of CHAp coating obtained at different magnifications.

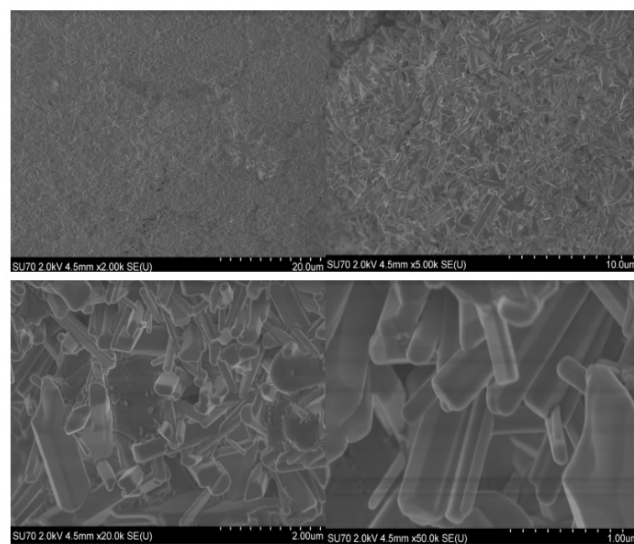


Figure 7. SEM micrographs of CHAp coating obtained after annealing at 900 °C.

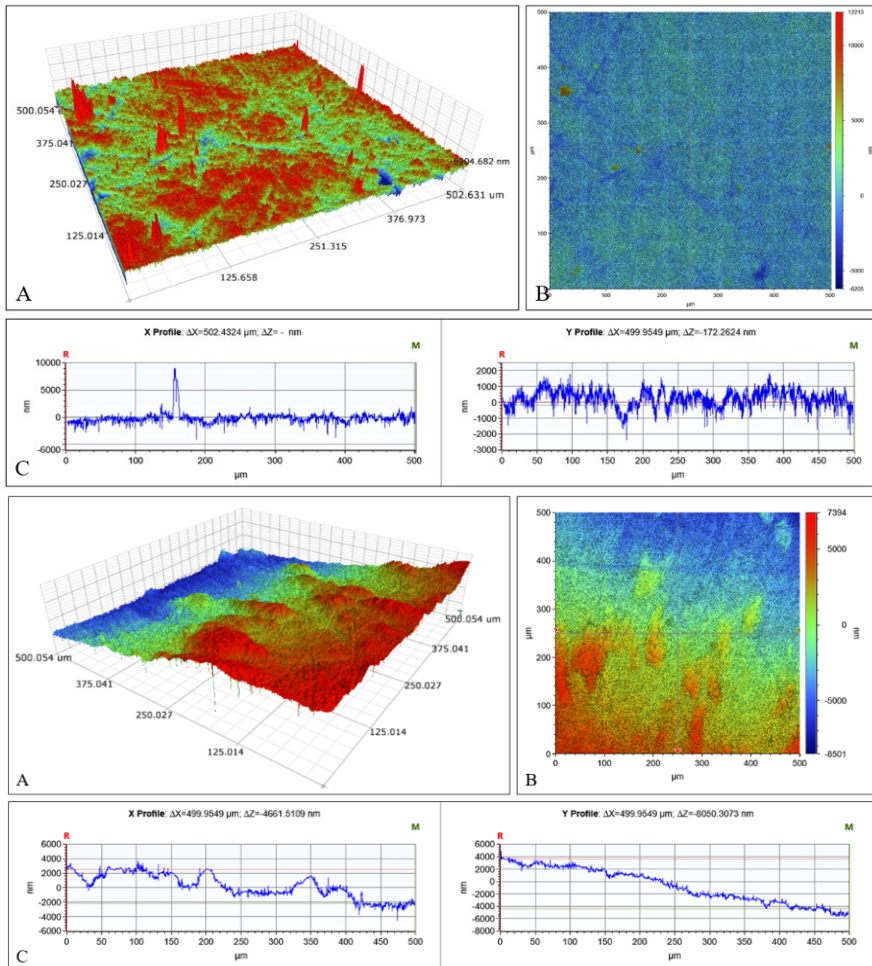


Figure 8. The results of optical 3D profilometry for Ti substrate (top) and CaCO₃ coating (bottom): optical 3D (A) and 2D contour (B) images and roughness (C) profiles.

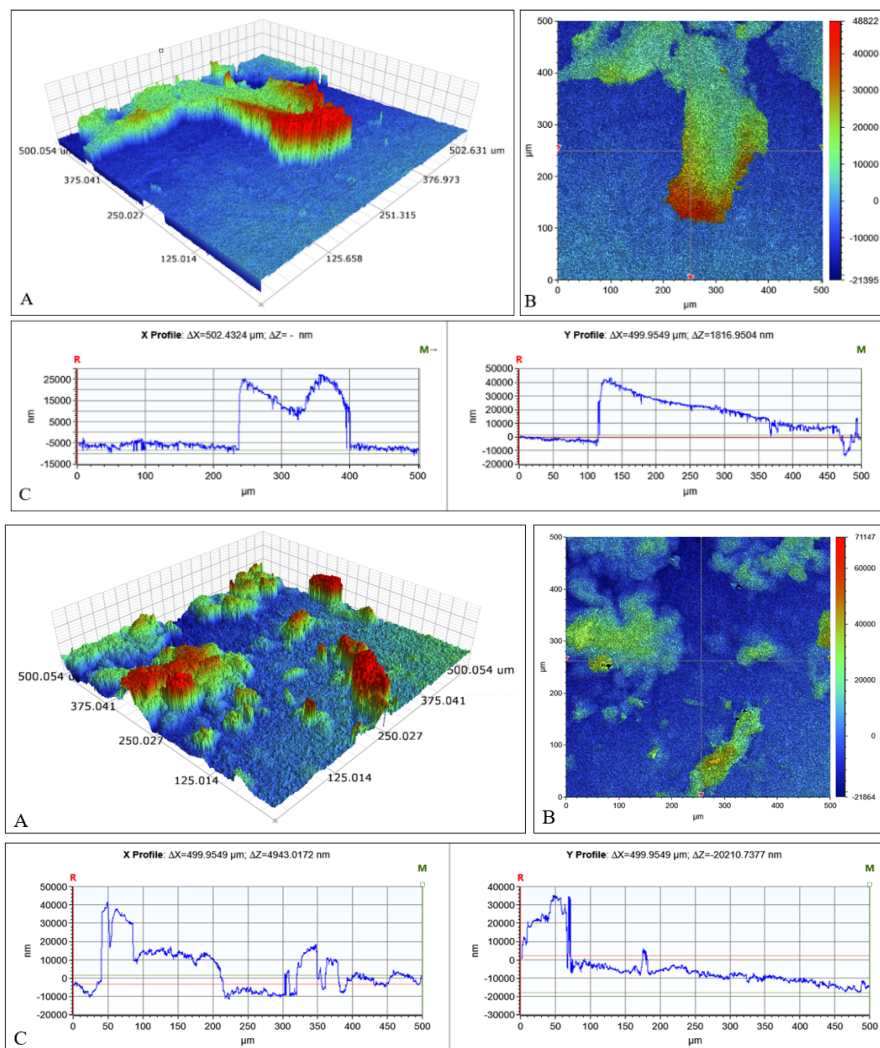


Figure 9. The results of optical 3D profilometry for the as-prepared CHAp coating (top) and that annealed at 900 °C (bottom): optical 3D (A) and 2D contour (B) images and roughness (C) profiles.

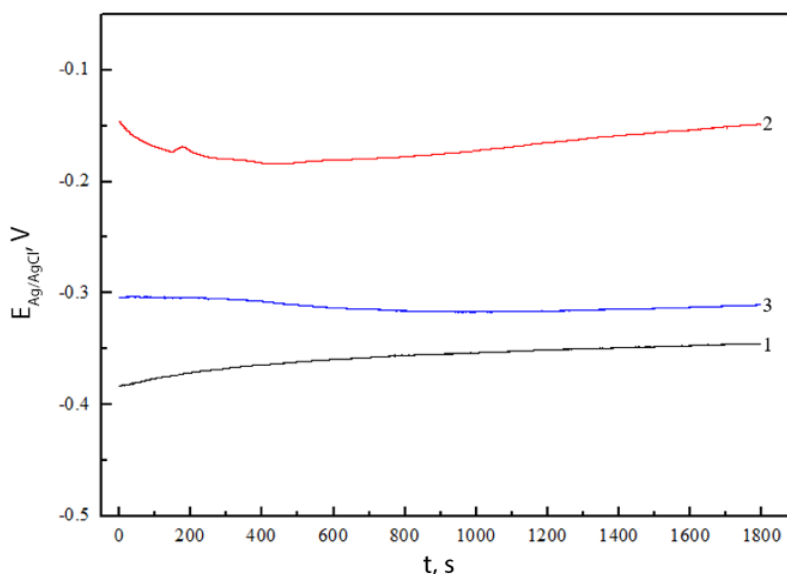


Figure 10. Exposure time dependences of the E_{ocp} potential of titanium/CHAp films in Hanks' solution: 1—annealed Ti substrate, 2—CHAp coating, 3—CHAp coating after annealing at 900 °C.

The open-circuit potential is a parameter that describes the relative corrosion stability of the sample in the solution. The stability of E_{ocp} shows that all the processes that determine its value are in a stationary state. The rates of spontaneous reactions have stabilized and the investigated electrode surface is stable. If E_{ocp} shifts to more positive values, it indicates a decrease in the corrosivity of the electrode, i.e., blocking of the surface by a passive layer. If E_{ocp} shifts to more negative potentials, it indicates that the investigated system is in the corrosion zone. As can be seen from Figure 10, the E_{ocp} value of the CHAp coating initially decreased to ~ -0.18 V, indicating that the corrosion activity increased, which is related to the formation of a protective layer of the formed CHAp coating. The E_{ocp} of the working electrode began to shift to more positive values after 7 min and reached a quasi-stationary value. In this case, a new passivation layer was formed on the surface of the tested electrode. The E_{ocp} of the annealed CHAp coating did not change much with increasing exposure time. It was observed that this coating reached a quasi-stationary value after ~ 6 min., and the passivation layer was formed quite quickly, which indicates the formation of stable coating. The E_{ocp} of the Ti substrate started to become positive in the initial stage of immersion, and the time-invariant value of the E_{ocp} settled after ~ 11 min. The difference in E_{ocp} values between the tested samples was negligible, indicating that the surface properties of formed CHAp coatings were similar.

The influence of the formed CHAp coating on the corrosion rate of the titanium in Hanks' balanced salt solution was evaluated using the Tafel dependences of the electrodes. The Tafel polarization curves were recorded when the E_{ocp} of the electrodes reached quasi-stationary values (Figure 11).

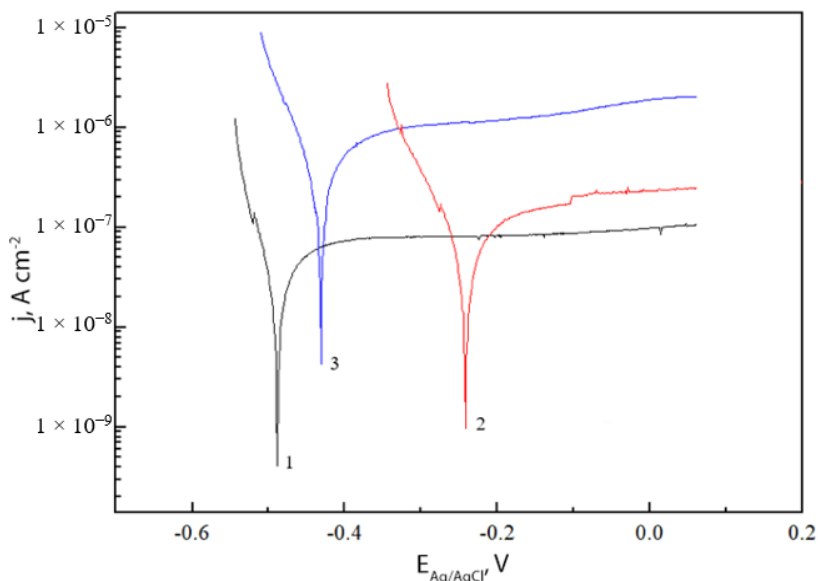


Figure 11. Tafel dependencies: 1—heated Ti substrate, 2—CHAp coating, 3—CHAp coating after annealing at 900 °C.

The corrosion rates (j_{corr}) were determined by extrapolation from linear ranges of cathodic and anodic Tafel dependencies. The determined corrosion rates are presented in Table 1.

Table 1. Corrosion parameters of the investigated coatings.

| Sample | b_c , V | b_a , V | j_{corr} , A·cm ⁻² |
|---------------------------------|-----------|-----------|--|
| Ti substrate | 0.0209 | 0.0163 | 2.27×10^{-8} |
| CHAp coating | 0.0302 | 0.0154 | 3.34×10^{-8} |
| CHAp coating annealed at 900 °C | 0.0420 | 0.0106 | 1.82×10^{-7} |

The polarization curves of the CHAp coating shifted towards more positive values, indicating a less active corrosion process. Table 1 also presents the tendencies of the cathodic (b_c) and anodic (b_a) Tafel dependencies of the tested samples. It can be seen that the CHAp coating was characterized by higher b_c values than the uncoated Ti substrate. The anodic tendency of the Tafel dependence of the obtained coatings decreased compared to that of the titanium substrate. The largest positive boost was determined for the as-prepared CHAp coating. Interestingly, the E_{ocp} of the post-annealed CHAp coating was lower. This may have been influenced by the porosity of the coating, which did not prevent the Hanks' balanced salt solution from contacting the metal and causing corrosion.

Evidently, these newly fabricated porous and sufficiently rough CHAp films can be successfully used not only as biomimetic nanotherapeutic coatings but also as electrochemical sensors [31], thermoluminescent sensors [32], or pH-sensitive fluorescent protein sensors [33]. The CHAp could be easily doped with lanthanide ions [34]. These nanostructures could be applied for the development of novel pH-responsive systems, which can determine the acidity of biofilms fluorometrically [35]. Finally, it is well known that pH is a critical indicator of bone physiological function and disease status. The suggested CHAp coatings fabricated at low temperatures could be applied for the development of

non-invasive and real-time sensing of bone pH in vivo [36]. Therefore, the application of our CHAp system as a bone pH sensor currently is under investigation.

3. Experimental

3.1. Materials and Synthesis

CHAp coatings were synthesized on a titanium substrate using a spin-coating technique from sol-gel-derived calcium carbonate following the dissolution-precipitation reaction at low temperatures. To prepare the Ca-O precursor solution, 20 mL of 2-propanol (C_3H_8O , 99.0%, Alfa Aesar, Haverhill, MA, USA) was mixed with 1.8 mL of acetylacetone ($C_5H_8O_2$, 99.9%, Merck, Roway, NJ, USA) at room temperature. A total of 1.1 g of calcium nitrate tetrahydrate ($Ca(NO_3)_2 \cdot 4H_2O$, 99.0%, Fluka, Buchs, Switzerland) was added to the resulting solution and stirred for 1 h. The resulting solution was mixed with PVA ($[-CH_2CHOH-]_n$, 99.5%, Aldrich, Burlington, MA, USA) at a ratio of 5:3 (v/v) [37]. The obtained Ca-O precursor solution was used for the synthesis of calcium carbonate coatings on the Ti substrate at 600 °C by the spin-coating technique. Finally, the synthesized $CaCO_3$ thin films were immersed in a 1 M Na_2HPO_4 solution for 28 days at 80 °C. A schematic diagram of the preparation of CHAp coatings is shown in Figure 12. The titanium substrates (Alfa Aesar, 1 mm titanium alloy sheet, 15 mm diameter, 0.5 mm thick discs and 10×10 mm squares) before the deposition of Ca-O precursor solution were carefully mechanically polished with 600-, 800- and 1200-grit sandpaper wet with ethanol-based oil (Struers, DP-Lubricant Brown, Cleveland, OH, USA). During the mechanical polishing of the surface, the oxide film formed in the air and surface defects were removed. The polished substrates were immersed in a 5 M NaOH solution and left at a temperature of 60 °C for 24 h. Before the deposition procedure, the substrates were washed with distilled water and dried at room temperature.

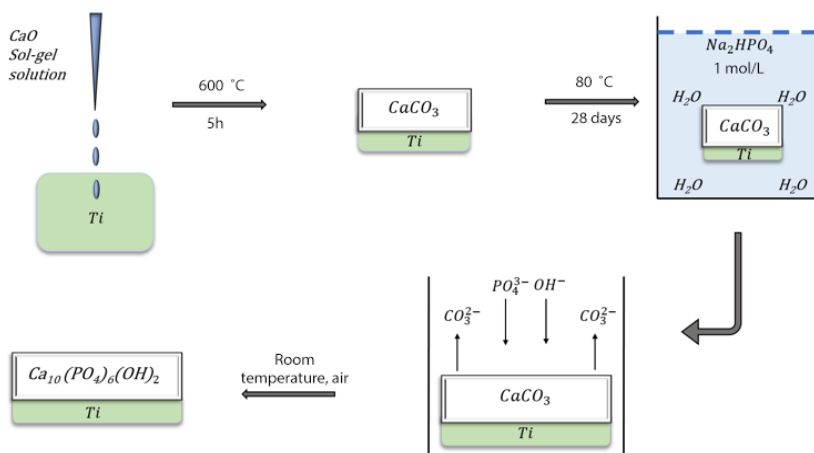


Figure 12. The schematic diagram of preparation of CHAp coatings on Ti substrate using low-temperature sol-gel and dissolution-precipitation methods.

During the spin-coating process, several drops of the precursor solution were placed onto the substrates and spin-coated for 30 s @ 3000 rpm (acceleration was 1000 rpm/s). After each spin-coating procedure, the samples were dried for 10 min in the oven at 200 °C. Finally, the samples were annealed for 5 h at 600 °C (with a heating rate of 5 °C/min.). Spin-coating and annealing procedures were repeated 10 and 20 times.

3.2. Characterization

To determine the phase purity of synthesized products, X-ray diffraction (XRD) measurements were performed with Rigaku miniFlex II or SmartLab (Rigaku) diffractometers using Cu K α 1 radiation. Raman spectroscopy studies were performed using a scanning near-field spectroscopy system with a Raman spectroscopy attachment (Alpha300R, WiTec, Ulm, Germany). Infrared spectra were obtained with an FTIR spectrophotometer Perkin Elmer Spectrum TWO with an ATR accessory. In order to study the morphology of the samples, a field-emission scanning electron microscope (FE-SEM) Hitachi SU-70 (FE-SEM, Hitachi, Tokyo, Japan) was used. Surface morphology images of coatings on titanium substrates were also obtained using an optical 3D profilometer Contour GT-K (Bruker, Billerica, MA, USA). This system works in non-contact mode using white-light and phase-shift interferometry. A 3D profilometer creates an electrical topographic image of the surface. The scanned area of the samples was 0.25 mm². Electrochemical measurements were performed using an electrochemical measurement system, Solartron 1280C (Ametek, Inc., Berwyn, PA, USA), and a three-electrode cell. The auxiliary electrode was a \sim 4 cm² platinum plate. A standard electrode of Ag/AgCl in a saturated KCl solution was used as the reference electrode, and a titanium pad was used as the working electrode. The working electrode was installed in a special window of the cell in such a way that only one side of the electrode was in contact with the solution and tightened through a silicone gasket. Contact with the coating was achieved through a Pt wire that was pressed against the electrode surface. The electrochemical cell was filled with Hanks' balanced salt solution (Sigma-Aldrich, St. Louis, MO, USA).

4. Conclusions

In this study, a low-temperature synthetic approach including sol-gel and dissolution-precipitation procedures was developed for the fabrication of calcium hydroxyapatite (CHAp) coatings on a titanium substrate. A spin-coating method was used for the formation of calcium carbonate layers from the Ca-O precursor solution. The final step of the synthesis of calcium carbonate coatings on the Ti substrate was performed at 600 °C. Finally, the synthesized CaCO₃ thin films were immersed in a 1 M Na₂HPO₄ solution for 28 days at 80 °C to obtain the CHAp phase. The structural properties, phase purity and morphology of the formed coatings were evaluated by X-ray diffraction analysis, FTIR and Raman spectroscopies, SEM and 3D optical profilometry. It was determined that CHAp with a small number of side phases formed on the titanium substrate. In the Raman and FTIR spectra, the characteristic CHAp absorption bands were observed. The CHAp surface formed on the Ti substrate was rough and porous with homogeneously distributed plate-like crystals and spherical particles. The results of the investigation of the surface morphology of CHAp films observed by optical 3D profilometer partially correlated with morphological features determined by SEM analysis. The corrosion behaviour of CHAp coatings in Hanks' solution was also evaluated. The CHAp coating increased the corrosion resistance of the titanium substrate. Additionally, the analysis of the corrosion behaviour and parameters of the electrochemical tests showed that the protective capacity of CHAp coatings obtained by the sol-gel and dissolution-precipitation methods was sufficiently high and increased after a CHAp coating of uniform thickness was formed. These CHAp thin films obtained by the suggested synthesis method may be potential candidates for use in the development of bone implants and different sensors for various analytes.

Author Contributions: Conceptualization, R.K. and A.K.; methodology, R.K.; software, A.Z.; formal analysis, G.B.; investigation, A.P., A.Z. and S.T.; data curation, A.P.; writing—original draft preparation, R.K.; writing—review and editing, A.K.; visualization, G.B.; supervision, A.K.; project administration, A.K.; funding acquisition, A.Z. All authors have read and agreed to the published version of the manuscript.

Funding: This project has received funding from European Social Fund (project No 09.3.3-LMT-K-712-19-0069) under grant agreement with the Research Council of Lithuania (LMTLT). Vilnius University is highly acknowledged for support from the Science Promotion Foundation (project no. MSF-JM-5/2021).

Data Availability Statement: Not applicable.

Conflicts of Interest: The authors declare no conflict of interest.

References



1. Ishikawa, K.; Garskaite, E.; Kareiva, A. Sol-gel synthesis of calcium phosphate-based biomaterials—A review of environmentally benign, simple, and effective synthesis routes. *J. Sol-Gel Sci. Technol.* **2020**, *94*, 551–572. [\[CrossRef\]](#)
2. Fox, K.; Tran, P.A.; Tran, N. Recent Advances in Research Applications of Nanophase Hydroxyapatite. *ChemPhysChem* **2012**, *13*, 2495–2506. [\[CrossRef\]](#) [\[PubMed\]](#)
3. Nayak, B.; Samant, A.; Misra, P.K.; Saxena, M. Nanocrystalline Hydroxyapatite: A Potent Material for Adsorption, Biological and Catalytic Studies. *Mater. Today Proc.* **2019**, *9*, 689–698. [\[CrossRef\]](#)
4. Desbord, M.; Soulie, J.; Rey, C.; Combes, C. Tunable Behavior in Solution of Amorphous Calcium Ortho/ Pyrophosphate Materials: An Acellular In Vitro Study. *ACS Biomater. Sci Eng.* **2022**, *8*, 2363–2374. [\[CrossRef\]](#) [\[PubMed\]](#)
5. Mahabole, M.P.; Aiyyer, R.C.; Ramakrishna, C.V.; Sreedhar, B.; Khairnar, R.S. Synthesis, characterization and gas sensing property of hydroxyapatite ceramic. *Bull. Mater. Sci.* **2005**, *28*, 535–545. [\[CrossRef\]](#)
6. Monkawa, A.; Ikoma, T.; Yunoki, S.; Yoshioka, T.; Tanaka, J.; Chakarov, D.; Kasemo, B. Fabrication of hydroxyapatite ultra-thin layer on gold surface and its application for quartz crystal microbalance technique. *Biomaterials* **2006**, *27*, 5748–5754. [\[CrossRef\]](#)
7. Petrucelli, G.C.; Kawachi, E.Y.; Kubota, L.T.; Bertran, C.A. Hydroxyapatite-based electrode: A new sensor for phosphate. *Anal. Commun.* **1996**, *33*, 227–229. [\[CrossRef\]](#)
8. Park, C.S.; Ha, T.H.; Kim, M.; Raja, N.; Yun, H.-S.; Sung, M.J.; Kwon, O.S.; Yoon, H.; Lee, C.-S. Fast and sensitive near-infrared fluorescent probes for ALP detection and 3d printed calcium phosphate scaffold imaging in vivo. *Biosens. Bioelectron.* **2018**, *105*, 151–158. [\[CrossRef\]](#)
9. Lahrach, S.; El Mhammedi, M.A. Review—Application of Deficient Apatites Materials in Electrochemical Detection of Heavy Metals: Case of Mercury (II) in Seawater and Fish Samples. *J. Electrochem. Soc.* **2019**, *166*, B1567–B1576. [\[CrossRef\]](#)
10. Casado, G.E.; Ivanchenko, P.; Paul, G.; Bisio, C.; Marchese, L.; Ashrafi, A.M.; Milosavljevic, V.; Degli Esposti, L.; Iafisco, M.; Mino, L. Surface and structural characterization of Cu-exchanged hydroxyapatites and their application in H₂O₂ electrocatalytic reduction. *Appl. Surf. Sci.* **2022**, *595*, 153495. [\[CrossRef\]](#)
11. Neacsu, I.A.; Arsenie, L.V.; Trusca, R.; Ardelean, I.L.; Mihailescu, N.; Mihailescu, I.N.; Ristoscu, C.; Bleotu, C.; Ficai, A.; Andronescu, E. Biomimetic Collagen/Zn²⁺-Substituted Calcium Phosphate Composite Coatings on Titanium Substrates as Prospective Bioactive Layer for Implants: A Comparative Study Spin Coating vs. MAPLE. *Nanomaterials* **2019**, *9*, 692. [\[CrossRef\]](#) [\[PubMed\]](#)
12. Singh, R.P.; Batra, U. Apatitic Nanopowders and Coatings: A Comprehensive Review. *Surf. Rev. Lett.* **2021**, *29*, 2230004. [\[CrossRef\]](#)
13. Puurunen, R.L. Surface chemistry of atomic layer deposition: A case study for the trimethylaluminum/water process. *J. Appl. Phys.* **2005**, *97*, 121301. [\[CrossRef\]](#)
14. Surmenev, R.A.; Surmeneva, M.A.; Grubova, I.Y.; Chernozem, R.V.; Krause, B.; Baumbach, T.; Loza, K.; Eppe, M. RF magnetron sputtering of a hydroxyapatite target: A comparison study on polytetrafluorethylene and titanium substrates. *Appl. Surf. Sci.* **2017**, *414*, 335–344. [\[CrossRef\]](#)
15. Mostafa, N.Y.; Kamel, M.M. Enhancement of adhesion bonding between titanium metal and electrodeposited calcium phosphate. *Surf. Eng. Appl. Electrochem.* **2016**, *52*, 520–523. [\[CrossRef\]](#)
16. Ishikawa, K.; Kareiva, A. Sol-gel synthesis of calcium phosphate-based coatings—A review. *CHEMIJA* **2020**, *31*, 25–41. [\[CrossRef\]](#)
17. Munir, M.U.; Salman, S.; Ihsan, A.; Elsamani, T. Synthesis, Characterization, Functionalization and Bio-Applications of Hydroxyapatite Nanomaterials: An Overview. *Int. J. Nanomed.* **2022**, *17*, 1903–1925. [\[CrossRef\]](#) [\[PubMed\]](#)
18. Chai, C.S.; Ben-Nissan, B. Bioactive nanocrystalline sol-gel hydroxyapatite coatings. *J. Mater. Sci. Mater. Electron.* **1999**, *30*, 465–469. [\[CrossRef\]](#)
19. Usinskas, P.; Stankeviciute, Z.; Beganskiene, A.; Kareiva, A. Sol-gel derived porous and hydrophilic calcium hydroxyapatite coating on modified titanium substrate. *Surf. Coatings Technol.* **2016**, *307*, 935–940. [\[CrossRef\]](#)
20. Ishikawa, K. Carbonate apatite bone replacement: Learn from the bone. *J. Ceram. Soc. Jpn.* **2019**, *127*, 595–601. [\[CrossRef\]](#)
21. Grigoraviciute-Puroniene, I.; Tanaka, Y.; Vegelyte, V.; Nishimoto, Y.; Ishikawa, K.; Kareiva, A. A novel synthetic approach to low-crystallinity calcium deficient hydroxyapatite. *Ceram. Int.* **2019**, *45*, 15620–15623. [\[CrossRef\]](#)
22. Sun, Y.; Wang, G.; Chen, X.; Li, W.; Umamoto, S.; Tajika, M.; Osaka, A. In vitro Assessment of Calcite-Hydroxyapatite Conversion of 3D-Printed Cube Honeycombs in Dilute Phosphate Solutions in the Neutral pH Range. *J. Mater. Res. Technol.* **2022**, in press. [\[CrossRef\]](#)
23. Lukong, V.T.; Ukoba, K.; Jen, T.-C. Review of self-cleaning TiO₂ thin films deposited with spin coating. *Int. J. Adv. Manuf. Technol.* **2022**, *122*, 3525–3546. [\[CrossRef\]](#)
24. Choi, G.; Choi, A.H.; Evans, L.A.; Akyol, S.; Ben-Nissan, B. A review: Recent advances in sol-gel-derived hydroxyapatite nanocoatings for clinical applications. *J. Am. Ceram. Soc.* **2020**, *103*, 5442–5453. [\[CrossRef\]](#)
25. Karalkeviciene, R.; Briedyte, G.; Murauskas, T.; Norkus, M.; Žarkov, A.; Yang, J.-C.; Kareiva, A. A novel method for the formation of bio ceramic nano-calcium hydroxyapatite coatings using sol-gel and dissolution-precipitation processing. *CHEMIJA* **2022**, *33*, 27–34. [\[CrossRef\]](#)
26. Pawlewicz, W.T.; Exarhos, G.J.; Conway, W.E. Structural characterization of TiO₂ optical coatings by Raman spectroscopy. *Appl. Opt.* **1983**, *22*, 1837–1840. [\[CrossRef\]](#)
27. Legodi, M.; de Waal, D.; Potgieter, J.; Potgieter, S. Rapid determination of CaCO₃ in mixtures utilising FT–IR spectroscopy. *Miner. Eng.* **2001**, *14*, 1107–1111. [\[CrossRef\]](#)

28. Grigoraviciute-Puroniene, I.; Stankeviciute, Z.; Ishikawa, K.; Kareiva, A. Formation of calcium hydroxyapatite with high concentration of homogeneously distributed silver. *Microporous Mesoporous Mater.* **2019**, *293*, 109806. [[CrossRef](#)]
29. Garskaite, E.; Gross, K.-A.; Yang, S.-W.; Yang, T.C.-K.; Yang, J.-C.; Kareiva, A. Effect of processing conditions on the crystallinity and structure of carbonated calcium hydroxyapatite (CHAp). *Crystengcomm* **2014**, *16*, 3950–3959. [[CrossRef](#)]
30. Nguyen, T.-L.; Tseng, C.-C.; Cheng, T.-C.; Nguyen, V.-T.; Chang, Y.-H. Formation and characterization of calcium phosphate ceramic coatings on Ti-6Al-4V alloy. *Mater. Today Commun.* **2022**, *31*, 103686. [[CrossRef](#)]
31. Gao, F.; Chen, X.; Tanaka, H.; Nishitani, A.; Wang, Q. Alkaline phosphatase mediated synthesis of carbon nanotube-hydroxyapatite nanocomposite and its application for electrochemical determination of luteolin. *Adv. Powder Technol.* **2016**, *27*, 921–928. [[CrossRef](#)]
32. Ortiz, S.L.; Lugo, V.R.; Salado-Leza, D.; Reyes-Valderrama, M.L.; Alcántara-Quintana, L.E.; González-Martínez, P.; Anaya, D.M. Dy₂O₃-unpurified hydroxyapatite: A promising thermoluminescent sensor and biomimetic nanotherapeutic. *Appl. Phys. A* **2021**, *127*, 893. [[CrossRef](#)]
33. Kollenda, S.; Kopp, M.; Wens, J.; Koch, J.; Schulze, N.; Papadopoulos, C.; Pöhler, R.; Meyer, H.; Eppler, M. A pH-sensitive fluorescent protein sensor to follow the pathway of calcium phosphate nanoparticles into cells. *Acta Biomater.* **2020**, *111*, 406–417. [[CrossRef](#)]
34. Prichodko, A.; Enrichi, F.; Stankeviciute, Z.; Benedetti, A.; Grigoraviciute-Puroniene, I.; Kareiva, A. Study of Eu³⁺ and Tm³⁺ substitution effects in sol-gel fabricated calcium hydroxyapatite. *J. Sol-Gel Sci. Technol.* **2016**, *81*, 261–267. [[CrossRef](#)]
35. Merkl, P.; Aschtgen, M.-S.; Henriques-Normark, B.; Sotiriou, G.A. Biofilm interfacial acidity evaluation by pH-Responsive luminescent nanoparticle films. *Biosens. Bioelectron.* **2021**, *171*, 112732. [[CrossRef](#)]
36. Li, Y.; Fu, Y.; Zhang, H.; Song, J.; Yang, S. FITC-Labeled Alendronate as an In Vivo Bone pH Sensor. *BioMed Res. Int.* **2020**, *2020*, 4012194. [[CrossRef](#)]
37. Zarkov, A.; Stanulis, A.; Sakaliuniene, J.; Butkute, S.; Abakeviciene, B.; Salkus, T.; Tautkus, S.; Orliukas, A.F.; Tamulevicius, S.; Kareiva, A. On the synthesis of yttria-stabilized zirconia: A comparative study. *J. Sol-Gel Sci. Technol.* **2015**, *76*, 309–319. [[CrossRef](#)]

Disclaimer/Publisher's Note: The statements, opinions and data contained in all publications are solely those of the individual author(s) and contributor(s) and not of MDPI and/or the editor(s). MDPI and/or the editor(s) disclaim responsibility for any injury to people or property resulting from any ideas, methods, instructions or products referred to in the content.

Article

Solvothermal Synthesis of Calcium-Deficient Hydroxyapatite via Hydrolysis of α -Tricalcium Phosphate in Different Aqueous-Organic Media

Rasa Karalkeviciene ¹, Eva Raudonyte-Svirbutaviciene ^{1,2}, Justina Gaidukevic ¹, Aleksej Zarkov ¹ 
and Aivaras Kareiva ^{1,*} 

¹ Institute of Chemistry, Faculty of Chemistry and Geosciences, Vilnius University, Naugarduko St. 24, LT-03225 Vilnius, Lithuania; rasa.karalkeviciene@nvspl.lt (R.K.); eva.raudonyte-svirbutaviciene@chgf.vu.lt (E.R.-S.); justina.gaidukevic@chgf.vu.lt (J.G.); aleksej.zarkov@chgf.vu.lt (A.Z.)

² Institute of Geology and Geography, Nature Research Centre, Akademijos Str. 2, LT-08412 Vilnius, Lithuania

* Correspondence: aivaras.kareiva@chgf.vu.lt

Abstract: In the present work, the effects of various organic solvents (solvent nature and fraction within the solution) and solvothermal conditions on the formation of calcium-deficient hydroxyapatite (CDHA) via hydrolysis of α -tricalcium phosphate (α -TCP) are investigated. The wet precipitation method is applied for α -TCP synthesis, and the hydrolysis reaction is performed in solutions with different water-to-organic solvent ratios under solvothermal conditions at 120 °C for 3 h and at 200 °C for 5 h. Ethyl alcohol, isopropyl alcohol, and butyl alcohol did not inhibit the hydrolysis of α -TCP, while methyl alcohol and ethylene glycol have a more prominent inhibitory effect on the hydrolysis, hence the formation of single-phased CDHA. From all the solvents analysed, ethylene glycol has the highest impact on the sample morphology. Under certain water to ethylene glycol ratios and solvothermal conditions, samples containing a significant fraction of rods are obtained. However, samples prepared with ethylene glycol are characterised by a particularly low BET surface area.

Keywords: calcium hydroxyapatite; α -tricalcium phosphate; water-organic solvent system; solvothermal synthesis



Citation: Karalkeviciene, R.; Raudonyte-Svirbutaviciene, E.; Gaidukevic, J.; Zarkov, A.; Kareiva, A. Solvothermal Synthesis of Calcium-Deficient Hydroxyapatite via Hydrolysis of α -Tricalcium Phosphate in Different Aqueous-Organic Media. *Crystals* **2022**, *12*, 253. <https://doi.org/10.3390/cryst12020253>

Academic Editor:
Carlos Rodriguez-Navarro

Received: 31 January 2022

Accepted: 11 February 2022

Published: 13 February 2022

Publisher's Note: MDPI stays neutral with regard to jurisdictional claims in published maps and institutional affiliations.



Copyright: © 2022 by the authors. Licensee MDPI, Basel, Switzerland. This article is an open access article distributed under the terms and conditions of the Creative Commons Attribution (CC BY) license (<https://creativecommons.org/licenses/by/4.0/>).

1. Introduction

Hydroxyapatite ($\text{Ca}_{10}(\text{PO}_4)_6(\text{OH})_2$, HAP) is a major inorganic component in human hard tissue and is one of the most investigated calcium phosphates (CaPs) [1–3]. Due to its bone-like chemical composition and crystalline structure, HAP is extensively applied as bioceramic material for bone grafting [4,5]. In addition to that, HAP has found applications in drug delivery [6], chromatography [7], and is a very promising material for the treatment of air, water, and soil pollution [8–11]. Since HAP is considered to be an environmentally benign functional material, and due to its remarkable adsorption capacity, HAP could be extremely useful in the field of environmental management [8]. Calcium-deficient hydroxyapatite (CDHA, $\text{Ca}_{10-x}(\text{HPO}_4)_x(\text{PO}_4)_{6-x}(\text{OH})_{2-x}$) is HAP with a Ca/P ratio from 1.50–1.67 [12]. Previous studies have reported a larger specific surface area and superior incorporating efficacy of CDHA when compared to other CaPs [13,14]. The chemical composition of HAP can be modified from the stoichiometric form to the Ca-deficient form by selecting an appropriate Ca/P molar ratio [15].

Solubility, specific surface area, surface wettability, and hence the adsorption characteristics of HAP crystals, depend greatly on their morphology and crystallinity [5,11]. Moreover, HAP contains the following two types of crystal planes: a (b)-plane, rich in positively charged Ca^{2+} ions, and a c-plane, exposing negatively charged phosphate and hydroxyl groups [10]. Hence, if the crystal growth along a specific direction is induced, HAP

could gain new desirable properties and be applied, for instance, as a selective adsorbent of negatively or positively charged compounds [9].

HAp could be obtained via different synthesis methods, including solid-state reactions, sol-gel technology, chemical precipitation, hydrolysis, hydrothermal, or solvothermal methods [2,16–18]. Among them, solvothermal synthesis is probably the most popular method, providing the possibility to obtain well-crystallized, single-phase HAp [1,19,20]. In addition to that, many groups have already reported the solvothermal synthesis of specifically shaped (plate-like and rod-like) HAp crystals using various additives in the reaction solution [1,20–22]. Several groups suggested that various alcohols could be successfully applied as HAp morphology-controlling agents during the solvothermal process. For instance, Goto et al. [16] has reported the synthesis of needle-like HAp crystals using ethyl alcohol-water solutions. Guo et al. [23] has observed that isopropyl alcohol has affected the crystallite size and crystallinity degree of the HAp crystals but had little effect on the sample morphology. However, as far as we know, no comprehensive study has ever been performed to compare the effects of different organic solvents on the hydrolysis of α -tricalcium phosphate (α -TCP) under solvothermal conditions. In this study, we aim to fill in this gap. To this end, solvothermal reactions were performed with different proportions of water-organic solvent. The organic solvents used were as follows: ethylene glycol, methyl alcohol, ethyl alcohol, isopropyl alcohol, and butyl alcohol. The effects of the solvothermal conditions, nature of the solvent, and organic solvent fraction in the solution on the phase purity and morphological features of HA were investigated.

2. Materials and Methods

2.1. Synthesis

First, metastable α -TCP was synthesized by wet precipitation method as a precursor for the further conversion to CDHA. An appropriate amount (3.42 g) of calcium nitrate tetrahydrate ($\text{Ca}(\text{NO}_3)_2 \cdot 4\text{H}_2\text{O}$, $\geq 99\%$, Roth, Karlsruhe, Germany) was dissolved in 20 ml of deionized water. A portion (1.27 g) of diammonium hydrogen phosphate ($(\text{NH}_4)_2\text{HPO}_4$, $\geq 98\%$, Roth, Karlsruhe, Germany) was dissolved in 15 ml of deionized water in a separate beaker. After dissolution, concentrated ammonium hydroxide (NH_4OH , 25%, Roth, Karlsruhe, Germany) was added to the latter solution until pH of the solution reached 10. After stirring for one minute, an aqueous solution of $\text{Ca}(\text{NO}_3)_2 \cdot 4\text{H}_2\text{O}$ was added rapidly. A white precipitate formed, which was stirred for 10 minutes at 400 rpm. The obtained precipitate was subsequently vacuum filtered and washed with an appropriate volume of deionized water and isopropyl alcohol [24]. The synthesis product was dried overnight in an oven at 50 °C. The dried powders were ground in agate mortar and annealed in a furnace at 700 °C for 5 h at a heating rate of 5 °C/min.

Solvothermal reactions were performed with different proportions of water and ethylene glycol (EG, $>99\%$, Roth, Karlsruhe, Germany), water-methyl alcohol (MeOH, $>99.9\%$, Roth, Karlsruhe, Germany), water-ethyl alcohol (EtOH, $>96\%$, Roth, Karlsruhe, Germany), water-isopropyl alcohol (PrOH, $>99.5\%$, Roth, Karlsruhe, Germany), and water-butyl alcohol (BuOH, $>99.5\%$, Roth, Karlsruhe, Germany). The water to alcohol v/v ratios of 0:100, 20:80, 40:60, 60:40, and 80:20 were applied. For the synthesis, 0.3 g of α -TCP powder was placed into 90 ml polytetrafluoroethylene-lined stainless-steel pressure vessels and diluted with 20 ml of water-organic solvent mixture. Solvothermal treatment was performed at 120 °C for 3 h and at 200 °C for 5 h. Finally, the resulting powders were filtered, washed with EtOH, and dried at 50 °C overnight.

The sample notations and treatment conditions are given in Table 1. Water to alcohol v/v ratios of 0:100, 20:80, 40:60, 60:40, and 80:20; 100:0 were applied to all the solvents under both conditions of solvothermal treatment.

Table 1. Sample codes, solvents applied, and solvothermal treatment conditions.

| Notation | Solvothermal Conditions | Organic Solvent Applied | Water-to-Organic Solvent (W:O) |
|------------|-------------------------|-------------------------|--------------------------------|
| 120-W-EG | 120 °C, 3 h | ethylene glycol | |
| 120-W-MeOH | 120 °C, 3 h | methyl alcohol | |
| 120-W-EtOH | 120 °C, 3 h | ethyl alcohol | 0:100 |
| 120-W-PrOH | 120 °C, 3 h | isopropyl alcohol | 20:80 |
| 120-W-BuOH | 120 °C, 3 h | butyl alcohol | 40:60 |
| 200-W-EG | 200 °C, 5 h | ethylene glycol | 60:40 |
| 200-W-MeOH | 200 °C, 5 h | methyl alcohol | 80:20 |
| 200-W-EtOH | 200 °C, 5 h | ethyl alcohol | 0:100 |
| 200-W-PrOH | 200 °C, 5 h | isopropyl alcohol | |
| 200-W-BuOH | 200 °C, 5 h | butyl alcohol | |

2.2. Characterization

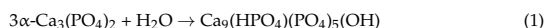
Powder X-ray diffraction data were collected on a Rigaku MiniFlex II diffractometer (Rigaku, The Woodlands, TX, USA) operating in Bragg–Brentano ($\theta/2\theta$) geometry, using Ni-filtered Cu K α radiation. The data were collected within a 2θ angle range from 10 to 60° at a step width of 0.01° and speed of 5°/min. Infrared (FTIR) spectra were recorded in the range of 4000–400 cm⁻¹ employing Bruker ALPHA ATR spectrometer (Bruker, Billerica, MA, USA). In order to study the morphology of the samples, a field-emission scanning electron microscope (FE-SEM) Hitachi SU-70 (FE-SEM, Hitachi, Tokyo, Japan) was used.

Textural properties of the prepared samples were estimated from N₂ adsorption/desorption isotherms at −196 °C using a Micromeritics TriStar 3020 analyser (Micromeritics, Norcross, GA, USA). Before the measurements, all the samples were outgassed in the N₂ atmosphere at 100 °C. The total surface area (S_{BET}) was estimated using the Brunauer–Emmet–Teller (BET) equation, while Barrett–Joyner–Halenda (BJH) equation was used to calculate pore size distribution of the samples [25].

3. Results and Discussion

The characteristics of the α -TCP precursor are presented in Figure 1. As it could be seen from the XRD diffraction pattern (Figure 1a), all the peaks match the standard XRD data of monoclinic Ca₃(PO₄)₂ (ICDD #00-070-0364) very well. The starting powders consisted of agglomerates of nanodimensional, mostly uniform elongated particles of irregular shape (Figure 1c). The sample exhibited type IV isotherms and displayed an H3 hysteresis loop (Figure 1b). Based on the pore size distribution results, illustrated in the inset image of Figure 1b, the sample was mainly characterised by pores smaller than 10 nm, albeit larger pores up to 55 nm were also present. The BET surface area (S_{BET}) of the precursor was 10.22 m² g⁻¹.

Under the reaction with water, α -TCP hydrolyses and converts to CDHA as described by the following equation [16]:



A sufficient amount of water is required for the first stage to occur. The phase crystallinity and purity of synthesized CDHA powders were investigated by XRD analysis, which revealed some differences among the obtained products. The samples treated with organic solvent only (0:100) showed no evidence of CDHA formation. Due to the absence of water, no hydrolysis reaction occurred, and the phase of such samples remained α -TCP (ICDD 00-070-0364). This was true for all the organic solvents used under different solvothermal treatments.

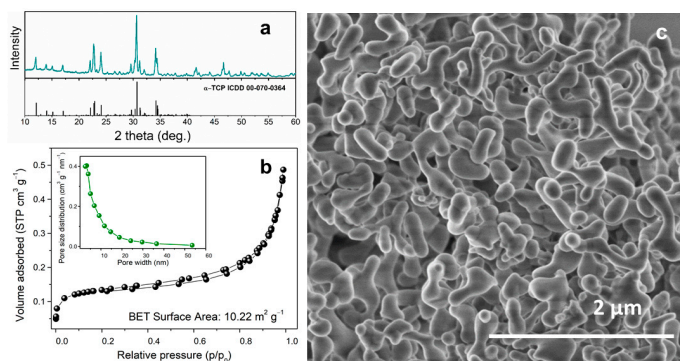


Figure 1. Characteristics of the obtained α -TCP precursor: XRD pattern (a), nitrogen adsorption-desorption isotherms and the corresponding BJH pore-size distribution (b), and SEM image (c).

In the case of EtOH, PrOH, and BuOH, the introduction of even a small fraction (20:80) of water resulted in the formation of single-phased CDHA (ICDD 00-76-0694), while an increasing water content provided the same results. This was observed under various applied solvothermal conditions. Under harsher solvothermal conditions (200 °C for 5 h), the formation of monetite was observed in the presence of EtOH, PrOH, and BuOH. This was especially notable in the case of BuOH. For comparison between the solvents, XRD patterns of the samples prepared under different solvothermal conditions using a W:O ratio of 40:60 are given in Figure 2 as representative.

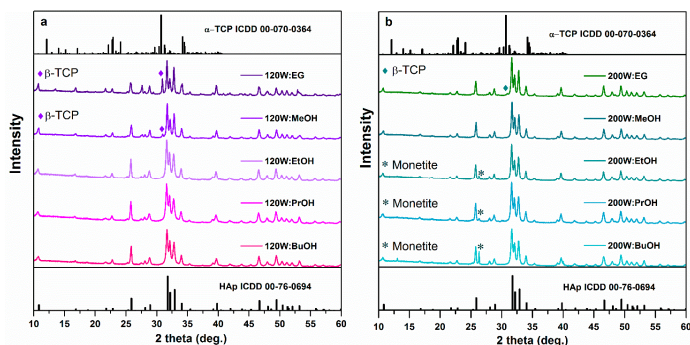


Figure 2. XRD patterns of the samples prepared using water-to-organic solvent ratio of 40:60 after a solvothermal treatment at 120 °C for 3 h (a) and at 200 °C for 5 h (b).

In contrast, MeOH and EG had a stronger inhibitory effect on α -TCP hydrolysis. These effects were especially notable for EG under the milder solvothermal conditions. Figure 3 shows the powder XRD patterns of the samples prepared under different solvothermal treatments (120 °C for 3 h and 200 °C for 5 h) using varying water to MeOH and water to EG ratios. After a treatment at 120 °C for 3 h, the sample with a water to EG ratio of 20:80 remained a single phase α -TCP (ICDD 00-070-0364, Figure 3b). Increasing water content induced the formation of CDHA, but a strong peak attributed to β -tricalcium

phosphate (β -TCP, ICDD 00-070-2065) was visible in the sample 120-W-EG-40:60, while only a trace of β -TCP could be observed in the XRD pattern of 120-W-EG-60:40 (Figure 3b). MeOH has also inhibited the formation of CDHA, albeit to a lesser extent. The sample 120-W-MeOH-20:80 contained large fractions of CDHA, β -TCP and α -TCP. Traces of β -TCP were detected in the sample 120-W-MeOH-40:60, while the samples with a larger amount of water consisted of single-phase CDHA (Figure 3a).

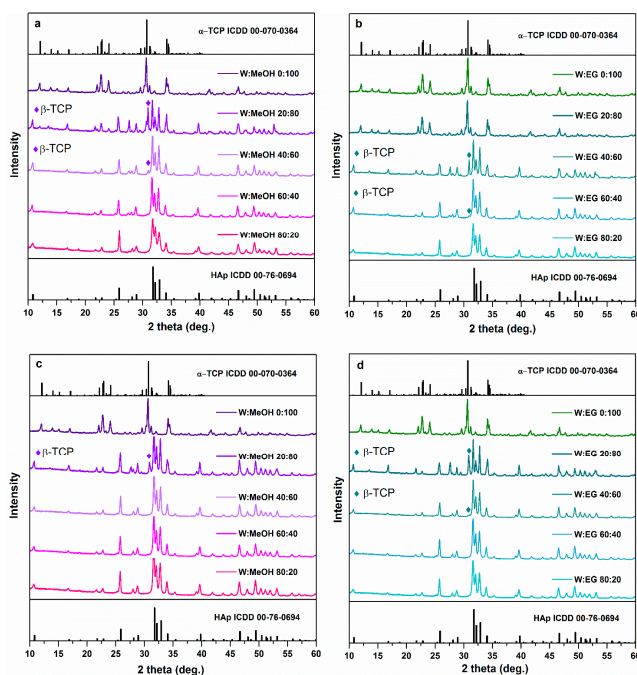


Figure 3. XRD patterns of the samples prepared using different water to MeOH (a,c) and water to EG (b,d) ratios under the following different solvothermal conditions: 120 °C for 3 h (a,b) and 200 °C for 5 h (c,d).

The increased temperature and prolonged time of the solvothermal synthesis caused the following shift in the inhibitory effect: single-phase CDHA was observed for the sample 200-W-EG-60:40, only a trace of β -TCP was detected in the XRD pattern of 200-W-EG-40:60, whereas the formation of CDHA was also obvious in 200-W-EG-20:80, even though a significant fraction of β -TCP was still present in the latter sample (Figure 3d). A higher temperature and longer reaction time have also resulted in a decreased β -TCP fraction in the sample 200-W-MeOH-20:80 (Figure 3c).

The FTIR spectra of the products prepared by the solvothermal treatment are presented in Figure 4. The FTIR range of 1500–400 cm^{-1} was chosen as representative since the main bands attributed to HAp and TCP polymorphs could be observed in this region, and the differences between the samples were hardly distinguishable in the full range spectra. The stretching modes of the hydroxyl group usually observed at 3572 cm^{-1}

were hardly visible in our case, and their intensity was similar in all the samples [26]. Several absorption bands at around 1095–960 and 636–550 cm^{-1} were observed in all the samples. The bands centred at 561–556 and 603–599 cm^{-1} are assigned to ν_4 O–P–O bending mode of CDHA [3]. Bands centred at 1020–1017 and 1090–1084 cm^{-1} correspond to ν_3 asymmetric P–O stretching vibrations, while the peak centred at 961–960 cm^{-1} corresponds to symmetric P–O stretching vibrations (ν_1) of CDHA [3]. The peak centred at 633–625 cm^{-1} corresponds to the bending vibrational mode of the hydroxyl (–OH) group [3,16]. An absorption band centred at 871–868 cm^{-1} is assigned to the P–O(H) stretching mode of the HPO_4^{2-} group, which is present in the structure of calcium-deficient CDHA [12]. The aforementioned bands were visible in the FTIR spectra of all the samples.

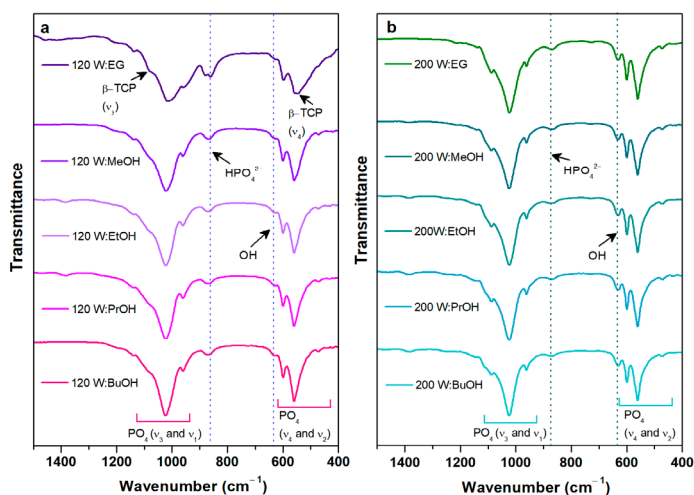


Figure 4. FTIR spectra of the samples prepared using water-to-organic solvent ratio of 40:60 after solvothermal treatment at 120 °C for 3 h (a) and at 200 °C for 5 h (b).

The additional bands attributed to β -TCP phase were only visible in the FTIR spectra of the samples prepared using larger fractions of EG (120-W-EG-20:80; 120-W-EG-40:60; 200-W-EG-20:80). As it could be seen from Figure 4a, bands at 544 and 1083 cm^{-1} of the sample 120-W-EG-40:60 could be attributed to β -TCP phase (ν_4 and ν_3 , respectively) [27]. Such results are in agreement with the XRD data.

The morphology of the obtained samples varied from plate-shaped to rod-shaped. Samples fabricated without organic solvents consisted of plate-shaped crystals arranged into flower-like structures. In this study, only slight effects on morphology were observed due to the introduction of EtOH and PrOH. Under the milder solvothermal conditions (120 °C for 3 h), large proportion of EtOH and PrOH (120-W-EtOH-20:80; 120-W-PrOH-20:80) caused the formation of large plates with no prominent self-assembly (Figures S2 and S3). With an increasing proportion of water (W:O 40:60; 60:40; and 80:20), the formation of narrower plates and some rods was observed; moreover, the crystals were arranged in flower-like structures. When the reaction time and temperature were increased, higher proportions of EtOH, PrOH, and BuOH resulted in the formation of rods. Moreover, more rods have formed at the same W:O ratio under harsher conditions. However, plate-like crystals were still prevalent in all of the samples. SEM images of the samples prepared under different solvothermal conditions using a W:O ratio of 40:60 are presented in Figure 5.

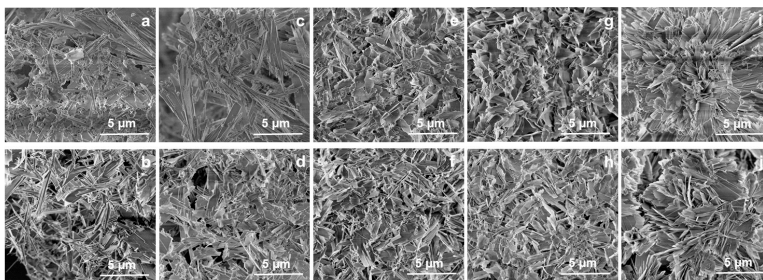


Figure 5. SEM images of the samples after solvothermal treatment with W:O ratio 40:60: (a) 120-W-EG-40:60; (b) 200-W-EG-40:60; (c) 120-W-MeOH-40:60; (d) 200-W-MeOH-40:60; (e) 120-W-EtOH-40:60; (f) 200-W-EtOH-40:60; (g) 120-W-PrOH-40:60; (h) 200-W-PrOH-40:60; (i) 120-W-BuOH-40:60; (j) 200-W-BuOH-40:60.

The use of MeOH (Figures 5c,d and S1) and BuOH (Figure 5i,j) had a more prominent effect on the sample morphology than the previously described solvents (Figures S3 and S4). In this case, the samples were also dominated by plate-like crystals, but a trend of long and narrow plate formation was observed. Moreover, more rods were present in the MeOH and BuOH treated samples when compared to the samples prepared in W-EtOH and W-PrOH solutions.

From all the solvents analysed, EG had the highest impact on the sample morphology. Under the milder solvothermal conditions (120 °C for 3 h), the formation of HAp was completely suspended in the sample 120-W-EG-20:80 (Figure 6c). Sample 120-W-EG-40:60 consisted of large plates, some rods, and some particles of different shapes, which could probably be attributed to β -TCP phase (Figure 6e). Sample 120-W-EG-60:40 was characterised by a large number of rods in addition to the plates (Figure 6g). In contrast, no rods were observed in a sample prepared with a minimal amount of EG (120-W-EG-80:20; Figure 6i). Prolonged reaction time and increased temperature resulted in a rod-dominated morphology of the CDHA samples. The sample 200-W-EG-20:80 was characterised by larger and smaller rods, as well as some minor particles of different shapes, which should be attributed to β -TCP phase (Figure 6d). A slightly lower proportion of EG (samples 200-W-EG-40:60 and 200-W-EG-60:40; Figure 6f,h) resulted in the formation of both plate-shaped and a large number of rod-shaped crystals. No rods were observed in a sample prepared with a minimal amount of EG (200-W-EG-80:20; Figure 6j).

It is assumed that the solvothermally assisted formation of rod-like crystals comprises the following two main stages: the nucleation step (reaction of ions), when small crystalline nuclei are formed in a supersaturated matrix, and the growth step, during which nuclei grow into their final shape and size [28]. In our case, the changes in crystal morphology might be related to the decreased supply of water when more organic solvents are introduced to the system. This would limit the hydrolysis reaction of α -TCP [16]. Previous studies stated that the increasing amount of alcohol in the aqueous reaction solution reduces the solubility of α -TCP and hence limits the supply of Ca^{2+} and PO_4^{3-} ions [16,29,30]. Such an effect is related to the changes in dielectric constant ($\epsilon_r(\omega)$) of the solution: with a decreasing dielectric constant of the solvent, solubility decreases due to the decreased solvation energy [31,32]. Dielectric constant of pure water is 78.5 at 25 °C, whereas the dielectric constants of alcohols are significantly lower. The dielectric constants at 25 °C of the organic solvents used in this study are as follows: $\epsilon_r(\omega)_{\text{EG}} = 38.5$; $\epsilon_r(\omega)_{\text{MeOH}} = 32.70$; $\epsilon_r(\omega)_{\text{EtOH}} = 24.3$; $\epsilon_r(\omega)_{\text{PrOH}} = 19.92$; $\epsilon_r(\omega)_{\text{BuOH}} = 17.5$ [32]. Variations in $\epsilon_r(\omega)$ of water-organic solvent mixtures depend on the composition of the solution, but in general, $\epsilon_r(\omega)$ values decrease with the increasing fraction of organic solvent [33]. Solvents with different

physicochemical properties influence solubility, crystal nucleation, and growth rate, which in turn has an effect on the crystallinity and morphology of the final products [32]. When the hydrolysis reaction is not suspended and the solution is supersaturated with Ca^{2+} and PO_4^{3-} ions, nucleation takes dominance over the crystal growth and smaller crystals are formed. On the contrary, when the supply of Ca^{2+} and PO_4^{3-} ions is limited, fewer nuclei form and larger crystals tend to grow [28,32]. Other properties of different solvents might have also affected the processes of α -TCP hydrolysis and HAp crystallisation. For instance, the presence of EG in the reaction mixture would significantly change the viscosity of the suspension [34,35]. Subsequently, ion mobility and diffusion rates would be reduced, which would in turn inhibit the hydrolysis reaction and retard the nucleation process [35]. The viscosity of the reaction media decreases with the increasing temperature, and thus the inhibitory effects of EG are less significant when the solvothermal synthesis is performed at higher temperatures (Figure 3b,d).

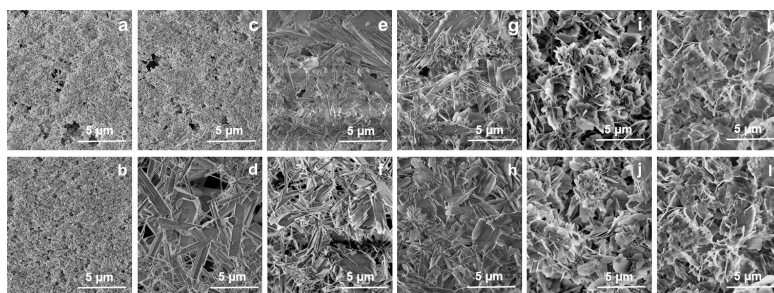


Figure 6. SEM images of the samples prepared with different ratios of water and ethylene glycol: (a) 120-W-EG-0:100; (b) 200-W-EG-0:100; (c) 120-W-EG-20:80; (d) 200-W-EG-20:80; (e) 120-W-EG-40:60; (f) 200-W-EG-40:60; (g) 120-W-EG-60:40; (h) 200-W-EG-60:40; (i) 120-W-EG-80:20; (j) 200-W-EG-80:20; (k) 120-W-EG-100:0; (l) 200-W-EG-100:0.

It is worth noting that the results obtained in this study differ from those reported by Goto et al. [16], who managed to prepare needle-like CDHA crystals arranged into flower-like structures by using water-ethyl alcohol solutions. We assume such discrepancies could originate due to the different starting materials used and slightly different solvothermal conditions applied. In their study, Goto et al. applied commercial α -TCP (Taihei Chemical Industrial Co., Ltd., Osaka, Japan) synthesized at a high temperature and consisting of large particles, while in our study we used low-temperature synthesized metastable α -TCP.

Figure 7 shows the nitrogen adsorption-desorption isotherms and the corresponding BJH pore-size distribution for CDHA particles. According to the new classification by the IUPAC, all the samples exhibited type IV isotherms and displayed H3 hysteresis loops. This type of isotherm indicates the existence of mesopores in the structure of all the samples. The hysteresis loop type H3 is associated with the existence of aggregated plate-like particles [36]. Such results are in agreement with SEM data (Figures 5 and 6). Based on the pore size distribution results illustrated in the inset image of Figure 7a,b, there were no significant differences between the samples. All the samples were characterised by a wide pore size distribution. Multi-scale pores ranged from 2.6 to 128 nm, suggesting that both mesopores and macropores were present in the CDHA structure. All the samples except those prepared with EG contained both mesopores of smaller sizes (from 2.6 nm up to 9.0 nm) and a small number of larger mesopores (from 9.0 nm up to 128 nm). On the contrary, in the sample 120-W-EG-40:60, mainly mesopores of larger width (from 23.0 nm up to 50.2 nm) were found. We assume the pores of smaller sizes presented in the structure of this sample were probably partially blocked by the viscous ethylene glycol. As it can be

seen from Figure 7c, the mesoporous 120-W-PrOH-40:60 had the highest BET surface area (S_{BET}) of $24.3 \text{ m}^2 \text{ g}^{-1}$. An extremely low surface area was observed for the samples prepared using EG: S_{BET} of $2.1 \text{ m}^2 \text{ g}^{-1}$ and $11.3 \text{ m}^2 \text{ g}^{-1}$ were obtained for the samples 120-W-EG-40:60 and 200-W-EG-40:60, respectively. One reasonable explanation for this decrease is that residues of EG may have increased blockage of the nitrogen gas penetration. Moreover, this decrease in S_{BET} could be the result of the structural changes occurring during the synthesis of CDHA. The remaining samples were characterised by similar S_{BET} values ranging from 9.9 to $22.4 \text{ m}^2 \text{ g}^{-1}$.

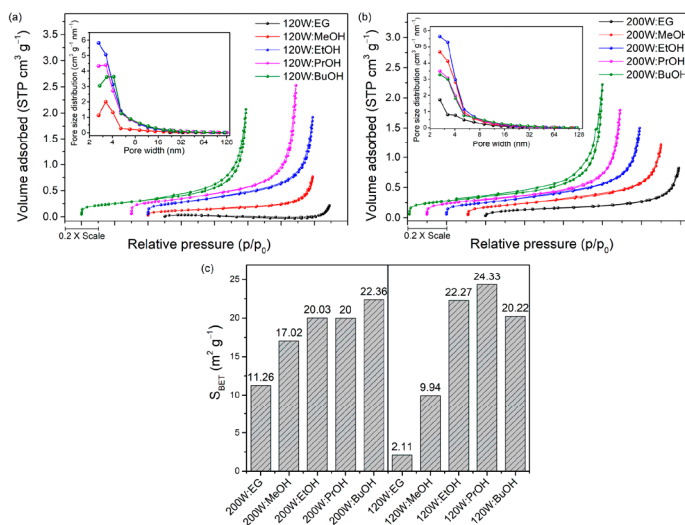


Figure 7. Nitrogen adsorption-desorption isotherms and the corresponding BJH pore-size distribution for the samples after solvothermal treatment with a W:O ratio of 40:60: (a) 120 °C; (b) 200 °C; and (c) BET surface area for the samples after solvothermal treatment with a W:O ratio of 40:60 at 120 °C and 200 °C.

4. Conclusions

A comprehensive study was performed to compare the effects of different organic solvents on the hydrolysis of α -TCP and its conversion to CDHA under different solvothermal conditions. Methyl alcohol and ethylene glycol had a stronger inhibitory effect on α -TCP hydrolysis than ethyl alcohol, isopropyl alcohol, and butyl alcohol. This was especially notable under milder solvothermal conditions. The morphology of the obtained samples varied from plate-shaped to rod-shaped. Samples containing some rods were obtained by applying certain ethyl alcohol and isopropyl alcohol proportions, albeit plate-like structures were still prevailing. The use of water-methyl alcohol and water-butyl alcohol mixtures leads to the formation of more rods in addition to the long and narrow plates. From all the solvents analysed, ethylene glycol had the highest impact on the sample morphology. Under certain water to ethylene glycol ratios and solvothermal conditions, samples containing a significant fraction of rods were obtained.

Supplemental Materials: The following supporting information can be downloaded at: <https://www.mdpi.com/article/10.3390/cryst12020253/s1>, Figure S1: images of the samples after solvothermal treatment with W-MeOH; Figure S2: SEM images of the samples after solvothermal treatment with W-EtOH; Figure S3: SEM images of the samples after solvothermal treatment with W-PrOH; Figure S4: SEM images of the samples after solvothermal treatment with W-BuOH.

Author Contributions: Conceptualization, R.K., E.R.-S., J.G., A.Z. and A.K.; methodology, R.K., E.R.-S. and A.Z.; formal analysis, R.K.; investigation, R.K. and J.G.; resources, E.R.-S., A.Z. and A.K.; data curation, R.K., E.R.-S., J.G., A.Z. and A.K.; writing—original draft preparation, E.R.-S.; writing—review and editing, R.K., E.R.-S., J.G., A.Z. and A.K.; supervision, A.Z. and A.K.; funding acquisition, E.R.-S., A.Z. and A.K. All authors have read and agreed to the published version of the manuscript.

Funding: This research has received funding by the European Social Fund under the No 09.3.3-LMT-K-712 “Development of Competences of Scientists, other Researchers and Students through Practical Research Activities” measure (project No 09.3.3-LMT-K-712-23-0070).

Data Availability Statement: Data is contained within the article.

Conflicts of Interest: The authors declare no conflict of interest.





References

1. In, Y.; Amornkitbamrung, U.; Hong, M.H.; Shin, H. On the Crystallization of Hydroxyapatite under Hydrothermal Conditions: Role of Sebacic Acid as an Additive. *ACS Omega* **2020**, *5*, 27204–27210. [[CrossRef](#)] [[PubMed](#)]
2. Cüneyt Tas, A. Synthesis of biomimetic Ca-hydroxyapatite powders at 37 °C in synthetic body fluids. *Biomaterials* **2000**, *21*, 1429–1438. [[CrossRef](#)]
3. Gopi, D.; Shinyjoy, E.; Karthika, A.; Nithiya, S.; Kavitha, L.; Rajeswari, D.; Tang, T. Single walled carbon nanotubes reinforced mineralized hydroxyapatite composite coatings on titanium for improved biocompatible implant applications. *RSC Adv.* **2015**, *5*, 36766–36778. [[CrossRef](#)]
4. Šupová, M. Problem of hydroxyapatite dispersion in polymer matrices: A review. *J. Mater. Sci. Mater. Med.* **2009**, *20*, 1201–1213. [[CrossRef](#)] [[PubMed](#)]
5. Zhuang, Z.; Fujimi, T.J.; Nakamura, M.; Konishi, T.; Yoshimura, H.; Aizawa, M. Development of a,b-plane-oriented hydroxyapatite ceramics as models for living bones and their cell adhesion behavior. *Acta Biomater.* **2013**, *9*, 6732–6740. [[CrossRef](#)] [[PubMed](#)]
6. Melde, B.J.; Stein, A. Periodic Macroporous Hydroxyapatite-Containing Calcium Phosphates. *Chem. Mater.* **2002**, *14*, 3326–3331. [[CrossRef](#)]
7. Bernardi, G. Chromatography of Nucleic Acids on Hydroxyapatite. *Nature* **1965**, *206*, 779–783. [[CrossRef](#)]
8. Zhao, J.; Hu, Q.; Lei, Y.; Gao, C.; Zhang, P.; Zhou, B.; Zhang, G.; Song, W.; Lou, X.; Zhou, X. Facile synthesis of ultralong hydroxyapatite nanowires using wormlike micelles as soft templates. *CrystEngComm* **2021**, *23*, 5498–5503. [[CrossRef](#)]
9. Foroutan, R.; Peighambaroust, S.J.; Aghdasinia, H.; Mohammadi, R.; Ramavandi, B. Modification of bio-hydroxyapatite generated from waste poultry bone with MgO for purifying methyl violet-laden liquids. *Environ. Sci. Pollut. Res.* **2020**, *27*, 44218–44229. [[CrossRef](#)]
10. Ibrahim, M.; Labaki, M.; Giraudon, J.M.; Lamonié, J.F. Hydroxyapatite, a multifunctional material for air, water and soil pollution control: A review. *J. Hazard. Mater.* **2020**, *383*, 121139. [[CrossRef](#)]
11. Hao, L.; Lv, Y.; Song, H. The morphological evolution of hydroxyapatite on high-efficiency Pb²⁺ removal and antibacterial activity. *Microchem. J.* **2017**, *135*, 16–25. [[CrossRef](#)]
12. Sinusaite, L.; Popov, A.; Raudonyte-Svirbutaviciene, E.; Yang, J.-C.; Kareiva, A.; Zarkov, A. Effect of Mn doping on hydrolysis of low-temperature synthesized metastable alpha-tricalcium phosphate. *Ceram. Int.* **2021**, *47*, 12078–12083. [[CrossRef](#)]
13. Deng, Y.; Liu, M.; Chen, X.; Wang, M.; Li, X.; Xiao, Y.; Zhang, X. Enhanced osteoinductivity of porous biphasic calcium phosphate ceramic beads with high content of strontium-incorporated calcium-deficient hydroxyapatite. *J. Mater. Chem. B* **2018**, *6*, 6572–6584. [[CrossRef](#)] [[PubMed](#)]
14. Ravi, N.D.; Balu, R.; Sampath Kumar, T.S. Strontium-Substituted Calcium Deficient Hydroxyapatite Nanoparticles: Synthesis, Characterization, and Antibacterial Properties. *J. Am. Ceram. Soc.* **2012**, *95*, 2700–2708. [[CrossRef](#)]
15. Sekine, Y.; Motokawa, R.; Kozai, N.; Ohnuki, T.; Matsumura, D.; Tsuji, T.; Kawasaki, R.; Akiyoshi, K. Calcium-deficient Hydroxyapatite as a Potential Sorbent for Strontium. *Sci. Rep.* **2017**, *7*, 2064. [[CrossRef](#)]
16. Goto, T.; Kim, I.Y.; Kikuta, K.; Ohtsuki, C. Hydroxyapatite formation by solvothermal treatment of α -tricalcium phosphate with water-ethanol solution. *Ceram. Int.* **2012**, *38*, 1003–1010. [[CrossRef](#)]
17. Kaviyarasu, K.; Mariappan, A.; Neyvasagam, K.; Ayeshamariam, A.; Pandi, P.; Palanichamy, R.R.; Gopinathan, C.; Mola, G.T.; Maaza, M. Photocatalytic performance and antimicrobial activities of HAP-TiO₂ nanocomposite thin films by sol-gel method. *Surf. Interfaces* **2017**, *6*, 247–255. [[CrossRef](#)]

18. Teshima, K.; Lee, S.; Sakurai, M.; Kamenno, Y.; Yubuta, K.; Suzuki, T.; Shishido, T.; Endo, M.; Oishi, S. Well-Formed One-Dimensional Hydroxyapatite Crystals Grown by an Environmentally Friendly Flux Method. *Cryst. Growth Des.* **2009**, *9*, 2937–2940. [[CrossRef](#)]
19. Suchanek, K.; Bartkowiak, A.; Perzanowski, M.; Marszałek, M. From monetite plate to hydroxyapatite nanofibers by monoethanolamine assisted hydrothermal approach. *Sci. Rep.* **2018**, *8*, 15408. [[CrossRef](#)]
20. Tomozawa, M.; Hiromoto, S. Microstructure of hydroxyapatite- and octacalcium phosphate-coatings formed on magnesium by a hydrothermal treatment at various pH values. *Acta Mater.* **2011**, *59*, 355–363. [[CrossRef](#)]
21. Wang, Y.-c.; Wang, J.-n.; Xiao, G.-y.; Huang, S.-y.; Xu, W.-l.; Yan, W.-x.; Lu, Y.-p. Investigation of various fatty acid surfactants on the microstructure of flexible hydroxyapatite nanofibers. *CrystEngComm* **2021**, *23*, 7049–7055. [[CrossRef](#)]
22. Horiuchi, N.; Shibata, K.; Saito, H.; Iwabuchi, Y.; Wada, N.; Nozaki, K.; Hashimoto, K.; Tanaka, Y.; Nagai, A.; Yamashita, K. Size Control Synthesis of Hydroxyapatite Plates and Their Application in the Preparation of Highly Oriented Films. *Cryst. Growth Des.* **2018**, *18*, 5038–5044. [[CrossRef](#)]
23. Guo, X.; Xiao, P. Effects of solvents on properties of nanocrystalline hydroxyapatite produced from hydrothermal process. *J. Eur. Ceram. Soc.* **2006**, *26*, 3383–3391. [[CrossRef](#)]
24. Sinusaite, L.; Grigoravičiute-Puroniene, I.; Popov, A.; Ishikawa, K.; Kareiva, A.; Zarkov, A. Controllable synthesis of tricalcium phosphate (TCP) polymorphs by wet precipitation: Effect of washing procedure. *Ceram. Int.* **2019**, *45*, 12423–12428. [[CrossRef](#)]
25. Brunauer, S.; Emmett, P.H.; Teller, E. Adsorption of Gases in Multimolecular Layers. *J. Am. Chem. Soc.* **1938**, *60*, 309–319. [[CrossRef](#)]
26. Bogdanovicene, I.; Beganskiene, A.; Tõnsuaadu, K.; Glaser, J.; Meyer, H.J.; Kareiva, A. Calcium hydroxyapatite, Ca₁₀(PO₄)₆(OH)₂ ceramics prepared by aqueous sol–gel processing. *Mater. Res. Bull.* **2006**, *41*, 1754–1762. [[CrossRef](#)]
27. Carrodegua, R.G.; De Aza, S. α -Tricalcium phosphate: Synthesis, properties and biomedical applications. *Acta Biomater.* **2011**, *7*, 3536–3546. [[CrossRef](#)]
28. Sadat-Shojai, M.; Khorasani, M.-T.; Dinpanah-Khoshdargi, E.; Jamshidi, A. Synthesis methods for nanosized hydroxyapatite with diverse structures. *Acta Biomater.* **2013**, *9*, 7591–7621. [[CrossRef](#)]
29. Larsen, M.J.; Thorsen, A.; Jensen, S.J. Ethanol-induced formation of solid calcium phosphates. *Calcif. Tissue Int.* **1985**, *37*, 189–193. [[CrossRef](#)]
30. Lerner, E.; Azoury, R.; Sarig, S. Rapid precipitation of apatite from ethanol-water solution. *J. Cryst. Growth* **1989**, *97*, 725–730. [[CrossRef](#)]
31. Termine, J.D.; Peckauskas, R.A.; Posner, A.S. Calcium phosphate formation in vitro: II. Effects of environment on amorphous-crystalline transformation. *Arch. Biochem. Biophys.* **1970**, *140*, 318–325. [[CrossRef](#)]
32. Wu, J.; Lü, X.; Zhang, L.; Huang, F.; Xu, F. Dielectric Constant Controlled Solvothermal Synthesis of a TiO₂ Photocatalyst with Tunable Crystallinity: A Strategy for Solvent Selection. *Eur. J. Inorg. Chem.* **2009**, *2009*, 2789–2795. [[CrossRef](#)]
33. Wyman, J. The dielectric constant of mixtures of ethyl alcohol and water from -5 TO 40°. *J. Am. Chem. Soc.* **1931**, *53*, 3292–3301. [[CrossRef](#)]
34. Bohne, D.; Fischer, S.; Obermeier, E. Thermal, Conductivity, Density, Viscosity, and Prandtl-Numbers of Ethylene Glycol-Water Mixtures. *Ber. Der Bunsenges. Für Phys. Chem.* **1984**, *88*, 739–742. [[CrossRef](#)]
35. Ma, M.-G.; Zhu, Y.-J.; Chang, J. Monetite Formed in Mixed Solvents of Water and Ethylene Glycol and Its Transformation to Hydroxyapatite. *J. Phys. Chem. B* **2006**, *110*, 14226–14230. [[CrossRef](#)]
36. Thommes, M.; Kaneko, K.; Neimark, A.V.; Olivier, J.P.; Rodriguez-Reinoso, F.; Rouquerol, J.; Sing, K.S.W. Physisorption of gases, with special reference to the evaluation of surface area and pore size distribution (IUPAC Technical Report). *Pure Appl. Chem.* **2015**, *87*, 1051–1069. [[CrossRef](#)]

Article

Solvothermal Synthesis of Calcium Hydroxyapatite via Hydrolysis of Alpha-Tricalcium Phosphate in the Presence of Different Organic Additives

Rasa Karalkeviciene ¹, Eva Raudonyte-Svirbutaviciene ¹, Aleksej Zarkov ^{1,*}, Jen-Chang Yang ², Anatoli I. Popov ³ and Aivaras Kareiva ¹

¹ Institute of Chemistry, Faculty of Chemistry and Geosciences, Vilnius University, Naugarduko 24, LT-03225 Vilnius, Lithuania

² Graduate Institute of Nanomedicine and Medical Engineering, College of Biomedical Engineering, Taipei Medical University, 250 Wu-Hsing St., Taipei 11052, Taiwan

³ Institute of Solid State Physics, University of Latvia, Kengaraga 8, LV-1063 Riga, Latvia

* Correspondence: aleksej.zarkov@chf.vu.lt

Abstract: In this study, the effects of sodium lauryl sulfate and various amino acids (DL-aspartic acid, dodecanedioic acid, and suberic acid) on the formation of calcium-deficient hydroxyapatite via hydrolysis of α -tricalcium phosphate (α -TCP) were investigated; moreover, a combined effect of these additives and ethylene glycol as a synthesis medium was also estimated. The hydrolysis reaction was performed in solutions containing different concentrations of additives in aqueous and mixed aqueous–organic media under solvothermal conditions. It was demonstrated that the nature and the concentration of organic additives influence the phase purity and morphology of the final product. Higher concentrations of sodium lauryl sulfate and dodecanedioic acid induced the formation of impurities in addition to hydroxyapatite, while aspartic and suberic acid did not affect the phase purity. The morphology of the samples varied from plate- to rod-like depending on the concentrations of specific organic additive.



Citation: Karalkeviciene, R.; Raudonyte-Svirbutaviciene, E.; Zarkov, A.; Yang, J.-C.; Popov, A.I.; Kareiva, A. Solvothermal Synthesis of Calcium Hydroxyapatite via Hydrolysis of Alpha-Tricalcium Phosphate in the Presence of Different Organic Additives. *Crystals* **2023**, *13*, 265. <https://doi.org/10.3390/cryst13020265>

Academic Editor: Ruikang Tang

Received: 5 January 2023

Revised: 30 January 2023

Accepted: 1 February 2023

Published: 3 February 2023



Copyright: © 2023 by the authors. Licensee MDPI, Basel, Switzerland. This article is an open access article distributed under the terms and conditions of the Creative Commons Attribution (CC BY) license (<https://creativecommons.org/licenses/by/4.0/>).

Keywords: calcium hydroxyapatite; α -tricalcium phosphate; amino acids; organic additives; solvothermal synthesis

1. Introduction

Calcium phosphates (CPs) are the group of materials which are widely used in different areas, including medicine and bone regeneration [1], catalysis [2], sorption of organic pollutants [3], and heavy metals [4], as host matrices for the development of optical materials [5] and many others. Probably, the most popular member of the CPs family is calcium hydroxyapatite ($\text{Ca}_{10}(\text{PO}_4)_6(\text{OH})_2$, HAp), which is the main inorganic component of human hard tissues.

HAp crystallizes in a hexagonal crystal structure with a space group $P6_3/m$. The crystal structure of HAp is notable due to the fact that it has two types of crystal planes, namely, *a*-face and *c*-face. The *a*-face is positively charged due to calcium ions, while the *c*-face is negatively charged due to oxygen atoms belonging to phosphate ions [6]. Anisotropic growth of HAp crystals in one or another crystallographic direction is an important factor from the point of view of specific interaction of oriented crystals with other substances, which may lead to enhanced performance and specific application of this material. For example, the adsorption of proteins on HAp crystals depends on their morphology. Different types of proteins, such as basic and acidic proteins, can adsorb selectively on the crystal planes of HAp [7,8]. Another effect of crystallographically oriented HAp particles was shown by Goto et al. [3] who demonstrated that tuning the morphology of HAp crystals may lead to enhanced or selective adsorption of cationic or anionic dyes. In this light,

the controllable synthesis of plate-like or rod-like crystals with different aspect ratios and surface charges is an important task for many industries and purification technologies.

Synthetic HAp can be obtained in a variety of ways, including solid-state reaction [9], sol-gel method [10], as well as wet precipitation [11], hydrothermal [12] and solvothermal syntheses [13], and others. Another group of synthetic approaches employed for the synthesis of HAp considers the phase conversion from other less stable CPs. For instance, Ca-deficient HAp can be obtained through the transformation from alpha-tricalcium phosphate ($\text{Ca}_3(\text{PO}_4)_2$, α -TCP) or amorphous CP in aqueous medium [14]. Synthetic pathways employing high-temperature treatment, such as solid-state reaction or sol-gel, usually result in the formation of large agglomerated particles and do not lead to the anisotropic growth of the crystals. Crystallographically oriented products are usually obtained by low-temperature wet chemical methods.

Functional groups of organic substances, such as carboxyl or amino, can specifically interact with the planes of HAp particles during the crystal growth process and affect particle growth in one or another direction. Different additives were previously employed in order to investigate their effect on the crystal growth, morphology, and properties of HAp. For instance, Suchanek et al. [15] successfully synthesized HAp nanofibers in the presence of monoethanolamine under hydrothermal conditions. In et al. [16] investigated the role of sebacic acid on the formation of HAp and demonstrated that sebacic acid can accelerate nucleation and act as an inhibitor in the specific direction of HAp crystal growth. Jiang et al. [17] showed that poly(acrylic acid), depending on its concentration, can promote or inhibit HAp crystallization; moreover, the composition of mixed aqueous-organic reaction medium also has an effect on the crystallization and morphology of HAp [18].

In the present work, a comprehensive study has been performed to investigate the influence of various organic additives on the phase purity and morphology of HAp synthesized via a hydrolysis of α -TCP under hydrothermal/solvothermal conditions. The effects of different concentrations of sodium lauryl sulfate (SLS, $\text{CH}_3(\text{CH}_2)_{11}\text{OSO}_3\text{Na}$) and three amino acids—dodecanedioic acid ($\text{C}_{12}\text{H}_{22}\text{O}_4$), DL-aspartic acid ($\text{C}_4\text{H}_7\text{NO}_4$), and suberic acid ($\text{C}_8\text{H}_{14}\text{O}_4$)—were studied and compared. To the best of our knowledge, the effect of these additives on the hydrolysis of low-temperature synthesized metastable α -TCP and simultaneous formation of HAp had never been investigated. These compounds have different functional groups and different carbon chain length. Two of the selected molecules contain only carboxyl groups (dodecanedioic and suberic acids); however, they have different chains containing 12 and 8 carbon atoms, respectively. Aspartic acid has a very short chain having only 4 carbon atoms. At the same time, in addition to the carboxyl group, there is a $-\text{NH}_2$ group in this molecule. Finally, sodium lauryl sulfate has a long chain (C12) and an SO_4^- functional group, which is absent in other selected molecules; moreover, a complex effect of amino acids and ethylene glycol was studied as well.

2. Materials and Methods

2.1. Synthesis

Starting α -TCP powders were synthesized following the procedure described elsewhere [19]. Briefly, a certain amount (3.42 g) of calcium nitrate tetrahydrate ($\text{Ca}(\text{NO}_3)_2 \cdot 4\text{H}_2\text{O}$, 99%, Roth, Karlsruhe, Germany) was dissolved in 20 mL of deionized water and a portion of diammonium hydrogen phosphate ($(\text{NH}_4)_2\text{HPO}_4$, 98%, Roth, Karlsruhe, Germany) (1.27 g) was dissolved in a separate beaker in 15 mL of deionized water. After a full dissolution, 5 mL of concentrated ammonium hydroxide (NH_4OH , 25%, Roth, Karlsruhe, Germany) was added to the $(\text{NH}_4)_2\text{HPO}_4$ solution and stirred; subsequently, the Ca-containing solution was added, rapidly resulting in the formation of white precipitates, which were aged in the solution for 10 min. Next, the precipitates were filtered and washed with 100 mL of deionized water and 150 mL of isopropyl alcohol. The synthesis product was dried overnight in an oven at 50 °C and annealed at 700 °C for 5 h with a heating rate of 5 °C/min.

The α -TCP was further used as a precursor for the synthesis of hydroxyapatite (HAp) via a hydrolysis reaction under hydrothermal conditions. The reactions were performed in the presence of different concentrations of sodium lauryl sulfate (SLS, $\text{NaC}_{12}\text{H}_{25}\text{SO}_4$, $\geq 99\%$, Roth, Karlsruhe, Germany) and amino acids—dodecanedioic acid (DDDA, $\text{C}_{12}\text{H}_{22}\text{O}_4$, 99%, Sigma Aldrich, Darmstadt, Germany), DL-aspartic acid (Asp, $\text{C}_4\text{H}_7\text{NO}_4$, 99%, Sigma Aldrich, Darmstadt, Germany), and suberic acid (Sa, $\text{C}_8\text{H}_{14}\text{O}_4$, 99%, Sigma Aldrich, Darmstadt, Germany). In a typical procedure, 0.3 g of α -TCP powder and appropriate amount of SLS or amino acids were placed into a 90 mL polytetrafluoroethylene-lined stainless-steel pressure vessel, diluted with 20 mL of water, and treated at 200 °C for 5 h.

Solvothermal reactions were performed in the presence of different concentrations of DL-aspartic acid and suberic acid in water and ethylene glycol (W:EG) mixture (*v/v* ratio of 40:60). The synthetic procedure was analogical to that with aqueous solutions.

After the hydrothermal treatment the resulting powders were filtered, washed with ethyl alcohol, and dried at 50 °C overnight. The sample notations and concentrations of additives in the reaction solution are given in Table 1.

Table 1. Sample codes, used organic additive, concentration of additives, and reaction media.

| Notation | Organic Additive | Concentration of Additive | Water to Ethylene Glycol Ratio (<i>v/v</i>) |
|------------|-----------------------|---------------------------|---|
| SLS:005 | Sodium lauryl sulfate | 0.005 mol/L | 100:0 |
| SLS:025 | Sodium lauryl sulfate | 0.025 mol/L | 100:0 |
| SLS:05 | Sodium lauryl sulfate | 0.05 mol/L | 100:0 |
| SLS:075 | Sodium lauryl sulfate | 0.075 mol/L | 100:0 |
| SLS:1 | Sodium lauryl sulfate | 0.1 mol/L | 100:0 |
| DDDA:005 | Dodecanedioic acid | 0.005 mol/L | 100:0 |
| DDDA:025 | Dodecanedioic acid | 0.025 mol/L | 100:0 |
| DDDA:05 | Dodecanedioic acid | 0.05 mol/L | 100:0 |
| DDDA:075 | Dodecanedioic acid | 0.075 mol/L | 100:0 |
| DDDA:1 | Dodecanedioic acid | 0.1 mol/L | 100:0 |
| Asp:005 | DL-Aspartic acid | 0.005 mol/L | 100:0 |
| Asp:025 | DL-Aspartic acid | 0.025 mol/L | 100:0 |
| Asp:05 | DL-Aspartic acid | 0.05 mol/L | 100:0 |
| Asp:075 | DL-Aspartic acid | 0.075 mol/L | 100:0 |
| Asp:1 | DL-Aspartic acid | 0.1 mol/L | 100:0 |
| Sa:005 | Suberic acid | 0.005 mol/L | 100:0 |
| Sa:025 | Suberic acid | 0.025 mol/L | 100:0 |
| Sa:05 | Suberic acid | 0.05 mol/L | 100:0 |
| Sa:075 | Suberic acid | 0.075 mol/L | 100:0 |
| Sa:1 | Suberic acid | 0.1 mol/L | 100:0 |
| Asp:005:EG | DL-Aspartic acid | 0.005 mol/L | 40:60 |
| Asp:025:EG | DL-Aspartic acid | 0.025 mol/L | 40:60 |
| Asp:05:EG | DL-Aspartic acid | 0.05 mol/L | 40:60 |
| Asp:075:EG | DL-Aspartic acid | 0.075 mol/L | 40:60 |
| Asp:1:EG | DL-Aspartic acid | 0.1 mol/L | 40:60 |
| Sa:005:EG | Suberic acid | 0.005 mol/L | 40:60 |

Table 1. Cont.

| Notation | Organic Additive | Concentration of Additive | Water to Ethylene Glycol Ratio (w/v) |
|-----------|------------------|---------------------------|--------------------------------------|
| Sa:025:EG | Suberic acid | 0.025 mol/L | 40:60 |
| Sa:05:EG | Suberic acid | 0.05 mol/L | 40:60 |
| Sa:075:EG | Suberic acid | 0.075 mol/L | 40:60 |
| Sa:1:EG | Suberic acid | 0.1 mol/L | 40:60 |

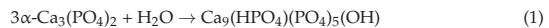
2.2. Characterization

Powder X-ray diffraction data were collected on a Rigaku miniFlex II diffractometer (Rigaku, The Woodlands, TX, USA) working in Bragg–Brentano ($\theta/2\theta$) geometry, using Ni-filtered Cu $K\alpha_1$ radiation. The data were collected within a 2θ angle range from 10 to 60° at a step width of 0.01° and speed of $5^\circ/\text{min}$. Infrared (FTIR) spectra were taken in the range of $4000\text{--}400\text{ cm}^{-1}$ with Bruker Alpha ATR spectrometer (Bruker, Billerica, MA, USA). To study the morphological features of the samples, a field-emission scanning electron microscope (FE-SEM), the Hitachi SU-70 (FE-SEM, Hitachi, Tokyo, Japan), was employed.

3. Results

The XRD pattern and FTIR spectrum of starting α -TCP powder used for the synthesis of CDHA are shown in Figures S1 and S2 (see Supplementary Materials), respectively. The XRD pattern did not reveal the presence of neighboring crystalline CP, such as β -TCP or others, and all diffraction peaks were ascribed to α -TCP. The FTIR spectrum confirms the results of XRD analysis. The shape of the spectrum is in a good agreement with those reported in literature [20]; moreover, the absence of absorption band at around 729 cm^{-1} indicates the absence of calcium pyrophosphate, which is a commonly observed impurity in TCP powders synthesized by wet precipitation [21].

In aqueous medium α -TCP reacts with water and converts to calcium-deficient hydroxyapatite ($\text{Ca}_9(\text{HPO}_4)(\text{PO}_4)_5(\text{OH})$, CDHA), as described by the following equation [13]:



The characteristics of the CDHA sample prepared in aqueous solution under hydrothermal conditions without any additives are given in Figure 1. As seen from the XRD pattern, under selected synthesis conditions α -TCP was fully converted to CDHA, and all diffraction peaks matched the standard XRD data of $\text{Ca}_{10}(\text{PO}_4)_6(\text{OH})_2$ (ICDD #00-76-0694). There were no peaks associated with the starting material. The SEM image revealed that the morphology of the sample was dominated by plate-like particles of micrometric dimensions. HAp of slightly different morphology was obtained from commercial α -TCP by Goto et al. [13]. The difference might be due to the different starting α -TCP, since the authors used commercial α -TCP of micrometric size, whereas our α -TCP consisted of smaller particles [20].

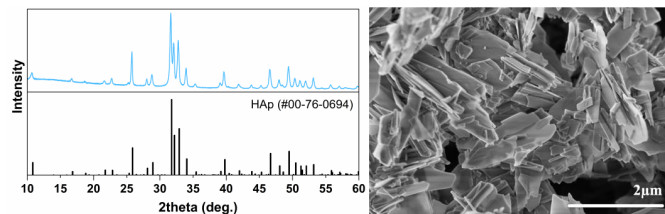


Figure 1. XRD pattern (left) and SEM image (right) of HAp prepared from α -TCP without additives.

Different results were observed when varying concentrations of SLS and amino acids were applied as additives. The XRD patterns of the final products are given in Figure 2. The lowest concentration of SLS (0.005 mol/L) did not affect the formation of CDHA in terms of phase purity; however, increasing the SLS amount in the reaction solution resulted in the formation of neighboring phase (Figure 2a). In addition to the typical CDHA diffraction pattern, a sharp peak at ca. 25.4° could be seen, and the intensity of this peak gradually increased with an increase in the SLS concentration. This peak was attributed to calcium sulfate (CaSO_4 , ICDD #00-072-0503). The observed results suggest that under selected synthesis conditions the released Ca^{2+} ions were more easily precipitated by SO_4^{2-} counterions rather than phosphate species. A similar trend was observed for DDDA: the lowest concentration of DDDA (0.005 mol/L) did not affect the formation of CDHA, but higher DDDA content resulted in the formation of secondary crystal phase (Figure 2c). The diffraction peak centered at ca. 13.6° emerged in the XRD pattern of the sample prepared using 0.025 mol/L DDDA. The intensity of this peak increased significantly with an increase in DDDA concentration. This peak corresponded to calcium hydrogen phosphate hydrate ($\text{CaH}_3\text{O}_5\text{P}$, ICDD #00-046-0494). Hydrothermal reactions in the presence of DL-aspartic and suberic acids resulted in the formation of single-phase CDHA, regardless of the concentration of additives (Figure 2b,d). No formation of impurities or traces of TCP were observed in these cases. It should be noted that in the case of suberic acid (Figure 2d) the intensity of three major peaks varied depending on the concentration of the additive, which could suggest the change in the powders' morphology. To summarize, two of four selected additives led to the formation of secondary phases, while two others did not affect the phase purity.

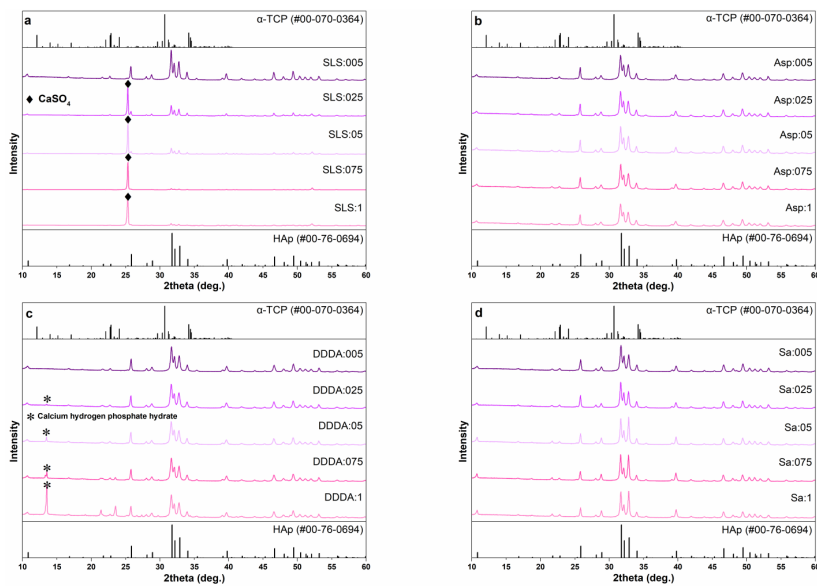


Figure 2. XRD patterns of the samples prepared using various concentrations of SLS (a), DL-aspartic acid (b), dodecanedioic acid (c), and suberic acid (d) after a hydrothermal treatment at 200°C for 5 h.

In this study, we also aimed to check the combined effect of amino acids and organic solvents on the phase purity and morphology of the sample. Since single-phase CDHA was obtained using DL-aspartic and suberic acids, these two additives were used for further experiments. Our previous study revealed that among various organic solvents, ethylene glycol had the greatest influence on the sample morphology [18]. The highest effect on morphology was observed with water to ethylene glycol ratio of 40:60; hence, solvothermal synthesis with DL-aspartic and suberic acids was performed with this mixture. The XRD patterns of the reaction products are demonstrated in Figure 3.

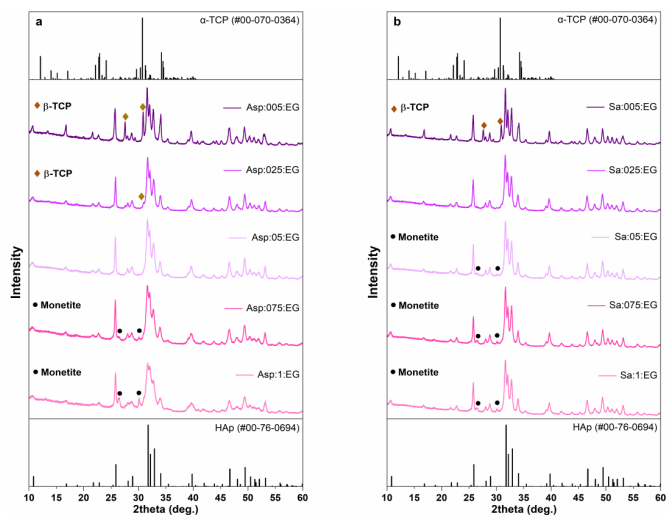


Figure 3. XRD patterns of the samples prepared using various concentrations of DL-aspartic (a) and suberic (b) acids in water–ethylene glycol mixture (40:60, *v/v*) after a solvothermal treatment at 200 °C for 5 h.

It is seen that phase composition strongly depends on the concentration of additive. With the lowest concentration of DL-aspartic acid (0.005 mol/L), a significant amount of neighboring β -TCP phase was obtained along with a major CDHA phase; however, the amount of β -TCP was reduced with an increase in the concentration of additive (Figure 3a). The XRD pattern of the sample synthesized with 0.05 mol/L of aspartic acid did not reveal the presence of any secondary crystal phase. At the same time, the diffraction peaks attributed to monetite (CaHPO_4) emerged in the XRD patterns with the highest concentrations of acid (0.075 and 0.1 mol/L). The presence of suberic acid demonstrated a very similar effect (Figure 3b) with a minor difference in phase composition. In this case, a negligible amount of monetite was detected already in the sample with the concentration of acid of 0.05 mol/L. In our previous study [18], the formation of monetite in the presence of organic solvents was also observed at higher temperatures (200 °C) of the solvothermal treatment; however, in this case, increasing concentrations of amino acids promoted the formation of monetite revealing the complex nature of phase transitions in CPs.

Figures 4 and 5 present the FTIR spectra of the samples prepared by hydrothermal and solvothermal treatments.

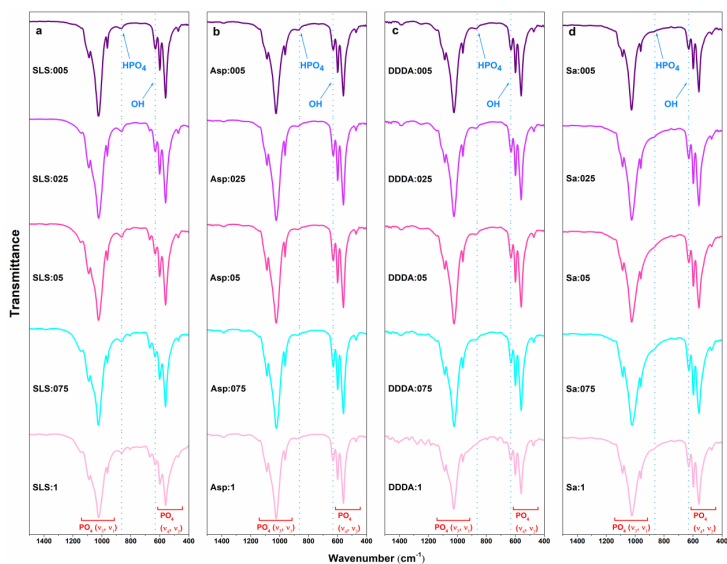


Figure 4. FTIR spectra of the samples prepared using various concentrations of SLS (a), DL-aspartic acid (b), dodecanedioic acid (c), and suberic acid (d) after a hydrothermal treatment at 200 °C for 5 h.

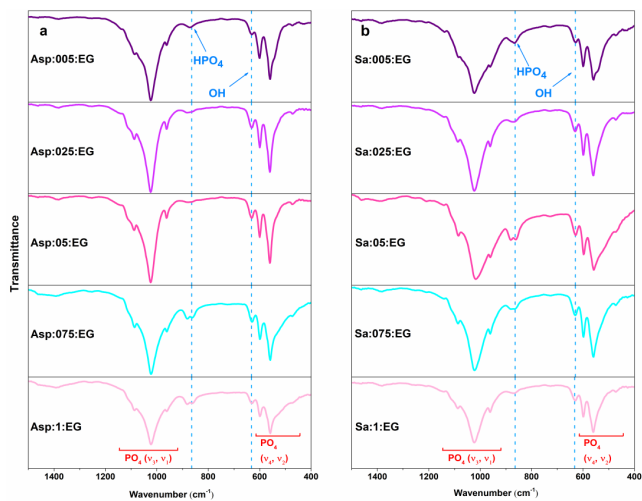


Figure 5. FTIR spectra of the samples prepared using various concentrations of DL-aspartic (a) and suberic (b) acids in water–ethylene glycol mixture (40:60, *v/v*) after a solvothermal treatment at 200 °C for 5 h.

The spectral range of 1500–400 cm^{-1} was chosen as representative, because in this range the main absorption bands assigned to CDHA can be observed. As was expected, all the spectra exhibited the absorption bands characteristic of CDHA [22]. The absorption bands of phosphate group in CDHA structure were observed at ca. 560 and 603 cm^{-1} (ν_4), 1020 and 1090 cm^{-1} (ν_3), 960 cm^{-1} (ν_1) which were assigned to O–P–O bending, asymmetric P–O stretching, and symmetric P–O stretching vibrations, respectively. The O–P–O bending vibration mode (ν_2) was observed at 470 cm^{-1} and the band at ca. 630 cm^{-1} was assigned to the hydroxyl group [22]. The absorption band centered at around 870 cm^{-1} was ascribed to the P–O(H) stretching mode of the HPO_4^{2-} group, which confirms the formation of CDHA, since this group is absent in stoichiometric non-deficient HAp [14]. Other bands of low intensity (Figure 4a,c) can be ascribed to the impurities formed during the synthesis and identified by XRD.

The FTIR spectra of synthesized products in the range from 4000 to 400 cm^{-1} are provided in Figures S3–S8; moreover, the spectra of the used organic additives are shown for comparison. The broader range additionally reveals the presence of absorption band centered at ca. 3570 cm^{-1} , which corresponds to the stretching mode of the hydroxyl group [22]. It is seen that in most cases the absorption bands corresponding to additives are absent in the spectra of fabricated CDHA powders, which suggests that the additives were removed from the surface during the washing procedure or the amount of residual organic species is negligible and cannot be detected by FTIR spectroscopy. The only exceptions are the products synthesized with DDDA (Figure S5). The absorption band of DDDA at 1690 cm^{-1} is visible in the spectra of samples synthesized with concentrations of 0.05 mol/L and higher.

The particle size and morphology of HAp are important characteristics of this material due to several reasons [23]. For instance, Dey et al. [24] studied the influence of HAp particle size, morphology, and crystallinity on proliferation of HCT116 colon cancer cells. It was demonstrated that decreasing the HAp powder crystallite size significantly increases the cell inhibition. Another study investigated the effect of nano-HAp particles of different sizes on the proliferation of odontoblast-like MDPC-23 cells comparing them with conventional HAp [25]. The results revealed that nano-HAp expressed an obvious growth-promoting effect. Wen et al. [26] showed that the larger specific surface area associated with the smaller particle size was beneficial for the drug-loading properties of HAp.

The morphology of the samples was found to be dependent both on the nature and concentration of the organic additive. When a small amount of SLS (0.005 mol/L) was used in the hydrothermal reaction, the plate-like crystals dominated in the sample; however, a small number of rods were also seen (Figure 6a). After increasing the amount of organic compound (0.05–0.1 mol/L), the morphology of the CDHA powders changed considerably and rod-shaped assemblies started to form (Figure 6e,i). The huge plate seen in Figure 6i corresponds to CaSO_4 . The use of low concentration of DL-aspartic acid resulted in the formation of micrometric plate-like particles (Figure 6b), while increasing the amount of acid first led to the reduction of particle size (Figure 6f) and further formation of some rods (Figure 6j). The effect of DDDA was similar to that of aspartic acid and the morphology evolution from plate-like particles to the mixture of plates and rods was observed with an increase in additive concentration. The influence of suberic acid on the morphology of CDHA samples was found to be minor, and plate-like particles were obtained regardless of the concentration of acid. We assume that the effect on the sample morphology might become prominent if the concentrations of suberic acid were further increased.

The SEM images of the samples synthesized in a mixture of water and ethylene glycol in the presence of DL-aspartic and suberic acids are given in Figure 7. In the case of aspartic acid, the presence of the lowest concentration of additive resulted in the formation of a mixture of relatively long rods and short rods (Figure 7a). Using a higher concentration of aspartic acid obtained powders which consisted of micrometric agglomerates, which, in turn, were composed of smaller plate- and rod-like particles (Figure 7b–e). The size of the particles was significantly smaller compared to those synthesized in the aqueous medium

(Figure 6). In the case of suberic acid, relatively large plate-like particles were obtained regardless of the concentration of additive (Figure 7f–j). The morphology was comparable with that of powders obtained by the hydrothermal synthesis with no additives.

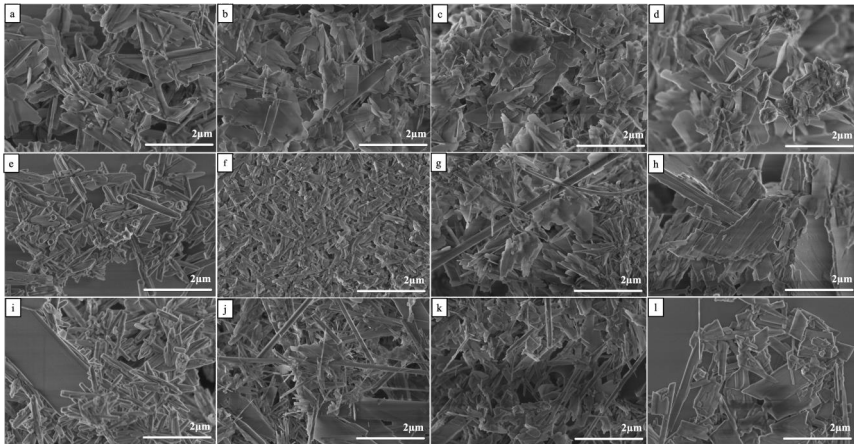


Figure 6. SEM micrographs of the samples after hydrothermal treatment SLS:0.05 (a), SLS:0.5 (e), and SLS:1 (i); Asp:0.05 (b), Asp:0.5 (f), and Asp:1 (j); DDDA:0.05 (c), DDDA:0.5 (g), and DDDA:1 (k); and Sa:0.05 (d), Sa:0.5 (h), and Sa:1 (l).

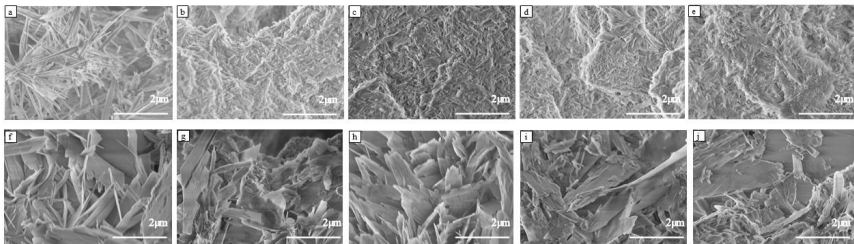


Figure 7. SEM micrographs of the samples after solvothermal treatment under ratio 40:60 of water to ethylene glycol Asp:0.05:EG (a), Asp:0.25:EG (b), Asp:0.5:EG (c), Asp:0.75:EG (d), and Asp:1:EG (e); and Sa:0.05:EG (f), Sa:0.25:EG (g), Sa:0.5:EG (h), Sa:0.75:EG (i), and Sa:1:EG (j).

To summarize, different impact of additives on the morphology of HAP is probably related to different structures and chemical compositions of organic additives, which leads to a different interaction with HAP particles during the nucleation and crystal growth process.

4. Conclusions

A comprehensive experimental study was carried out to compare the effects of sodium lauryl sulfate and three amino acids (DL-aspartic acid, dodecanedioic acid, and suberic acid) on the formation of calcium-deficient hydroxyapatite via a hydrolysis of α -tricalcium phosphate. It was demonstrated that the phase purity and morphology of the final product strongly depends on the nature and the concentration of organic additives. In aqueous

medium at particular concentrations of sodium lauryl sulfate and dodecanedioic acid, the formation of impurities in addition to hydroxyapatite was observed. On the other hand, the use of aspartic and suberic acids did not affect the phase purity. The different impacts of additives on the morphology of hydroxyapatite are probably related to the different structures and chemical compositions of the organic additives, which lead to different interactions with hydroxyapatite particles during the nucleation and crystal growth process. The morphology of the samples prepared in the aqueous medium varied from plate- to rod-like depending on the concentrations of the specific organic additive. The use of a mixture of water and ethylene glycol led to the formation of significantly smaller particles having a shape of rods and narrow plates.

Supplementary Materials: The following supporting information can be downloaded at: <https://www.mdpi.com/article/10.3390/cryst13020265/s1>, Figure S1: XRD pattern of α -TCP used for the synthesis of CDHA; Figure S2: FTIR spectrum of α -TCP used for the synthesis of CDHA; and Figures S3–S8: FTIR spectra of the samples prepared using various concentrations of SLS, DL-aspartic acid, dodecanedioic acid, and suberic acid in the range from 4000 to 400 cm^{-1} .

Author Contributions: Conceptualization, R.K., A.Z. and A.K.; methodology, R.K.; validation, E.R.-S., J.-C.Y. and A.I.P.; formal analysis, R.K. and A.I.P.; investigation, R.K., E.R.-S., A.I.P. and J.-C.Y.; resources, A.K.; data curation, A.I.P.; writing—original draft preparation, R.K.; writing—review and editing, A.K.; visualization, R.K.; supervision, A.K.; project administration, A.Z.; and funding acquisition, A.Z. All authors have read and agreed to the published version of the manuscript.

Funding: This research was funded by the grant WHITERAM (No. S-LJB-22-1) from the Research Council of Lithuania.

Institutional Review Board Statement: Not applicable.

Informed Consent Statement: Not applicable.

Data Availability Statement: Not applicable.

Conflicts of Interest: The authors declare no conflict of interest.

References

1. Habraken, W.; Habibovic, P.; Epple, M.; Bohner, M. Calcium phosphates in biomedical applications: Materials for the future? *Mater. Today* **2016**, *19*, 69–87. [\[CrossRef\]](#)
2. Zikrata, O.V.; Larina, O.V.; Valihura, K.V.; Kyriienko, P.I.; Balakin, D.Y.; Khalakhan, I.; Veltruská, K.; Krajnc, A.; Mali, G.; Soloviev, S.O.; et al. Successive Vapor-Phase Guerbet Condensation of Ethanol and 1-Butanol to 2-Ethyl-1-hexanol over Hydroxyapatite Catalysts in a Flow Reactor. *ACS Sustain. Chem. Eng.* **2021**, *9*, 17289–17300. [\[CrossRef\]](#)
3. Goto, T.; Cho, S.H.; Ohtsuki, C.; Sekino, T. Selective adsorption of dyes on TiO_2 -modified hydroxyapatite photocatalysts morphologically controlled by solvothermal synthesis. *J. Environ. Chem. Eng.* **2021**, *9*, 105738. [\[CrossRef\]](#)
4. Ivanets, A.; Zarkov, A.; Prozorovich, V.; Venhlinkaya, E.; Radkevich, A.; Yang, J.-C.; Papynov, E.; Yarusova, S.; Kareiva, A. Effect of Mg^{2+} , Sr^{2+} , and Fe^{3+} -substitution on ^{85}Sr and ^{60}Co adsorption on amorphous calcium phosphates: Adsorption performance, selectivity, and mechanism. *J. Environ. Chem. Eng.* **2022**, *10*, 107425. [\[CrossRef\]](#)
5. Sinusaite, L.; Antuzevics, A.; Popov, A.I.; Rogulis, U.; Misevicius, M.; Katelnikovas, A.; Kareiva, A.; Zarkov, A. Synthesis and luminescent properties of Mn-doped alpha-tricalcium phosphate. *Ceram. Int.* **2021**, *47*, 5335–5340. [\[CrossRef\]](#)
6. Zhuang, Z.; Fujimi, T.J.; Nakamura, M.; Konishi, T.; Yoshimura, H.; Aizawa, M. Development of a,b-plane-oriented hydroxyapatite ceramics as models for living bones and their cell adhesion behavior. *Acta Biomater.* **2013**, *9*, 6732–6740. [\[CrossRef\]](#)
7. Kawasaki, T.; Takahashi, S.; Ideda, K. Hydroxyapatite high-performance liquid chromatography: Column performance for proteins. *Eur. J. Biochem.* **1985**, *152*, 361–371. [\[CrossRef\]](#)
8. Kawasaki, T.; Ikeda, K.; Takahashi, S.; Kuboki, Y. Further study of hydroxyapatite high-performance liquid chromatography using both proteins and nucleic acids, and a new technique to increase chromatographic efficiency. *Eur. J. Biochem.* **1986**, *155*, 249–257. [\[CrossRef\]](#)
9. Ezerskyte-Miseviciene, A.; Kareiva, A. Everything old is new again: A reinspection of solid-state method for the fabrication of high quality calcium hydroxyapatite bioceramics. *Mendeleev. Commun.* **2019**, *29*, 273–275. [\[CrossRef\]](#)
10. Bogdanoviciene, I.; Beganskiene, A.; Tonsuaadu, K.; Glaser, J.; Meyer, H.J.; Kareiva, A. Calcium hydroxyapatite, $\text{Ca}_{10}(\text{PO}_4)_6(\text{OH})_2$ ceramics prepared by aqueous sol-gel processing. *Mater. Res. Bull.* **2006**, *41*, 1754–1762. [\[CrossRef\]](#)
11. Ferraris, S.; Yamaguchi, S.; Barbari, N.; Cazzola, M.; Cristallini, C.; Miola, M.; Vernè, E.; Spriano, S. Bioactive materials: In vitro investigation of different mechanisms of hydroxyapatite precipitation. *Acta Biomater.* **2020**, *102*, 468–480. [\[CrossRef\]](#) [\[PubMed\]](#)

12. Jung, K.-W.; Lee, S.Y.; Choi, J.-W.; Lee, Y.J. A facile one-pot hydrothermal synthesis of hydroxyapatite/biochar nanocomposites: Adsorption behavior and mechanisms for the removal of copper(II) from aqueous media. *Chem. Eng. J.* **2019**, *369*, 529–541. [[CrossRef](#)]
13. Goto, T.; Kim, I.Y.; Kikuta, K.; Ohtsuki, C. Hydroxyapatite formation by solvothermal treatment of α -tricalcium phosphate with water–ethanol solution. *Ceram. Int.* **2012**, *38*, 1003–1010. [[CrossRef](#)]
14. Sinusaite, L.; Popov, A.; Raudonyte-Svirbutaviciene, E.; Yang, J.-C.; Kareiva, A.; Zarkov, A. Effect of Mn doping on hydrolysis of low-temperature synthesized metastable alpha-tricalcium phosphate. *Ceram. Int.* **2021**, *47*, 12078–12083. [[CrossRef](#)]
15. Suchanek, K.; Bartkowiak, A.; Perzanowski, M.; Marszalek, M. From monetite plate to hydroxyapatite nanofibers by monoethanolamine assisted hydrothermal approach. *Sci. Rep.* **2018**, *8*, 15408. [[CrossRef](#)]
16. In, Y.; Amornkitbamrung, U.; Hong, M.-H.; Shin, H. On the Crystallization of Hydroxyapatite under Hydrothermal Conditions: Role of Sebacic Acid as an Additive. *ACS Omega* **2020**, *5*, 27204–27210. [[CrossRef](#)]
17. Jiang, S.; Cao, Y.; Li, S.; Pang, Y.; Sun, Z. Dual function of poly(acrylic acid) on controlling amorphous mediated hydroxyapatite crystallization. *J. Cryst. Growth* **2021**, *557*, 125991. [[CrossRef](#)]
18. Karalkeviciene, R.; Raudonyte-Svirbutaviciene, E.; Gaidukevic, J.; Zarkov, A.; Kareiva, A. Solvothermal Synthesis of Calcium-Deficient Hydroxyapatite via Hydrolysis of α -Tricalcium Phosphate in Different Aqueous-Organic Media. *Crystals* **2022**, *12*, 253. [[CrossRef](#)]
19. Sinusaite, L.; Kareiva, A.; Zarkov, A. Thermally Induced Crystallization and Phase Evolution of Amorphous Calcium Phosphate Substituted with Divalent Cations Having Different Sizes. *Cryst. Growth Des.* **2021**, *21*, 1242–1248. [[CrossRef](#)]
20. Sinusaite, L.; Grigoraviciute-Puroniene, I.; Popov, A.; Ishikawa, K.; Kareiva, A.; Zarkov, A. Controllable synthesis of tricalcium phosphate (TCP) polymorphs by wet precipitation: Effect of washing procedure. *Ceram. Int.* **2019**, *45*, 12423–12428. [[CrossRef](#)]
21. Torres, P.M.C.; Vieira, S.I.; Cerqueira, A.R.; Pina, S.; da Cruz Silva, O.A.B.; Abrantes, J.C.C.; Ferreira, J.M.F. Effects of Mn-doping on the structure and biological properties of β -tricalcium phosphate. *J. Inorg. Biochem.* **2014**, *136*, 57–66. [[CrossRef](#)] [[PubMed](#)]
22. Koutsopoulos, S. Synthesis and characterization of hydroxyapatite crystals: A review study on the analytical methods. *J. Biomed. Mater. Res.* **2002**, *62*, 600–612. [[CrossRef](#)] [[PubMed](#)]
23. Zhou, H.; Lee, J. Nanoscale hydroxyapatite particles for bone tissue engineering. *Acta Biomater.* **2011**, *7*, 2769–2781. [[CrossRef](#)] [[PubMed](#)]
24. Dey, S.; Das, M.; Balla, V.K. Effect of hydroxyapatite particle size, morphology and crystallinity on proliferation of colon cancer HCT116 cells. *Mater. Sci. Eng. C* **2014**, *39*, 336–339. [[CrossRef](#)]
25. Li, N.; Wu, G.; Yao, H.; Tang, R.; Gu, X.; Tu, C. Size effect of nano-hydroxyapatite on proliferation of odontoblast-like MDPC-23 cells. *Dent. Mater. J.* **2019**, *38*, 534–539. [[CrossRef](#)]
26. Wen, Y.; Li, J.; Lin, H.; Huang, H.; Song, K.; Duan, K.; Guo, T.; Weng, J. Improvement of Drug-Loading Properties of Hydroxyapatite Particles Using Triethylamine as a Capping Agent: A Novel Approach. *Crystals* **2021**, *11*, 703. [[CrossRef](#)]

Disclaimer/Publisher's Note: The statements, opinions and data contained in all publications are solely those of the individual author(s) and contributor(s) and not of MDPI and/or the editor(s). MDPI and/or the editor(s) disclaim responsibility for any injury to people or property resulting from any ideas, methods, instructions or products referred to in the content.

NOTES

Vilnius University Press
9 Saulėtekio Ave., Building III, LT-10222 Vilnius
Email: info@leidykla.vu.lt, www.leidykla.vu.lt
bookshop.vu.lt, journals.vu.lt
Print run 20